Programa de Doctorado
Química y Tecnologías Químicas
Materiales y Nanotecnología

International PhD Thesis

Clinkering, processing and characterisation of Alite-Belite-Ye'elimite eco-cements: from basic to applied science

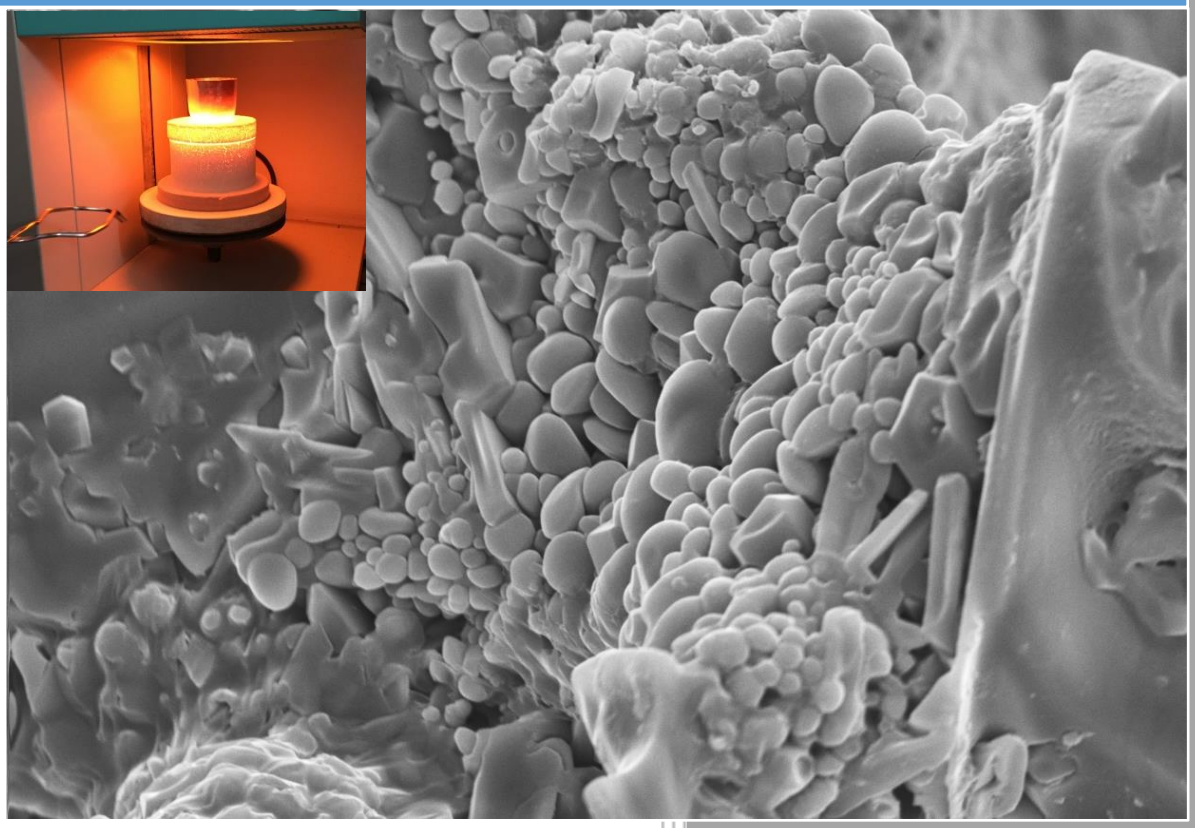

Jesús David Zea García

SUPERVISORS:

María Isabel Santacruz Cruz, PhD

María de los Ángeles Gómez de la Torre, PhD.

Universidad de Málaga

Facultad de Ciencias

Málaga, 2020

AUTOR: Jesús David Zea García

https://orcid.org/0000-0001-9469-7117

EDITA: Publicaciones y Divulgación Científica. Universidad de Málaga

DECLARACIÓN DE AUTORÍA Y ORIGINALIDAD DE LA TESIS PRESENTADA PARA OBTENER EL TÍTULO DE DOCTOR

D./Dña JESÚS DAVID ZEA GARCÍA
Estudiante del programa de doctorado QUÍMICA Y TECNOLOGÍAS QUÍMICAS. MATERIALES Y NANOTECNOLOGÍA de la Universidad de Málaga, autor/a de la tesis, presentada para la obtención del título de doctor por la Universidad de Málaga, titulada: CLINKERING, PROCESSING AND CHARACTERISATION OF ALITE-BELITE-YE'ELIMITE ECO-CEMENTS: FROM BASIC TO APPLIED SCIENCE

Realizada bajo la tutorización de MARÍA ISABEL SANTACRUZ CRUZ y dirección de MARÍA ISABEL SANTACRUZ CRUZ Y MARÍA DE LOS ÁNGELES GÓMEZ DE LA TORRE (si tuviera varios directores deberá hacer constar el nombre de todos)

DECLARO QUE:

La tesis presentada es una obra original que no infringe los derechos de propiedad intelectual ni los derechos de propiedad industrial u otros, conforme al ordenamiento jurídico vigente (Real Decreto Legislativo 1/1996, de 12 de abril, por el que se aprueba el texto refundido de la Ley de Propiedad Intelectual, regularizando, aclarando y armonizando las disposiciones legales vigentes sobre la materia), modificado por la Ley 2/2019, de 1 de marzo.

Igualmente asumo, ante a la Universidad de Málaga y ante cualquier otra instancia, la responsabilidad que pudiera derivarse en caso de plagio de contenidos en la tesis presentada, conforme al ordenamiento jurídico vigente.

En Málaga, a 10 de FEBRERO de 2020

Fdo.: JESÚS DAVID ZEA GARCÍA

PhD Thesis

Clinkering, processing and characterisation of Alite-Belite-Ye'elimite eco-cements: from basic to applied science

Jesús David Zea García

Universidad de Málaga
Facultad de Ciencias
Departamento de Química Inorgánica, Mineralogía y Cristalografía
Málaga, España
2020

PhD Thesis

Clinkering, processing and characterisation of Alite-Belite-Ye'elimite eco-cements: from basic to applied science

Autor:

Fdo: [redacted]

Jesús David Zea García

Tesis doctoral presentada como requisito para optar al título de:

Doctor en Química y Tecnologías Químicas. Materiales y Nanotecnología

"Mención Internacional"

Directoras:

Fdo: [redacted] **Fdo:** [redacted]

Dra. María Isabel Santacruz Cruz **Dra. Mª Ángeles Gómez de la Torre**

Universidad de Málaga
Facultad de Ciencias
Departamento de Química Inorgánica, Mineralogía y Cristalografía
Málaga, España

2020

Dra. MARÍA ISABEL SANTACRUZ CRUZ, Profesora Titular de la Universidad de Málaga y Dra. MARÍA DE LOS ÁNGELES GÓMEZ DE LA TORRE, Profesora Titular de la Universidad de Málaga, ambas pertenecientes al Departamento de Química Inorgánica, Cristalografía y Mineralogía de la Facultad de Ciencias de la Universidad de Málaga,

CERTIFICAN:

Que la presente memoria realizada por D JESÚS DAVID ZEA GARCÍA, titulada: "**Clinkering, processing and characterisation of Alite-Belite-Ye'elimite eco-cements: from basic to applied science**", ha sido realizada bajo nuestra dirección en el Departamento de Química Inorgánica, Cristalografía y Mineralogía de la Facultad de Ciencias de la Universidad de Málaga. Este trabajo reúne, a nuestro juicio, contenido científico suficiente y las condiciones necesarias para ser presentado y defendido ante el tribunal correspondiente para optar al título de Doctor.

Málaga a 10 de Febrero de 2020

[redacted]

UNIVERSIDAD DE MÁLAGA · DPTO. DE QUÍMICA INORG. · FACULTAD DE CIENCIAS

[redacted]

Fdo.: Dra. María Isabel Santacruz Cruz

Fdo.: Dra. María de los Ángeles Gómez de la Torre

Dr. PEDRO JESÚS MAIRELES TORRES, Catedrático de la Universidad de Málaga y Director del Departamento de Química Inorgánica, Cristalografía y Mineralogía de la Facultad de Ciencias de la misma universidad,

INFORMA:

Que la presente memoria realizada por D JESÚS DAVID ZEA GARCÍA, titulada: "**Clinkering, processing and characterisation of Alite-Belite-Ye'elimite eco-cements: from basic to applied science**", ha sido realizada bajo la dirección de las Profesoras Titulares Dª María Isabel Santacruz Cruz y Dª María de los Ángeles Gómez de la Torre en el Departamento de Química Inorgánica, Cristalografía y Mineralogía de la Facultad de Ciencias de la Universidad de Málaga. Este trabajo constituye la Memoria de Tesis Doctoral del interesado, cuya presentación autorizo en Málaga a 10 de Febrero de 2020.

Málaga a 10 de Febrero de 2020

UNIVERSIDAD DE MÁLAGA DPTO. DE QUÍMICA INORG. FACULTAD DE CIENCIAS

[redacted]

Fdo.:

Dr. Pedro Jesús Maireles Torres

AGRADECIMIENTOS

Mis primeros agradecimientos han de dirigirse hacia la Universidad de Málaga, y más concretamente al Departamento de Química Inorgánica, Cristalografía y Mineralogía perteneciente a esta misma universidad por darme la oportunidad de llevar a cabo este intenso trabajo de investigación. También he de agradecer a los Servicios Centrales de Apoyo a la Investigación (SCAI) de la Universidad de Málaga el haber podido hacer uso de sus instalaciones y equipos.

Esta memoria de tesis ha sido desarrollada gracias al interés y esfuerzo de muchas personas, las cuales de manera directa o indirecta han contribuido en la parte profesional y personal. Por ello, quiero dedicar las siguientes palabras a todos ellos y ellas.

Han sido cuatro años de muy duro trabajo, que sin duda alguna no habría podido concluir sin los consejos, la guía, el apoyo y el saber de mis directoras, la Dra. Mª Isabel Santacruz Cruz y la Dra. Mª de los Ángeles Gómez de la Torre, que han logrado que esta tesis doctoral saliera delante de manera muy satisfactoria. Les tengo que agradecer la oportunidad que me dieron para trabajar con ellas, desarrollar una investigación y convertirme en investigador. Ni que decir tiene lo importante que es tener unas directoras con las que se pueda contar para poder aclarar dudas, inquietudes o simplemente hablar de la vida, son cosas que hacen que el doctorando coja apego y ánimos para continuar y llegar a finalizar este trabajo.

Agradecer también a mi grupo de investigación del cual, además de mis directoras, hay otras personas que han contribuido con mi desarrollo y adquisición de conocimiento. Al Dr. Miguel Ángel García Aranda y la Dra. Ana Cuesta García que han sido un pilar para poder adentrarme en el mundo del PDF aplicado a los cementos. A la ya Dra. Diana Londoño Zuluaga (mi compañerita) que estuvo a mi lado desde el comienzo de mi tesis y que como cabe esperar sus consejos y aportaciones han sido muy importantes para mí. Al Dr. Wenzhong Zhu por recibirme e instruirme durante mi estancia en escocia (University of the West of Scotland). A Susana que desde la distancia (Noruega) ha contribuido a mi trabajo. A Oriol por lo atento que ha sido cada vez que hemos realizado un experimento en ALBA. A Edmundo por esa cámara de HP y HT que desarrolló para hacer medidas. A Ariel por esas estancias predoctorales que ha pasado con nosotros y por su humor. A Alejandro por haberme acompañado en la última etapa de mi tesis y que cuenta con un sentido del humor que puede hacer que te

olvides de los problemas. A Shiva, que aunque no he tenido el placer de trabajar a su lado, los ratos de charla en ingles han sido muy fructíferos. Y por último a todos los estudiantes de máster y grado, que he podido conocer a lo largo de mi doctorado, los cuales siempre me han aportado nuevas ideas y perspectivas que han sido muy enriquecedoras.

A todas y todos los miembros del departamento de Química Inorgánica, Cristalografía y Mineralogía, tengo que agradecer a muchas personas por la ayuda prestada en cualquier momento, por los buenos ratos que hemos pasado y por los consejos y posibles soluciones a problemas que para mí se presentaban difíciles de resolver. Un fuerte abrazo al Dr. Enrique Losilla y al Dr. Aurelio por estar siempre dispuesto a escuchar y a ayudar. Al Dr. Pedro Jesús Maireles Torres, por ser un director de departamento siempre atento. A los doctores y doctoras Pepe Santa, Pepe Jiménez, Pascual, Enrique Castellón, Laureano, Ramón, Toñi, Pili y Pepi (todos ellos/as profesores/as del departamento que en un momento dado me han ayudado de una forma u otra).

Un fuerte agradecimiento a Antonio Morales que como técnico de laboratorio del departamento, no solo me ha ayudado cuando necesitaba cualquier material para poder llevar a cabo mi trabajo, sino que también ha sido un pilar con el que hablar y pedir consejos.

Agradecer a la Dra. Laura León Reina y Estefanía por haber sido unas técnicas de DRX tan eficientes, simpáticas y cercanas.

Otro agradecimiento a los posdoc y predoc del departamento “los becarios”: José, Inés, María José, Lucía, Montse, Sandra, Adri, Rosario, Javi, Cristina, Juan, Irene, Elena, Carmen, Dani… que en mayor o menor medida, me han ayudado con cualquier problema, dado consejos o me han puesto una sonrisa en la cara cuando más lo necesitaba. De ellos y ellas me traigo no solo una buena relación profesional, sino también de amistad.

En general, un fuerte abrazo y ¡MUCHAS GRACIAS! a todos/as los que han formado parte de esta tan enriquecedora etapa de mi vida (mencionados o no).

Ahora es el momento de dar paso a mi familia, que bien diría yo que han contribuido de una forma más personal que profesional, pero que sin duda alguna, para mí esto presenta una importancia igualmente significativa a la hora de desarrollar y acabar mi tesis.

A mi novia Isa, por estos más de diez años que llevamos juntos, ella es quien me ha escuchado, aguantado, aconsejado y ayudado a solucionar mis dificultades y preocupaciones (que no han sido pocas), siempre buscando la manera de quitarle importancia a esos problemas que para mí eran muy duros e intentando siempre hacerme lo más feliz posible. Si eso no es amor, no sé qué otra cosa puede ser. Y tengo muy claro que es la persona que quiero que me acompañe durante el resto de mi vida.

A mis padres, que me dieron la vida, que me han mantenido, se han esforzado en que yo siguiera con mis estudios y han conseguido que a día hoy sea el hombre que he llegado a ser. A mis hermanos/as, parte importante de mi vida, con los cuales he reído y llorado, y a los cuales no cambio por nada del mundo. A mis abuelos/as por haber formado/seguir formando parte de mi vida.

Y por último, agradecer a la familia que uno elige, los AMIGOS, personas que han estado ahí cuando ha hecho falta contar con ellos, tanto para hablar de problemas, ahogar penas o celebrar algo. Siempre hay un motivo para salir con ellos.

Para finalizar, me gustaría destacar y agradecer la aportación económica recibida a través del Ministerio de Economía y Competitividad (MINECO) BIA2014-57658-C2-1-R, BIA2014-57658-C2-2-R y BIA2017-82391-R estos dos últimos cofinanciados por los fondos FEDER, la financiación recibida a través del contrato I+D+i por Armigon S.L. (8.06/5.41.4958) y la financiación adicional asociada al contrato Ramón y Cajal I3 (IEDI-2016-0079). Sin esta financiación no habría sido posible la realización de esta tesis doctoral.

TABLE OF CONTENTS

I. LIST OF FIGURES

Figure 4.4. Experimental PDF data from 1.35 to 70 Å for alite pastes: 0.46 (black), 0.55 (red), 0.65 (blue) and 0.80 (green) at 34 days of hydration. Adapted from article #1 in Annex I.

Figure 4.5. Experimental (blue circles) and fitted (red solid line) PDF for anhydrous mC_3S-2015 sample in the 2 to 50 Å r-range. Difference curve is shown as a grey line. Taken from article #1 in Annex I.

Figure 4.6. Experimental (blue circles) and fitted (red solid line) PDF for mC_3S paste at 0.80 w/s in the 40 to 70 Å r-range. Difference curve is shown as a grey line. Taken from article #1 in Annex I.

Figure 4.7. Experimental (blue circles) and fitted (red solid line) PDF for mC_3S-2015 paste at 0.80 w/s mass ratio at 34 days of hydration in the 10 to 25 Å r-range. a) The fit include only crystalline CH and mC_3S, b) The fit include CH, mC_3S and T3_14sc phases. Difference curves are shown as a grey line. R_W values are included. Adapted from article #1 in Annex I.

Figure 4.8. a) Experimental (blue circles) and fitted (red solid line) PDF patterns for mC_3S-2015 w/s=0.80 34 days paste in the 2 to 10 Å r-range and the difference curve is shown as a grey line. b) Simulated PDF curves for a single layer (red) and a double layer (blue) of calcium hydroxide, bulk portlandite (black), alite (green) and clinotobermorite T3_14sc (pink) are also included. Taken from article #1 in Annex I.

Figure 4.9. PSD of a) as-received mC_3S-2016, b) vibratory milled mC_3S-2016 and c) attrition milled mC_3S-2016. Adapted from article #2 in Annex I.

Figure 4.10. Calorimetry data. Cumulative heat (dash lines) and Heat flow (solid lines) for mC_3S-2016_21µm_0.45w/s (black), mC_3S-2016_21µm_0.80w/s (blue), mC_3S_7µm_0.80w/s (green), mC_3S-2016_3µm_0.80w/s (red). Adapted from article #2 in Annex I.

Figure 4.11. Quantitative phase analysis results from SXRPD. a) mC_3S-2016_21µm_0.45w/s, b) mC_3S-2016_21µm_0.80w/s and c) mC_3S-2016_7µm_0.80w/s. mC_3S anhydrous (black), C-S-H gel (blue) and CH (green). Adapted from article #2 in Annex I.

Figure 4.12. LXRPD Rietveld plot (Mo$K\alpha_1$ radiation, λ=0.70932 Å) with internal standard for the mC_3S-2016_3µm_0.80w/s paste hydrated for 16 days. The main peaks are labelled as follow: CH (P) and the added internal standard, α-Al_2O_3 (α). R_{WP} value is included. Adapted from article #2 in Annex I.

Figure 4.13. ^{29}Si-MAS-NMR spectra for mC_3S-2016_3µm_0.80w/s_stopped:16days. Spinning rate of 15 kHz and a magnetic field of 14.1 T. Taken from article #2 in Annex I.

Figure 4.22. LXRPD patterns for tC_3S_0.50w/s_RT (black), tC_3S_0.50w/s_RT_stop (blue) and tC_3S_050w/s_50ºC_stop (red).

Figure 4.23. LXRPD patterns for oSK-2016_gyp_1.20w/s (black), oSK-2016_bas_1.20w/s (red) with internal standard (α-Al_2O_3) (MoKα_1 radiation, λ = 0.70932 Å). The peaks are labelled as: α= α-Al_2O_3, Y=ye'elimite, E=ettringite, and G=gibbsite.

Figure 4.24. Thermogravimetric data of oSK-2016_gyp_1.20w/s at 21 days (black line) and oSK-2016_bas_1.20w/s at 14 days (red line) at room temperature. It is presented the weight percentage and derivative weight percentage.

Figure 4.25. a) Synchrotron X-ray powder raw diffraction data, λ = 0.18972 Å intensity *vs* 2θ and b) Experimental real-space distribution of interatomic distances G(r) obtained at Q_{max} 24 A^{-1} for oSK-2016_gyp_1.20w/s_21d (black line) and oSK-2016_bas_1.20w/s_14d (red line) pastes.

Figure 4.26. Experimental (blue circles) and fitted (red solid line) PDF patterns in the 30 to 50 Å r-range for a) oSK-2016_gyp_1.20w/s_21d and b) oSK-2016_bas_1.20w/s_14d pastes hydrated at room temperature. Difference curves are shown as grey lines. Adapted from article #1 of Annex I.

Figure 4.27. Experimental (blue circles) and fitted (red solid line) PDF patterns for the low r-range, 1.6 to 35 Å, for a) oSK-2016_gyp_1.20w/s_21d and b) oSK-2016_bas_1.20w/s_14d pastes hydrated at room temperature. Below: enlarged view of 1.6 to 10 Å (b and d). Difference curves are shown as grey lines. Adapted from article #1 in Annex I.

Figure 4.28. a) LXRPD Rietveld plot (MoKα_1 radiation, λ = 0.70932 Å) of oSK-2017 (fitted with ICSD # 237892). R_{WP} value is also included and the arrow points C_3A main diffraction peak. b) PDF refinement of oSK-2017 from 2 to 50 Å r-range. R_W is included. Taken from article #3 in Annex I. Reproduced with permission of ICE Publishing (Annex IV).

Figure 4.29. a) SXRPD patterns all pastes of orthorhombic ye'elimite-2017 mixed with different amounts of anhydrite and hydrated at different w/s ratios. The main peaks arising from the different phases are labelled, E=ettringite, A=AFm-c, *A=AFm-n, Y=ye'elimite. b) G(r) plots from 1 to 10 Å r-range for all pastes. Taken from article #3 in Annex I. Reproduced by permission of ICE Publishing (Annex IV).

Figure 4.30. Experimental (blue circles) and fitted (red solid line) PDF patterns for a) and d) oSK-2017_31anh_0.85w/s; b) and e) oSK-2017_15.5anh_0.85w/s; and c) and f) oSK-2017_0.0anh_0.85w/s pastes hydrated at room temperature at low r-range: 1.6 to 35 Å a), b) and c); and high r-range: 30 to 50 Å d) e) and f). Difference curves are shown as grey lines. Adapted from article #3 in Annex I.

Figure 5.29. Evolution of a) AFt , b) ACn and c) FW with time at 1, 7, 28 and 56 days of hydration of the four selected pastes prepared at 0.40 w/c and 1.0wt% SP and at 0.50w/c with 0.4wt% SP. Taken from article #5 in Annex I. Copyright (2019) with permission from Elsevier (Annex IV).

II. LIST OF TABLES

III. NOTATION

Cement notation of oxide compounds as the used cement nomenclature:

C = CaO	A = Al_2O_3	S = SiO_2	F = Fe_2O_3
N = Na_2O	H = H_2O	$\bar{S}$ = SO_3	$\bar{C}$ = CO_2
M = MgO	K = K_2O	Z = ZnO	B = B_2O_3

Notation of all the compounds used in this thesis:

Chemical formula	Oxide compounds	Cement nomenclature	Name
	Anhydrous compounds		
Ca_3SiO_5	$3CaO{\cdot}SiO_2$	C_3S	alite
Ca_2SiO_4	$2CaO{\cdot}SiO_2$	C_2S	belite
$Ca_4Al_2Fe_2O_{10}$	$4CaO{\cdot}Al_2O_3{\cdot}Fe_2O_3$	C_4AF	brownmillerite
$Ca_3Al_2O_3$	$3CaO{\cdot}Al_2O_3$	C_3A	tricalcium aluminate
$Ca_{12}Al_{14}O_{33}$	$12CaO{\cdot}7Al_2O_3$	$C_{12}A_7$	mayenite
$Ca_4Al_6SO_{16}$	$4CaO{\cdot}3Al_2O_3{\cdot}SO_3$	$C_4A_3\bar{S}$	ye'elimite or Klein salt
$Ca_{10}Si_3S_3O_{24}F_2$	$CaF_2{\cdot}9CaO\ 3SiO_2{\cdot}3SO_3$	CaF_2-$C_9S_3\bar{S}_3$	fluorellestadite
$Ca_2K_2S_3O_{12}$	$2CaO\ K_2O{\cdot}3SO_3$	$C_2K\bar{S}_3$	calciolangbeinite
$CaSO_4(H_2O)_2$	$CaO\ SO_3{\cdot}2H_2O$	$C\bar{S}H_2$	gypsum/gyp
$CaSO_4(H_2O)_{1/2}$	$CaO\ SO_3{\cdot}0.5H_2O$	$C\bar{S}H_{1/2}$	bassanite/bas
$CaSO_4$	$CaO\ SO_3$	$C\bar{S}$	anhydrite/anh
CaO	CaO	C	free lime
MgO	MgO	M	periclase
	Hydrated compounds		
$Ca(OH)_2$	$CaO{\cdot}H_2O$	CH	portlandite
$Ca_{1.8}SiO_{3.8}(H_2O)_4$	$1.8CaO{\cdot}SiO_2{\cdot}4H_2O$	$C_{1.8}SH_4$	C-S-H gel
$Ca_6Al_2S_3O_{18}(H_2O)_{32}$	$6CaO{\cdot}Al_2O_3{\cdot}3SO_3{\cdot}32H_2O$	$C_6A\bar{S}_3H_{32}$	ettringite (AFt)
$Ca_4Al_2SO_{10}(H_2O)_{12}$	$4CaO{\cdot}Al_2O_3{\cdot}SO_3{\cdot}12H_2O$	$C_4A\bar{S}H_{12}$	AFm
$Ca_2Al_2SiO_7(H_2O)_8$	$2CaO{\cdot}Al_2O_3{\cdot}SiO_2{\cdot}8H_2O$	C_2ASH_8	stratlingite
$Ca_3Al_2SiO_8(H_2O)_4$	$3CaO{\cdot}Al_2O_3{\cdot}SiO_2{\cdot}4H_2O$	C_3ASH_4	katoite
$2Al(OH)_3$	$Al_2O_3{\cdot}3H_2O$	AH_3	gibbsite
$2Fe(OH)_3$	$Fe_2O_3{\cdot}3H_2O$	FH_3	iron hydroxide
$CaCO_3$	$CaO{\cdot}CO_2$	$C\bar{C}$	calcite

List of acronyms

ABY:	Alite-Belite-Ye'elimite cement (standard)
ACn:	Amorphous and non-quantified crystalline phases
BSE:	Backscattered Electron
BAY:	Belite–Alite-Ye'elimite cement
BYF:	Belite-Ye'elimite-Ferrite cement
BET:	Brunauer, Emmett and Teller
CSA:	Calcium Sulphoaluminate Cement
ρ:	density
dABY:	doped-ABY cement
EDS/EDX:	Energy-Dispersive X-Ray Spectroscopy
eq.:	equation
ESRF:	European Synchrotron Radiation Facility
FW:	Free Water
FEG-SEM:	Field Emission Gun - Scanning Electron Microscopy/microscope
HBC:	High Belite Cements
ID22:	High resolution powder diffraction beamline
HR-TEM:	High Resolution-Transmission Electron Microscopy/Microscope
ICP-OES:	Inductively Coupled Plasma Optical Emission Spectrometry
LXRPD:	Laboratory X-ray Powder Diffraction
***la-*:**	large amount
LGP:	Large Gel Pores
LoI:	Loss on Ignition
MAS-NMR:	Magic Angle Spinning Solid-state Nuclear Magnetic Resonance
ID15A:	Materials Chemistry and Materials Engineering beamline (ESRF)
MSPD:	Materials Science and Powder Diffraction beamline (ALBA)
$D_{v,10}$:	maximum particle diameter below which 10% of the sample volume exists
$D_{v,50}$:	maximum particle diameter below which 50% of the sample volume exists
$D_{v,90}$:	maximum particle diameter below which 90% of the sample volume exists
MCL:	Mean Chain Length
***ma-*:**	medium amount
mC_3S:	monoclinic alite
βC_2S:	monoclinic belite
$\alpha'_H C_2S$:	orthorhombic belite
$oC_4A_3\bar{S}$ or oSK:	orthorhombic ye'elimite

PDF:	Pair Distribution Function
PSD:	Particle Size Distribution
PC:	Portland Cement
$cC_4A_3\bar{S}$ or cSK:	pseudo-cubic ye'elimite
QPA:	Quantitative Phase Analysis
react.:	reaction
RH:	Relative Humidity
RQPA:	Rietveld Quantitative Phase Analysis
RT:	Room Temperature
***sa*-:**	small amount
SGP:	Small Gel Pores
SpØ:	Spdiameter:
SP:	Superplasticiser
SCMs:	Supplementary Cementitious Materials
SXRPD:	Synchrotron X-ray Powder Diffraction
TGA-DTA:	Thermogravimetric Analysis - Differential Thermal Analysis
TG-DTG:	Thermogravimetric - Differential Thermogravimetric
tC_3S:	triclinic alite
η:	viscosity
w/c:	water to cement mass ratio
w/s:	water to solid mass ratio
XRF:	X-Ray Fluorescence

IV. ABSTRACT

An eco-friendly industrial production is essential to protect our environment. The risk of climate change is considered to be one of the main environmental challenges for the society, where carbon dioxide footprint is one of the major greenhouse gases. Anthropogenic sources of CO_2 come mainly from the combustion of fossil fuels, deforestation, unsustainable combustion of biomass and industrial decomposition of mineral sources such as limestone.

The most widely used manufactured material in the world is PC concrete, which is mainly composed by water, aggregates (rocks and sand) and PC. Since the first PC was produced in 1843, there has been a continuous process of evolution in cement process technology and cement itself. Cement is used to bind materials together and is categorized as either non-hydraulic or hydraulic. Hydraulic cements are composed of silicates and oxides that can set and harden even when exposed to water.

The synthesis process of PC generates greenhouse gas emissions. The production of 1 ton of Portland clinker releases about 1 ton of carbon dioxide (CO_2). This is due to different aspects during the synthesis process. On the one hand, the clinkering temperature oscillates around 1400-1450°C, and consumes a high quantity of fossil fuels to achieve these temperatures. On the other hand, the raw mixture releases a great quantity of carbon dioxide due to the decomposition of limestone (the main component of the raw meal) during the heating process to achieve the desired composition after clinkering. Last but not least, the grinding process of the raw materials and clinker with other additives to obtain the final cement also consumes electricity, contributing to indirect greenhouse gas emissions.

Apart from these environmental issues, the cement industry is under increasing scrutiny to reduce CO_2 emissions, including the energy used in the production of PC. In addition, PC is not the ideal binder for all construction applications, as it may suffer durability problems in specific aggressive environments. For these reasons, there is a growing interest in the design, processing, characterisation, and implementation of alternatives binders to PC, which develop similar mechanical performances.

The cement production is a highly energy demanding industrial process. The major challenge in cement production is to reduce the high input of raw material and fuel in clinker production. These reductions can be addressed by

adopting a suitable processing method. This can be reduced by using blended cement with highly efficient clinker cooler, dryer, separators, calciner, pre-calciner and waste heat recovery system.

After analysing the amount of carbon dioxide released in each step of the PC production, the alternatives to diminish the greenhouse gas emissions are:

i) The use of alternative fuels, in order to decrease the amount of fossil fuels used. Substitutes like waste materials are part of the circular economy and may contribute to reduce the costs of cement production by maintaining the product quality. In addition, waste materials can be also used as raw materials.

ii) SCM. The partial substitution of clinker by SCM to produce blended or special cements is a good approach to reduce the carbon dioxide release. Fly ash, silica fume or slags are examples of SCM coming from waste materials.

iii) The carbon dioxide capture is another alternative for reducing the CO_2 releases to the atmosphere. However, this option is nowadays uneconomical without supporting regulations and funds.

iv) The formulation of new alternative low-carbon binders is another possible approach. This is the line chosen in this work because it can save important amounts of CO_2 emissions. These cements will be formed by low calcite demanding phases to decrease carbon dioxide emissions during clinkering. It is essential that this new materials show good final performances (mechanical properties and durability), equivalent to those of PC.

To design the composition of a new clinker or cement, firstly it is needed to know the mineralogical composition of PC clinker: 50-70 wt% of alite, 15-30 wt% of belite, 5-15 wt% of ferrite and 5-10 wt% of tricalcium aluminate. All the components are highly calcite demanding, especially alite that generates 0.58 tons of CO_2 per ton of phase. Clinker is usually mixed with gypsum or other sulphate source to obtain cement.

The hydration reaction of PC consists of two main reaction groups: i) the calcium silicate phases (alite and belite) that can represent more than 80 wt% of a clinker and ii) the calcium aluminate phases (ferrite and tricalcium aluminate). On the one hand, in the first group, alite reacts with water quickly and contributes to the early-age mechanical properties. Belite reaction is slower than alite, and because of that, this phase contributes to the long-term mechanical properties development. The hydration products for both silicates are calcium silicate hydrate (C-S-H gel) and portlandite. On the other hand, the aluminate phases

react with a sulphate source. In this case, tricalcium aluminate reacts faster than ferrite, and contributes to the mechanical properties at early ages of hydration. The main hydration product from these aluminate phases is ettringite.

After analysing the phase components of PC, some important alternatives can be used to synthesise environmentally friendly cements. The substitution of the main phase (alite) by belite, also named as HBC cement, results in up to 12% reduction of CO_2 due to the lower limestone and fuel requirements for the formation of belite. The clinkering temperature for this type of cements is usually close to 1350°C, which is about 100°C lower than the average for PC, which leads to somewhat lower kiln heat consumption, so on less use of fuel. Concerning durability, HBCs preserve satisfying long-term properties due to the lower amount of portlandite in the mortars. Nevertheless, the substitution of C_3S by C_2S compromises the early-age mechanical strength development due to the slow reactivity of the latter. The performances in these materials can be improved by activating/doping these clinkers (adding activators/stabilizers such as borax, Na_2CO_3 or K_2CO_3), favouring the formation of alpha forms of belite which hydration is faster than the beta form, where the latter is present in PC. However, the consumption of electricity during the grinding process is slightly higher due to its little friability.

Ye'elimite is another important hydraulic active crystalline phase, not present in PC, but present in other cements. It is a low calcite demanding phase that just generates 0.22 tons CO_2 per ton of component. Therefore, it supposes almost a third part of the CO_2 released by alite (the main phase in PC). Ye'elimite-rich cements have strong potential to be a possible substitute of PC to reduce the CO_2 footprint. Nevertheless, the use of these alternatives in Europe is limited and hence just used for niche applications due to the absence of regulations for structural applications based on EN 206-1. Just one company obtained a procedure that allowed its use for structural applications.

CSA cements are known since Alexander Klein patented an expansive cement in 1963, with the aim to decrease the shrinkage of PC. CSA cements contain around 50-80 wt% of ye'elimite, along with other minor phases such as belite and ferrite. These cements have been produced in China since 1970 and were named as 'Third Cement Series'. Depending on the composition, these CSA manufacture process releases up to 37% less carbon dioxide when compared with PC. In addition, the properties and applications of this type of cements are influenced by many factors: i) the chemistry and mineralogy of the clinker due to the presence of minor phases; ii) the type and amount of sulphate source; iii) the water to cement mass ratio used; vi) blending with other cements or SCM. In

general, these CSA cements present the following properties: fast setting, high early mechanical strengths, high durability, self-levelling and shrinkage compensation. Nevertheless, these types of cements have a high cost, since high amounts of Al_2O_3 are need and bauxites are normally used as raw material.

There are other alternatives based on ye'elimite and belite, also named as BYF cements (belite-ye'elimite-ferrite). These cements try to overcome the disadvantages of high belite cements and calcium sulphoaluminate cements, but maintaining a low carbon footprint, i.e. ~22% less CO_2 emissions than PC. These cements are composed by belite, ye'elimite and ferrite. The clinkering temperature is around 1200-1300°C, much lower than the PC one (1450°C). An additional advantage is the energy saving because of the easier clinker grinding process due to their friability. Nevertheless, it presents a drawback concerning the mechanical strengths at early hydration ages, i.e. they develop low mechanical strengths at early ages, especially between 1 and 7 days. To overcome this technological problem, two approaches have been proposed: i) the use of dopants to stabilize the alpha polymorphs of belite, and ii) manufacturing clinkers with some amount of alite.

The first approach consists on the production of doped-BYF cements that involves the stabilisation of highly reactive C_2S polymorphs, the α-forms react faster with water than β-form. These doped-BYF cements were patented by Lafarge and contain Klein's salt and α-forms of belite as main phases. The reduction of CO_2 is maintained but the resulting material presents enhanced properties at early ages.

The second approach consists on the preparation of clinkers with belite, alite and ye'elimite as main phases, being BAY (belite-alite-ye'elimite) or ABY (alite-belite-ye'elimite) depending on the quantity of each phase. Their production can release up to 18% less CO_2 than PC, depending on their composition.

However, the synthesis of a clinker with both alite and ye'elimite is not an easy task. Ye'elimite decomposes around 1350°C while alite starts to be formed at that temperature and higher. To solve this problem, some mineralizers can be used, acting as fluxes, to reduce the formation temperature of alite to get a coexistence of both phases. This type of cement integrates the characteristics of both CSA and PC.

This PhD thesis is focused in the production and characterisation of cements with alite, belite and ye'elimite phases. It has been gathered in two

blocks: on the one hand, a deep characterisation of the hydration of the main phases of this type of cements, alite and ye'elimite pure phases, has been performed to understand them. The corresponding hydration products (which contain nanocrystalline and crystalline phases) have been characterized through PDF methodology. On the other hand, the synthesis, hydration understanding, processing and the corresponding characterisation of ABY cements and mortars have been performed. Here, both standard (ABY, composed by beta-belite) and doped (dABY, with alpha-belite) cements/mortars have been prepared and characterised.

PDF is a technique that describes the real space structure and gives the probability of finding a pair of atoms at a distance r. The PDF method has been used in the study of liquids, glasses and other amorphous materials which have no long range order and crystalline materials as well. The structures of these materials are determined just based upon the information provided by the position and intensity of the Bragg peaks, whereas additional information regarding deviations from the perfect lattice is obtained, through the study of diffuse scattering. This treats both the Bragg and diffuse scattering on an equal basis, which is known as a total scattering technique. PDF takes advantage of the Fourier relationship between measurable diffraction intensities and the real space arrangement of pairs of atoms. This function gives the probability of finding an atom at a given distance r from another atom. It can be said that PDF is an useful tool in the characterisation of amorphous/nanocrystalline phases, and with the suitable strategy, crystalline/nanocrystalline/amorphous phases can even be quantified.

The study of the cement chemistry strikes with the difficulties of characterising amorphous or nanocrystalline phases. To fully understand the performances of the possible alternatives or even of PC, new methodologies of characterisation need to be proposed. The full characterisation of the hydration of a cement means to describe the nanocrystalline and amorphous hydration products together with the crystalline phases. X-ray diffraction involves a technique that allows the hydration reactions to be followed through the identification and quantification of crystalline phases, and the total quantification of the amorphous and non-quantified crystalline material. The PDF methodology, since it gives information of the local atomic environments of the materials without the need of long-range order, is a suitable approach to tackle this issue.

An important part of this PhD thesis is focused on the application of the PDF methodology to deeply study and characterise two sets of cement-related samples (alite and ye'elimite) as model ones. The hydration products of both alite

and ye'elimite contain not only crystalline phases but also nanocrystalline and amorphous phases. At this stage, the terms nanocrystalline and amorphous should be defined. The atomic structure of a nanocrystalline phase can be described by using the crystal structure truncated in the real space by a nanosized shape function and employing finite models that take into account surface relaxation effects. Conversely, an amorphous compound cannot be properly described by this approach.

Thus, here, a PDF multi-r range analysis approach to characterise the different components, crystalline, nanocrystalline and amorphous, of the alite and ye'elimite pastes has been established. For alite pastes, this multi-r range methodology consists on the use of the high r-range (40 to 70 Å) to refine the parameters of the crystalline phases, since the contribution of nanocrystalline and amorphous phases to this range is negligible. Then, these refined parameters were kept constant while analysing the middle r-range (∼10 to 25 Å). By using this multi-r range method, the structure of the nanocrystalline phases was modelled but also a quantitative analysis including nanocrystalline and crystalline phases was obtained. The scattering from the amorphous phases contributes at the low r-range (∼1 to 10 Å). Ye'elimite pastes were analysed with high r-range (30 to 50 Å) to refine the parameters of the crystalline phases and a middle-low r-range (1.6 to 35 Å) to refine the parameters of the nanocrystalline/amorphous components. The multi-r range method was used to determine the influence of the type of alite polymorph, the water content, the temperature and the particle size on the nature of the hydration products. Hydrated ye'elimite was also studied without and with different sulphate sources and also, with different water contents and temperatures to identify the influence of these parameters on the amorphous/nanocrystalline components.

First of all, the study of alite pastes was performed by synchrotron PDF (at MSPD-ALBA beamline) and additional characterisation techniques. Here, the studied parameters were the different w/s mass ratio, particle size, temperature and polymorphs. A preliminary Rietveld and thermogravimetric characterisation of monoclinic alite, with four different water contents (0.46, 0.55, 0.65 and 0.80 w/s) indicated that the samples contain a small amount of calcium carbonate, ∼1 wt%, from the partial carbonation, and the amount of unreacted alite ranged 8–12 wt%. The PDF analysis in the 40 to 70 Å r-range confirmed the crystalline phase contents, already determined by Rietveld methodology, crystalline remaining alite and portlandite. Mainly, the analysis of the data in the 10 to 25 Å r-range indicates that clinotobermorite fits the total scattering data of C-S-H gel better than jennite or tobermorite-14. The stoichiometry corresponding to this defective tobermorite

was $Ca_{11}Si_9O_{28}(OH)_2(H_2O)_{8.5}$ with a calculated theoretical density of 2.49 g/cm^3 and an average silicate chain length of 3.0. For all the pastes, clinotobermorite invariably gave better fits. However, it is well established that the overall Ca/Si ratio in C-S-H gel ranges between 1.7-1.9, meanwhile the Ca/Si ratio of this clinotobermorite is 1.22. The analysis of the PDF data in the 2 to 10 Å r-range helps to address this issue as another component is needed in order to justify the measured scattering data. In this case, the needed component is amorphous since it contributes to the low r-range of the PDF. The theoretical scattering data from a single layer with structure of CH justify the PDF data. We have named this component amorphous CH to distinguish its scattering contribution from that of crystalline CH, already observed in the 40 to 70 Å r-range, as well as in the Rietveld analysis. This allows us to understand that the gel is composed by nanocrystalline defective tobermorite, amorphous (single layer) portlandite and water within the gel pores. This pore water should not be confused with capillary (free water) which is removed when arresting the hydration reaction.

Therefore, this study has confirmed the stoichiometry of alite hydration reaction to yield crystalline CH and C-S-H gel with $(CaO)_{1.8}SiO_2(H_2O)_{4.0}$ average composition. Through the use of high-resolution synchrotron PDF analysis, it has been found that C-S-H gel is heterogeneous at the nanoscale being composed of defective tobermorite, with approximate composition $Ca_{11}Si_9O_{28}(OH)_2(H_2O)_{8.5}$, and CH monolayers. With these results and different observations by HRTEM, a multiscale model for the hydration of alite has been proposed which explains the observed mass densities and Ca/Si atomic ratios at the significant scales. At the nanoscale, below 100 Å, C-S-H gel is composed of a fine intermixing of defective tobermorite, with particle size ranging from 30 to 50 Å, a Ca/Si ratio close to 1.2 and $\rho\sim2.5$ g/cm^3; monolayers of CH, $\rho\sim2.1$ g/cm^3; and gel pore water. This description justifies the average stoichiometry $(CaO)_{1.8}SiO_2(H_2O)_{4.0}$ and a density of $\sim$2.6 g/cm^3.

Studies comparing different particle sizes of alite (21, 7 and 3 μm), different polymorphs (triclinic and monoclinic C_3S), temperatures (RT, 35 and 50^{o}C) and hydration procedure (in-situ, ex-situ) were carried out. The characterisation of the hydration of all groups has shown no differences in the precipitated C-S-H gel structure, with very similar atomic local order. Consequently, nor the particle size, nor the type of polymorph, nor temperature neither hydration procedure affects the stoichiometry and local order of C-S-H gel formed from alite, where the structural description that better fits the PDF data, in the 10 to 25 Å r-region, is tobermorite 11 Å in all the pastes.

Secondly, a ye'elimite hydration study with different sulphate sources and different water contents has been developed to identify the amorphous/nanocrystalline phases using synchrotron PDF data. The precipitation of aluminium hydroxide gel has been demonstrated, as one of the hydration reaction product together with ettringite or AFm (depending on the presence of the sulphate source). The Spdiameter values for nanocrystalline aluminium hydroxide, which is directly related with the average particle sizes, are 30 Å for the sulphoaluminate pastes studied in this PhD thesis. Moreover, the analysis of the thermogravimetric data for the ye'elimite pastes gave a large water content, close to $Al(OH)_3(H_2O)_{0.7}$. It is speculated that the very small particle sizes of the gel in the ye'elimite pastes, close to 30 Å, retain the water in the inter-particle pores. This particle size of nanocrystalline aluminium hydroxide has been determined to be ~30 Å independently of the type of the sulphate source or the data collection.

The influence of the anhydrite dosage and w/c mass ratio on ye'elimite hydration has been also studied by PDF. It is worth noting that this analytical tool does not require arresting the hydration of the pastes before characterisation. For the pastes without anhydrite, ettringite was not quantified and two AFm phases were found. One of them consists on the well-known crystalline AFm phase but the second one is nanocrystalline, with a particle size of ~60 Å, and a significantly small *c*-unit cell parameter value. A smaller amount (6 wt%) of this nanocrystalline-AFm phase was found when an intermediate anhydrite amount (15.5 wt%) was added. For a large anhydrite dosage, 31 wt%, ettringite is the main crystalline phase with the aluminium hydroxide gel having nano-gibbsite local structure.

All the PDF analyses have been performed by the multi-r range methodology and the quantitative results have been compared with those obtained with Rietveld methodology obtaining very satisfactory correlations.

Summarising, this first part of the PhD has enabled us to establish a multi-r range methodology for the analysis by PDF of mixtures of crystalline/nanocrystalline/amorphous components. Moreover, C-S-H gel has been characterised and described as nanocrystalline defective tobermorite, monolayers of portlandite and water pore, independently of the polymorphism of alite, particle size, water to solid mass ratio or temperature. Finally, aluminium hydroxide gel obtained from the hydration of ye'elimite has also been described. The type and amount of the sulphate source seems not to have any influence on the nanocrystalline nature of this phase.

The main goal of the second part of this PhD thesis was to obtain a clinker with alite as main phase but also with belite and ye'elimite, called ABY clinker. The maximum quantity of alite and ye'elimite, using natural raw materials, limestone, kaolinite, mineral gypsum, sand and iron ore, and some dopant agents, as fluorite and $ZnSO_4$, was sought. The clinkering temperature was 1300ºC with the associated energy saving and the reduction of emissions. In addition, once the ABY clinker was obtained (named as standard-ABY), a step forward was proposed, to obtain a clinker with alite and ye'elimite and the active forms of belite, $\alpha'_H C_2S$, (named as doped-ABY). The clinkering was optimised, where the effect of different dopants was studied (Na_2CO_3, K_2CO_3, and borax), being the latter the best candidate. The clinkering and the procedure to prepare ~2 kg of both clinkers (standard and doped) have been divided in three steps: firstly, a small amount of the desired clinker (5 g, named as *sa*-) was achieved, secondly, a medium amount (90 g, named as *ma*-) was obtained, and finally, the procedure was adjusted to prepare a large amount (2 kg, also named as *la*-).

On the one hand, standard Alite-belite-ye'elimite (ABY) clinkers were successfully synthesised by combining natural raw materials, and 1 wt% of CaF_2 and 1 wt% of ZnO; the dosage has presented an important influence on the mineralogical composition. From the *sa*-ABY to *la*-ABY step, no changes were needed, just the use of higher amount of material. The final phase assemblage obtained was 41.5(2) wt% of alite, 28.4(3) wt% of β-belite, 17.4(3) wt% of ye'elimite, 4.3(2) wt% of fluorellestadite and 3.8(1) wt% of ferrite.

On the other hand, the stabilization of α'_H-form of C_2S by adding dopants to the standard raw mixture has been achieved. In the first step of the clinkering, Na_2O or K_2O was added to the raw meal, as Na_2CO_3 and K_2CO_3, respectively; however, this strategy was ruled out because $\alpha'_H C_2S$ was not formed. After that, 2.0 wt% of B_2O_3, added as borax was used, jointly with increasing amounts of CaF_2; however, this amount of boron hindered the formation of alite. Therefore, the amount of boron was decreased down to 0.5 wt%, to prepare 5 grams of clinker. Before the large amount was obtained, *la*-dABY, an optimization of the quantity of the dopant agent in the *ma*-ABY was needed. Finally, ~2 kg of dABY, with the coexistence of $\alpha'_H C_2S$, C_3S and $C_4A_3\bar{S}$, were obtained by adding 0.6 wt% of B_2O_3 and 0.3 wt% of Na_2O, as borax, jointly with 1 wt% of CaF_2 and 1 wt% of ZnO, the latter added as $ZnSO_4 \cdot H_2O$. The mineralogical composition of doped-ABY was determined by Rietveld method as 15.7(2) wt% of alite, 41.8(2) wt% of β-belite, 18.0(3) wt% of α'_H-belite, 7.7(2) wt% of ye'elimite, 6.6(1) wt% of mayenite, 3.2(1) wt% of ferrite and 3.1(1) wt% of fluorellestadite. The EDS (FEG-SEM) study revealed that, in both clinkers, the added Zn and F were incorporated in both

ferrite and alite. The elemental composition of the amorphous fraction of the clinkers has been determined by a joint study of XRF data and EDS (FEG-SEM), being mainly a calcium aluminate phase. The chemical formula of main phases of both clinkers, C_3S and belite, has been determined using a semi-quantitative EDS analysis (FEG-SEM). Thus, $Ca_{1.79}(Si_{0.85}Al_{0.08}S_{0.07})O_{3.75}$ and $Ca_{2.64}Mg_{0.06}Al_{0.05}(Si_{0.95}Al_{0.05})O_{4.75}$ formulations have been proposed in this research.

Finally, *la*-ABY and *la*-dABY clinkers were mixed with the stoichiometric amount of anhydrite (14 wt%) to completely react with ye'elimite and calcium aluminates to form ettringite. These synthesised cements (ABY and dABY) have been hydrated and studied.

An *in-situ* SXRPD study of the first hydration hours was performed (using w/c mass ratio of 0.5). Moreover, these results were compared with the ones obtained by an ex-situ hydration study at different hydration ages. The main aim of this part was to prove that the high temperature form of belite ($\alpha'_H C_2S$), stabilised at RT by the addition of borax, hydrates at a higher pace than β-form, and consequently, it develops higher mechanical properties. The challenge here is to unravel the hydration mechanism of these cements, the effect of w/c mass ratio and to check the impact on the corresponding mechanical properties. The behaviour of the cement pastes at very early-ages (the first hours of hydration) was investigated by rheology, calorimetry, SXRPD and LXRPD. RQPA was the main technique used to investigate the content of crystalline and ACn phases in pastes (in-situ and ex-situ studies). A thermogravimetric analysis was employed to confirm the mineralogy of the pastes and to determine chemically bounded and free water content.

During the first minutes of hydration, the ABY paste (prepared at w/c=0.50 without SP) shows higher viscosity than the dABY one likely due to the lower (agglomerate) size of this cement which is related with higher particle interactions. However, 10 minutes after hydration, the viscosity of the dABY paste suffers a harsh increase, which is much higher than that for the ABY paste, in agreement with the higher cumulative heat released by dABY up to 3 hours of hydration. This is related to the higher dissolution/reactivity degree of some crystalline phases, such as $C_{12}A_7$ in dABY cement, which is the responsible of the fast formation of ettringite.

Nevertheless, the viscosity of the dABY paste, at w/c 0.4, was higher than that for the ABY one during the whole studied time. This fact is not only related to the quick dissolution of certain phases, mainly mayenite (and anhydrite), as

discussed above, but also with the dramatic loss of workability of dABY paste with the reduction of the water content.

Furthermore, the quick increase in viscosity of both pastes, mainly of dABY, does not allow the preparation of homogeneous mortars; this was more dramatic for dABY pastes/mortars. To overcome this drawback, the addition of a polycarboxylate-based superplasticiser was optimised. It allowed the preparation of low-viscosity and homogeneous pastes, at w/c 0.4 and 0.5, where the increase in viscosity was also delayed due to the nature of the additive. The amount of superplasticiser and water content were optimised through the rheological behaviour and compressive strength of pastes and mortars, respectively. ABY optimised pastes and mortars were those prepared at 0.40 w/c with 1.0 wt% SP, and the dABY ones were those prepared at 0.50 w/c with 0.4 wt% SP. Optimised ABY and dABY mortars showed mechanical strengths similar to PC at certain ages, but releasing up to ~17% less CO_2. The optimised ABY mortar showed compressive strengths of ~53, 72, 77, 87, 98 MPa at 1, 7, 28, 56 and 180 days, respectively, and the values for the optimised dABY mortar were ~17, 41, 75, 82 and 83 MPa at the same ages, respectively. The ABY mortar shows higher compressive strengths than the boron-bearing one (dABY) at 1 and 7 days of hydration, likely due to the higher $C_4A_3\bar{S}$ and C_3S contents of the anhydrous cement. It is worth noting that the optimised dABY mortar showed a rush increase in the compressive strength from 7 to 28 days due to the higher content of belite and faster reaction of α'_HC_2S than βC_2S polymorph. The enhanced reactivity of belite in dABY has been proved, comparing both ABY and dABY pastes, by the determination of the degree of reaction from Rietveld results and by MAS-NMR where higher amounts of C-S-H gel were quantified. This research has also verified that the addition of borax in the dABY paste delayed the acceleration period up to ~15 hours. The study of the hydration at late ages by LXRPD, MAS-NMR and thermogravimetric techniques confirms that, in both systems (ABY and dABY), stratlingite was not found. Conversely, the hydration of alite and belite gives C-S-H gel. The nature of this C-S-H gel is similar in both systems, even though dABY paste has shown higher degree of reaction of belite polymorph (β or α'_H) and consequently, a higher amount of this hydration product was formed. Despite of all explained before, the hydrated phase assemblage of these samples did not present a clear tendency that justifies the differences on mechanical strengths. Therefore, the optimisation of the processing parameters resulted to be key to assure homogeneity, workability and thus, high mechanical strengths.

All the results obtained from this second part of the research work have allowed fulfilling the specific objectives of synthesizing, “scaling-up” and hydration

understanding for both ABY and dABY cements, which mortars show similar performances than PC but ~17% less CO_2 emissions. In addition, the goal of enhancing the performances of these types of materials by doping with boron has been achieved as the ratio CO_2/MPa has decreased from 0.018 to 0.011 at 28 days when compared to PC (w/c=0.50).

V. RESUMEN

Una producción industrial respetuosa con el medioambiente es esencial para proteger nuestro planeta. El cambio climático es considerado como uno de los desafíos medioambientales más importantes para la sociedad, donde el dióxido de carbono es uno de los principales gases de efecto invernadero, siendo fundamental el control de sus emisiones. Las fuentes antropogénicas de CO_2 provienen principalmente del uso de combustibles fósiles, la deforestación, la combustión insostenible de biomasa y la descomposición industrial de fuentes minerales como la roca caliza.

El material manufacturado más utilizado en el mundo es el hormigón de cemento Portland (PC), compuesto principalmente por agua, agregados (rocas y arena) y PC. Desde que se fabricó el primer PC en 1843, ha habido un proceso continuo de evolución en la tecnología de su producción y en el cemento en sí mismo. Éste se usa para unir otros materiales y se clasifica como hidráulico o no hidráulico. Los cementos hidráulicos están compuestos de silicatos y óxidos que pueden endurecerse incluso cuando están inmersos al agua.

El proceso de síntesis del PC genera emisiones de gases de efecto invernadero. La producción de 1 tonelada de clínker Portland libera aproximadamente 1 tonelada de dióxido de carbono. Esto es debido a diferentes aspectos durante el proceso de síntesis. Por un lado, la temperatura de clinkerización oscila alrededor de 1400-1450°C, y consume gran cantidad de combustibles fósiles para alcanzar esas temperaturas. Por otro lado, el crudo libera una gran cantidad de dióxido de carbono debido a la descomposición de la roca caliza (el componente principal del crudo) durante el proceso de calentamiento para conseguir la composición deseada. Por último, el proceso de molienda de las materias primas y el clínker con otros aditivos para obtener el cemento también consume electricidad, lo que contribuye a emisiones indirectas de gases de efecto invernadero.

Además de estos problemas medioambientales, la industria del cemento está bajo un escrutinio creciente para reducir las emisiones de CO_2, incluyendo la energía utilizada en la producción de PC. Además, el PC no es el aglutinante ideal para todas las aplicaciones de construcción, ya que puede sufrir problemas de durabilidad en entornos agresivos. Por estas razones, existe un creciente interés en el diseño, procesamiento, caracterización e implementación de aglutinantes alternativos al PC, que desarrollen unas propiedades mecánicas similares.

La producción de cemento es un proceso industrial que necesita mucha energía. El principal desafío en su producción es reducir el alto aporte de materia prima y combustible para producir el clínker. Además, se ha buscado la eficiencia energética en todas las partes del proceso productivo: enfriador de clínker, secador, separadores, precalcinadores, horno de clinkerización y sistema de recuperación de calor residual.

Después de analizar la cantidad de dióxido de carbono liberado en cada paso de la producción de PC, las alternativas para disminuir las emisiones de gases de efecto invernadero son:

i) Usar combustibles alternativos para disminuir la cantidad de combustibles fósiles utilizados. Sustituirlos por materiales de desecho como parte de una economía circular y que puede contribuir a reducir los costes de producción del cemento al mantener la calidad del producto. Además, estos materiales de desecho también pueden usarse como materias primas.

ii) Materiales cementantes suplementarios (SCM). La sustitución parcial de clínker por SCM para producir cementos especiales es un buen enfoque para reducir la liberación de dióxido de carbono. Las cenizas volantes, el humo de sílice o las escorias son ejemplos de SCM provenientes de materiales de desecho.

iii) La captura de dióxido de carbono es otra alternativa para reducir las emisiones de CO_2 a la atmósfera. Sin embargo, esta opción hoy en día no es rentable, sin una normativa específica y fondos económicos que lo respalden.

iv) La formulación de cementos alternativos con bajas emisiones de CO_2 en su fabricación, es otra posible alternativa. Esta es la línea de investigación escogida en este trabajo ya que supone un ahorro importante de CO_2 emitido. Estos cementos deben estar compuestos por fases de baja demanda de calcita, disminuyendo así las emisiones de dióxido de carbono durante el proceso de clinkerización. Es esencial que estos nuevos materiales muestren buenas propiedades mecánicas y de durabilidad, al menos equivalentes a los del PC.

Para diseñar la composición de un nuevo clínker o cemento, primero es necesario conocer la composición mineralógica del clínker Portland: 50-70 %p de alita, 15-30 %p de belita, 5-15 %p de ferrita y 5- 10 %p de aluminato tricálcico. Todos estos componentes requieren mucha calcita, especialmente la alita que genera 0,58 toneladas de CO_2 por tonelada de esta fase. El clínker generalmente se mezcla con yeso u otra fuente de sulfato para obtener cemento.

Durante la hidratación del PC tienen lugar dos tipos de reacciones: i) las relacionadas con las fases de silicato cálcico (alita y belita) que pueden representar más del 80 %p de un clínker y ii) las relacionadas con las fases de aluminato cálcico (ferrita y aluminato tricálcico).

Por un lado, en el primer grupo, la alita reacciona con agua rápidamente y contribuye a las propiedades mecánicas a edades tempranas. La reacción de la belita es más lenta que la alita, y debido a eso, esta fase contribuye al desarrollo de propiedades mecánicas a mayores edades. Los productos de hidratación para ambos silicatos son silicato cálcico hidratado (gel C-S-H) y portlandita. Por otro lado, las fases de aluminato reaccionan con una fuente de sulfato. En este caso, el aluminato tricálcico reacciona más rápido que la ferrita y contribuye a las propiedades mecánicas en las primeras edades de hidratación. El principal producto de hidratación de estas últimas fases es la ettringita.

Después de analizar la composición de fases del PC, es posible el diseño de cementos más ecológicos. Así, la sustitución de la fase principal (alita) por belita, en los denominados cementos HBC, da como resultado una reducción del 12% de emisiones de CO_2 debido a la menor cantidad de caliza usada para la formación de esta fase. Además, la temperatura de clinkerización para este tipo de cementos es ~1350°C, que es aproximadamente 100°C menos que para el PC, lo que se traduce en un ahorro energético y de combustible. Con respecto a la durabilidad, los HBC conservan buenas propiedades a largas edades debido a la menor cantidad de portlandita en los morteros. No obstante, la sustitución de C_3S por C_2S dificulta el desarrollo de altas resistencias mecánicas a edades tempranas debido a su lenta reactividad. Las prestaciones de estos materiales se podrían mejorar activando/dopando el clínker (agregando activadores/estabilizadores como bórax, Na_2CO_3 o K_2CO_3), favoreciendo de esta manera la formación de otros polimorfos de la belita (alfa) y cuya hidratación es más rápida que la forma beta. Sin embargo, el consumo de electricidad durante el proceso de molienda de este cemento activado es ligeramente mayor debido a su mayor dificultad para molerlo.

La ye'elemita es otra fase cristalina hidráulicamente activa relevante, no presente en el PC, aunque sí en otros cementos. Es una fase con una baja demanda de calcita y que sólo genera 0,22 toneladas de CO_2 por tonelada de material. Por lo tanto, supone casi una tercera parte del CO_2 liberado por la alita. Los cementos ricos en ye'elemita tienen mucho potencial para ser un posible sustituto del PC. No obstante, el uso de este tipo de cementos en Europa es limitado y, por lo tanto, sólo se usa en aplicaciones específicas debido a la ausencia de regulaciones para aplicaciones estructurales basadas en la norma EN

206-1. Sólo una compañía italiana obtuvo un procedimiento que permitió su uso para aplicaciones estructurales.

Los cementos CSA son conocidos desde que Alexander Klein patentó un cemento expansivo en 1963, con el objetivo de disminuir la contracción del PC. Estos cementos están formados por 50-80 %p en ye'elemita, junto con otras fases minoritarias como la belita y la ferrita. Se producen en China desde 1970 y fueron nombrados como "Cementos de Tercera Serie". Dependiendo de la composición, este proceso de fabricación de CSA puede llegar a liberar hasta un 37% menos de dióxido de carbono en comparación con el PC. Además, las propiedades y aplicaciones de este tipo de cementos dependen de diversos factores: i) la química y la mineralogía del clínker debido a la presencia de fases minoritarias; ii) el tipo y la cantidad de fuente de sulfato; iii) la relación de agua/cemento utilizada; vi) la mezcla con otros cementos o SCM. En general, los cementos CSA presentan las siguientes propiedades: fraguado rápido, altas resistencias mecánicas a edades tempranas, alta durabilidad, se pueden usar como autonivelantes y compensador de la contracción. Sin embargo, estos cementos tienen un alto coste, ya que se necesitan grandes cantidades de Al_2O_3 y normalmente se usan las bauxitas como materia prima (siendo éstas caras y escasas).

Existen otras alternativas basadas en ye'elemita y belita, también llamadas cementos BYF. Estos cementos intentan superar las debilidades de los cementos con alto contenido de belita y los cementos de sulfoaluminato cálcico, aunque manteniendo una baja huella de carbono, es decir, ~22% menos de emisiones de CO_2 que el PC. Estos cementos están compuestos por belita, ye'elemita y ferrita como fases principales. La temperatura de clinkerización es ~1200-1300°C, por lo que es mucho más baja que la del PC (1450°C). Una ventaja adicional es el ahorro energético debido a su mayor facilidad a la hora de la molienda. Sin embargo, presenta un inconveniente con respecto a las resistencias mecánicas a edades tempranas de hidratación, es decir, desarrollan bajas resistencias mecánicas, especialmente entre 1 y 7 días. Por lo tanto, para superar este problema, se han propuesto dos enfoques: i) el uso de dopantes para estabilizar los polimorfos alfa de la belita, y ii) la fabricación de clínker con cierta cantidad de alita.

El primer enfoque consiste en la producción de cementos BYF dopados para estabilizar los polimorfos de C_2S más reactivos, es decir, las formas α, ya que reaccionan más rápido con agua que la forma β. Estos cementos BYF dopados fueron patentados por Lafarge y contienen las formas α de belita y ye'elemita como fases principales. La reducción de CO_2 se mantiene y el material resultante

presenta propiedades mejoradas a edades tempranas, cuando se compara con el BYF sin dopar.

El segundo enfoque consiste en la preparación de clínker con belita, alita y ye'elemita como fases principales, siendo BAY (belítico-alítico-ye'elemítico) o ABY (alítico-belítico-ye'elemítico) dependiendo de la cantidad de cada fase. Dependiendo de su composición, la producción de estos cementos puede liberar hasta un 18% menos de CO_2 que el PC.

No obstante, la síntesis de un clínker con alita y ye'elemita no es una tarea fácil. La ye'elemita se descompone alrededor de 1350°C mientras que la alita comienza a formarse a esa temperatura, o incluso superior. Para resolver este problema, se pueden utilizar fundentes, para reducir la temperatura de formación de la alita y así lograr la coexistencia de ambas fases. Este tipo de cemento integra las características de los CSA y los PC.

Esta tesis doctoral se centra en la producción y caracterización de cementos compuestos por las fases de alita, belita y ye'elemita. Se ha dividido en dos bloques: por un lado, se ha realizado una profunda caracterización de la hidratación de las fases principales de estos cementos, alita y ye'elemita como fases puras. Los productos de hidratación correspondientes (que contienen fases nanocristalinas y cristalinas) se han caracterizado mediante la metodología PDF. Por otro lado, se ha realizado la síntesis, la comprensión de la hidratación, el procesamiento y la caracterización de los correspondientes cementos y morteros ABY. Aquí, se llevó a cabo la preparación y caracterización de cementos y morteros estándar (ABY, compuestos por beta-belita) y dopados (dABY, con alfa-belita).

PDF es una técnica que describe la estructura espacial real y brinda la posibilidad de encontrar un par de átomos a una distancia interatómica r. El método PDF se ha utilizado en el estudio de líquidos, vidrios y otros materiales amorfos que no tienen un orden a largo alcance y también en materiales cristalinos. La técnica PDF usa todo el difractograma de polvo para extraer información. Por un lado la posición y la intensidad de los picos de Bragg aportan información de las estructuras de los materiales, mientras que la dispersión difusa proporciona información adicional sobre las desviaciones de la red perfecta. De esta forma las señales de Bragg y la dispersión difusa tienen el mismo peso, conociéndose esta técnica como de dispersión total. PDF aprovecha la transformada de Fourier entre las intensidades de difracción y la disposición en el espacio real entre los pares de átomos. Esta función da la probabilidad de encontrar dos átomos a una distancia r dada. Se puede decir que PDF es una

herramienta útil en la caracterización de fases amorfas/nanocristalinas, y con la estrategia adecuada, incluso se pueden cuantificar las cantidades de fases cristalinas/nanocristalinas/amorfas.

El estudio de la química del cemento lidia con las dificultades de caracterizar las fases amorfas o nanocristalinas. Para comprender completamente el desempeño de las posibles alternativas o incluso del PC, se deben proponer nuevas metodologías de caracterización. La caracterización completa de la hidratación de un cemento significa describir los productos de hidratación nanocristalinos y amorfos junto con las fases cristalinas. La difracción de rayos X implica una técnica que permite seguir las reacciones de hidratación a través de la identificación y cuantificación de fases cristalinas, y la cuantificación total del amorfo y material cristalino no cuantificable. La metodología PDF, brinda información de los entornos atómicos locales de los materiales sin la necesidad de un orden a largo alcance, este es un enfoque adecuado para abordar el problema.

Una parte importante de esta tesis doctoral se centra en la aplicación de la metodología PDF para estudiar a fondo y caracterizar dos conjuntos de muestras relacionadas con el cemento, alita y ye'elemita, como modelos. Los productos de hidratación de la alita y la ye'elemita contienen no sólo fases cristalinas sino también fases nanocristalinas y amorfas. Llegados a este punto se deben definir los términos nanocristalino y amorfo. La estructura atómica de una fase nanocristalina puede describirse utilizando la estructura cristalina truncada en el espacio real por una función de forma nanométrica y empleando modelos finitos que tienen en cuenta los efectos de relajación de superficie. Por el contrario, un compuesto amorfo no puede describirse adecuadamente mediante este enfoque.

En esta tesis se ha empleado el enfoque de análisis del PDF en distintos rangos de distancias interatómicas (r) para caracterizar los diferentes componentes, cristalinos, nanocristalinos y amorfos, de las pastas de alita y ye'elemita. Esta metodología se denomina de rango r-múltiple. Para las pastas de alita, la metodología de rango r-múltiple consiste en el uso de un rango r alto (de 40 a 70 Å) para refinar los parámetros de las fases cristalinas, ya que la contribución de las fases nanocristalinas y amorfas en este rango es insignificante. Posteriormente, estos parámetros refinados se mantuvieron fijos mientras se analizaba el rango r medio (~10 a 25 Å). Mediante el uso de este método de rango r-múltiple, se modeló la estructura de las fases nanocristalinas, aunque también se obtuvo un análisis cuantitativo que incluye las fases nanocristalinas y las cristalinas. La dispersión de las fases amorfas contribuyen en el rango r bajo (~1 a 10 Å). Las pastas de ye'elemita se analizaron con un rango r alto (30 a 50 Å) para refinar los parámetros de las fases cristalinas y un rango r medio-bajo (1.6 a

35 Å) para refinar los parámetros de los componentes nanocristalinos/amorfos. El efecto de parámetros como: el tipo de polimorfo de alita, el contenido de agua, la temperatura y el tamaño de partícula se ha evaluado mediante este método para entender la naturaleza de los productos de hidratación obtenidos. La ye'elemita hidratada se estudió con y sin diferentes fuentes de sulfato y con diferentes contenidos de agua y temperatura para identificar la influencia de estos parámetros en los componentes amorfos/nanocristalinos.

En primer lugar, se estudiaron las pastas de alita mediante PDF (en la línea de luz MSPD del sincrotrón ALBA) y con técnicas básicas complementarias de caracterización. Aquí, los parámetros estudiados fueron: la diferente relación másica de agua/sólido y tamaño de partícula de la alita. La caracterización preliminar de las pastas de alita monoclínica por Rietveld y por termogravimetría, con cuatro contenidos diferentes de agua/sólido (0,46, 0,55, 0,65 y 0,80) indicaron que las muestras contenían una pequeña cantidad de carbonato cálcico, ~1 %p, de la carbonatación parcial, y que la cantidad de alita sin reaccionar varió de un 8 a un 12 %p. El análisis por PDF en el rango r de 40 a 70 Å confirmó el contenido de fases cristalinas determinado por la metodología Rietveld, la alita sin reaccionar y la portlandita. En el rango medio de r, 10 a 25 Å, la contribución principal es la del gel C-S-H nanocristalino. El análisis de los datos de este rango indicó que la clinotobermorita ajustaba mejor los datos de dispersión total del gel C-S-H que la jennita o la tobermorita-14. La estequiometría correspondiente a esta tobermorita defectuosa fue $Ca_{11}Si_9O_{28}(OH)_2(H_2O)_{8,5}$ con una densidad teórica calculada de 2,49 g/cm^3 y una longitud promedio de la cadena de silicatos de 3,0. Para todas las pastas, la clinotobermorita invariablemente dio mejores ajustes. Sin embargo, está bien determinado que la relación general de Ca/Si en el gel C-S-H oscila entre 1,7-1,9, mientras que la relación Ca/Si de esta clinotobermorita es 1,22. El análisis de los datos de PDF en el rango r de 2 a 10 Å ayudó a abordar este problema, ya que se necesitó otro componente para justificar los datos de dispersión medidos. En este caso, el componente necesario es amorfo ya que contribuye al bajo rango de distancias interatómicas, r, del PDF. Los datos de dispersión teóricos de una sola capa con estructura de CH justifican los datos de PDF. Hemos denominado a este componente CH amorfo para distinguir su contribución de dispersión de la del CH cristalino, ya observado en el rango r de 40 a 70 Å, así como en el análisis de Rietveld. Esto nos permite comprender que el gel está compuesto por tobermorita defectuosa nanocristalina, portlandita amorfa (monocapa) y agua dentro de los poros del gel. Esta agua de poro no debe confundirse con agua capilar (agua libre) que se elimina al detener la reacción de hidratación.

En consecuencia, este estudio ha confirmado la estequiometría de la reacción de hidratación de la alita para producir CH cristalino y gel C-S-H con una composición promedio de $(CaO)_{1,8}SiO_2(H_2O)_{4,0}$. Mediante el análisis por PDF sincrotrón de alta resolución, se ha desvelado que el gel C-S-H es heterogéneo a nanoescala y que está compuesto por tobermorita defectuosa, con una composición aproximada de $Ca_{11}Si_9O_{28}(OH)_2(H_2O)_{8,5}$, monocapas de CH y agua en los poros. Con estos resultados y diferentes observaciones por HRTEM, se ha propuesto un modelo multiescala para la reacción de hidratación de la alita que explica las densidades observadas y las relaciones atómicas de Ca/Si a escalas significativas. En la nanoescala, por debajo de 100 Å, el gel C-S-H se compone de una mezcla delgada de tobermorita defectuosa, con un tamaño de partícula que varía de 30 a 50 Å, una relación Ca/Si cercana a 1,2 y $\rho\sim2,5$ g/cm^3; monocapas de CH, $\rho\sim2,1$ g/cm^3; y agua en los poros del gel. Esta descripción justifica la estequiometría promedio $(CaO)_{1,8}SiO_2(H_2O)_{4,0}$ y una densidad de $\sim2,6$ g/cm^3.

Además, se llevaron a cabo estudios de otras pastas de alita mediante PDF (en la línea de luz ID15A del sincrotrón ESRF), donde se compararon diferentes polimorfos (C_3S triclínico y monoclínico), temperaturas (RT, 35 y 50°C) y distintos procedimientos de hidratación (*in-situ* y *ex-situ*). El estudio de la hidratación de todos estos grupos no ha mostrado diferencias en la estructura del gel C-S-H precipitado, con un orden atómico local muy similar. Se confirma que ni el tamaño de partícula, ni el tipo de polimorfo, ni la temperatura y ni el procedimiento de hidratación afectan a la estequiometría y el orden local del gel C-S-H formado a partir de la alita, donde la estructura que mejor se ajusta, en todas las pastas, a los datos PDF en el rango r de 10 a 25 Å, es la tobermorita 11 Å.

En segundo lugar, se ha llevado a cabo otro estudio de hidratación de la ye'elemita usando diferentes fuentes de sulfato y diferentes contenidos de agua para identificar las fases amorfas/nanocristalinas utilizando la metodología PDF. Durante la hidratación de la ye'elemita precipita gel de hidróxido de aluminio junto con ettringita o AFm (dependiendo de la cantidad de fuente de sulfato). La metodología PDF, además de dar información de los entornos locales y cuantificar las diferentes fases presentes, aporta información acerca del tamaño de las fases amorfas y nanocristalinas, a través del valor del parámetro Spdiameter. Para el hidróxido de aluminio nanocristalino se obtuvo un valor de ~30 Å en las pastas de sulfoaluminato que se han estudiado en esta tesis doctoral. Además, el análisis de los datos por termogravimetría en las pastas de ye'elemita dio como resultado un contenido en agua superior al estequiométrico de la gibbsita, $Al(OH)_3(H_2O)_{0,7}$. Se especula que los tamaños de partícula muy pequeños ~30 Å de este gel, retienen agua en los poros entre partículas. Se ha determinado que el tamaño de partícula

de este hidróxido de aluminio nanocristalino es de ~30 Å independientemente del tipo de fuente de sulfato o de la toma de datos.

Por PDF también se ha estudiado cómo influye la cantidad de anhidrita (como fuente de sulfato) y la relación másica de agua/sólido en la hidratación de ye'elemita. Cabe destacar que esta técnica analítica no necesita detener la hidratación de las pastas antes de la caracterización, eliminando la posible alteración o modificación por el tratamiento de parado de las fases presentes. En las pastas sin anhidrita, no se formó ettringita y en cambio, aparecieron dos fases AFm, que se diferenciaban en su cristalinidad. Una de ellas era la fase cristalina AFm, y la segunda fue de naturaleza nanocristalina, con un tamaño de partícula de ~60 Å, y un valor de parámetro de celda unidad c significativamente más pequeño. La cantidad de esta fase nanocristalina fue inferior al 6 %p en las muestras con un contenido intermedio de anhidrita (15,5 %p). Para una cantidad mayor de anhidrita, 31 %p, la ettringita es la fase cristalina principal junto al gel de hidróxido de aluminio que tiene una estructura local de nano-gibbsita.

Todo el estudio por PDF se ha realizado usando la metodología de rango r-múltiple y los resultados cuantitativos se han comparado con los obtenidos por el método de Rietveld, con unos resultados muy similares y satisfactorios.

En resumen, esta primera parte del doctorado ha permitido establecer una metodología de rango r-múltiple para llevar a cabo el análisis de mezclas de componentes cristalinos/nanocristalinos/amorfos por PDF. Además, el gel C-S-H se ha caracterizado y descrito como tobermorita defectuosa nanocristalina, monocapas de portlandita y agua de poro, independientemente del polimorfo de alita, el tamaño de partícula, la relación másica de agua/sólido o la temperatura. Finalmente, también se ha descrito el gel de hidróxido de aluminio obtenido en la reacción de hidratación de ye'elemita, concluyendo que el tipo y la cantidad de la fuente de sulfato parecen no tener influencia en la naturaleza nanocristalina de esta fase.

El objetivo principal de la segunda parte de la tesis doctoral fue obtener un clínker con alita como fase principal, aunque también con belita y ye'elemita, denominado como clínker ABY. Para que el clínker presente la máxima cantidad de alita y ye'elemita, se utilizaron materias primas naturales: piedra caliza, caolinita, yeso mineral, arena y mineral de hierro, así como algunos agentes mineralizadores y fundentes, como fluorita y $ZnSO_4$. La temperatura de clinkerización fue de 1300ºC, con el consecuente ahorro energético, ya que se ha reducido 150ºC con respecto al PC, y la correspondiente reducción en emisiones de CO_2. Una vez que se obtuvo el clínker ABY (nombrado como ABY estándar,

ABY), se propuso dar un paso más para obtener un clínker con alita, ye'elemita y la forma activa de la belita, α'_HC_2S, (nombrado como ABY dopado, dABY). El proceso de clinkerización se optimizó, ya que se estudió el efecto de diferentes dopantes (Na_2CO_3, K_2CO_3 y bórax), siendo este último el mejor candidato. El clínker y el procedimiento para preparar ~2 kg de ambos clínkeres (estándar y dopado) se dividió en tres pasos: en primer lugar, se preparó una pequeña cantidad del clínker (5 g, denominado con prefijo *sa*-), en segundo lugar, se preparó una cantidad intermedia (90 g, denominada con prefijo *ma*-), y finalmente, el procedimiento se ajustó para preparar una cantidad mayor (2 kg, denominada con prefijo *la*-).

Por un lado, el clínker ABY estándar se sintetizó con éxito, mezclando materias primas naturales y 1 %p de CaF_2 y 1 %p de ZnO. La cantidad añadida de ambos dopantes presenta un importante papel en la composición mineralógica final. Para la obtención de *la*-ABY se siguió la misma composición y ciclo de clinkerización que para *sa*-ABY, no siendo necesario ninguna optimización extra. El ensamblaje de fases final obtenido fue 41,5(2) %p de alita, 28,4(3) %p de β-belita, 17,4(3) %p de ye'elemita, 4,3(2) %p de fluorellestadita y 3,8(1) %p de ferrita.

Por otro lado, se logró estabilizar la forma α'_H de C_2S al añadir diferentes dopantes a la mezcla cruda estándar. En el primer paso de la clinkerización (*sa*-ABY), se añadió Na_2O o K_2O al crudo, añadido como Na_2CO_3 y K_2CO_3, respectivamente; sin embargo, esta estrategia se descartó porque el α'_HC_2S no se formó. Después, se usó 2.0 %p de B_2O_3, agregado como bórax, junto a cantidades crecientes de CaF_2; sin embargo, esta cantidad de boro dificultó la formación de alita. Por ello, la cantidad de boro se optimizó y se redujo a 0,5 %p. Antes de obtener *la*-dABY, se necesitó otra optimización de la cantidad del agente dopante en el *ma*-dABY. Finalmente, se obtuvieron ~2 kg de dABY, donde coexisten α'_HC_2S, C_3S y $C_4A_3\bar{S}$, al agregar 0,6 %p de B_2O_3 y 0,3 %p de Na_2O, como bórax, junto con 1 %p de CaF_2 y 1 %p de ZnO, este último agregado como $ZnSO_4{\cdot}H_2O$. La composición mineralógica del dABY se determinó por el método de Rietveld obteniéndose la siguiente composición de fases: 15,7(2) %p de alita, 41,8(2) %p de β-belita, 18,0(3) %p de α'_H-belita, 7,7(2) %p de ye'elemita, 6,6(1) %p de mayenita, 3,2(1) %p de ferrita y 3,1(1) %p de fluorellestadita. El estudio de EDS (FEG-SEM) reveló que, en ambos clínkeres, el Zn y F añadidos se incorporaron tanto a la ferrita como a la alita. La composición elemental de la fracción amorfa de ambos clínkeres, determinada por el estudio conjunto de datos XRF y EDS (FEG-SEM), dio como resultado una fase de aluminato de calcio. La fórmula química de las fases principales de ambos clínkeres, alita y belita, se determinó mediante el análisis "semicuantitativo" de EDS (FEG-SEM). Por lo tanto, en esta investigación se

proponen las siguientes fórmulas para alita y belita: $Ca_{2,64}Mg_{0,06}Al_{0,05}(Si_{0,95}Al_{0,05})O_{4,75}$ y $Ca_{1,79}(Si_{0,85}Al_{0,08}S_{0,07})O_{3,75}$, respectivamente.

Finalmente, los clínkeres *la*-ABY y *la*-dABY se mezclaron con una cantidad estequiométrica de anhidrita (14 %p) para que reaccione completamente con la ye'elemita y aluminatos de calcio para formar ettringita. Estos cementos sintetizados (ABY y dABY) se han hidratado y estudiado.

Así, se realizó un estudio de hidratación *in-situ* mediante SXRPD en ambos cementos, de las primeras horas de hidratación (usando la relación másica agua/cemento de 0.5). Estos resultados se compararon con los obtenidos mediante el estudio de hidratación *ex-situ* a diferentes edades de hidratación. El objetivo principal de esta parte fue demostrar que la forma de la belita de alta temperatura ($\alpha'_H C_2S$), estabilizada a temperatura ambiente mediante la adición de bórax, se hidrata a una mayor velocidad que la forma β y, en consecuencia, desarrolla mayores resistencias mecánicas. El desafío aquí es desentrañar el mecanismo de hidratación de estos cementos, determinar el efecto de la relación másica de agua/cemento y verificar el impacto en sus propiedades mecánicas. El comportamiento de las pastas de cemento a edades muy tempranas (primeras horas de hidratación) se investigó mediante reología, calorimetría, SXRPD y LXRPD. Para determinar el contenido de fases cristalinas y el ACn en las pastas la técnica principal utilizada fue la difracción de rayos-X, combinada con RQPA, tanto para estudios *in-situ* como *ex-situ*. También se usó el análisis termogravimétrico para confirmar la mineralogía de las pastas y determinar el contenido de agua químicamente enlazada y libre.

A través del estudio del comportamiento reológico de las pastas, se observó que, durante los primeros minutos de hidratación, la pasta ABY (w/c=0.50 y sin superplastificante) mostraba mayor viscosidad que la pasta dABY correspondiente; esto puede ser debido al menor tamaño de partícula/aglomerado del cemento ABY, lo que está relacionado con una mayor interacción entre partículas. Sin embargo, 10 minutos después de la hidratación, la viscosidad de la pasta dABY aumenta rápidamente, siendo mayor que la de ABY, lo cual coincide con un mayor calor desprendido, medido por calorimetría, en las primeras 3 h de hidratación. Esto es debido a un mayor grado de disolución/reactividad de algunas fases cristalinas, como es el caso del $C_{12}A_7$, presente en dABY, que es responsable de una rápida formación de ettringita.

En el caso de pastas concentradas (w/c=0.40), la viscosidad de dABY era mayor que la de ABY en todo el tiempo estudiado. Este hecho no sólo está relacionado por la disolución/reacción de ciertas fases, principalmente mayenita

(y anhidrita) como se ha comentado arriba, sino también con la dramática pérdida de trabajabilidad de la pasta dABY al disminuir el contenido en agua.

El rápido aumento de viscosidad de ambos sistemas no permite la preparación de morteros homogéneos, siendo esto más dramático para morteros/pastas dABY. Para superar este inconveniente, se optimizó la adición de un superplastificante basado en policarboxilato. Esto permitió la preparación de pastas homogéneas con baja viscosidad, a valores de w/c de 0.40 y 0.50, donde el aumento de la viscosidad durante los primeros minutos también se retrasó debido a la naturaleza retardante del aditivo. La cantidad de superplastificante y el contenido de agua se optimizaron a través del comportamiento reológico de las pastas y los resultados se compararon con los datos de resistencia a la compresión de los morteros correspondientes. Las pastas y morteros optimizados de ABY fueron los preparados a 0.40 w/c con 1.0 %p de SP, y los optimizados para dABY fueron los preparados con 0.50 w/c y 0.4 %p de SP. Los morteros ABY y dABY optimizados mostraron resistencias mecánicas similares a las del PC a ciertas edades, pero liberando hasta ∼17% menos CO_2. Concretamente, los morteros ABY optimizados mostraron resistencias a la compresión de ∼53, 72, 77, 87, 98 MPa a 1, 7, 28, 56 y 180 días, respectivamente, y los valores para los morteros dABY optimizados fueron ∼17, 41, 75, 82 y 83 MPa a las mismas edades, respectivamente. Los morteros ABY muestran mayores resistencias a la compresión que el dABY, a 1 y 7 días de hidratación, probablemente debido a los mayores contenidos de $C_4A_3\overline{S}$ y C_3S en el cemento anhidro. Cabe destacar que los morteros optimizados dABY mostraron un rápido crecimiento en la resistencia a la compresión de 7 a 28 días debido al mayor contenido de belita y a la reacción más rápida de ambos polimorfos de belita, que la forma βC_2S de ABY. Con estos estudios se ha demostrado que los polimorfos de la belita presentes en dABY son más reactivos. Esto ha sido posible a través de la determinación del grado de reacción con los resultados de RQPA y MAS-NMR, donde se cuantificaron mayores cantidades de gel C-S-H. Esta investigación también ha verificado que la adición de bórax en la preparación de dABY retrasó el período de aceleración hasta ∼15 horas. Los resultados del estudio de hidratación a mayores edades obtenidos mediante LXRPD, MAS-NMR y termogravimetría confirman que, en ambos sistemas (ABY y dABY) no se encontró estratlingita. Por el contrario, se obtuvo gel C-S-H de la hidratación de alita y belita. La naturaleza de este gel C-S-H es similar en ambos sistemas, a pesar de que la pasta dABY ha mostrado un mayor grado de reacción en los polimorfos de belita (β o α'_H) y, por ende, se formó una mayor cantidad de este producto de hidratación. A pesar de todo lo dicho anteriormente, el ensamblaje de fases en estas muestras hidratadas no presentó una tendencia clara que justifique las diferencias en las resistencias mecánicas.

Por lo que cabe concluir, que la optimización de los parámetros de procesamiento resultó ser clave para asegurar la homogeneidad, trabajabilidad y, por lo tanto, las altas resistencias mecánicas.

Todos los resultados obtenidos en esta segunda parte del trabajo de investigación han permitido cumplir los objetivos específicos de síntesis, optimización del "escalado" y la comprensión de la hidratación para los cementos ABY y dABY, a la vez que se han obtenido morteros con resistencias mecánicas comparables al PC, pero emitiendo ~17% menos CO_2 que el PC. Además, el objetivo de mejorar el rendimiento de este tipo de materiales mediante el dopaje con boro se ha logrado ya que la relación CO_2/MPa ha disminuido de 0,018 para PC a 0,011 para dABY a los 28 días de curado (w/c=0.50).

1. INTRODUCTION OF CEMENTS AND ENVIRONMENTAL PROBLEMS

1.1 Problem statement and state of the art

Global warming is the major environmental and economic problem in our time. Mahlia (2002) and Zhang et al. (2012) [5, 6], among others, point that GHG emissions are suffering an alarming increase due to the rapid industrial expansion and the increase of the transport. The GHGs connected to human activities are the main cause of climate change, so their reduction has become one of the greatest challenges from the beginning of the twenty-first century. The design and development of low GHG emission products are crucial for mitigating climate change. What the product designers have to face is how to design products that emit dramatically less GHG than has been common practice in recent decades.

According to the World Business Council about sustainable development of a country, there are three fundamental pillars which are necessary to achieve: economic growth, ecological balance and social progress; they are intrinsically linked, and are associated with the capacity of building.

One of the most used manufactured materials in the world is Portland cement concrete, which is mainly composed by water, aggregates (rocks and sand) and PC. Since the first Portland cement was produced in 1843 by William Aspdin [7], there has been a continuous evolution process in the cement process and composition. Cement is used to bind material together and is classified as either non-hydraulic or hydraulic. Hydraulic cements are composed of silicates and oxides that can set and harden even when exposed to water.

PC has become the most commonly used binder material in construction, due to its versatility, durability and cost. Every year ~4 billion tons of PC are produced globally [8]. Its production annually consumes 10^{19}-$1.1 \cdot 10^{19}$ Joules, which represents ~2-3% of the use of world primary energy [9]. In 2018, the world consumption of PC per capita was ~560 kg, where ~3500 million ton/year were produced [1, 10]. Due to the global demand for concrete and future grow of the population, cement production for the future will be expected to reach up to 4.4 billion tons in 2050 (i.e. to increase 2.5 times between 2005 and 2050) [8, 11]. As a consequence of this, the CO_2 footprint will increase considerably. Figure 1.1 shows the evolution of cement production by countries. China produces the highest amount of the worldwide cement, ~2.4 billion metric tons, followed by India with 290 million metric tons in 2018 [1].

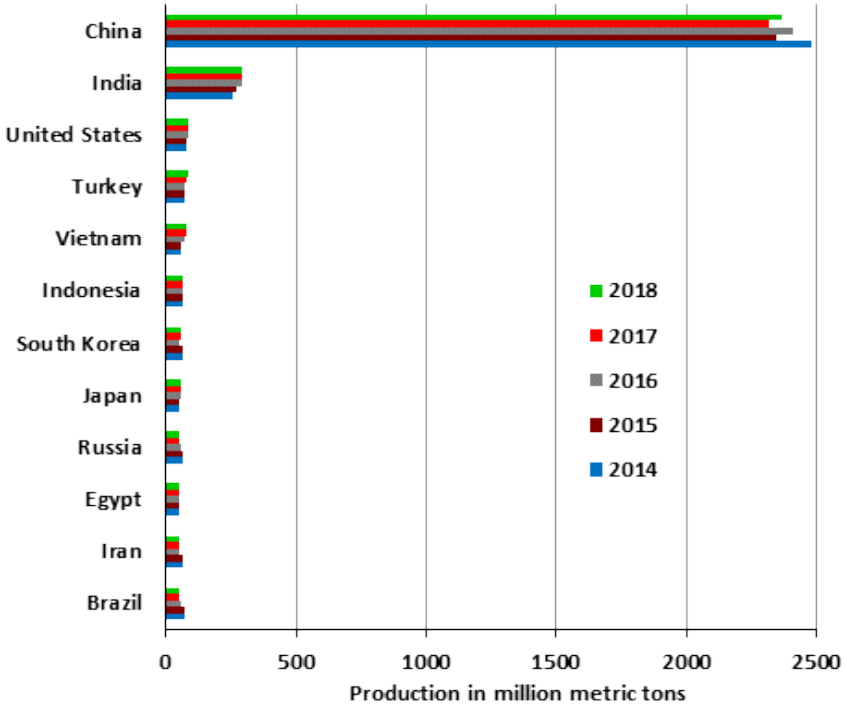

Figure 1.1. The worldwide cement production, by major producing countries, from 2014 to 2018. Modified from [1].

The process for obtaining the final PC generates huge GHG emissions as described below. The clinker is produced by heating (~1400-1500°C) grinded natural raw materials, such as limestone and clays; after that it is ground with a sulphate source, such as gypsum (and others additives) to obtain the cement. The whole production typically emits about ~0.97 tons CO_2 per ton of Portland cement [12, 13]. This emission comes from two main sources: 1) raw meal-derived CO_2 is released from the calcination of limestone in the kiln (about 60% of the total direct CO_2 emissions): $CaCO_3(s) + Heat \rightarrow CaO(s) + CO_2(g)$; and 2) the fuel-derived CO_2 is released from combustion of the fuels used to heat the kiln (direct emissions) and also excavation, transportation, milling and grinding processes (indirect emissions) (about 40% of the total CO_2 released) [2, 12, 14–16]. Figure 1.2 shows a simple diagram of the cement production process and the carbon footprint in each step.

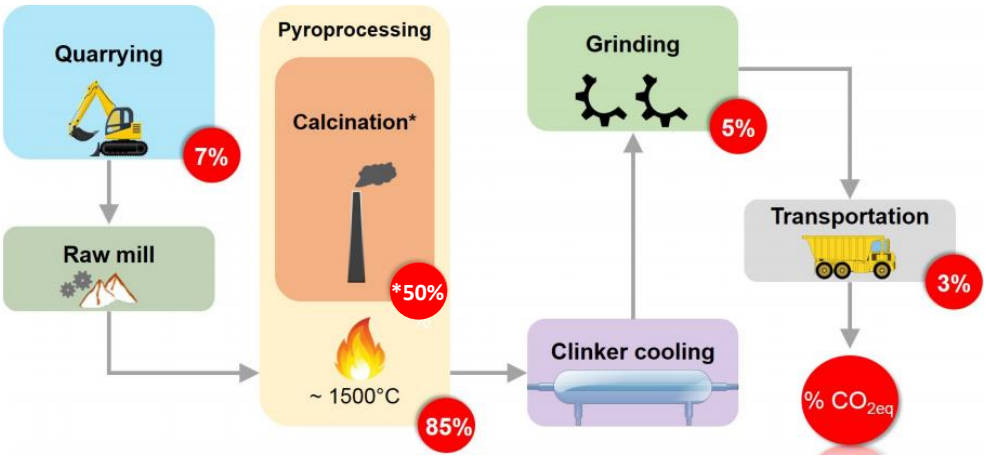

Figure 1.2. Simple diagram of the cement production process. Red circles indicate the percentage of CO_2 emissions associated with manufacturing. (∗)50% of the emissions associated with pyroprocessing arises from direct release of CO_2 from calcination and the remaining 35% from fuel and energy consumption. Taken from [2], open access under the terms of the Creative Commons CC-BY license.

1.2 GHG emissions solving approaches

Due to this fact, an important part of the global human GHG emissions (~8%) comes from the cement industry [17, 18]. In practice, the only greenhouse gas that concern here is CO_2, because the other ones (NO_x, SO_x, CO and material particles) are emitted in small amounts by the cement industry in comparison with carbon dioxide footprint. Because of that, some years ago there has been also a significant increase in the research and development of new ways to reduce these GHG emissions and the pollution of the cement industry. Four key lines are under research, with their own challenges and rewards:

1) Alternative raw materials and fuels. The traditional fuels used in traditional kilns include coal, oil, petroleum coke and natural gas. However, the substitution of fossil fuels by alternative fuels in the production of cement clinker is important for cement producers and for society because it conserves fossil fuel reserves and, in the case of biogenic wastes, reduces GHG emissions. Furthermore, the use of alternative fuels can help to reduce the costs of cement production. Energy costs and environmental concerns have encouraged cement companies worldwide to evaluate to what extent conventional fuels can be replaced by waste materials, such as waste oils, mixtures of non-recycled plastics and paper, used tires, biomass wastes, and even waste water sludge. The clinker firing process is well suited for various alternative fuels; the goal is to optimise the

process control and alternative fuel consumption while maintaining clinker quality. Many years of industrial experience have shown that the use of wastes as alternative fuels by cement plants is both ecologically and economically justified [19]. However, the cement kilns conditions should provide enough oxygen concentration, residence time for reaction and high temperatures to destroy all the organic present in the alternative fuels [19, 20].

2) Partial substitution of PC by SCM. This line is one of the most effective ways to reduce GHG emissions from PC manufacture, due to the reduction of the clinker amount, known as lowering the clinker factor. These SCM include natural rocks, minerals and industrial derivatives (slags, fly ash, silica fume, limestone, calcined clays, and so on [21–23].

Points 1 and 2 have already been applied by the industry, as there is a relatively direct change. Nevertheless, its improvement capacity is limited [21]. The present levels of alternative fuel consumption have shown no impact on GHG emissions from cement kilns and their use is more often related to improve the economic performance of the process than its environmental performance [24]. Moreover, there is a real need to search for new sources of SCMs since the supplies of traditional SCMs are becoming restricted [25].

3) CO_2 capture and sequestration is unpleasant to cement producers since it requires major funds in plant equipment to perform the capture [26] and is currently uneconomical without supporting regulation schemes to incentivise its adoption.

4) Formulation of new alternative low-carbon binders is a really important line for changing the composition of the binder and reducing the use of limestone in the cement manufacture. However, this option is delayed by the absence of standardisation, which in turn, delays the subsequent use of these new binders by the construction industry in massive structural applications. Nevertheless, new binders can reduce mid-term emissions with none major disruptive changes nor large capital investments in plant redesign [27]. The design of new cements, from the chemical point of view, is aimed at the search for good final performances (resistance and durability), global energy savings in the production process [13, 28, 29], and the reduction of CO_2 emissions [2, 9]. This last point can be addressed through the design of the composition of cements with less calcite-demanding phases than those present in PC, since decarbonation is the step with the greatest CO_2 emission.

Before designing the composition of a new clinker/cement it is needed to know the phases present in PC, whose main mineralogical crystalline composition are: 50-70 wt% of alite, 15-30 wt% of belite, 5-15 wt% of ferrite and 5-10 wt% of tricalcium aluminate [30]. These crystalline phases need a high amount of CaO for their formation, being limestone the main source. Table 1.1 shows the CO_2 emissions during the formation of the four main phases of the PC, which are directly related to calcite demand. Several other minor phases, such as alkaline sulphates, magnesium oxide and calcium oxide are also present in small amounts. To obtain the final cement up to 5 wt% of gypsum is added to the clinker as setting regulator [7, 30, 31].

Table 1.1. Composition of PC clinker in weight percentage. Tons of CO_2 released into the atmosphere for the synthesis of each crystalline compound of PC, considering $CaCO_3$ as calcium oxide source.

Composition (wt%)	Components	t_{CO2} / $t_{component}$
50-70	Alite	0.58
15-30	Belite	0.51
5-10	Tricalcium Aluminate	0.49
5-15	Ferrite	0.36

Among these four main PC phases, **alite** is the most important one, not only because it is the most abundant but also due to its hydration reaction which is quick and its hydration products contribute to the early-age mechanical properties. The hydration reaction of **belite** is slow, so it contributes to the long-term mechanical properties development. These two silicate rich phases represent ~80 wt% of Portland cement composition and their hydration products are calcium silicate hydrate (C-S-H gel) and portlandite [30], although react. 1.1 and 1.2 (in italics the nanocrystalline/gel components) are still under strong debate in spite of one century of focused investigations:

$C_3S + 5.2H \rightarrow 1.2CH + \mathit{C_{1.8}SH_4}$ react. 1.1

$C_2S + 4.2H \rightarrow 0.2CH + \mathit{C_{1.8}SH_4}$ react. 1.2

C-S-H gel ($\mathit{C_{1.8}SH_4}$) is the main responsible for the properties related with the hydration development (for instance, setting and compressive strength) in Portland cement. In addition, gypsum is used in Portland cement as setting regulator (regulates the hydration reactions) of aluminate rich phases (**ferrite** and **C_3A**). Their hydration products are ettringite (AFt or $C_6A\bar{S}_3H_{32}$) (which also contributes to the mechanical properties at early ages) and aluminium hydroxide gel with stoichiometry close to gibbsite [7, 30–32], reactions 1.3 and 1.4 (in italics the nanocrystalline/gel components).

$C_4AF + 3C\bar{S}H_x + (36\text{-}3x)H \rightarrow C_6A\bar{S}_3H_{32} + CH + FH_3$ react. 1.3

$C_3A + 3C\bar{S}H_x + (32\text{-}3x)H \rightarrow C_6A\bar{S}_3H_{32}$ react. 1.4

1.3 Cement alternatives for reducing the CO_2 footprint

From the previously pointed four key lines, the formulation of alternative low-carbon binders has been selected as one of the most achievable lines of research for reducing the carbon footprint in the cement industry. The reduction of the alite content is the main focus in this research line of this PhD Thesis, since alite is the most abundant phase in PC, where it requires high lime contents and a high formation temperature. The partial substitution of this main phase by belite, maintaining the same mineralogy (i.e. C_2S-C_3S-C_3A-C_4AF in the system) results in up to 12% reduction of CO_2 emissions due to the lower limestone requirement. They are commonly known as high belite cements, HBC [33–37]. The clinkering temperature for HBC is usually close to 1350°C, which is about 100°C lower than the average for PC, with the consequent reduction of heat consumption and fuel. Physically, they preserve satisfying long-term properties due to the lower alkalinity of the pastes and lower porosity [38]. Nevertheless, substituting the main phase, C_3S, by C_2S compromises the early-age property development due to the slow reactivity of this phase. In addition, the consumption of electricity during the grinding process is higher due to its little friability. In the last years, there has been some publications focused on the activation of HBC by doping [34, 39–41], Consequently, more research is needed to overcome all these problems [33].

Calcium sulphoaluminate based cements are also an alternative in which the components are low calcite demanding phases. **Ye'elimite** (Klein salt, $C_4A_3\bar{S}$ or $Ca_4Al_6SO_{16}$) is the main phase of this type of cements. This phase just releases 0.22 tons CO_2/ton of component, that supposes almost a third part of CO_2 released by alite (the main PC phase). Ye'elimite-rich cements, not just present lower calcite demand, but also are produced at lower temperature with the corresponding fuel and electricity savings since they are also easier to be ground. To sum up, the CO_2 emissions are further reduced. Cements with ye'elimite can be gathered in three types depending on the quantity of this phase: 1) Calcium sulphoaluminate (CSA) cement, which has 50-80 wt% of ye'elimite, 2) Belite Calcium sulphoaluminate (BCSA, also called BYF for its composition: belite-ye'elimite-ferrite) and 3) Belite-alite calcium sulphoaluminate (BACSA, also called BAY for its composition: belite-alite-ye'elimite). The acronym could be modified according to the amount of each phase, for instance ABY means that alite is more abundant than belite. The

different types of ye'elimite rich clinkers [42] are described in the following section in more detail.

Figure 1.3 shows the carbon dioxide footprint of each type of clinker in the production of 1 ton, as well as the percentage of raw materials needed to obtain them and the final composition of the calculated clinkers.

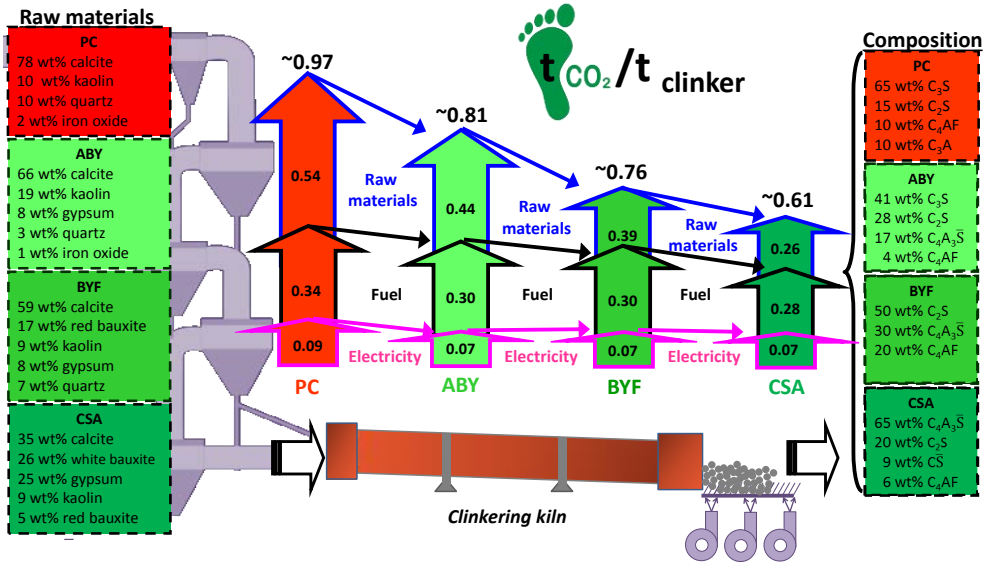

Figure 1.3. Schematic representation of raw materials (left), clinker phase compositions (right) and CO_2 released during the process in each step of the production process (centre) for PC and calcium sulphoaluminate based clinkers.

Ye'elimite-rich cements are an environmental alternative to PC to reduce the carbon dioxide footprint. However, in Europe the use of these alternative cements is only used in niche applications. This is due to the lack of existing regulations, since they cannot be used in massive structural applications in accordance to EN 206-1. Nevertheless, in this decade, three CSA cement formulations produced by Buzzi Unicemen Trino (Italy), obtained in June 2013 a CE mark based on an ETA procedure, published by DIBt, allowing its use for structural applications [43, 44]. This is very promising and requires the complete knowledge of the hydration and performance of these cements before they can be used in structural applications.

1.3.1. CSA cement

It is composed by **ye'elimite** (50-80 wt%), belite and ferrite (see Figure 1.3) and other minor phases such as: anhydrite, free lime, calcium aluminates (CA and

mayenite), perovskite and/or gehlenite [29, 45, 46]. Depending on its composition, it can reduce CO_2 emissions up to 37% compared to PC. In addition, their hardening is very quickly due to the ye'elimite hydration reaction with a sulphate source and water to obtain ettringite, which provides very high mechanical strength, even at early ages [47], see react. 1.5 (in italics the nanocrystalline/gel components). They also have satisfactory durability, dimensional stability and can be used as self-levelling cements [47–51]. These cements are an example of an eco-material that is environmentally attractive [13, 14, 28, 29, 52]. Its clinkering temperature is ~200°C lower than that for PC, and the resulting clinker is easier to grind so it will need less energy. Nevertheless, these types of cements have a high cost (for the use of bauxite as raw material that provides Al_2O_3 to the clinker). To reduce the cost, it can be partially substituted by waste materials such as fly ash [53] or can be mixed with other types of cements, such as PC [54–56]. The former would involve a triple benefit, such as the reduction of CO_2 emissions, economic savings and the valorisation of waste products. However, the scope of this substitution is limited by the reduction in mechanical resistance and just small amounts of SCMs can be used.

$C_4A_3\overline{S} + 2C\overline{S}H_x + (38\text{-}2x)H \rightarrow C_6A\overline{S}_3H_{32} + \textit{2}AH_3$ react. 1.5

1.3.2. BYF cement

This type of cement come from an attempt to overcome the disadvantages present in HBC and CSA but keeping the advantages of the low-CO_2 emissions [57–60]. It is important to note that BYF cement has been manufactured on a large scale in the USA since the 1980s [61]. Its production releases up to 22% less CO_2 than PC. They are mainly formed by belite (C_2S), ye'elimite and ferrite [48, 59, 62–67], (see Figure 1.3). The synthesis temperature of these materials is around 1250-1350°C, which also represents a considerable energy saving when is compared to PC (1450°C). In addition, the grinding of this type of clinker is also easier than PC, with the associated electricity savings. Despite all these advantages, and even developing similar mechanical strengths at middle and late ages, there is a problem derived from BYF cements, related to their low mechanical strengths at early ages, due to the slow hydration reaction of belite [50]. Nevertheless, this problem can be overcome in two ways: 1) The use of dopants (B_2O_3 and Na_2O) to stabilize the alpha polymorphs of belite (α'_HC_2S and αC_2S forms) since these polymorphs react faster than βC_2S [58, 64, 68, 69]. Although the activation of BYF cements increases considerably their mechanical

strengths, at early ages, it is still much lower than PC [64]. 2) Producing belite-ye'elimite clinkers with a certain amount of alite, i.e. **BAY** clinkers [70, 71].

1.3.3. Belite, Alite and ye'elimite containing cements. BAY (belite-alite calcium sulphoaluminate or Belite-Alite-Ye'elimite) or ABY (alite-belite calcium sulphoaluminate or Alite-Belite-Ye'elimite)

In these types of materials, the goal is to obtain a material with jointly alite and ye'elimite, since these two phases will yield to high mechanical strengths at early ages. The clinkers which main phase is belite (~50 wt%), i.e. BAY, are synthesized between ~1250-1300°C [72] and release up to 18% less CO_2 in their production (see Figure 1.3), depending on the composition. However, their production presents some difficulties because ye'elimite decomposes around 1350°C while alite synthesis starts at this temperature. These problems have been solved by adding a small amount of mineralisers, such as CaF_2, CuO and ZnO to the raw mixture, which act as fluxes and mineralisers. They will decrease the formation temperature of alite, so that it can coexist with ye'elimite in the clinker [70, 71, 73–75]; the amount of sulphur has to be under control in the kiln due to some volatilization [71]. However, the mechanical strengths at early hydration ages could still be quite low [71].

With the aim of overcoming the previous mentioned drawbacks of BAY cements, ABY cements are proposed. ABY, with alite as main phase, integrate both the characteristics of calcium sulphoaluminate and Portland cement. However, the CO_2 reduction will range from 10% to 20%, depending on the amount of alite, Figure 1.3. Both ye'elimite and alite provide high mechanical strengths at early ages, and the latter will also favour the pozzolanic reaction with SCMs since it forms portlandite (CH). This would entail a fourfold benefit, three described in the CSA section and one more due to an increase in mechanical strengths due to the pozzolanic reaction at longer ages, when it is mixed with SCMs. However, this substitution in BAY cements has been proved not to increase mechanical strengths [76] mainly due to the absence of portlandite during hydration.

A step forward to activate these materials is by activating/stabilizing alpha forms of belite with dopants.

These type of cements (BAY/ABY) have been the focus of this PhD Thesis. Before they could be used, the hydration of this cements need to be under control. This is described below.

1.4 Hydration behaviour of alite-belite-ye'elimite cements

The hydration procedure of cements involves three steps: dissolution of the anhydrous phases, saturation of the liquid medium, and formation of new phases, with the resultant water consumption. As soon as the water is added to the cement, both ye'elimite ($C_4A_3\bar{S}$) and the sulphate source (gypsum, bassanite and/or anhydrite) start to dissolve. The reaction of ye'elimite with the sulphate and water is shown in react. 1.5, where ettringite ($C_6A\bar{S}_3H_{32}$) and amorphous aluminium hydroxide (AH_3) are formed. Formation of ettringite will continue while calcium sulphate is present. Once the sulphate source is depleted and there is enough free water available, monosulphoaluminate also known as AFm ($C_4A\bar{S}H_{12}$) will be formed [47] according to react. 1.6.

$C_4A_3\bar{S} + 18H \rightarrow C_4A\bar{S}H_{12} + 2AH_3$ react. 1.6

These two reactions, react. 1.5 and 1.6, may take place in the early hydration of CSA, BYF, BAY and ABY cements. The most important reactions of the most common minor phases are detailed below. Minor phases also react with water or calcium sulphate and somewhat contribute to rapid hardening, according to the following reactions [29, 55, 77], reacts 1.7 and 1.8.

$C_{12}A_7 + 12C\bar{S}H_x + (137\text{-}12x)H \rightarrow 4C_6A\bar{S}_3H_{32} + 3AH_3$ react. 1.7

$3CA + 3C\bar{S}H_x + (38\text{-}3x)H \rightarrow C_6A\bar{S}_3H_{32} + 2AH_3$ react. 1.8

Ettringite crystallizes in these reactions during the first hours of hydration. Depending on the availability of calcium sulphates source, there are other alternative reactions for the direct hydration of these phases at room temperature [78], reacts 1.9 to 1.11:

$C_4AF + 16H \rightarrow 2C_2(A_{0.5}F_{0.5})H_8$ react. 1.9

$C_{12}A_7 + 51H \rightarrow 6C_2AH_8 + AH_3$ react. 1.10

$2CA + 11H \rightarrow C_2AH_8 + AH_3$ react. 1.11

Aluminium or iron hydroxides (AH_3 or FH_3) are initially considered as amorphous phases as they cannot be directly detected by X-Ray Powder Diffraction (XRPD) so its presence may be confirmed by DTA-TG techniques [63, 65, 79]. Later, these aluminium rich amorphous phases may crystallize as gibbsite.

Although silicate phases, alite and belite, react with water according to react. 1.1 and 1.2, in cements with ye'elimite, the hydration mechanism is slightly different as represented in react. 1.12, forming stratlingite or C_2ASH_8 (another AFm type phase):

$C_2S + AH_3 + 5H \rightarrow C_2ASH_8$ react. 1.12

Furthermore, at late ages, katoite formation could come from C_2S/C_3S in the presence of amorphous AH_3 and/or CH, react. 1.13 and 1.14 [80, 81]. Ferrite can also be hydrated to form these type of phases, react. 1.15 [82].

$C_2S + AH_3 + CH \rightarrow C_3ASH_4$ react. 1.13

$C_3S + AH_3 \rightarrow C_3ASH_4$ react. 1.14

$C_2S + x\ C_4AF + 10x\ H \rightarrow C_3A_{1-x}F_xSH_4 + (4x-1)\ CH + (2x-1)\ AH_3$ react. 1.15

The hydration reactions of this type of materials need to be completely understood to control the mechanical properties. They are also related to both processing and phase assembly.

1.5 Homogeneity of pastes and mortars. Sample treatment and processing

A good sample preparation is essential to achieve flawless samples with improved performances. It is needed to control the sampling, grinding, homogenisation and storage of anhydrous binders joining with the optimisation of the preparation and curing of pastes and mortars [83]. Homogeneous and dense materials can be obtained through the preparation of well dispersed cement pastes [84, 85]. Furthermore, low water contents, within certain limits, are usually related with improved mechanical properties [86, 87]. The use of additives, such as superplasticisers, is a common practice in the building industry since it helps the dispersion of the cement particles, reduces viscosity and allows the preparation of mortars with lower water-to-cement (w/c) ratios. The superplasticiser causes the repulsion of the particles through electrostatic, steric

or electrosteric repulsions [88–92]. Polycarboxylate-based superplasticisers create repulsion between particles through electrosteric mechanism [93]. They are considered as third generation SP, and usually provide ~20 min of workability, although this depends on the dosage. The effect onto the paste will depend on the superplasticiser (type and amount) [94], the composition of the cement powder, particle size distribution, specific surface area, and so on. Specific additives (retarders and/or specific superplasticisers, such as polycarboxylate-based superplasticisers) can delay the reactions which may be beneficial to increase the workability in particular systems [87, 93]. The addition of the right amount of chemical admixture is really important to improve the dispersion, diminish the viscosity and control the setting time, to finally develop the homogeneity and performance of the corresponding cements and mortars. Due to that, in this work, the superplasticiser content and the water to cement mass ratio have been optimised.

1.6 Total scattering diffraction

Cements and pastes have been widely characterized by XRPD, combined with Rietveld methodology [83, 95, 96]. Not a long time ago, new materials, necessary in many technological fields, have issued challenges not only in synthesis and production, but also in structural characterization, especially those highly disordered, amorphous, nanoparticles, etc. [97]. The structures of these materials are determined just based upon the information provided by the position and intensity of the Bragg peaks, whereas additional information regarding deviations from the perfect lattice is obtained through the study of diffuse scattering. This approach makes sense when the deviations are small, but if the structure is extensively disordered it fails in practice. This treats both the Bragg and diffuse scattering on an equal basis, the so-called **total scattering technique**. Data from throughout reciprocal space, over a wide range of Q-values, are used. This technique is both straightforward and easy to comprehend. A suitable tool here is the Fourier transformation. Analysing a complex function, Fourier analysis quite often provides distinct and useful information that is easier to interpret. In diffraction, the Fourier transformation has a very well defined physical meaning, analysing the total scattering data known as atomic PDF analysis [97]. PDF takes advantage of the Fourier relationship between measurable diffraction intensities and the real space arrangement of pairs of atoms [98]. This function gives the probability of finding an atom at a given distance r from another atom [97], i.e. indicating the existence of a pair of atoms

with the separation of the peak position in the function. Basically, PDF analysis provides information about atomic arrangements. Moreover, this technique gives a complete description of the material at the different length scales depending on the degree of crystallinity, crystalline, nanocrystalline or amorphous Figure 1.4. On the one hand, the term nanocrystalline is referred to phases whose atomic structure can be described by using the crystal structure truncated in the real space by a nanosized shape function and employing finite models that take into account surface relaxation effects. On the other hand, an amorphous compound cannot be properly described by this approach.

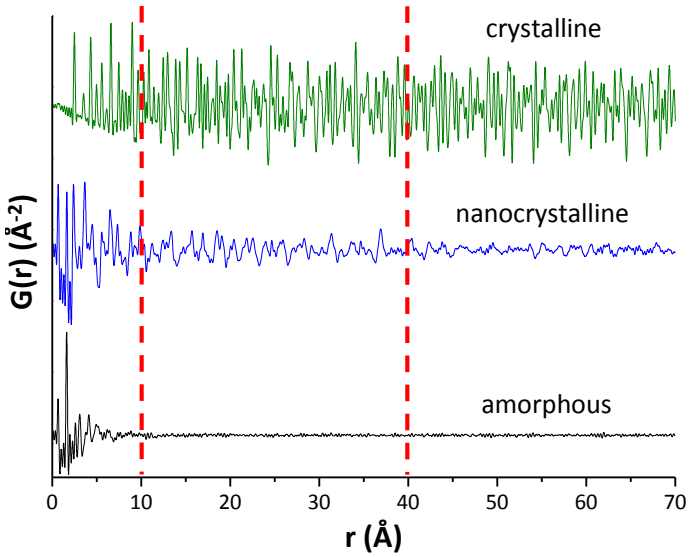

Figure 1.4. PDF analysis of a crystalline material (green line), a nanocrystalline material (blue line) and an amorphous material (black line). Three r-ranges are separated by red dashed lines indicating the contribution to the PDF scattering of the different length scales.

Figure 1.4 reveals disorder on the local structure (low r-range) which is gradually averaged as radius range increases up to give an average order cubic structure (high r-range). This figure shows the potential of the Pair Distribution Function investigation which will allow studying structure at different length scales by choosing adequate radius ranges to perform the refinements. A mixture of phases with different degree of order/crystallinity will yield to a mixture of PDF signals. This powerful tool can be used in cement and concrete research to characterize amorphous and poorly crystalline phases.

1.6.1 PDF theoretical background

The reduced PDF function, also known as G(r), give us the possibility of finding pairs of atoms separated by an r distance. G(r) is obtained from equation 1.1 [99]:

$$G(r) = 4\pi r[\rho(r) - \rho_0] = \frac{2}{\pi}\int_0^\infty Q[S(Q) - 1]\sin(Qr)dQ \qquad \text{eq. 1.1}$$

ρ(r) is the microscopic atomic pair density, ρ_0 is the average atomic number density, S(Q) is the total scattering structure function, Q is the momentum transfer.

This function is a sine Fourier transform of S(Q) of the measured intensity and takes both, Bragg and diffuse scattering into account. The Bragg scattering contribution can be analysed by the conventional Rietveld approach with high degree of accuracy in reciprocal space and provides information on the average and periodic structure regarding long-range order. The diffuse scattering, which lies between and beneath the Bragg reflections, yields information regarding the short range order and, consequently, local deviations from the average structure [97] . It has weaker intensities compared to Bragg reflections and dominates at higher scattering angles where the Bragg reflections are weak due to the Debye-Waller factor. In conventional Rietveld refinements, the diffuse scattering contribution is usually discarded.

F(Q) is known as the reduced total scattering structure function and defined in terms of S(Q) in eq. 1.2 as:

$$F(Q) = Q\,[S(Q) - 1] \qquad \text{eq. 1.2}$$

F(Q) oscillates around zero when Q goes to high Q-values. Diffuse scattering can be seen more clearly in F(Q) than in S(Q).

G(r) is called the PDF and it is a one-dimensional function oscillating around zero. Positive peaks in G(r) show the probability of finding interatomic distances where microscopic pair density exceeds the average number density ($\rho(r)>\rho_0$). In addition, negative peaks correspond to a real space vector not having atoms where a microscopic pair density is lower than average ($\rho(r)<\rho_0$). In the case of neutron diffraction, positive peaks correspond to two nuclei with either both negative or both positive scattering lengths, while negative peaks correspond to pairs with one negative and one positive scattering length of the nucleus.

1.6.2 High quality of PDF recorded data

The PDF method needs high maximum momentum transfer, Q_{max} (for good resolution in real space), high Q-resolution (for a broad extension in real space), good counting statistics at high Q-values and low to be able to be subtracted background scattering. The PDF method carries no less information than Rietveld method.

The main difference from an experimental point of view between data for conventional Rietveld refinements and PDF is the necessity to measure to as large Q-values as possible for PDF. The real space resolution of the PDF is given in eq. 1.3 and is directly related to the maximum Q-value, Q_{max} [100] and the real space resolution gets better with increasing the Q_{max} value.

$$\delta r \approx \pi / Q_{max} \qquad \text{eq. 1.3}$$

In practice, the data cannot be measured up to infinite momentum transfer, Q, i.e. Q_{max} is limited. Hereafter, the finite Q-range of the data introduces errors into the experimental PDF, known as termination **ripples**. The termination ripples are spurious oscillations at small r-values, typically lower than reasonable nearest neighbour distances and vanish at increasing r. In practical applications, the Fourier sine transform of F(Q) does not go from zero to infinite, but from minimum to maximum Q-values [101]. The termination ripples can be described by convoluting the G(r) with a step function cutting at Q_{max}. The S(r) step function is given by eq. 1.4:

$$S(r) = \sin (Q_{max} \cdot r) / r \qquad \text{eq. 1.4}$$

The termination ripples oscillate with a wavelength $\sim 2\pi/Q_{max}$ in G(r),which increases with decreasing Q_{max} [97]. In addition, the convolution of G(r) with S(r) results in a Gaussian like peak broadening. Nevertheless, thermal motion of atoms always broadens the PDF and the additional broadening due to termination is negligible if a high enough Q-value is chosen. If Q_{max} is larger than 30 $Å^{-1}$, termination produces minimal errors [102].

X-ray diffraction techniques measure the differential scattering cross-section. The measurements are generally represented in Q space, or commonly known as reciprocal space. This vector (Q), is the difference between the wave vectors of the incident and scattering X-rays. For elastic scattering, the magnitude of Q is given by eq. 1.5, where λ is the wavelength, and 2θ is the angle of scattering. The maximum experimental Q-range is limited to $4\pi/\lambda$, since $\sin \theta \leq 1$ [97]. High energy synchrotron sources, such as European Synchrotron Radiation

Facility (Grenoble, France), use wavelengths around 0.19 Å, allowing a dramatically wider Q-range compared to a standard laboratory X-ray diffraction instrument using CuKα radiation.

$$Q = 4\pi \cdot \sin \theta / \lambda \qquad \text{eq. 1.5}$$

The amplitudes of ripples increase with the lower value of Q_{max} [97, 102, 103]. Total scattering data analysed by PDF methodology allow distinguishing between components that are amorphous, nanocrystalline and/or crystalline by focus the analysis in the appropriate r-windows, Figure 1.4. Besides to local bonding environment information, PDF can also provide quantitative information concerning phase contents [97, 104, 105]. One important thing in the PDF analysis is the instrumental parameters such as the dampening parameter (Q_{damp}) [97] and the peak broadening parameter (Q_{broad}) [102]. Both are specific for every experimental setup and can be determined with a high crystalline material used as standard (nickel in many cases). The Q_{damp} parameter is straightly related with the finite Q-resolution through the Gaussian shape of the peak attenuation. Therefore, it is important to collect balanced diffraction data up to the largest possible Q-value. A comparison of the resulting PDF data for three time-of-flight neutron powder diffractometers has been recently reported [106]. Powder diffraction data with higher reciprocal space resolution led to PDF data with much lower damping.

Currently, several kinds of materials that combine amorphous/nanocrystalline/crystalline phases are presented in our daily life, as cements, pharmaceuticals, glass-ceramics, etc. The characterization of nanocrystalline/amorphous mixture samples with crystalline phases is very challenging. This is the case of hydrated cements (anhydrous and hydrated phases). As mentioned before, some hydration products are nanocrystalline, like C-S-H gel [107], according to react. 1.1 or nanocrystalline aluminium hydroxide in the ye'elimite based cements (react. 1.5) [29].

The use of the PDF methodology with high-energy synchrotron radiation to the study of different hydrated cement samples has been already reported [108, 109]. Some important studies have been developed using this methodology, such as the local structure of C-S-H gel. It was found that the gel has a nanocrystalline nature with a local atomic ordering close to 40 Å [110–112]. In addition, it has been recently reported that this C-S-H gel is composed by two phases: a nanocrystalline defective clinotobermorite, $C_{11}S_9H_{9.5}$, and an amorphous component which was described as isolated monolayers of CH [113].

1.6.3 PDF interpretation

PDF methodology represents the probability of finding pairs of atoms at different interatomic distances, see Figure 1.5. The obtained peaks coincides with a greater probability to find a pair of them, whereas function returns to its baseline if there is zero probability of finding atoms separated by that distance [114]. The obtained G(r) from a XRPD pattern gives information related with the atomic bond lengths presented as r in Å (x axis), Figure 1.5. The shape and intensity of every peak depend on different effects:

i) A great proportion of highly ordered structure with distances related to a certain radius must have similar values. Because of that, the distance distributions will be a narrow forming peak with high intensity and sharp shape.

ii) The atomic disorder (with a high atomic displacement parameter from the ideal lattice sites) will produce a broadening and less intense signal for the atom-atom (r) distances. It is important to highlight that the peak intensity is also linked to the chemical species involved in the bond lengths. In addition, the bonds of heavy elements will contribute more than lighter ones due to the atomic form factor differences, which increase with the atomic weights when using X-rays.

iii) The dampening of the signal depends on the crystal sizes. The peak-peak signal amplitude in the G(r) from a microcrystalline sample gradually decreases due to the finite Q resolution of the measurement. Nevertheless, in nanosize crystals samples with a low degree of structural order, the signal amplitude in G(r), falls off faster than dictated by the Q resolution and this becomes a useful measurement of the structural coherence of the sample, i.e to evaluate the diameter of nanoparticles [97].

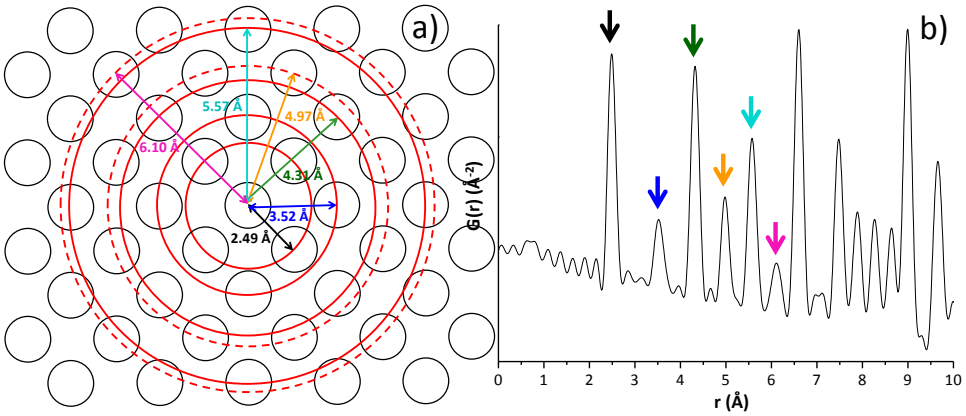

Figure 1.5. Relation between a) structure and b) G(r): interatomic distances cause maxima (peaks) in G(r) at Q_{max} 24 A^{-1}. Nickel sample at the first coordination spheres.

1.6.4 PDF Structural analysis

A PDF structural analysis uses a full-profile fitting method analogous to the Rietveld method, but where the function to be fitted is the G(r). Structural and experiment dependent parameters are allowed to vary until achieving the best fit between calculated G(r) from the model and the data using a least squares approach [114]. Lattice parameters, atomic fractional coordinates, displacement, occupancies of the crystallographic sites and ADP could be then refined in order to obtain a good agreement between calculated and observed functions. The goodness of the fit is assessed by the so called **Rw** value. This value takes into account the sum over all data points, the observed PDF data, the calculated PDF data and the weight of each data point [115], see Figure 1.6.

The obtained PDF can be analysed and studied using different r-ranges meaning the different length scales: the multi r-range method. The structural information in each r-range may be different and it depends on the type and complexity of the samples. The structural knowledge at the local level or average length scale can be deduced by choosing the appropriated r-ranges. Thanks to this multi r-range PDF method, the atomic structure, coherent correlation length and its evolution can be studied. Nevertheless, the samples studied in this PhD work present G(r) functions with different short and long r-ranges due to their heterogeneous nature, i.e. they may contain crystalline, nanocrystalline and amorphous phases. Consequently, it is needed to start to model the local atomic arrangement with an improved structure, refining parameters and changing structural constrains to improve the goodness of the fits. Sometimes it is

necessary to break the average symmetry to obtain a good fit by increasing the disorder of the model. This methodology, named small box modelling [115], takes into account just few atoms that are restricted to crystallographic rules in order to simplify calculations. PDFgui software [116] has been used in this PhD to use this methodology.

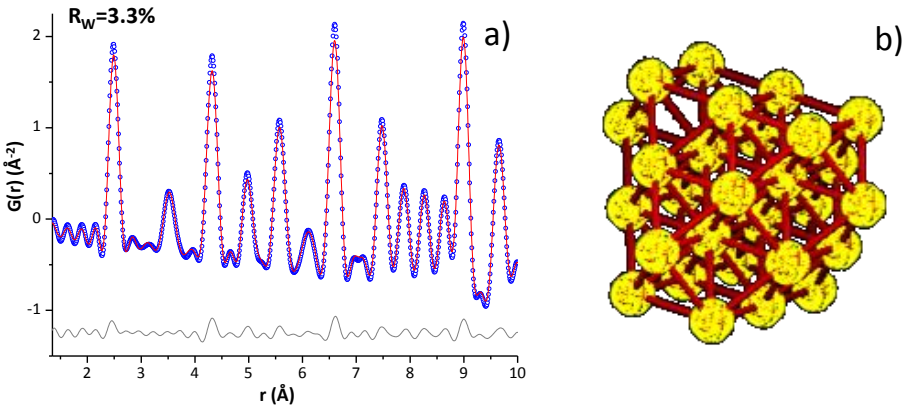

Figure 1.6. a) Experimental (blue circles) and fitted (red solid line) PDF fit profiles for a crystalline nickel sample, Q_{max}=24 $Å^{-1}$. MSPD synchrotron data for 1.35-10 Å r-range. Difference curve is shown as grey line. R_W value is also included. b) Crystallographic structure obtained from the refined PDF.

2. MATERIALS AND METHODS

This work concerns two parts:

i. Basic science: synchrotron X-ray PDF methodology was applied to quantitatively analyse the atomic structure of the amorphous/nanocrystalline gels in model cement pastes.

ii. Applied science: clinkering, processing, hydration and characterisation of two laboratory-synthesized cement types, standard and doped ABY, were performed.

This "Materials and Methods" section has been gathered in three subsections: a) description of the materials, b) preparation of the hydrated samples, and c) description of the used facilities, working conditions, and data treatment.

2.1. Materials

2.1.1. Nickel

Nickel was used as crystalline standard for PDF experiments. This sample is a commercial powder sample, from Strem Chemical INC., with a purity of 99.9% and a particle size between 3-7 μm.

2.1.2. Triclinic tricalcium silicate, tC_3S

The hydration of a commercial stoichiometric tC_3S (100 wt% of C_3S triclinic polymorph) was studied through PDF. It was purchased from Mineral Research Processing (M.R.PRO) and it is a single crystalline phase. It shows an elemental composition of 73.8 wt% of CaO and 26.1 wt% of SiO_2, which was determined by XRF. The particle size was measured by laser diffraction, see Table 2.1. That table shows $D_{v,10}$, $D_{v,50}$ and $D_{v,90}$ values of tC_3S and other materials used in this PhD thesis that will be described in the following sections. Values of measured density (He picnometer) and specific area (BET) are also shown in the same table.

Table 2.1. Particle size ($D_{v,10}$, $D_{v,50}$, $D_{v,90}$), density and specific area (BET) of all the studied materials.

Materials	$D_{v,10}$	$D_{v,50}$	$D_{v,90}$	ρ (g/cm^3)	BET (m^2/g)
tC_3S*$^{\$}$	0.8	4.6	11.0	3.15(1)	1.9(1)
mC_3S-2015*$^{\$}$	1.7	13.8	35.8	3.14(1)	0.8(1)
mC_3S-2016*$^{\$}$	3.1	20.8	70.7	3.16(1)	0.3(1)
mC_3S-2017*$^{\$}$	0.9	6.3	25.6	3.17(1)	1.0(1)
$oC_4A_3\bar{S}$-2016$^{\$}$	1.5	9.0	28.7	2.56(1)	1.2(1)
$oC_4A_3\bar{S}$-2017$^{\$}$	1.3	7.1	22.1	2.61(1)	1.1(1)
Anhydrite$^{\$}$	1.5	10.1	42.6	2.93(1)	2.6(1)
***la*-ABY clinker$^{\$}$**	1.3	7.9	38.8	3.09(1)	1.6(1)
***la*-dABY clinker$^{\$}$**	1.6	8.9	19.4	3.12(1)	1.2(1)
ABY cement$^{\&}$	1.3	9.1	67.6	3.07(1)	1.8(1)
***d*ABY cement$^{\&}$**	1.6	9.8	75.3	3.10(1)	1.4(1)

*as-received samples

$^{\$}$ PSD measured in a Mastersizer S model, Malvern, within a wet chamber filled up with ethanol.

$^{\&}$ PSD measured in a Mastersizer 2000 model, Malvern, within a dry chamber.

2.1.3. Monoclinic tricalcium silicate, mC_3S

Monoclinic tricalcium silicate was purchased from Mineral Research Processing (M.R.PRO). Three different batches of this commercial powder, acquired in different years (2015, 2016 and 2017), were used for the studies. Since relevant differences were found between them, they will be named hereafter as mC_3S-2015, mC_3S-2016 and mC_3S-2017. The composition obtained by XRF and XRD is shown in Table 2.2. Particle size, density and surface area (BET) of these as-received samples are shown in Table 2.1. The RQPA showed around 2-3 wt% βC_2S of impurity in all of them. The sample mC_3S-2016 was milled using two different methods: vibratory milling (Retsch, mod. MM200) in a dry medium for 140 min, and attrition milling within isopropanol for 4 h (24 cycles of 10 min and 10 minute rest-time each, to avoid heating). The particle size of these milled powders is described in Chapter 4. These samples were hydrated to understand the kinetic and degree of hydration as a function of particle size, temperature and w/c mass ratio.

Table 2.2. Elemental and mineralogical composition obtained by FRX and RQPA, respectively for the three batches.

wt%	mC_3S-2015	mC_3S-2016	mC_3S-2017
Elemental composition			
CaO	71.5	72.3	72.6
SiO_2	25.8	25.5	26.2
MgO	1.3	0.5	0.7
Fe_2O_3	0.7	1.1	0.3
Al_2O_3	0.7	0.5	0.2
Crystalline composition			
mC_3S	97.0	98.4	97.5
βC_2S	2.1	1.6	2.5
MgO	0.9	-	-

2.1.4. Ye'elimite, $C_4A_3\overline{S}$

Stoichiometric (orthorhombic) ye'elimite was synthesized following the methodology described by Winnefeld et al. [117]. $CaCO_3$ (99.95%, Alfa Aesar), Al_2O_3 (99.997%, Alfa Aesar), and gypsum (ground natural single-crystal from Malaga) were used. The raw mixture was mixed for 1 h in an agate mortar with ethanol. The resultant powder was die-pressed (20 mm diameter) and heated at 1300°C for 4 h (heating rate of 5 °C/min) and lastly it was slowly cooled down. Orthorhombic ye'elimite powder was prepared in 2016 and 2017, named hereafter as $oC_4A_3\overline{S}$-2016 and $oC_4A_3\overline{S}$-2017. According to RQPA, the 2016 batch was composed by 99.4(1) wt% of $oC_4A_3\overline{S}$ and 0.6(1) wt% of C_3A, and the 2017 one by 99.5wt% of $oC_4A_3\overline{S}$ and 0.5 wt% of C_3A. C_3A is present as impurity. These results were published in articles #1 and #3 from Annex I. The particle size, density and specific surface of both powders are shown in Table 2.1.

These two powders were used to study the effect of the sulphate source and the effect of w/c mass ratio (without sulphate source) during hydration, (articles #1 and #3 from Annex I).

Once all the pure phases (triclinic tricalcium silicate, monoclinic tricalcium silicate and stoichiometric ye'elimite) were studied, the obtained knowledge was applied to laboratory-prepared cements (alite-belite-ye'elimite cements) as detailed below.

2.1.5. Alite-Belite-Ye'elimite (ABY) clinkers and cements

Two different ABY clinkers (standard and doped, named hereafter as ABY and dABY, respectively) were prepared using natural limestone and natural gypsum (both from Financiera y Minera cement factory, Spain), Kaolin (ref. NC-35 from Caolines Vimianzo, Spain), natural sand and iron ore (by product of the sulphuric acid industry) as raw materials. The chemical composition of these raw materials was measured by XRF and is showed in Table 2.3. The addition of CaF_2 (99.0–102.0% pure, Sigma-Aldrich), $ZnSO_4 \cdot H_2O$ (≥99% pure, Sigma-Aldrich) and $Na_2B_4O_7 \cdot 10H_2O$ (VWR, Prolabo) as mineralisers/activators was studied. dABY clinker was prepared by adding to the raw mixture both B_2O_3 and Na_2O, added as borax ($Na_2B_4O_7 \cdot 10H_2O$).

Table 2.3. Elemental composition of the raw materials expressed in weight percentage of oxides.

wt%	CaO	SiO_2	SO_3	Al_2O_3	Fe_2O_3	MgO	K_2O	ZnO	CuO	LoI*
Limestone	54.0(3)	0.8(1)	-	0.20(2)	0.10(1)	0.50(3)	-	-	-	44.4(3)
Gypsum	32.6(2)	4.7(1)	33.8(2)	1.2(1)	0.9(1)	1.5(1)	2.1(2)	-	-	23.0(3)
Kaolin	-	46.5(3)	-	34.5(2)	1.1(1)	0.20(1)	1.8(1)	-	-	15.7(4)
Sand	3.1(1)	85.0(2)	-	1.9(1)	2.5(1)	2.0(1)	0.50(1)	-	-	5.2(2)
Iron ore	0.30(2)	3.2(2)	3.2(1)	0.8(1)	72.3(2)	0.30(2)	0.30(1)	2.3(1)	1.1 (1)	17.0(3)

*LoI: Loss on Ignition at 1050°C, performed three times to obtain the standard deviation.

The targeted ABY composition was 45 wt% of alite, 25 wt% of βC_2S and 20 wt% of ye'elimite, 5 wt% of ferrite and 5 wt% of anhydrite. Firstly, small batches of 5 grams of both clinkers were prepared by optimising the type and amount of the dopant agent in the raw mixture to get the goal. Once this was achieved, medium batches of 90 g were prepared and in a last step, a large batch of 2 kg was synthesized. The parameters were re-optimised in each batch. The procedure and amount of raw materials and dopants are described below.

2.1.5.1. Small batches *(sa-)* of 5 g of ABY and dABY clinkers

As a first step, to obtain small batches of 5 g of clinker, ~8 g of raw materials were mixed and homogenised in an agate mortar by hand for 30 min.

The used quantities of raw materials and mineralisers/dopants to obtain small batches (*sa*-) of the optimised ABY and dABY clinkers are:

- ABY clinker: Limestone: 5.133 g; Gypsum: 0.658 g; Kaolin: 1.510 g; Sand: 0.272 g; iron-ore: 0.071 g; CaF_2:0.051 g; $ZnSO_4 \cdot H_2O$: 0.108 g.

- dABY clinker: Limestone: 5.108 g; Gypsum: 0.653 g; Kaolin: 1.502 g; Sand: 0.271 g; iron-ore: 0.064 g; CaF_2: 0.051 g; $ZnSO_4 \cdot H_2O$: 0.108 g; $Na_2B_4O_7 \cdot 10H_2O$: 0.071 g.

After that, the raw mixture was die-pressed in batches of ~3 g of 20 mm diameter and 10 tons of pressure. Three pellets were prepared per batch and placed into Pt/Rh crucibles. It was followed a three-step clinkering procedure: firstly, samples were heated at 900ºC (5 ºC/min heating rate) and hold there for 30 min; from there, the temperature was increased up to 1300°C for 15 min with the same heating rate, and finally, clinkers were quenched by forced air convection. All the resulting clinkers were ground by hand in an agate mortar for 30 min and sieved through 75 µm. The same process was used to prepare 5 g of dABY clinker.

2.1.5.2. Medium batches *(ma-)* (90 g) and large batches *(la-)* (2 kg) of ABY and dABY clinkers

The following quantities of raw materials were mixed and used to obtain the medium batch (*ma*-) and after the corresponding optimisation, to obtain 2 kg of clinkers:

- ABY clinker: Limestone: 2053.3 g; Gypsum: 263.1 g; Kaolin: 604.2 g; Sand: 108.7 g; iron-ore: 28.6 g; CaF_2: 20.2 g; $ZnSO_4 \cdot H_2O$: 43.1 g.

- dABY clinker: Limestone: 2040.5 g; Gypsum: 260.9 g; Kaolin: 599.9 g; Sand: 108.3 g; iron-ore: 25.4 g; CaF_2: 20.2 g; $ZnSO_4 \cdot H_2O$: 43.3 g; $Na_2B_4O_7 \cdot 10H_2O$: 35.3 g.

These raw mixtures (~3 kg) were pre-homogenised for 90 min in a micro-Deval equipment (A0655, Proeti S.A., Spain) at 100 rpm and with steel balls (9 balls of 30 mm, 10 balls of 18 mm and 20 of balls of 10 mm).

Three pellets of 35 g and 55 mm diameter were die-pressed under 12 tons and clinkered in a big Pt/Rh crucible. ~90 g of each clinker were obtained per batch; these samples are hereafter named as medium amount (*ma*-). The resulting clinkers were grounded with a disc mill and sieved through a 75 µm mesh.

Finally, ~2 Kg of both ABY and dABY clinkers were prepared; for that, six pellets of 35 g each (55 mm diameter) were clinkered per batch. The same three-step clinkering cycle was used (900ºC-30min, 1300ºC-15min and quenching by forced air convection). These resulting clinkers were named as large amounts (*la*-). *la*-clinkers were milled, using a disc mill, and sieved through 75 µm.

2.1.5.3. ABY and dABY cements

ABY and dABY cements were prepared by mixing 14 wt% of anhydrite referred to the total mass powder (as sulphate source) in a micro-Deval machine at 100 rpm with ABY and dABY *la*-clinkers during 60 min and using 3 steel balls of 90 mm diameter to facilitate the homogenisation process. The particle size, density and specific surface (BET) of both cements are presented in Table 2.1. The quantity of anhydrite was calculated taking into account the hydration reactions of aluminate containing phases to get ettringite as final hydration product, see reacts. 1.3-1.5 and 1.7 of the Introduction chapter. The anhydrite was obtained from commercial bassanite (BELITH S.P.R.L., Belgium) by heating at 700ºC for 1 h.

2.1.6. Polycarboxylate-based superplasticiser (SP)

A commercial polycarboxylate-based superplasticiser (SP), Floadis 1623 (provided by Adex Polymer S.L., Madrid, Spain), which contains 25 wt% of active matter, was used to prepare cement pastes and mortars. The amount of SP was optimised by adding from 0.0 to 1.0 wt% of active matter of SP referred to the cement content. The water added with the SP was taken into account for the final w/c ratio (0.40 and 0.50).

2.2. Preparation of hydrated samples

2.2.1. Paste preparation

Pastes were prepared by adding deionized water in a specific water to solid mass ratio (w/s), and following UNE-EN 196-3 specification (time procedure). This means that, once the powder was added to the water, the paste was mechanically stirred during 90 s. After that, the stirring was stopped for 30 s, and in a third step,

it was stirred again for 90 s. In all cases, the stirring speed was fixed at 800 rpm, which was previously optimised. When needed, the SP was added to water.

The as-prepared pastes were cast into hermetically closed polytetrafluoroethylene (PTFE) cylinders and rotated at 16 rpm for 24 hours of hydration at 20±1 °C. After this time, the pastes were demoulded and stored in water at 20±1 °C. Table 2.4 shows the w/s ratio and the curing time of the studied pastes. If SP was added or not is also indicated.

Table 2.4. Water to solid mass ratios (w/s) of each sample and curing ages for analysis.

sample	w/s	Curing ages (days)
tC_3S[¥]	0.50	47, 48, 56 and 63
mC_3S[¥]	0.45, 0.46, 0.50, 0.55, 0.65, 0.80	*in-situ*, 16, 34 and 100
$C_4A_3\bar{S}$+gyp/bas/anh[¥]	0.58, 0.70, 0.85, 1.20	14, 21 and 35
ABY	0.40, 0.50	*in-situ*[¥], 1[$], 7[$], 28[$], 56[Δ], 90[¥] and 180*
dABY	0.40, 0.50	*in-situ*[¥], 1[$], 7[$], 28[$], 56[Δ], 90[¥] and 180*

[¥]Pastes prepared without SP.
[$]Pastes prepared with and without SP.
[Δ]Pastes prepared with SP.
*Only mortars were tested at this age.

For the specific study of *in-situ* SXRPD, pastes were prepared by mixing by hand the powder with water in a glass container. Immediately after that, the paste was introduced in a glass capillary of 0.7 mm diameter with a syringe and finally sealed with grease to avoid water loss.

2.2.2. Stopping hydration of pastes

At the selected curing ages indicated in Table 2.4, the hydration process of pastes was stopped for further ex-situ characterisation (LXRPD, thermogravimetric analysis, and solid-state MAS-NMR). The cylinders were grinded by hand into fine powder in an agate mortar, and the hydration was stopped. The stopping process consists on washing the grinded sample twice with isopropanol and once with diethyl ether. A Whatman device with Whatman filters of 70 mm diameter, 2.5 µm of pore size and a Teflon® support was used.

2.2.3. Mortar preparation

ABY and dABY mortars were prepared following UNE-EN196-1 specification, at a cement/sand ratio of 1/3, and w/c mass ratios of 0.40 and 0.50. Mortars were made with selected amounts of SP (0.4 and 1.0 wt%). For the sake of comparison, PC mortars (CEMI 52.5N) at w/c 0.40 with 0.2 wt% of SP were prepared. CEN EN196-1 standard sand was used in all mortars. Mortar cubes were prepared with dimensions of 3 x 3 x 3 cm^3 and were moulded and cured at 20±1 °C and 99% of relative humidity (RH) for 24 hours. Then, these cubes were demoulded and cured (submerged in tap water) at 20±1 °C until testing. Compressive strength was measured at the selected curing ages given in Table 2.4.

2.3. Analytical Methods

Table 2.5, at the end of the chapter, shows all the studied samples and the characterisation technique used for all of them.

2.3.1. XRF and ICP-OES

The elemental composition of pure phases, raw materials, and final clinkers (ABY and dABY) was measured through XRF using a Thermo Fisher equipment (ARL ADVANT'XP+). The LOI was determined by drying samples at 105°C for 1 h and heating them at 1050°C for 2 h. Boron and sodium contents present in the final clinkers were determined by ICP-OES using a 7300DV (Perkin Elmer) equipment. These facilities are located at Servicios Centrales de Apoyo a la Investigación (SCAI) at University of Malaga (Spain).

The chemical composition of the raw materials used to prepare the cements is shown in Table 2.3, and the corresponding values of the clinkers are shown in the section 5.1 of this manuscript (New eco-cements – Applied science chapter).

2.3.2. LXRPD

LXRPD was used to characterise pure samples, clinkers, cements and pastes. These samples were recorded on a diffractometer (X'Pert MPD PRO, PANalytical).

The diffractometer contains a Ge (111) primary Johanson monochromator that provides strictly monochromatic CuKα_1 radiation (λ=1.54059Å) and a X'Celerator RTMS (Real Time Multiple Strip) detector device, working in scanning mode with maximum active length. The X-ray tube worked at 45 kV and 40 mA. Data were acquired from 5° to 70° (2θ) with a step size of 0.016° during ~2 h per pattern using a spinning sample-holder (16 rpm) in order to increase the particle statistics. This equipment was used to apply the external standard approach method (G-factor approach) [118] to quantify ACn content for the *ex situ* hydration studies.

Anhydrous cements, arrested-hydration pastes and other hydrated samples were characterised with a D8 ADVANCE DaVinci (Bruker AXS, Germany) diffractometer using an X-ray tube of Molybdenum and a Johansson Ge (111) primary monochromator to get a monochromatic MoKα_1 radiation, λ=0.7093 Å. The X-ray tube worked at 50 kV and 50 mA. The linear energy-dispersive detector device LYNXEYE XE 500 µm is optimised for high energy radiation and used with the maximum opening angle. In these conditions, the sample measurements were between 3 and 35° (2θ) with a step size of 0.020° during 4 h of total measuring time by spinning the sample at 10 rpm.

Both diffractometers are located at Servicios Centrales de Apoyo a la Investigación (SCAI) at University of Malaga (Spain).

la-ABY and *la*-dABY clinkers were mixed with ~20 wt% of SiO_2 (99.5%, Alfa Aesar) referred to the total mass powder, as internal standard [119] and were homogenised for 10 min in a McCrone micronising mill with isopropanol. The solvent was removed by filtering the sample with the Whatman device (with Whatman filters of 70 mm diameter, 2.5 µm of pore size and a Teflon® support) and after that, by drying it in a stove at 40ºC for 24 h. The LXRPD patterns of these samples were collected in the D8 ADVANCE diffractometer.

2.3.3. SXRPD

Prior to SXRPD characterisation, the samples were introduced into 0.7 mm diameter glass capillaries. They were rotated at during data collection to improve diffracting particle statistics and hence to have reliable intensity values.

SXRPD has been used to perform PDF analysis, that involves the Bragg and diffuse scattering, and traditional powder diffraction for in-situ studies. Two different beamlines were used: ID15A (at ESRF) and MSPD (at ALBA).

2.3.3.1. ID15A beamline at ESRF

The white synchrotron beam was monochromatised by a liquid nitrogen cooled double Laue Si monochromator and the selected wavelength was 0.18972 Å (65.35 KeV). The beam size was 100 µm horizontal and 100 µm vertical to avoid beam size-dependent Q-broadening. The SXRPD data were collected in transmission geometry using a Pilatus3 X CdTe 2M hybrid photon counting 2D detector with 172 µm of pixel size located in a motorized stage. The detector was off-centered with respect the incident beam and located close to the sample in order to acquire the largest possible range of the pair distribution function G(r). The detector distance was calibrated with CeO_2 and it was found to be 181.592 mm, which allows reaching a $Q_{max\ ins}$ close to 30 $Å^{-1}$. The data acquisition time was 8 seconds per individual image. For the hydrated pastes, and in order to increase the statistics of the final data sets, eight images of 8 seconds were collected and merged with local software. Samples were rotated during data collection for improving the diffracting particle statistics.

Table 2.5, at the end of this chapter, gives the samples measured under this configuration.

2.3.3.2. MSPD beamline at ALBA

The synchrotron white beam was monochromatised by a double-crystal Si (111) monochromator and the wavelength was 0.41236(1) Å (30.067 keV) [120]. The data were collected in transmission geometry using 6 modules MYTHEN 1D detector (strip-pitch: 50 µm, radius: 550 mm, covered angular range: 40˚). The shortest usable wavelength is dictated by the efficiency of the Si-detector as higher energy X-ray, which would allow a larger Q-range to be probed, would yield poorer signal as a fraction of the scattered photons will not be measured by this detector. In addition, the data acquisition time was 37 minutes per each individual pattern. Three patterns were collected for the anhydrous samples and five for the hydrated pastes in order to improve the signal-to-noise ratio in the large recorded angular range, 1 to 120° (2θ). The maximum momentum transfer obtained was $Q_{max\ ins}$ of 25 $Å^{-1}$.

Furthermore, an *in-situ* RQPA study of the hydration of ABY and dABY cements was performed. Pastes were prepared as mentioned before with 0.50 w/c mass ratio, and mixed with ~12 wt% quartz, referred to the total mass, as internal standard. SXRPD data were collected in Debye-Scherrer (transmission)

mode [120] with a wavelength of 0.61931 Å (20 keV). The diffractometer is armed with a MYTHEN detector system especially suited for time resolved experiments and good signal to noise ratio experiments. The glass capillaries were rotated at 20 rpm during data collection. A pattern of 6 minutes was collected at different hydration times to obtain at least two patterns per hour during the first 14 hours of hydration over the angular range from 2 to 40° (2θ). Normalised SXRPD patterns were analysed by using the Rietveld methodology to obtain RQPA data.

Table 2.5, at the end of this chapter, gives the samples measured under this configuration.

2.3.4. PDF data treatment

2.3.4.1. PDF generation

Once the total scattering data was collected, see Figure 2.1a, additional routes were made to obtain the PDF data: corrections of absorption, polarisation, multiple scattering and inelastic scattering. Nevertheless, these experimental effects are broad smoothly varying functions of Q. Therefore any systematic errors due to these corrections can also be expected to be broad smoothly varying functions of Q [102]. A consequent step requires corrections for instrument background and scattering from the container [114]. Basically, a subtraction of the non-related intensities for the sample scattering is needed. Corrected data is normalized and finally Fourier transformed. There are several data correction available software that take care of the corrections and normalizations needed to obtain PDFs from raw data [114]. PDFgetX3 is a code that incorporates atomic scattering factors and Compton factors [121] and includes *ad hoc* data reduction algorithms. Thanks to this, the additive contributions are corrected by fitting and subtracting low degree polynomial to produce the proper asymptotic behaviour in the F(Q) (where F(Q)=Q[S(Q)-1]). This still leaves some differences, but that signal is of a low frequency in Q and therefore, after Fourier transformation, produces noise only in a very low-r region in the PDF. In addition, the multiplicative differences (as sample self-absorption and polarisation) are not corrected, but they tend to vary at a very low rate in Q then they are expected to just slightly change the shape of peak profiles in the PDF, see Figure 2.1b

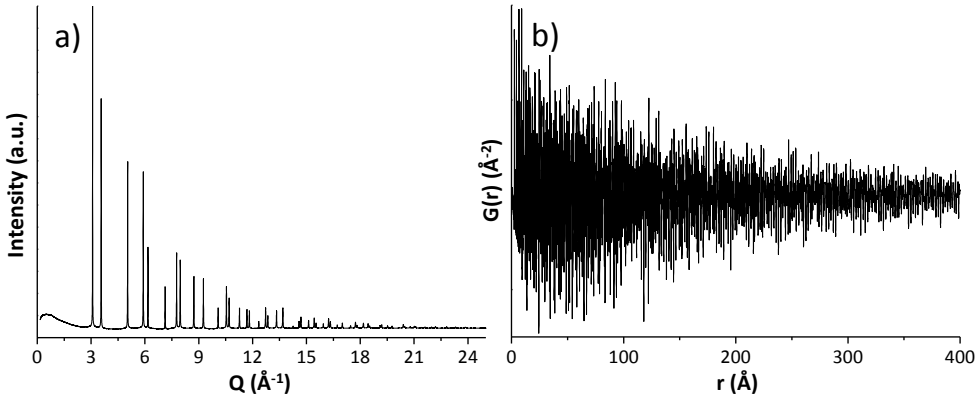

Figure 2.1. a) SXRPD raw data, intensity *vs* Q and b) Experimental real-space distribution of interatomic distances G(r) obtained at Q_{max} 24 A^{-1} for a nickel standard sample.

2.3.4.2. PDF Structural analysis

In our specific case, PDF experimental data analysis G(r) was obtained by using PDFgetX3 [121] with different usable Q_{max} 29 and 24 $Å^{-1}$ for the experimental configurations studied in ID15A and MSPD datasets, respectively. Structural and quantitative phase analysis results were obtained from the PDF data by the PDFGui software [116]. The instrumental parameters were got using crystalline nickel as standard to optimise/determine: scale factor, unit cell parameter, delta2 parameter (low-r correlated motion peak sharpening factor) [122, 123], the instrumental parameters Q_{damp} and Q_{broad}, and ADPs for the nickel sample as standard.

For the rest of samples, the optimised parameters were scale factors, unit cell parameters, delta2 parameter (for the fits of the low-r regions) and ADPs. In some cases, atomic positional coordinates were also varied. Moreover, the spdiameter parameter was also adjusted to fit the nanocrystalline component in some samples.

2.3.5. LXRPD and SXRPD data analysis for RQPA and ACn determination

After all the LXRPD or SXRPD patterns were recorded, all the crystalline phases were identified using the X'Pert HighScore Plus software from Panalytical; for that, the pattern structures included in Inorganic Crystal Structure Database (ICSD) and PDF database were used. After that, the patterns were analysed by

Rietveld methodology using GSAS [124, 125] software package, by using a pseudo-Voigt peak shape function with the asymmetry correction included [126, 127], to obtain RQPA. The refined overall parameters were: background coefficients, phase scale factors, unit cell parameters, zero-shift error, peak shape parameters and preferred orientation coefficient if needed (march-Dollase ellipsoidal preferred orientation correction algorithm [128]).

Internal and External standard approach methods were used to quantify ACn content in the samples [129, 130]. For the former, 20 wt% of Quartz (99.5%, Alfa Aesar) referred to the total mass sample was used, and for the latter, G-factor method was followed. The internal standard method allows the quantification of the ACn content by comparing the weight value of the standard, W_{st}, and the obtained value from RQPA, R_{st}, to derive a quantification of amorphous phases [129]. The external standard method or G-factor approach, consists on obtaining the diffractometer constant, K_e, with an appropriate standard, in our case, alumina NIST Standard [130–132].

2.3.6. Rheological behaviour of cement pastes

Rheological measurements of the cement pastes were carried out to optimise superplasticiser and water contents. A Thermo Haake viscometer (Model VT550, Karlsruhe, Germany) with a serrated coaxial cylinder sensor, SV2P, provided with a lid to reduce evaporation was used. Two types of measurements were performed with this equipment: i) flow curves (controlled rate measurements) where ramp times of 6 s were recorded in the shear rate range between 2 and 350 s^{-1}, for a total of 12 ramps (up-curve). A further decrease from 350 to 2 s^{-1} shear rate was performed by following the same ramp times (down-curve). Prior to any measurement, pastes were pre-sheared at 350 s^{-1} for 30 s and held at 0 s^{-1} for 5 s; the data were acquired after ~5 min the cement was added to water. ii) Viscosity vs. time measurements, at a fixed shear rate of 5 s^{-1}.

2.3.7. DTA-TGA

The Differential Thermal Analysis and Thermogravimetry analysis have been performed to quantify phases in cements and pastes (after stopping hydration, see section 2.2.2), including the free water content. These measurements were performed in a SDT-Q600 analyser (TA instruments, New Castle, DE). The

temperature was varied from RT to 1000°C at a heating rate of 10 °C/min. Measurements were carried out in open platinum crucibles under air flow.

It allows the determination of different phases (e.g. calcium silicate hydrate, ettringite, gypsum, monosulphate, aluminium hydroxide and calcium hydroxide in the cement pastes) through the corresponding dehydration of endothermic peaks [133–135]. In addition, the overall calcite content (700-800°C) or portlandite (~450°C) can be determined from their decomposition temperatures [136, 137].

The free water content (FW), in weight percentage, was calculated for each cement paste using eq. 2.1 and 2.2:

$$BW = (BW_{ATD} \cdot CM) / (100 - BW_{ATD}) \quad \text{eq. 2.1}$$

$$FW = TW – BW \quad \text{eq. 2.2}$$

Where BW corresponds to chemically bound water content, TW is the total water content, BW_{ATD} is the loss of mass measured up to 600°C from DTA-TGA curves (which is considered bound water in a paste after stopping hydration), and CM is the cement content (all the numbers in weight percentage).

2.3.8. SEM and FEG-SEM

Both anhydrous clinker powders after milling (ABY and dABY) and the surface and fracture cross-section of both anhydrous clinker pellets before milling were observed by SEM (Jeol JSM-840, Japan) using secondary electrons at 20 kV to obtain the different morphologies between the components. Before SEM observation, all samples were sputtered with gold. This facility is located at Servicios Centrales de Apoyo a la Investigación (SCAI) at University of Malaga (Spain).

In addition, both pellets of both anhydrous clinkers were embedded in epoxy resin, and polished with diamond down to 6 µm. The elemental composition was quantified by EDS (with a X-Max 50 mm2 detector, Oxford Instruments) in a FEG-SEM (FEI, Helios Nanolab 650). BSE images were taken at 15 kV with a retractable circular backscatter detector CBS (annular solid-state device). This equipment is located at Edificio de Bioinnovación at University of Malaga (Spain).

2.3.9. HRTEM

HRTEM measurements were performed with a FEI Talos F200X microscope armed with X FEG and super-X EDS system with four silicon drift detectors (SDDs) which works at an accelerating voltage of 200 kV. This facility is located at Servicios Centrales de Apoyo a la Investigación (SCAI) at University of Malaga (Spain).

2.3.10. MAS-NMR

^{29}Si MAS-NMR spectrum for ABY and dABY (anhydrous and hydrated) samples were recorded at RT on a Bruker AVIII HD 600 NMR spectrometer (field strength of 14.1 T) at 119.8 MHz with a 2.5 mm triple-resonance DVT probe using zircona rotors at 15 kHz spinning rates. The experiments were made with 1H decoupling (cw sequence) by applying a single pulse (π/2), an excitation pulse of 5 µs, 30 s relaxation stay and 10800 scans. The Chemical shift was referenced to an external solution of tetramethylsilane (TMS).

^{27}Al MAS-NMR spectra were recorded at similar conditions of ^{29}Si MAS-NMR but at 156.4 MHz and the rotors give 20 kHz spinning rates. The experiments were performed with (Hpedec) and without (one pulse) 1H decoupling (cw sequence) by applying a single pulse (π/12), an excitation pulse of 1 µs and 5.0 s relaxation delay and 200 scans. The chemical shift was referenced to an external solution of $Al(NO_3)_3$, 1 M.

This facility is located at Servicios Centrales de Apoyo a la Investigación (SCAI) at University of Malaga (Spain).

2.3.11. Isothermal calorimetry

Isothermal calorimetry measurements were performed in an eight channel Thermal Activity Monitor instrument using glass ampoules. In order to collect data from the very beginning of the hydration, an automatic admix device was used to mix the samples inside the calorimeter by shaking the sample during the first 2 minutes. The heat flow was collected up to 7 days at 20°C.

2.3.12. Specific surface measurements

Specific surface area determination was carried out in an automatic MICROMERITICS ASAP 2020 (Micromeritics Instrument Corp, GA, USA), and determined by BET method. Isotherms at low partial pressures of the inert gas (N_2 at room temperature) were used to determine specific surface areas.

The specific surface area was also measured by the **Blaine method**, UNE-EN 196-6:2010. The results are an estimation of the surface area per unit mass of a powder, expressed in cm^2/g. The Blaine surface area is determined indirectly by measuring the time of a known volume of air passing through a pellet of powder with an effective pressure.

BET method gives more reliable results than Blaine method because it includes internal surfaces present in microcracks or in pores open only at one end [83].

2.3.13. Real density

The real density of powders was measured with helium Pycnometer (Accupyc II 1340 Pycnometer, Micromeritics). The used equipment possesses a chamber of 10 cm^3 and the measurement was carried out at RT with the supply of 19.5 Psi of He. The used mass depends on the density of the sample, because the pycnometer has a standard volume, so between 2 and 5 g of material can be used. This facility is located at Servicios Centrales de Apoyo a la Investigación (SCAI) at University of Malaga (Spain).

2.3.14. PSD

Two laser diffraction analysers (Mastersizer2000 and MastersizerS, both of them from Malvern, UK) were used to perform the PSD measurements. The former was provided with a dry sample cell and it is located at Financiera y Minera cement factory, Malaga, Spain, and the second one was provided with a wet sample, where measurements were performed in ethanol. Similar results were obtained with both equipments. In both cases, a laser beam goes through the sample that diffracts on the particles and the diffracted beam is recorded by a detector. From the measurement, information such as $D_{v,10}$, $D_{v,50}$ and $D_{v,90}$ can be obtained.

2.3.15. Compressive strength

The compressive strength of all mortars was measured in a testing machine by applying pressure according to the standard EN196-1 in a compression machine (Model Autotest 200/10 W, Ibertest, Spain) located at Financiera y Minera cement factory, Malaga. Since small specimens were measured, the conversion factor of 1.78 was used to obtain values comparable to those determined with standard prisms ($40 \times 40 \times 160$ mm^3).

The final results were obtained as an average of three compression values. The testing curing ages were 1, 7, 28, 56, and 180 days, which correspond to the same studied curing times of pastes.

2.3.16. Overview

To facilitate the reader, Table 2.5 shows all the tested samples, the studied parameters and the characterisation technique used in this PhD.

Table 2.5. Summary of all the studied samples classified with their studied parameters and characterisation techniques.

Samples		Studied parameters	Characterisation technique
Nickel		MSPD-ALBA, ID15A-ESRF	SXRPD, PDF
mC_3S	**2015**	anhydrous; w/s ratio (0.46, 0.55, 0.65, 0.80) MSPD-ALBA, RT, stopped	PSD, BET, density, XRF, DTA-TGA, LXRPD, SXRPD, PDF, RQPA
	2016	anhydrous; w/s ratio (0.45, 0.80) particle size ($D_{v,50}$=21, 7, 3 µm) MSPD-ALBA RT, non-stopped	PSD, BET, density, XRF, DTA-TGA, LXRPD, SXRPD, PDF, RQPA, SEM, HRTEM, Calorimetry, MAS-NMR
	2017	w/s=anhydrous, 0.50, ID15A-ESRF, RT non-stopped Polymorphism comparison	XRF, PSD, BET, ρ, LXRPD, SXRPD, PDF, Rietveld
tC_3S		anhydrous; w/s= 0.50 ID15A-ESRF Temperature (RT, 35ºC, 50ºC) stopped/non-stopped in-situ/ex-situ comparison	PSD, BET, density, LXRPD, SXRPD, PDF, RQPA
o-$C_4A_3\bar{S}$	**2016**	anhydrous; w/c=1.20 gypsum/bassanite MSPD-ALBA, RT stopped	PSD, BET, density, DTA-TGA, LXRPD, SXRPD, PDF, RQPA
	2017	anhydrous; w/c=0.58, 0.70 and 0.85 0.0, 15.5, 31.0 wt% anhydrite ID15A-ESRF, RT non-stopped	PSD, BET, density, LXRPD, SXRPD, PDF, RQPA
ABY	**clinker**	anhydrous	LXRPD, Rietveld, MAS-NMR, SEM, FEG-SEM-EDX
	cement	anhydrous; w/c=0.40, 0.50 0.0, 0.2, 0.3, 0.4, 0.5, 1.0 wt% SP first hours, 1, 7, 28, 56, 90 days stopped/non-stopped	PSD, BET, Blaine, density, DTA-TGA, LXRPD, SXRPD, RQPA , ICP-OES, SEM, Calorimetry, MAS-NMR, Rheology
	mortar	w/c=0.40, 0.50 0.4, 1.0 wt% SP 1, 7, 28, 56, 180 days non-stopped	Compressive strength
dABY	**clinker**	anhydrous	LXRPD, Rietveld, MAS-NMR, SEM, EDS-FEG-SEM
	cement	w/c=anhydrous, 0.40, 0.50 0.0, 0.2, 0.3, 0.4, 0.5, 1.0 wt% SP first hours, 1, 7, 28, 56, 90 days stopped/non-stopped	XRF, ICP-OES, PSD, BET, Blaine, density, DTA-TGA, SEM, Calorimetry, LXRPD, SXRPD, Rietveld, NMR, Rheology
	mortar	w/c=0.40, 0.50 0.4, 1.0 wt% SP 1, 7, 28, 56, 180 days non-stopped	Compressive strength

3. OBJECTIVES

The main objective of this PhD has been to obtain eco-cements that reduce CO_2 emissions (up to 17%) and develop as high mechanical strengths as PC (at any hydration age). To do so, two main goals have been pursued: i) The characterisation of pure phases (alite and ye'elimite) that are present in standard and doped Alite-Belite-Ye'elimite (ABY and dABY, respectively) eco-cements using the PDF methodology to find out the local structure of their hydration products. ii) The synthesis, processing, hydration and characterisation of two laboratory-prepared Alite-Belite-Ye'elimite eco-cements (standard and doped).

To reach these two sub-goals the next strategies were followed:

1. To establish a protocol to analyse the atomic structure of the amorphous/nanocrystalline gels in cement pastes by using synchrotron X-ray PDF methodology.

2. To work on the understanding of both the formation and the nanostructure of C-S-H gel formed during the hydration of alite.

3. To study the nanostructure of the aluminium hydroxide gels produced during the hydration of ye'elimite containing samples.

4. To obtain small batches (5 g) of an ABY eco-clinker, composed by alite and ye'elimite phases jointly with β-belite with a phase assemblage close to ~45 wt% C_3S, ~25 wt% βC_2S, ~20 wt% $C_4A_3\bar{S}$ and ~5 wt% C_4AF.

5. To produce small batches (5 g) of a dABY eco-clinker, composed by alite, ye'elimite and α-forms of belite, since these forms are more hydraulically active.

6. To develop the process of the production of ~2 kg of each eco-clinker ("scale-up"), by optimising the milling process and clinkering conditions.

7. To prepare cements with the "scaled–up" clinkers.

8. To work on the understanding of the hydration mechanism of ABY and dABY cement pastes, and to know the influence of different parameters such as w/c and the amount of superplasticiser on the hydration behaviour, with the final objective of enhancing mechanical strengths.

4. PAIR DISTRIBUTION FUNCTION – BASIC SCIENCE

This chapter is focused on the application of PDF methodology to deeply study and characterise pure cement-related samples.

4.1. Hydration study by PDF of monoclinic tricalcium silicate (mC_3S-2015)

4.1.1. Goals

The hydration products of two alite polymorphs with different water contents and temperatures were studied to identify the different amorphous/nanocrystalline phases with PDF methodology. In addition, a protocol has been established to analyse the atomic structure of the amorphous/nanocrystalline gels in cement pastes by using synchrotron X-ray PDF methodology.

4.1.2. Kinetic hydration study of mC_3S-2015 with different water to solid mass ratio (w/s)

Monoclinic C_3S is the most abundant phase of PC and ABY cements. Here, a hydration study is performed in order to unravel the effect of water to solid mass ratio on hydration behaviour of this phase. The degree of reaction of mC_3S was determined by RQPA combined with the internal standard method. This methodology enables to quantify the ACn content that is mainly C-S-H gel (nanocrystalline calcium silicate and any amorphous component as water pores or nanocrystalline CH). PDF methodology also gives the possibility to identify and quantify the crystalline and nanocrystalline phases.

To check the influence of w/s ratio on alite hydration, the as-received mC_3S-2015 was hydrated at w/s of 0.46, 0.55, 0.65 and 0.80. Firstly, a basic characterisation was performed of samples hydrated during 34 days, and after arresting the hydration (methodology detailed in section 2.2.2) to remove free water. Figure 4.1 shows the raw LXRPD plots of all alite pastes hydrated at different w/s ratios. All these stopped pastes were mixed with α-Al_2O_3 as internal standard to quantify the ACn content. Figure 4.2 displays the LXRPD Rietveld plots of alite paste hydrated at w/s 0.80 after 34 days and mixed with the internal standard, as a representative example. The crystalline phases are anhydrous mC_3S, CH, and $C\bar{C}$ (due to carbonation).

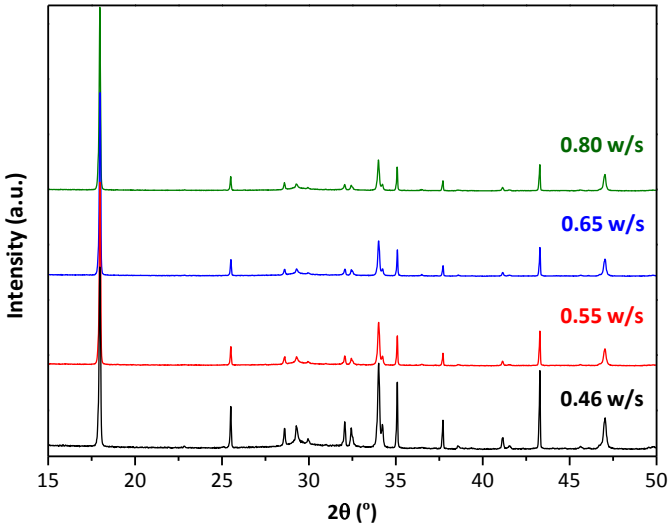

Figure 4.1. Raw LXRPD of all the alite (mC_3S-2015) pastes hydrated at four different w/s mass ratios (CuKα_1 radiation, λ=1.54059 Å).

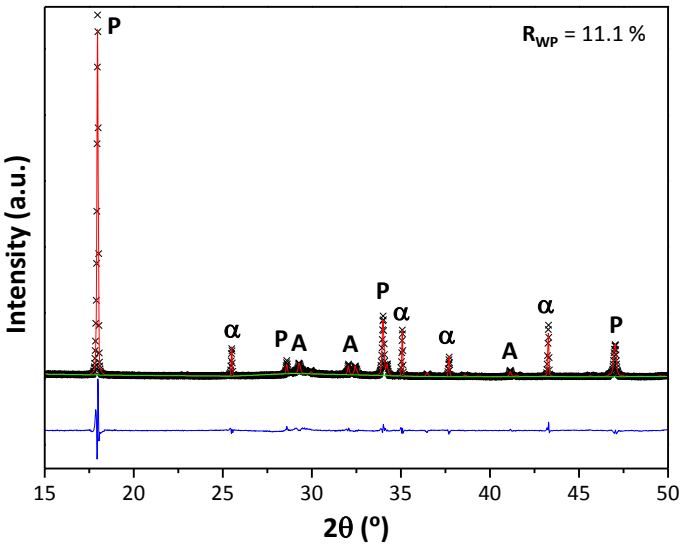

Figure 4.2. LXRPD Rietveld plot (CuKα_1 radiation, λ=1.54059 Å) with internal standard for the mC_3S-2015_0.80w/s paste hydrated for 34 days. The main peaks are labelled as follow: CH (P), mC_3S (A) and added internal standard, α-Al_2O_3 (α). R_{WP} value is included. Adapted from article #1 in Annex I.

To obtain the full phase assemblage of alite pastes, DTA-TGA measurements were performed for all the stopped pastes in order to determine the free water content. In these measurements, the weight loss up to 250ºC is considered to belong to C-S-H gel; between 250 and 400ºC could be due to the dehydration of amorphous CH; the weight loss from 400 to 600ºC is due to crystalline CH decomposition; the one above 600ºC is considered to be CO_2. This

carbon dioxide is due to carbonation of the paste during curing [136, 137]. Figure 4.3 shows the DTG-TGA curves for all these pastes.

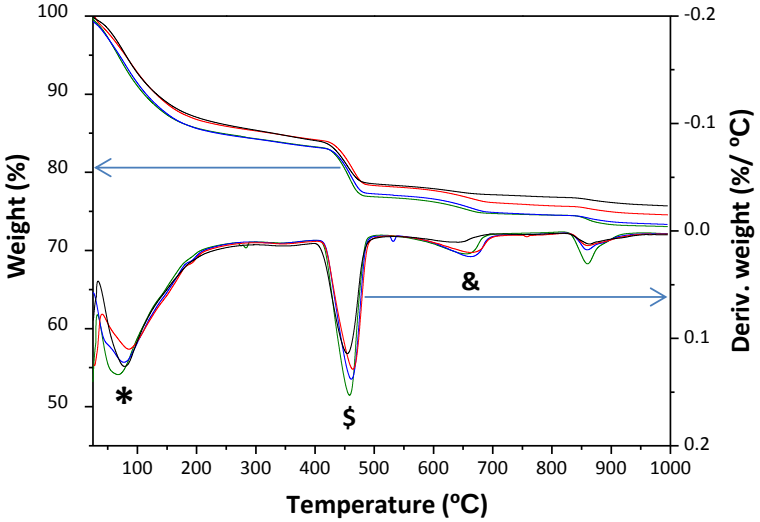

Figure 4.3. DTG-TGA curves for mC_3S-2015 stopped pastes hydrated for 34 days: 0.46 w/s (black); 0.55 w/s (red); 0.65 w/s (blue); 0.80 w/s (green). The main weight losses are labelled as follow: C-S-H gel (*), CH ($) and $C\bar{C}$ (&). Adapted from article #1 in Annex I.

The free water content, in weight percentage, was calculated for each cement paste using eq. 2.1 and 2.2 as it is shown in Materials and Methods chapter.

Table 4.1 shows the full phase assemblage of all the pastes determined by RQPA with the internal standard method, to obtain ACn, and free water (determined by DTA-TGA). It is important to point out that the amount of anhydrous alite goes from ~12 to ~8 wt% for the samples prepared at w/s from 0.46 to 0.80, see Table 4.1. In addition, a low carbonation was detected in all the samples but it is always less than 1.5 wt%. Alite reaction degree increases by increasing the water content, viz. from 82.6 to 86.2% for w/s ratios from 0.46 to 0.80 (Table 4.1).

Table 4.1. Phase assemblage of four mC_3S-2015 pastes at 34 days of hydration, including the ACn and FW content. Reaction degree of mC_3S is also included. Adapted from article #1 in Annex I.

Phase content (wt%)	0.46 w/s	0.55 w/s	0.65 w/s	0.80 w/s
mC_3S	11.7	9.5	8.7	7.5
CH	16.2	18.5	17.5	16.2
$C\bar{C}$	1.2	1.0	1.0	1.1
ACn	59.7	55.7	53.7	49.6
FW	11.2	15.3	19.2	25.7
Reaction degree of mC_3S (%)	82.6	85.0	85.4	86.2

Finally, the SXRPD patterns of the four stopped pastes (at 34 days of hydration) were collected in MSPD beamline (ALBA synchrotron) following the PDF methodology detailed in Materials and Methods section. The data acquisition time was 37 minutes per individual pattern. Three patterns (at different positions along the capillaries) were collected for anhydrous samples and five patterns for the hydrated ones, in order to improve the signal-to-noise ratio in the large recorded angular range, 1–120° (2θ). Therefore, final total scattering pattern took 1 h 51 min for anhydrous samples and 3 h 5 min for hydrated ones. No changes between individual patterns were observed. Figure 4.4 shows the raw PDF data obtained from SXRPD patterns for the four pastes. The first result that can be pointed out by observing the low r region of these graphs is that no significant differences between the four samples are appreciated. Consequently, the paste with the highest reaction degree, i.e. 0.80 w/s, was further analysed with PDFgui software [116]. The main goal of this work was to quantify the C-S-H gel content by determining the best crystal structure to fit the PDF signals.

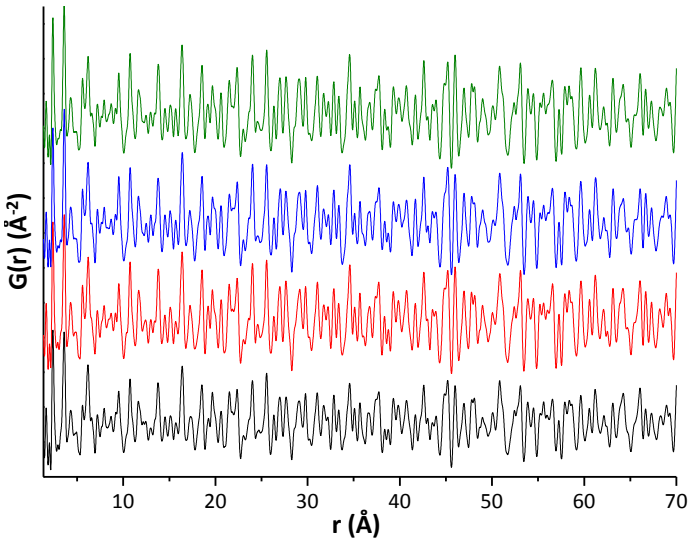

Figure 4.4. Experimental PDF data from 1.35 to 70 Å for alite pastes: 0.46 (black), 0.55 (red), 0.65 (blue) and 0.80 (green) at 34 days of hydration. Adapted from article #1 in Annex I.

From the basic characterisation by LXRPD and DTA-TGA, it has been determined that these alite pastes contained crystalline (CH and mC_3S), amorphous (nano-CH) and nanocrystalline (C-S-H gel) phases. Consequently, the refinement of the PDF data of the mC_3S-2015 paste is very challenging. Thus, a **multi-r range strategy** [112] was used for a reliable PDF fitting process. This methodology was previously reported by other authors [112] for similar systems. Firstly, high r-region (40-70 Å) was selected for refining the crystalline contribution, i.e. the contribution of remaining mC_3S and CH. The optimised parameters (unit cell and ADP values) for anhydrous mC_3S-2015 obtained from the PDF analysis, see Figure 4.5, were fixed and only the scale factor was refined. The contribution of crystalline CH was computed by optimising the scale factor, the unit cell parameters, the anisotropic ADPs values for Ca and O and the atomic position for O (Ca is located at a special position). Since the sample contained crystalline $C\bar{C}$ as impurity due to carbonation, the scale factor of this phase was also refined in this region. The final fit gives a R_W value of 28.8% and is displayed in Figure 4.6. The unit cell values for CH converged to a=3.594 Å and c=4.916 Å and the final ADPs values and atomic positions are reported in Table 4.2. All these values were kept constant in the fitting at low r-ranges.

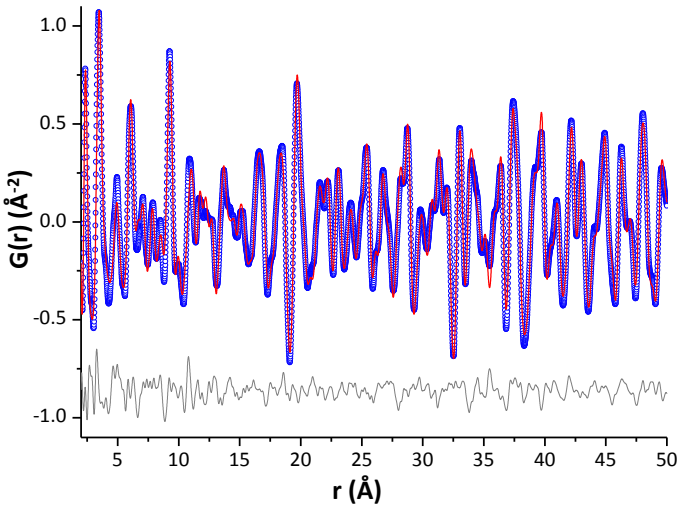

Figure 4.5. Experimental (blue circles) and fitted (red solid line) PDF for anhydrous mC_3S-2015 sample in the 2 to 50 Å r-range. Difference curve is shown as a grey line. Taken from article #1 in Annex I.

Table 4.2. Anisotropic atomic displacement parameters (ADPs) for CH in w/s=0.80 paste obtained in the PDF analysis. Note that the parameters for the hydrogen were not refined. Taken from article #1 in Annex I.

Atom	Ca1	O1	H
x	0	0.3333	0.3333
y	0	0.6667	0.6667
z	0	0.2161	0.4256
u11	0.0037	0.0084	0.0264
u22	0.0037	0.0084	0.0264
u33	0.0118	0.0212	0.0264
u12	0.0019	0.0042	0.0132
u13	0	0	0
u23	0	0	0

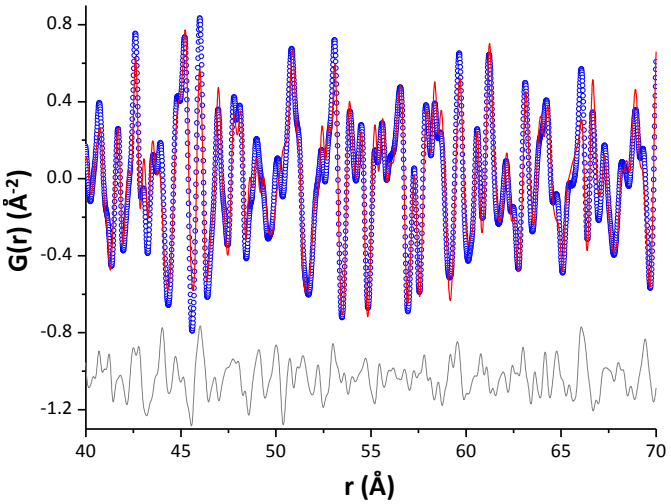

Figure 4.6. Experimental (blue circles) and fitted (red solid line) PDF for mC_3S paste at 0.80 w/s in the 40 to 70 Å r-range. Difference curve is shown as a grey line. Taken from article #1 in Annex I.

After the refinement at high r-range, the next step was to study the medium 10-25 Å r-range. Figure 4.7a shows this r-range fitted only with the crystalline mC_3S and crystalline CH. Some misfittings are observed, pointing at the contribution of the nanocrystalline phase (C-S-H gel). Due to the many crystal structures for C-S-H gel published [138], a study to check which one would yield to the best fitting, i.e. lower R_W values, was performed. Table 4.3 includes R_W values and the quantitative phase analysis results obtained by using different published crystal structures (tobermorite, clinotobermorite and jennite). Jennite structure led to the worst fit, Table 4.3. The defective tobermorite structure, named clinotobermorite T3_14sc [138], was selected as the best crystalline structure because of the lowest R_W value. Figure 4.7b shows the fitting of the medium r-

region where the arrows highlight the enhancement in the fitting by using clinotobermorite T3_14sc to describe C-S-H gel. The unit cell values converged to a=11.258 Å, b=7.307 Å, c=42.538 Å and β=94.3º. The obtained ADP values were 0.0065, 0.0833 and 0.0160 $Å^2$ for Ca, Si and O, respectively. This clinotobermorite structural description improved the PDF fit from 36.3 to 28.5 % of R_W values, Figure 4.7. All these parameters were kept constant to continue with the fitting of the lowest r-range of the PDF data.

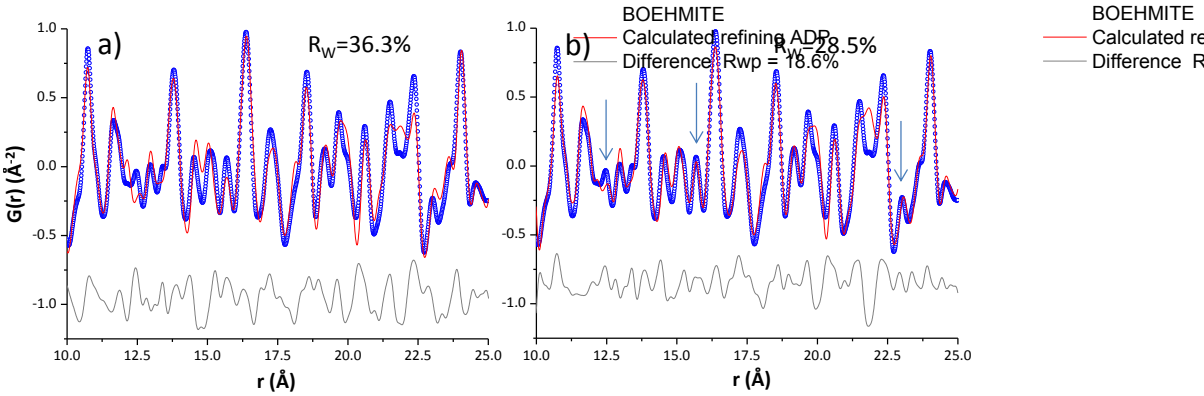

Figure 4.7. Experimental (blue circles) and fitted (red solid line) PDF for mC_3S-2015 paste at 0.80 w/s mass ratio at 34 days of hydration in the 10 to 25 Å r-range. a) The fit include only crystalline CH and mC_3S, b) The fit include CH, mC_3S and T3_14sc phases. Difference curves are shown as a grey line. R_W values are included. Adapted from article #1 in Annex I.

Table 4.3. Results obtained from synchrotron PDF analysis of mC_3S-2015_0.80w/s_34d paste in the 10-25 Å r-region, using different structural descriptions for the nanocrystalline C-S-H gel phase. Taken from article #1 in Annex I.

phase	R_W (%)	mC_3S (wt%)	$C\bar{C}$ (wt%)	Cryst-CH (wt%)	C-S-H gel (wt%)
Jennite (t) ICSD #151413 [139]	33.0	20.3	1.4	34.5	43.7
Tobermorite-14 (m) ICSD #152489 [140]	32.9	20.9	1.5	35.5	42.2
Tobermorite-11 (o) ICSD #92941 [141]	30.3	18.6	1.3	31.6	48.5
Tobermorite-11 (m) ICSD #87690 [142]	30.5	17.6	1.2	29.8	51.4
Tobermorite-11 (o) ICSD #100405 [143]	29.9	19.7	1.4	33.5	45.5
Clinotobermorite (m) ICSD #90036 [144]	28.8	13.8	1.0	23.4	61.9
Clinotobermorite (t)	28.5	14.1	1.0	23.9	61.0

ICSD #90034 [144]					
Clinotobermorite (m), T5_14sc [138]	29.2	15.4	1.1	26.2	57.4
Clinotobermorite (m), T5_11sc [138]	30.4	17.8	1.2	30.2	50.8
Clinotobermorite (m), T3_14sc [138]	**28.5**	**16.0**	**1.1**	**27.1**	**55.8**

(m), (o) & (t) denotes monoclinic, orthorhombic and triclinic, respectively.

The remaining hydrated alite samples at different w/s mass ratios, i.e. 0.46, 0.55, 0.65, were analysed with the same procedure (from 40 to 70 Å, the crystalline phases, and from 10 to 25 Å the C-S-H gel contribution). The results of the 10-25 Å fittings are shown in Table 4.4. It should be noted that for these fittings only clinotobermorite T3_14sc and jennite were tested, as the best and the worst in the study for the w/s 0.8 sample. The results given in Table 4.4 show that in all the samples clinotobermorite T3_14sc yielded the lowest R_W, consequently, the best fits.

Based on these results, it can be concluded that the w/s ratio has not affected the crystal structure of the nanocrystalline C-S-H gel formed.

Table 4.4. Quantitative phase analysis results obtained by PDF using two crystal structures for the nanocrystalline C-S-H gel in the alite (mC_3S-2015) w/s=0.46, 0.55 and 0.65 pastes at 34 days of hydration. R_W values are also included. Taken from article #1 in Annex I.

Sample	R_W (%)	mC_3S (wt%)	$C\bar{C}$ (wt%)	Cryst-CH (wt%)	C-S-H gel (wt%)
mC_3S_0.46w/s					
clinotobermorite T3_14sc	28.5	32.4	0.3	23.1	44.1
Jennite, ICSD #151413	30.0	36.8	0.4	26.3	36.5
mC_3S_0.55w/s					
clinotobermorite, T3_14sc	29.5	23.4	0.9	33.6	42.2
Jennite, ICSD #151413	32.5	24.9	0.9	35.9	38.3
mC_3S_0.65w/s					
clinotobermorite, T3_14sc	23.2	14.1	0.8	30.2	54.9
Jennite, ICSD #151413	27.4	13.2	0.8	28.5	57.5

However, there is another important result that underlays this study, the Ca/Si ratio of this clinotobermorite is 1.22 while it is well established that the overall Ca/Si ratio in the C-S-H gel ranges from 1.7–1.9. Consequently, more research was needed to obtain a full picture of this hydration product.

The last step of the multi-r-range methodology was to fit the lowest r-region 2-10 Å. To do so, a fix value of 2 $Å^2$ for delta2 (low-r correlated motion peak sharpening factor) was used. Figure 4.8a shows the PDF fit in this r-range. The observed misfittings and the high R_W of 45.6% indicate the presence of

additional scattering contribution in this r-range. The unfitted contribution underlines the needing of another phase that has no contribution in the high r-range. It has been suggested that this contribution may be due to an isolated single layer of CH [113]. Figure 4.8b includes the simulated PDF curves of crystalline (bulk) portlandite, alite, clinotobermorite, monolayer CH and two consecutives layers of CH. The signal calculated for the monolayer of CH seems to fit better the low r-range of the PDF data.

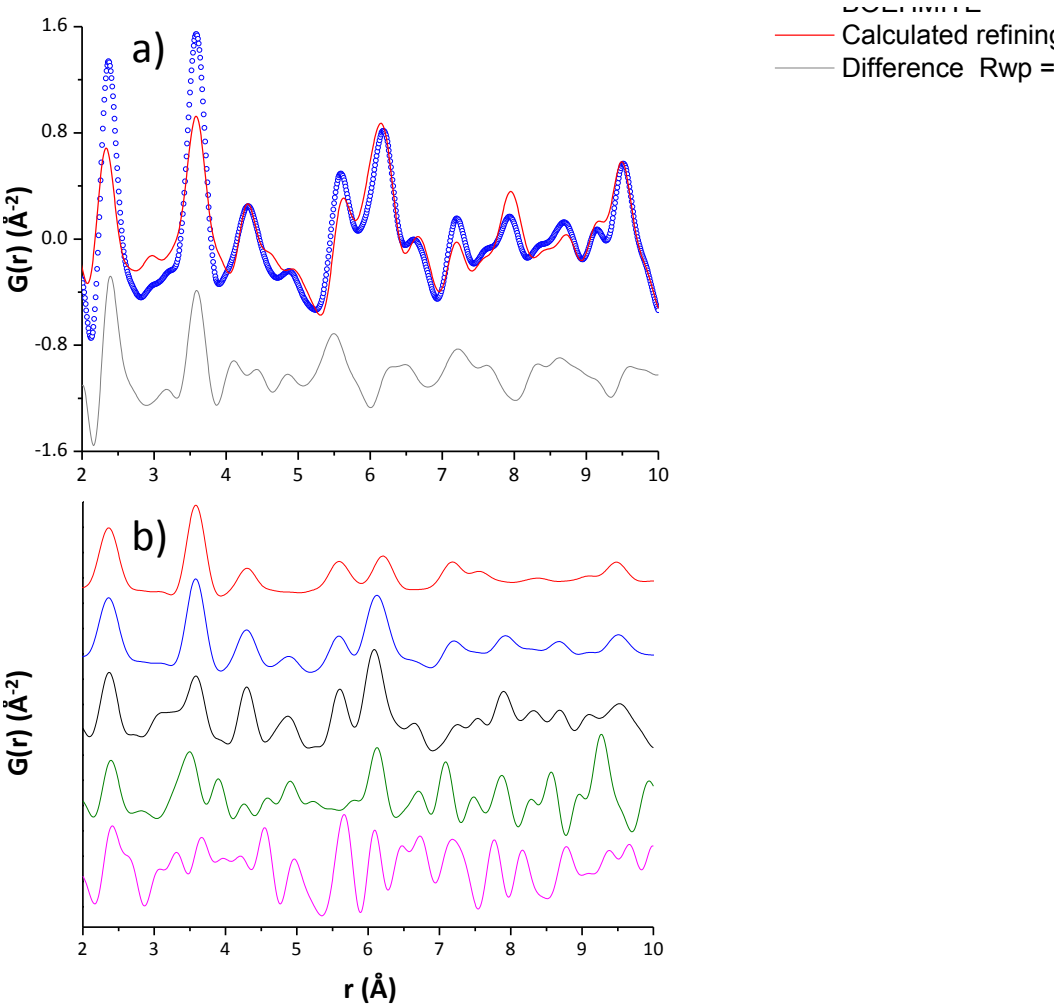

Figure 4.8. a) Experimental (blue circles) and fitted (red solid line) PDF patterns for mC_3S-2015 w/s=0.80 34 days paste in the 2 to 10 Å r-range and the difference curve is shown as a grey line. b) Simulated PDF curves for a single layer (red) and a double layer (blue) of calcium hydroxide, bulk portlandite (black), alite (green) and clinotobermorite T3_14sc (pink) are also included. Taken from article #1 in Annex I.

The multi-r-range methodology of the alite paste hydrated with 0.8 w/s ratio after 34 days allow us to present a model for C-S-H gel, composed of layers

of defective tobermorite with the next formula $Ca_{11}Si_9O_{28}(OH)_2(H_2O)_{8.5}$ and monolayers of CH. Nevertheless, to establish a full model of the complex heterogeneous system of the gel, SXRPD, Si-MAS-NMR studies jointly with the previous PDF analysis reports were needed and will be discussed below. This full study has given the possibility of presenting a multiscale picture for the hydration of alite that explains the observed mass densities and Ca/Si atomic ratios at the different scales.

4.1.3. Effect of particle size on the hydration of alite: in-situ hydration study

After the study of the influence of water to solid mass ratio on the hydration of alite, the effect of different PSD on hydration was checked. To do so, an in-situ SXRPD hydration study was performed at MSPD beamline at ALBA synchrotron and calorimetric measurements were also carried out.

The as-received mC_3S-2016 presented a $D_{v,50}$ value of 21 µm. This sample was milled to $D_{v,50}$ of 7 and 3 µm. Figure 4.9 shows the PSD of the as-received and these two milled alites.

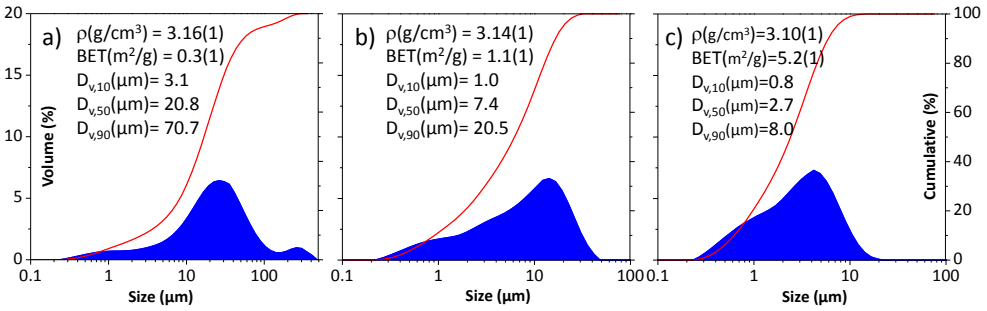

Figure 4.9. PSD of a) as-received mC_3S-2016, b) vibratory milled mC_3S-2016 and c) attrition milled mC_3S-2016. Adapted from article #2 in Annex I.

Cumulative heat and heat flow calorimetry curves have been recorded up to 7 days for the samples, and Figure 4.10 gives the calorimetric curves. The three samples with different particle size were studied at w/s mass ratio of 0.80. The as-received sample was also hydrated at w/s of 0.45 to see the effect of the water content.

Table 4.5 gives the values that can be extracted from the calorimetric study. The hydration degree of alite can be calculated using the overall heat of hydration for alite, 517 J/g [30]. This value has to be considered as an approximation, as it is

for a pure phase and consequently it does not take into account the impurities of the real samples, which could play an important role in the hydration kinetic. It is important to highlight the importance of the particle size in the hydration process.

Here, if we focus on Figure 4.10 and Table 4.5, some conclusions can be extracted. On the one hand, the same size (21 µm) with different w/s ratios (0.45 and 0.80) has been compared. The heat flow and the total heat are quite similar between both, so because of that the reaction degree is also similar. This is because the reaction surface is saturated with 0.45 w/s and the higher water content will not have any effect in comparison. On the other hand, the effect of the particle size ($D_{v,50}$ values of 21, 7 and 3 µm) on the pastes prepared at the same w/s mass ratio (0.80) was studied. As can be expected, the heat and reaction degrees are increasing with the lower particle size, due to the bigger active surface.

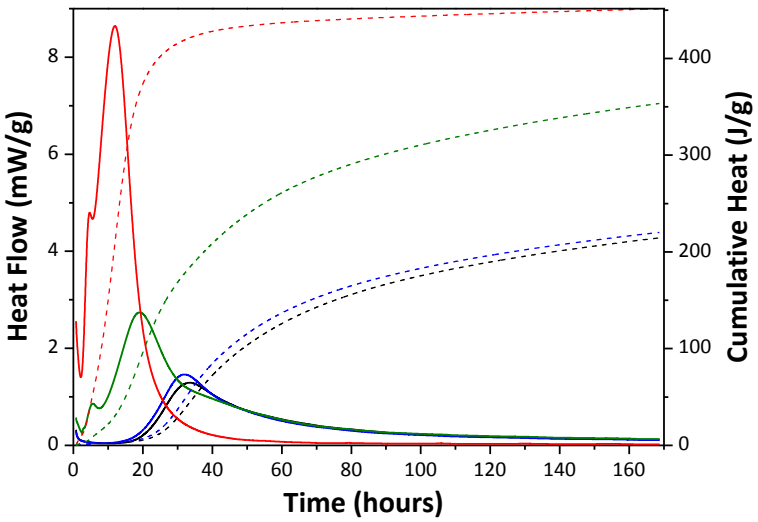

Figure 4.10. Calorimetry data. Cumulative heat (dash lines) and Heat flow (solid lines) for mC_3S-2016_21µm_0.45w/s (black), mC_3S-2016_21µm_0.80w/s (blue), mC_3S_7µm_0.80w/s (green), mC_3S-2016_3µm_0.80w/s (red). Adapted from article #2 in Annex I.

Table 4.5. Key values obtained from the mC_3S-2016 calorimetries. [1]Total heat at the maximum of the heat flow. [2]Total heat evolved at seven days. α Reaction degree calculated with 517 J/g. Taken from article #2 in Annex I.

Sample (mC_3S)	[1]Time (h)	[1]Heat (J/g)[1]	[1]α (%)	[2]Heat (J/g)	[2]α (%)
21µm 0.45 w/s	33	43.2	8.4	214.2	41.4
21µm 0.80 w/s	32	46.1	8.9	219.9	42.5
7µm 0.80 w/s	19	88.4	17.1	353.2	68.3
3µm 0.80 w/s	12	209.1	40.4	451.2	87.3

These three samples of alite were mixed with quartz as internal standard (see section 2.3.3.2 from Materials and Methods chapter) and SXRPD patterns were collected and further analysed by Rietveld methodology to obtain the full phase assemblage, including the amorphous contents [145]. Tables I, III and V of Annex III give the full phase assemblage of all the samples at all the studied ages. The obtained amorphous values, included in Tables I, III and V of Annex III combines the C-S-H gel and FW since the hydration reactions were not arrested. In order to derive the amount of these two amorphous contributions, the reaction of alite with water described in react. 1.1, from Introduction chapter, was considered as an approximation.

Consequently, taking into account the degree of reaction of alite derived from each full phase assemblage, the consumed water was calculated in each time of hydration and was rested to the total amorphous values given in Tables I, III and V of Annex III, to derive the FW value per hydration age. As a last step, the phase assemblage was renormalized by removing the FW content, Tables II, IV and VI of Annex III. Figure 4.11 displays the renormalized quantitative phase evolution of mC_3S, CH and C-S-H gel obtained from SXRPD and react. 1.1 (from Introduction chapter) for three of these studied samples: mC_3S-2016 with 0.80 w/s at different particle size ($D_{v,50}$ of 21 and 7 µm) and mC_3S-2016 with 21 µm of $D_{v,50}$ at two different water content (0.45 and 0.80 w/s). For the samples with $D_{v,50}$ of 21 µm it is worth noting that the first measurement was obtained at 5 hours of hydration. At this time, mC_3S_21µm was only dissolved ~3 and ~4 wt% and the precipitated C-S-H gel ~3 and ~4 wt% for mC_3S_21µm_0.45w/s and mC_3S_21µm_0.80w/s pastes, respectively. Furthermore, CH precipitation started later, at 7 h and 7.5 h, obtaining 1.0 and 2.8 wt% of crystalline CH after 14 h for mC_3S_21µm_0.45w/s and mC_3S_21µm_0.80w/s pastes, respectively. The kinetic of the hydration reaction progressed slowly up to 10 h hydration hours as it is shown in Figure 4.11. At 100 days of hydration, the main phase assemblage was 24.3, 17.8 and 57.9 wt% of mC_3S, CH and C-S-H gel, respectively for mC_3S_21µm_0.45w/s paste; and 11.8, 22.7 and 65.5 wt% of the same phases for mC_3S_21µm_0.80w/s paste. As expected, no relevant differences can be found between both pastes with the same particle size, only that the hydration reaction continues in the paste with the excess of water meanwhile in the other one it has been stopped. In addition, for the sample milled down $D_{v,50}$ of 7 µm (mC_3S_7µm_0.80w/s paste), the hydration kinetic was faster, as expected, and after 2 hours of hydration, 4.6 wt% of mC_3S was dissolved, precipitating ~4 wt% of C-S-H gel and ~0.4 wt% of crystalline CH. It is clearly observed that at 20 h the kinetic hydration decelerates. Finally, at 100 hydration days, 9.0, 25.3 and 65.8 wt% of mC_3S, CH and C-S-H gel, respectively, were present.

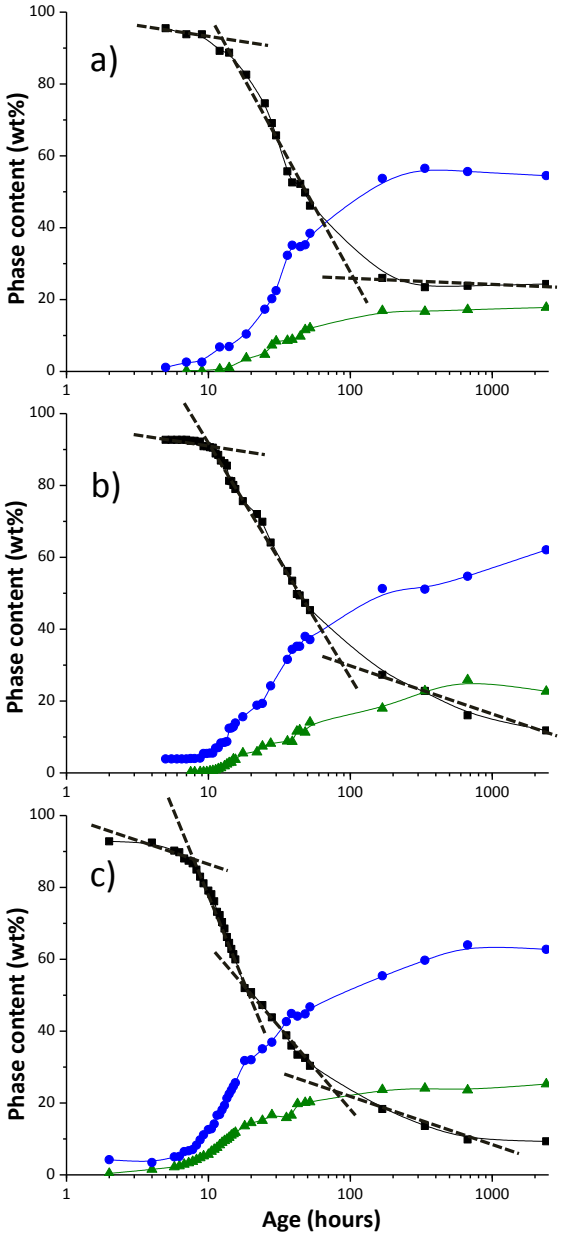

Figure 4.11. Quantitative phase analysis results from SXRPD. a) mC_3S-2016_21µm_0.45w/s, b) mC_3S-2016_21µm_0.80w/s and c) mC_3S-2016_7µm_0.80w/s. mC_3S anhydrous (black), C-S-H gel (blue) and CH (green). Adapted from article #2 in Annex I.

The hydration of the mC_3S-2016_3µm_0.80w/s paste (mC_3S-2016 with 0.80 w/s and 3 µm particle size) was stopped at 16 days. At this age the main Rietveld quantitative phase analysis was 20.5 wt% of CH, 2.5 wt% of $C\bar{C}$ and 75.9 wt% of ACn (mainly C-S-H gel but not only necessarily), see Figure 4.12.

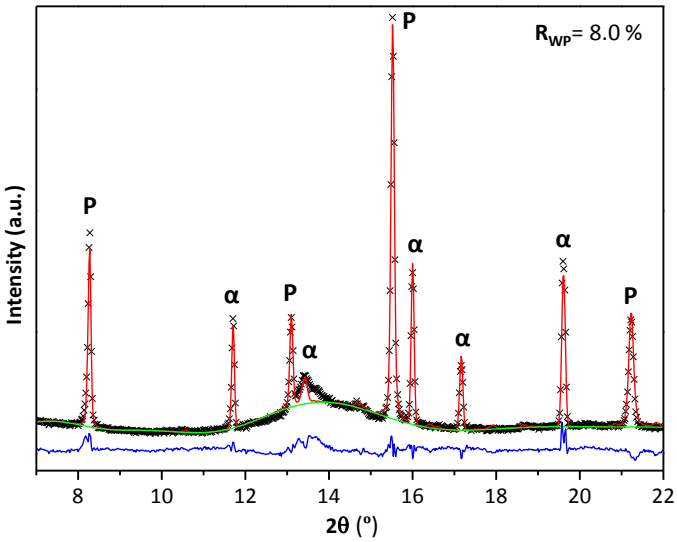

Figure 4.12. LXRPD Rietveld plot (MoKα_1 radiation, λ=0.70932 Å) with internal standard for the mC_3S-2016_3µm_0.80w/s paste hydrated for 16 days. The main peaks are labelled as follow: CH (P) and the added internal standard, α-Al_2O_3 (α). R_{WP} value is included. Adapted from article #2 in Annex I.

As it can be observed this paste was the one with the higher degree of reaction since the anhydrous mC_3S was negligible. Consequently, this sample was further studied by ^{29}Si-MAS-NMR, SEM and HRTEM methods. The study with ^{29}Si-MAS-NMR data gives direct information about the MCL in C-S-H gel. Figure 4.13 gives the ^{29}Si-MAS-NMR spectra of mC_3S-2016_3µm_0.80w/s stopped at 16 days. The weak signal at -72.4 ppm corresponds to isolated Q^0 tetrahedra from anhydrous mC_3S. The signals observed at -78.7 and -84.4 ppm were attributed to the Q^1 and Q^2 silicon units, respectively. Q^1 is associated with silicate end chain units and Q^2 indicates the presence of silicate in intermediate chain positions, as it is shown in Figure 4.14.

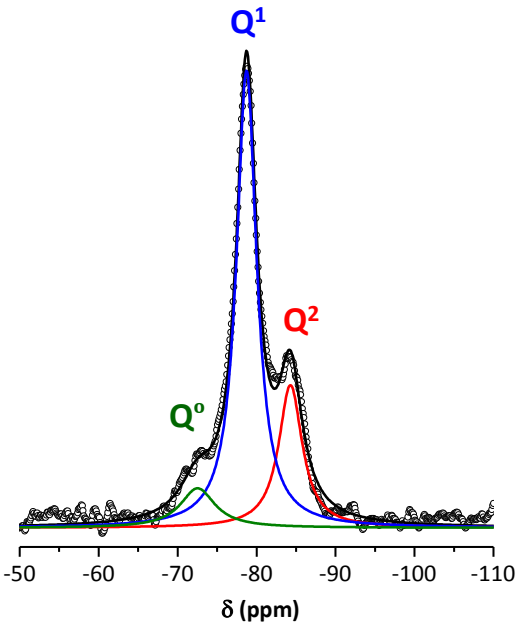

Figure 4.13. ^{29}Si-MAS-NMR spectra for mC$_3$S-2016_3µm_0.80w/s_stopped:16days. Spinning rate of 15 kHz and a magnetic field of 14.1 T. Taken from article #2 in Annex I.

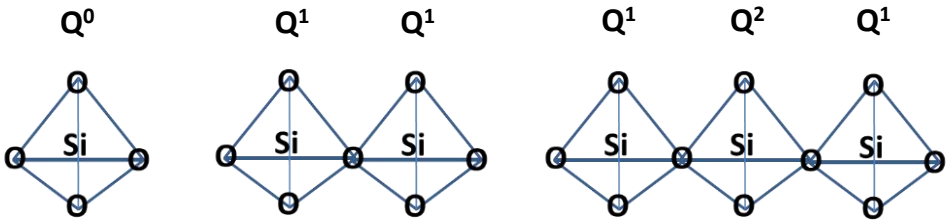

Figure 4.14. Different kind of Si-tetrahedra found in silicates. Q^0 isolated tetrahedron, Q^1 end chain silicate tetrahedron and Q^2 intermediate chain position silicate tetrahedron.

The MCL of silicates can be determined from the expression, $MCL=2(Q^1+Q^2)/Q^1$ [146]. The deconvoluted spectrum, Figure 4.13, yielded to 70.8% for Q^1 and 24.7% for Q^2, resulting a MCL of 2.70. This value agreed well with previous reports for early age alite hydrated pastes [146, 147]. In addition, the determination of the average Ca/Si ratio is also an important parameter in any investigation of a C-S-H gel. Figure 4.15 shows a HRTEM micrograph with EDS data of C-S-H gel, as an example. The average Ca/Si atomic ratio was 1.75 ± 0.16, obtained from 64 measurements. This figure also gives additional information about the alite hydration reaction at different length scales.

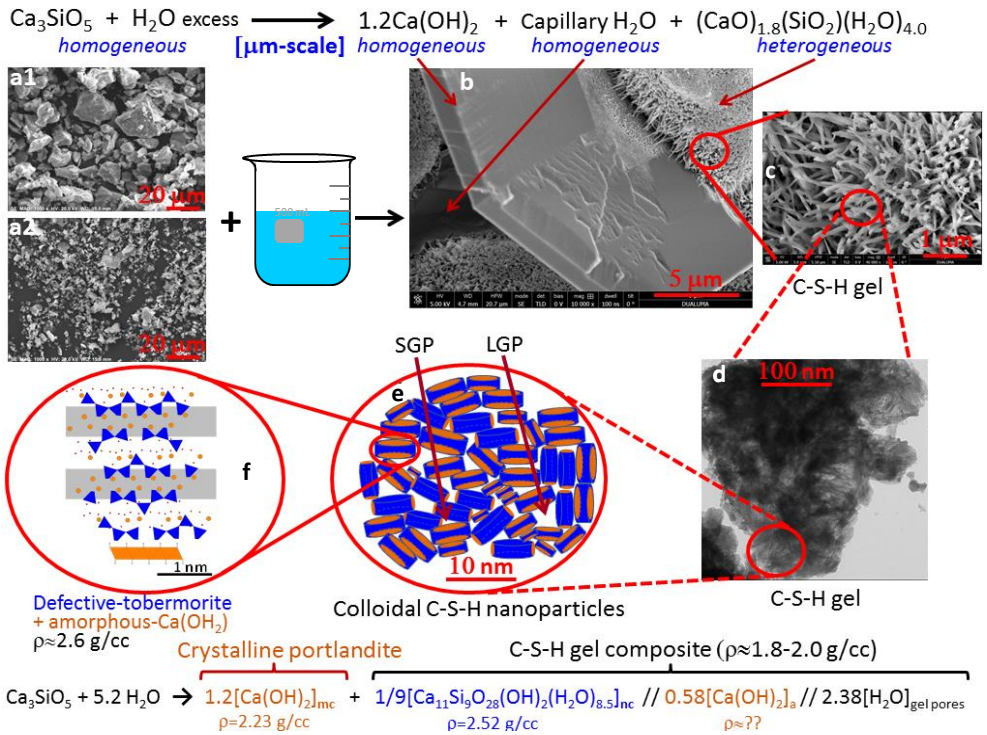

Figure 4.15. Schematic understanding of the alite hydration reaction at different length scales. (Top) Hydration reaction of tricalcium silicate at the microscale. a1) SEM micrograph of mC_3S-2016_21µm powder. a2) SEM micrograph of mC_3S-2016_3 µm powder. b) SEM micrograph of mC_3S-2016_21µm_0.80w/s paste showing a homogeneous portlandite plate microparticle, voids arising from capillary water, and three agglomerates of heterogeneous C-S-H gel. c) Enlarged view of a C-S-H gel region in b). d) TEM micrograph of mC_3S-2016_3µm_0.80w/s_stopped:16d showing interspersed foil-like C-S-H nanoparticles at the mesoscale. e) Schematic representation of C-S-H colloidal nanoparticles of clinotobermorite (blue) and monolayer CH (orange) generating the SGP and LGP of Jennings's model [3]. f) Schematic representation of a single C-S-H nanoglobule composed by defective clinotobermorite and two monolayers of CH at the nanoscale. (Bottom) Hydration reaction of tricalcium silicate at the nanoscale highlighting the three main components of colloidal C-S-H nanocomposite: nanocrystalline clinotobermorite, amorphous (monolayer) calcium hydroxide and gel pore water. The (approximate) densities, mass and volume percentages of the different components are also given for an overall water content of four water molecules per silicate. Adapted from article #2 in Annex I.

The multi-r range PDF methodology described previously was used to analyse the sample mC_3S-2016_3µm_0.80w/s arrested at 16 days since it is the sample with the higher alite hydration degree. Consequently, the high, 40-70 Å, r-range was analysed with the contributions of the crystalline phases, i.e. CH and mC_3S. The presence of $C\bar{C}$ was tested but its scale factor converged to zero during the refinement. The fits are displayed in Figure 4.16a. The parameters previously

refined were kept fixed in the analysis of the medium 10-25 Å r-range. In this range, the contribution from the nanocrystalline component of C-S-H gel was investigated. As detailed before, clinotobermorite structure T3_14sc was selected as it gave the best fit (lower R_W) and the most reliable CH/C-S-H ratio. The unit cell values for this structure converged to a = 11.255 Å, b = 7.320 Å, c = 42.415 Å and β = 94.2° and the isotropic ADPs values were 0.0083 and 0.0160 $Å^2$ for Ca, Si, respectively. The R_W was 27.7%, and the final fit is displayed in Figure 4.16b. The quantitative phase analysis results were: 2.2 wt% of anhydrous mC_3S, 33.5 wt% of crystalline-CH and 64.3 wt% of clinotobermorite.

Finally, the low r-range, from 2 to 10 Å, was studied. The PDF fit based on the contributions of crystalline CH and mC_3S and nanocrystalline defective clinotobermorite resulted in a noisy difference PDF curve, especially in the very low r-region. This noisy difference curve suggests an amorphous component, as mentioned before. The scattering misfits correspond to the theoretical PDF trace for an isolated monolayer of CH, Figure 4.8b [113]. Consequently, the scattering factor of a monolayer of CH was included in the fit. The fit indicates that this monolayer is expanded along *a* and *c* directions, 3.8 and 5.3%, respectively and compressed along *b* direction, 2.1%. Generally, the volume of this monolayer is expanded 7.0% when compared to the volume of crystalline portlandite. Thus, the expansion would lead to a density decrease from 2.24 g/cm^3 in bulk portlandite to 2.11 g/cm^3 in monolayer portlandite. The stretched monolayer portlandite structure was then used in the PDF refinement (see Figure 4.16c). As expected, the scale factors of monolayer and crystalline CH were strongly correlated (−55%) in this refinement. The R_W value for the final fit, without computing mC_3S was as low as 38% with the contribution of a CH monolayer.

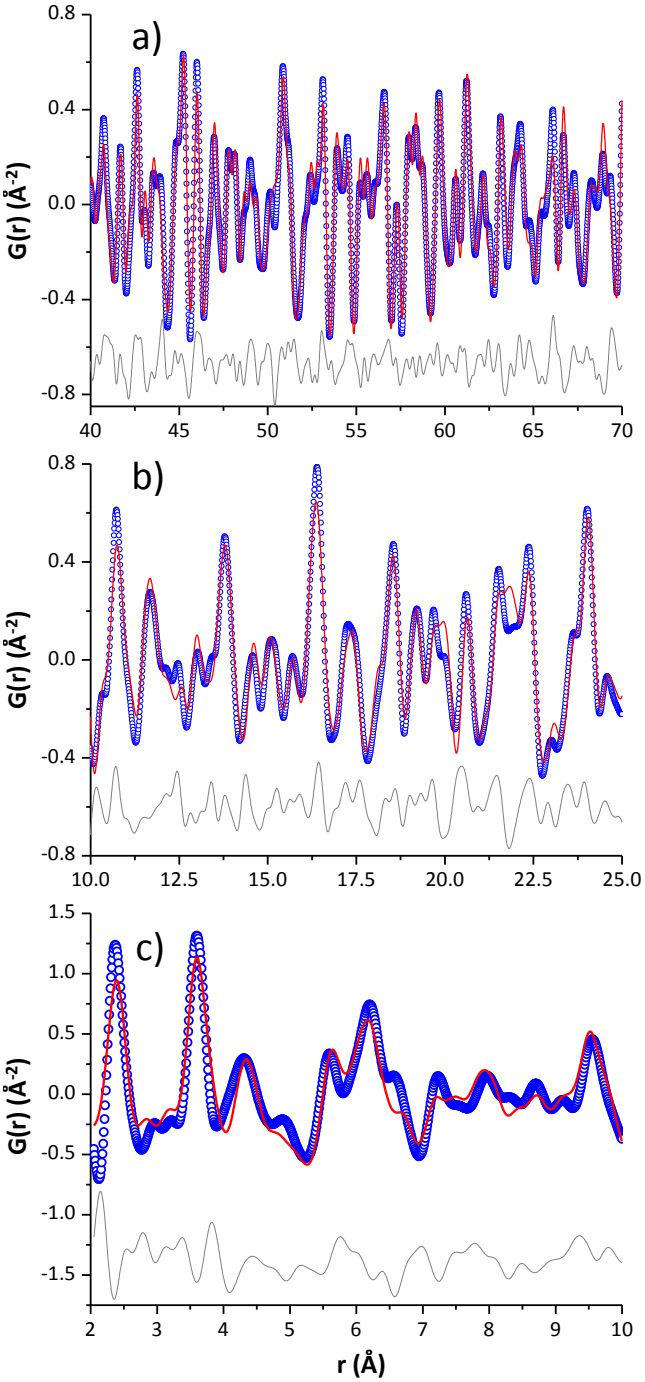

Figure 4.16. PDF refinements. Experimental (blue circles), fitted (red lines) and difference (grey lines) PDF patterns for mC_3S-2016_3µm_0.80w/s_arrested:16d a) from 40 to 70 Å; b) from 10 to 25 Å; and c) from 2 to 10 Å. For details of the fits, the readers are referred to the text. Taken from article #2 in Annex I.

The PDF analysis obtained from the total scattering data for C_3S-2016_3µm_0.80w/s_16d arrested agrees with our previous study, section 4.1.2.

The crystal structure which gave the best fit to the PDF data in the region 10 to 25 Å was clinotobermorite in all the studied cases. We have selected defective clinotobermorite T3_14sc, $Ca_{11}Si_9O_{28}(OH)_2(H_2O)_{8.5}$, because of the really good fit (lower R_W value) and this approximate structure represents a 'trimer' derived from a staggered-chain clinotobermorite [138].

In addition, more studies are needed to settle if this structural description is the best option for the hydration of alite under different conditions and in PC. Its average silicate chain length of 3.0 is in agreement with the MCL value, 2.7, obtained by ^{29}Si MAS-NMR. Nevertheless, its Ca/Si ratio, 1.22, does not agree with the Ca/Si ratio of the C-S-H gel determined by electron microscopy, 1.75, which is widely reported [30, 148] and confirmed by reaction react. 1.1 in the Introduction chapter. However, these Ca/Si ratios are not obtained at the same probing length scales. The Ca/Si ratio of defective tobermorite measured by PDF analysis is obtained at the nanoscale, probing scale: 10-30 Å. The Ca/Si ratio, measured by EDX-STEM, (using a HRTEM microscope) is obtained at the mesoscale, ~50-100 nm (where images were taken with TEM-CMOS and also STEM-HAADF detectors). The Ca/Si ratios determined from FEG-SEM and Rietveld refinement of SXRPD data are obtained at the microscale, probing scale >500 nm. The apparent disagreement in the Ca/Si ratios can be reconciled by the hypothesis that C-S-H gel aggregates arising from the hydration of alite, is a composite formed by a fine intermixing at the nanoscale of defective tobermorite nanoglobules, sizes ~40 Å, and amorphous CH, size <2 nm, see Figure 4.15.

To sum up, the *in situ* SXRPD study has confirmed the stoichiometry of alite hydration reaction to yield portlandite and C-S-H gel with $(CaO)_{1.8}SiO_2(H_2O)_{4.0}$ average composition. Mainly, by using high-resolution synchrotron PDF analysis, it has been found that C-S-H gel is heterogeneous at the nanoscale being composed of defective tobermorite, with approximate composition $Ca_{11}Si_9O_{28}(OH)_2(H_2O)_{8.5}$, and monolayers of CH. With these results and observations from electron microscopy and previous reports, a multiscale model for the hydration of alite has been proposed (see Figure 4.15), which explains the observed mass densities and Ca/Si atomic ratios at the relevant scales.

4.1.4. Comparison between C_3S polymorphs: monoclinic and triclinic

A pure triclinic tricalcium silicate (tC_3S) was hydrated and compared to mC_3S-2017. These anhydrous samples were previously characterised, Figure 4.17.

RQPA of LXRPD patterns showed that tC_3S was a single crystalline phase, and mC_3S-2017 sample is composed of 97.5(6) wt% of mC_3S and 2.5(2) wt% βC_2S.

The media particle size, $D_{v,50}$ values, were 4.6 µm for tC_3S and 6.3 µm for mC_3S-2017, for more details see Materials and Methods chapter (section 2.1.2 and 2.1.3).

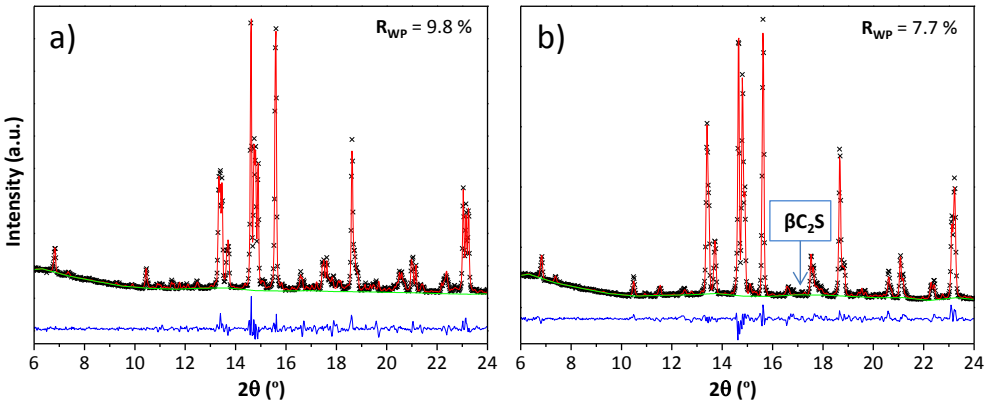

Figure 4.17. LXRPD Rietveld plot (MoKα_1 radiation, λ = 0.70932 Å) of a) tC_3S (ICSD #162744) and b) mC_3S-2017 (ICSD #94742). R_{WP} values are also included. The arrows point the minor. Adapted from article #1 of Annex II.

The PDF analyses for anhydrous triclinic and monoclinic C_3S were performed using the data collected in ID15A at ESRF Synchrotron. The resulting data obtained by these fits were maintained constant and used in the hydrated samples since there is a small amount of unreacted alite. The results obtained from PDF refinements of the anhydrous samples are presented in Table 4.6.

Table 4.6. Refinement parameters obtained from PDF analysis for anhydrous tC_3S and mC_3S-2017 samples. The positional parameters were not optimised.

Parameters		tC_3S	mC_3S-2017
R_W (%)		11.1	18.2
Unit Cell (Å)	a	11.611	12.224
	b	14.182	7.041
	c	13.625	9.257
	α	104.8º	-
	β	94.5º	115.9º
	γ	90.1º	-
ADP (Å^2)	Ca	0.0054	0.0175
	Si	0.0155	0.0112
	O	0.0050	0.0647

Both samples were hydrated at a w/c ratio of 0.5 and were introduced in a glass capillary, see Materials and Methods chapter. The PDF data for both hydrated alite samples were taken at 56 days of hydration, Figure 4.18.

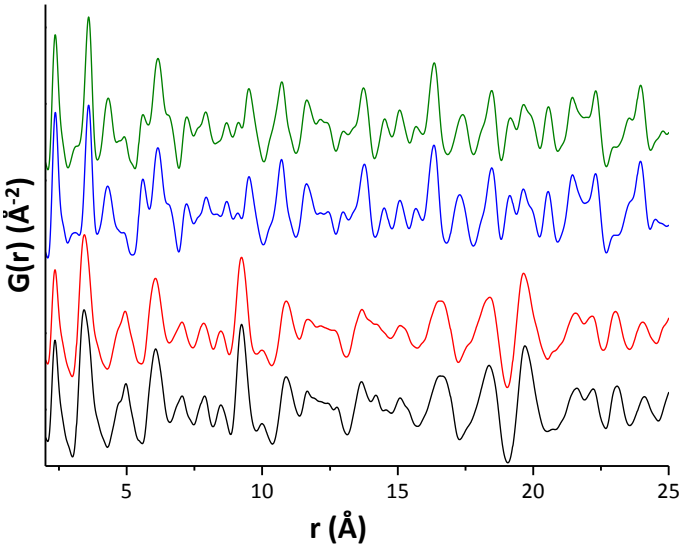

Figure 4.18. Experimental synchrotron PDF patterns from 2 to 25 Å for anhydrous tC_3S (black), anhydrous mC_3S-2017 (red), tC_3S_0.50w/s (blue) and mC_3S-2017_0.50w/s (green) at room temperature. Both pastes were measured at 56 days hydration.

As it was described above, the full PDF data for triclinic and monoclinic alite pastes are very complex due to the presence of different phases of different natures. All the PDF patterns for the hydrated samples were quantitative analysed using the previously reported multi-r range strategy. In summary, this methodology consists on analysing the large interatomic distance range, from 40-70 Å, for establishing the crystalline phase parameters, and then to analyse the medium interatomic distance range, here 10-25 Å, for establishing the nanocrystalline phase contents.

Table 4.7 gives the final R_W, the refined unit cell and refined ADP for crystalline CH obtained by fitting the 40-70 Å region values of both hydrated samples, tC_3S_0.5w/s and mC_3S-2017_0.5w/s. The unit cell and ADP for unreacted alites were kept constant and only their scale factor was refined. Final fits are given in Figure 4.19a and c.

Table 4.7. R_W, unit cells and ADPs for crystalline CH obtained by refining the 40-70 Å r-range for tC_3S_0.5w/s and mC_3S-2017_0.5w/s hydrated after 56 days samples.

Parameters			tC_3S_0.5w/s	mC_3S-2017_0.5w/s
R_W (%)			26.7	33.5
Unit Cell (Å)	a		3.587	3.587
	c		4.903	4.904
ADP ($Å^2$)	Ca	U11	0.0043	0.0071
		U12	0.0043	0.0071
		U33	0.0999	0.0063
		U12	0.0021	0.035
	O	U11	0.0091	0.0078
		U22	0.0091	0.0078
		U33	0.0117	0.0097
		U12	0.0045	0.0039

After that, all parameters for crystalline portlandite and unreacted alite were fixed and the 10-25 Å r-region was analysed to compute the nanocrystalline contribution of C-S-H gel, see Figure 4.19b and d. Four different crystal structures were tested to fit the PDF signals of the gel in this region for these samples, in the same way as above. Table 4.8 shows the R_W values for each PDF fit using the selected structural descriptions for the nanocrystalline gel and also includes the quantitative phase analysis results for the different phases. This study has enabled us to discriminate which structure, tobermorite-14Å, tobermorite-11Å, clinotobermorite (m) T3_14sc or jennite, gave the best refinement for these pastes. Jennite sometimes was directly discarded as mentioned before, since it yielded worse fits. Both crystal structures for tobermorite-11Å and clinotobermorite (m) T3_14sc have been tested here as before. These two structures are very similar; however, the tobermorite-11Å fits the structure of the nanocrystalline part of the C-S-H gel better than the others (lower R_W factors), see Table 4.8. This corroborates the results previously discussed above, from article #2 in Annex I, where the scattering misfit of this region corresponds to the theoretical PDF trace of isolated monolayers of CH.

Table 4.8. Quantitative phase analysis results obtained by PDF using different crystal structures for the nanocrystalline C-S-H gel between 10 to 25 Å r-range. R_W values are also included.

sample	R_W (%)	C_3S (wt%)	$C\bar{C}$ (wt%)	Cryst-CH (wt%)	C-S-H gel (wt%)
tC_3S_0.50w/s_RT					
Tobermorite-11 (o), ICSD #100405	**31.0**	**30.2**	**2.2**	**25.4**	**42.3**
Tobermorite-14 (m), ICSD #152489	34.4	28.9	2.1	24.3	44.7
Clinotobermorite (m), T3_14sc	35.4	32.4	2.3	27.2	38.1
Jennite (t), ICSD #151413	39.6	38.0	2.3	34.9	24.7

mC_3S-2017_0.50w/s_RT					
Tobermorite-11 (o), ICSD #100405	**37.4**	**26.2**	**-**	**25.9**	**47.9**
Tobermorite-14 (m), ICSD #152489	46.1	36.4	-	36.0	27.6
Clinotobermorite (m), T3_14sc	41.8	28.9	-	32.2	38.9
Jennite (t), ICSD #151413	42.9	26.9	-	29.9	43.2
tC_3S_0.50w/s_35ºC					
Tobermorite-11 (o), ICSD #100405	**33.5**	**10.4**	**3.2**	**32.1**	**54.3**
Tobermorite-14 (m), ICSD #152489	40.7	9.8	3.0	30.2	57.1
Clinotobermorite (m), T3_14sc	38.1	11.8	3.6	36.4	48.2

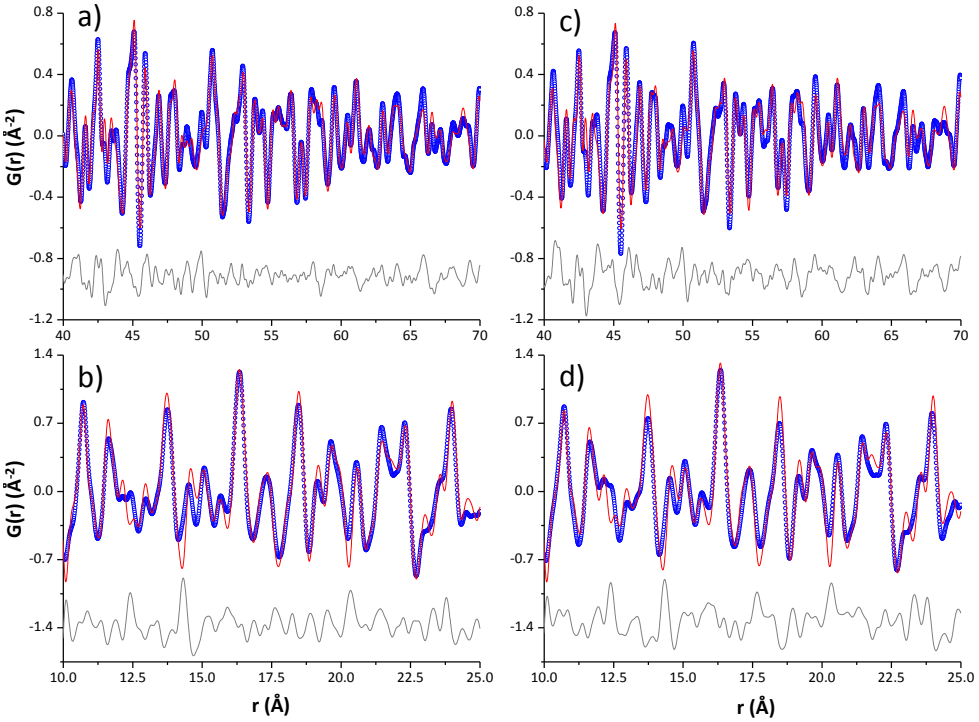

Figure 4.19. Experimental (blue circles), fitted (red lines) and difference (grey lines) PDF patterns. a) and b) for tC_3S_0.50w/s at RT; c) and d) for mC_3S-2017_0.50w/s at RT, both at two different r-ranges.

As it is observed in Table 4.8 and Figure 4.19b and d, the best fitted C-S-H gel in the 10-25 Å r-range in tC_3S_0.50w/s_RT and mC_3S-2017_0.50w/s_RT are very similar independently of the polymorphism. The crystal structure of tobermorite-11Å is the best option to fit the nanocrystalline contribution of the C-S-H gel for both C_3S pastes, triclinic and monoclinic (hydrated with the in-situ procedure at RT and w/s=0.50). Thus, it can be concluded that there is not a significant influence in the nanocrystalline part of the precipitated gel with the alite polymorphism.

4.1.5. Effect of temperature on the hydration of triclinic C_3S

The effect of temperature on the hydration of tC_3S was studied. To do so, the hydration was performed at RT and 35ºC, and analysed by PDF methodology. The results for the sample hydrated at RT have been described above. For the sample hydrated at 35ºC, the PDF data were taken at 63 days of hydration. The R_W value in the 40-70 Å r-region converged to 28.6%. The unit cell values for portlandite and the final anisotropic ADPs values were similar to that reported for the RT triclinic sample. The refined parameters in the high r-range were kept fixed for crystalline-CH and the scale factor for unreacted alite, the nanocrystalline contribution of C-S-H gel was refined in the r-region, 10-25 Å, as previously described. R_W values obtained for each PDF fit using the two selected structural descriptions for the nanocrystalline C-S-H gel and the quantitative phase analysis results are shown also in Table 4.8. In agreement with previous results at RT, the crystal structure of tobermorite-11Å fits better the nanocrystalline contribution of the C-S-H gel than tobermorite-14Å for the sample hydrated at 35ºC.

It can be observed that tobermorite-11Å fits better the nanocrystalline fraction of C-S-H for both tC_3S pastes. Thus, there is no significant influence in the local structure of the precipitated C-S-H gel within this temperature range. However, as it is expected, the reaction degree in the tC_3S_0.50w/s_35ºC sample was higher than that of the hydrated sample at RT. This is observed when comparing the amounts of unreacted alite for both pastes, see Table 4.8. The plot of the refinement for the tC_3S_0.50w/s_35ºC sample, in the 10-25 Å r-range, is presented in Figure 4.20.

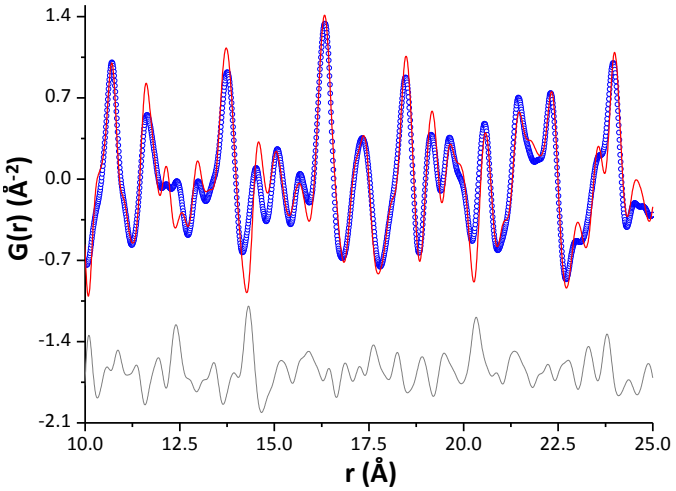

Figure 4.20. Experimental (blue circles), fitted (red lines) and difference (grey lines) PDF patterns for tC_3S_0.50w/s_35ºC modelling nanocrystalline C-S-H with tobermorite-11Å.

4.1.6. Effect of hydration procedure on C-S-H microstructure

In addition, another study was made to compare the ex-situ hydration (hydrated in a cylinder mould and water was arrested at the selected age) and the in-situ (hydrated in a capillary glass without stopping) methodologies. tC_3S was hydrated for 47 days and after that, the hydration was arrested and a capillary was filled up with it (tC_3S_0.50w/s_RT_stop). This capillary was measured and compared with the in-situ hydrated sample (tC_3S_0.50w/s_RT), previously described. The 40-70 Å r-region converged to 26.0%. The unit cell values for portlandite and the final anisotropic ADPs values were similar to that reported before. Then, the 10-25 Å r-region was used to fit the contribution of nanocrystalline C-S-H with the crystal structures of tobermorites, 11 Å and 14 Å, clinotobermorite and jennite, see Table 4.9. Figure 4.21a shows the final PDF fit for tC_3S_0.50w/s_RT_stop sample in the 10-25 Å r-region.

Table 4.9. Quantitative phase analysis results obtained by PDF using different crystal structures for the nanocrystalline C-S-H gel between 10 to 25 r-range for the samples of tC_3S hydrated w/c=0.5 by ex-situ method in which arresting was carried out at 47 days at RT and 50ºC. R_W values are also included.

sample	R_W (%)	C_3S (wt%)	$C\bar{C}$ (wt%)	Cryst-CH (wt%)	C-S-H gel (wt%)
tC_3S_0.50w/s_RT_stop					
Tobermorite-11 (o), ICSD #100405	**32.7**	**14.7**	**3.5**	**31.6**	**50.1**
Tobermorite-14 (m), ICSD #152489	35.9	14.0	3.3	30.1	52.6
Clinotobermorite (m), T3_14sc	36.5	14.9	3.6	32.2	49.3
Jennite (t), ICSD #151413	42.3	20.5	4.6	53.9	21.1
tC_3S_0.50w/s_50ºC_stop					
Tobermorite-11 (o), ICSD #100405	**29.8**	**-**	**-**	**42.3**	**57.6**
Tobermorite-14 (m), ICSD #152489	37.8	-	-	41.9	58.1
Clinotobermorite (m), T3_14sc	31.4	-	-	37.4	62.6
Jennite (t), ICSD #151413	31.8	-	-	36.4	63.6

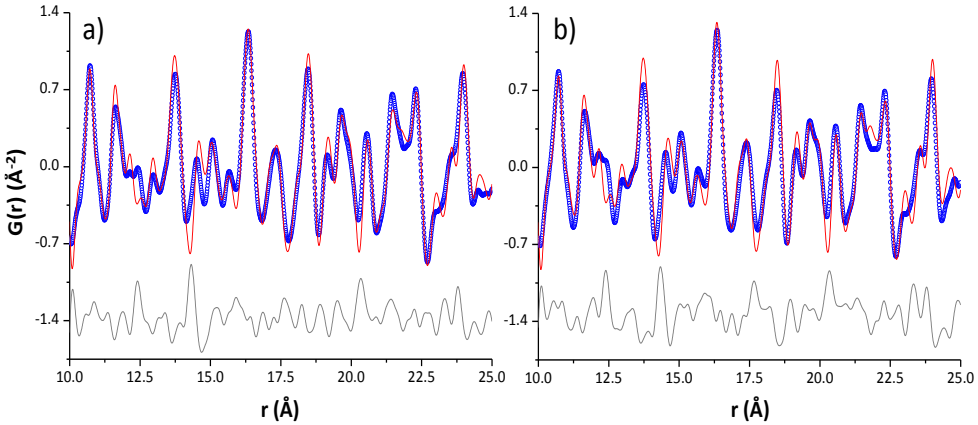

Figure 4.21. Experimental (blue circles), fitted (red lines) and difference (grey lines) PDF patterns for a) tC_3S_0.50w/s_RT_stop and b) tC_3S_0.50w/s_RT_50ºC_stop, both modelling nanocrystalline C-S-H with tobermorite-11Å.

It can be observed, for this stopped-hydration paste, which was prepared by the *ex-situ* procedure, tobermorite 11Å also fits the best for the crystal structure of the gel, as it was previously observed for the same paste prepared by the *in-situ* procedure. Thus, it seems that this different hydration procedure does not have a significant influence in the local atomic order of the precipitated C-S-H gel. An important difference between both samples is the degree of reaction, being higher for tC_3S_0.50w/s_RT_stop than for tC_3S_0.50w/s_RT. This is very likely due to the different hydration methodology. For the *in-situ* hydration, the volume of the paste inside the capillary is much smaller than that inside the cylinder (*ex-situ* hydration). We speculate that in the small capillary, the hydration products which precipitate with time can create passive layers that may avoid the progress of the hydration. In addition, it is not possible to guarantee that the amount of water is completely homogenously distributed within the capillary. Issues related with inhomogeneous water distribution within small capillaries have been already reported [149].

4.1.7. Effect of temperature on pastes hydrated by ex-situ methodology

The influence of the temperature in the hydration mechanism of tC_3S prepared by the ex-situ procedure was also studied by PDF method. The results for the tC_3S sample hydrated at 50ºC (and stopped) are hereby compared with the sample described above, tC_3S_0.50w/s_RT_stop (same procedure, but hydrated at

RT). For the tC_3S_0.50w/s_50ºC_stop sample, the PDF data were taken at 48 days of hydration. The final R_W value in the 40-70 Å r-region converged to 28.8%. Table 4.9 shows the R_W values in the 10-25 Å r-region for each PDF fit using the two selected crystal structures of tobermorite for the fitting of the nanocrystalline gel, where clinotobermorite and jennite fits results are also included. The fitted plot of this sample using tobermorite 11Å is shown in Figure 4.21b.

For this sample, there is no unreacted alite because of the high temperature employed in the hydration process, which has enhanced the hydration degree, as expected. Moreover, the absence of additional unreacted phases leads to a lower R_W value in the 10-25 Å r-region, Table 4.9. It can be also concluded here that the temperature does not significantly affects the local atomic order of the precipitated gel in this temperature range (hydration arrested).

After this PDF analysis, a LXRPD study was performed to carry out a double-check of the main results derived from the PDF. The LXRPD powder patterns of these samples also point out the presence of tobermorite-11Å (and the absence of tobermorite-14Å). The LXRPD patterns for the three samples, tC_3S_0.50w/s_RT, tC_3S_0.50w/s_RT_stop and tC_3S_0.50w/s_50ºC_stop, are shown in Figure 4.22. The high d-spacing (low angle region) allows identifying tobermorite-11Å and tobermorite-14Å, since there is a difference between both structures in the d-spacing of the (002) reflection. The reflection observed at 11.48 Å in all the patterns corresponds to tobermorite-11Å. However, there is no presence of any diffraction signal close to 14.0 Å. Consequently, the LXRPD study also discards the presence of tobermorite-14Å in the hydration pastes of tricalcium silicate.

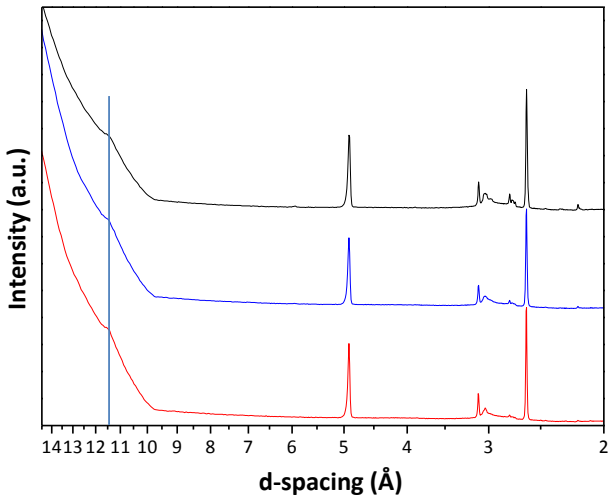

Figure 4.22. LXRPD patterns for tC_3S_0.50w/s_RT (black), tC_3S_0.50w/s_RT_stop (blue) and tC_3S_050w/s_50ºC_stop (red).

4.2. Calcium Sulphoaluminate related systems

4.2.1. Goals

The hydration products of ye'elimite without and with different sulphate sources and with different water to cement mass ratios were studied to identify the amorphous/nanocrystalline phases with PDF methodology. In addition, a protocol has been established to analyse the atomic structure of the amorphous/nanocrystalline gels in cement pastes by using synchrotron X-ray PDF methodology.

4.2.2. Effect of gypsum and bassanite as sulphate sources in the hydration process of $C_4A_3\bar{S}$

The first batch of the laboratory-prepared ye'elimite powder (orthorhombic, oSK-2016, prepared in 2016) was preliminary characterised through PSD and LXRPD techniques. The particle size ($D_{v,10}$, $D_{v,50}$ and $D_{v,90}$ values) and phase assemblage details of this powder are given in Table 2.1 and Section 2.1.4, respectively, from Materials and Methods chapter. Ye'elimite was mixed with i) gypsum and ii) bassanite. Both ye'elimite-sulphate source mixtures were here hydrated at RT and with a w/s mass ratio of 1.20 for 21 days the former and 14 days the latter. The samples were studied by LXRPD (see Figure 4.23) and the Rietveld method coupled with the internal standard. This kind of hydrated sample contains crystalline phases, ettringite, unreacted crystalline phases and also amorphous/nanocrystalline gel of aluminium hydroxide [150, 151]. RQPA of these two samples gave the following phase assemblages: for the ye'elimite-gypsum hydrated sample: 1.5 wt% of unreacted ye'elimite, 59.0 wt% of ettringite and 39.5 wt% of ACn; for the ye'elimite-bassanite hydrated sample: 63.9 wt% of ettringite and 36.1 wt% of ACn. The ACn values chiefly include the aluminium hydroxide gel content.

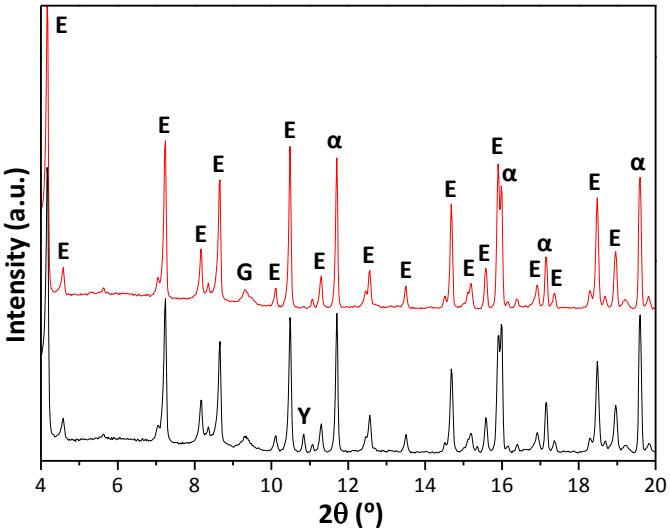

Figure 4.23. LXRPD patterns for oSK-2016_gyp_1.20w/s (black), oSK-2016_bas_1.20w/s (red) with internal standard (α-Al_2O_3) (MoKα_1 radiation, λ = 0.70932 Å). The peaks are labelled as: α= α-Al_2O_3, Y=ye'elimite, E=ettringite, and G=gibbsite.

The data obtained through thermogravimetry for the ye'elimite pastes are shown in Figure 4.24. The total weight losses up to 600°C were 43.5% and 46.5%, for oSK-2016_gyp_1.20w/s and oSK-2016_bas_1.20w/s pastes, respectively. These values are in agreement with previously reported data for a similar sample [151].

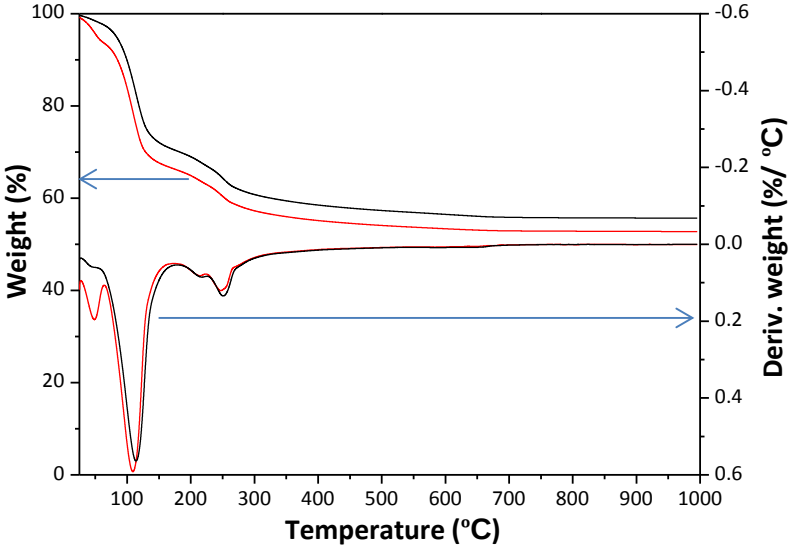

Figure 4.24. Thermogravimetric data of oSK-2016_gyp_1.20w/s at 21 days (black line) and oSK-2016_bas_1.20w/s at 14 days (red line) at room temperature. It is presented the weight percentage and derivative weight percentage.

The samples were measured at MSPD beam line at ALBA synchrotron to perform a PDF analysis. The SXRPD as well as the G(r) plot of both samples are given in Figure 4.25. It was important to take into account that the pastes recorded contained a mixture of crystalline (ettringite and anhydrous oSK) and gel (aluminium hydroxide) with crystal structure that it can be described as nanocrystalline gibbsite. The multi-r range PDF analysis strategy was adopted to fit the functions. Firstly, the high r-region, 30 to 50 Å, were fitted the crystal structure for the crystalline phases. Figure 4.26 shows the 30 to 50 Å r-range of the sample with gypsum (oSK-2016_gyp_1.20w/s_21d) and the sample with bassanite (oSK-2016_bas_1.20w/s_14d). In both samples, the crystal structure of ettringite was used. For both samples the optimised parameters were: the scale factors, unit cell and ADPs. Table 4.10 gives the refined unit cell value for ettringite, the final ADPs values and R_W for both fits. The unit cell, ADPs and R_W values for ettringite obtained in both samples indicates that both pastes are quite similar.

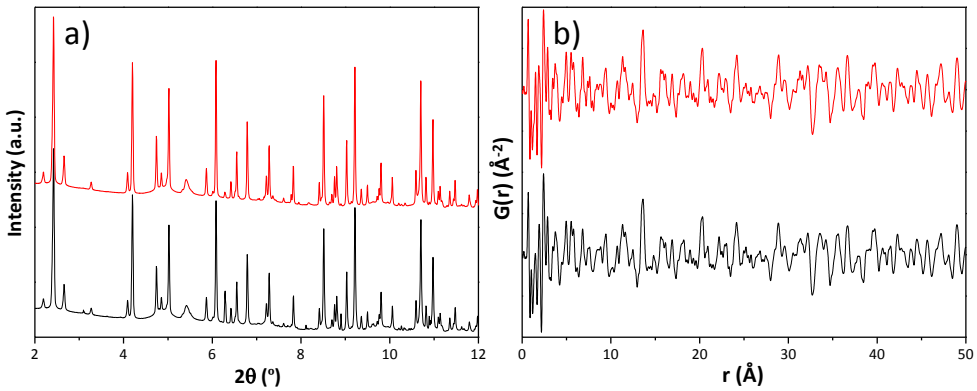

Figure 4.25. a) Synchrotron X-ray powder raw diffraction data, λ = 0.18972 Å intensity *vs* 2θ and b) Experimental real-space distribution of interatomic distances G(r) obtained at Q_{max} 24 A^{-1} for oSK-2016_gyp_1.20w/s_21d (black line) and oSK-2016_bas_1.20w/s_14d (red line) pastes.

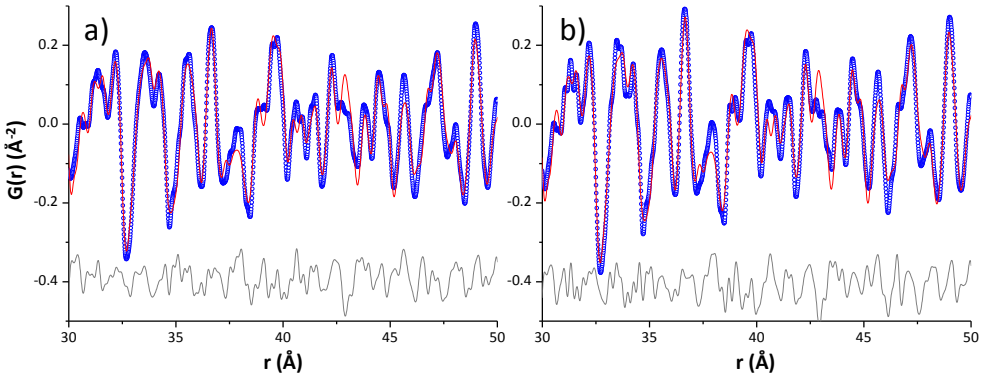

Figure 4.26. Experimental (blue circles) and fitted (red solid line) PDF patterns in the 30 to 50 Å r-range for a) oSK-2016_gyp_1.20w/s_21d and b) oSK-2016_bas_1.20w/s_14d pastes hydrated at room temperature. Difference curves are shown as grey lines. Adapted from article #1 of Annex I.

Table 4.10. Unit cell values and ADPs of ettringite obtained in the 30 to 50 Å r-range for the oSK-2016_gyp_1.20w/s_21d and oSK-2016_bas_1.20w/s_14d. R_W of the fits is also included.

Ettringite	oSK-2016_gyp_1.20w/s_21d	oSK-2016_bas_1.20w/s_14d
a(Å)	11.238	11.239
c(Å)	21.468	21.479
Ca-ADP(Å^2)	0.0087	0.0087
Al-ADP (Å^2)	0.0061	0.0073
S-ADP(Å^2)	0.0103	0.0083
O-ADP(Å^2)	0.0260	0.0293
R_W(%)	27.2	26.5

After fitting the 30 to 50 Å r-range, all the parameters for the crystalline ettringite phase were kept fixed and a low r-region, 1.6-35 Å, was used to fit the nanocrystalline aluminium hydroxide gel contribution. The gibbsite crystal structure was used for this nanocrystalline phase. The following parameters were optimised: the scale factor, unit cell parameters, ADPs, delta2, atomic parameters and Spdiameter. Table 4.11 gives the refined unit cell value for aluminium hydroxide gel, the final ADPs values and R_W for both fits. Figure 4.27 gives the final fits of the low r-range of these two samples, including an enlarged view of the smallest r-range (Figure 4.27b and d). The phase contents and Spdiameter values are given in Table 4.12.

Table 4.11. Unit cell values and ADPs of aluminium hydroxide obtained in the 1.6 to 35 Å r-range for the oSK-2016_gyp_1.20w/s_21d and oSK-2016_bas_1.20w/s_14d. R_W of the fits is also included.

Aluminium hydroxide	oSK-2016_gyp_1.20w/s_21d	oSK-2016_bas_1.20w/s_14d
a (Å)	8.815	8.851
b (Å)	4.982	4.985
c (Å)	9.507	9.517
β (º)	94.9	94.7
Al-ADP (Å^2)	0.0007	0.0007
O-ADP (Å^2)	0.0176	0.0224
R_W (%)	27.5	28.4

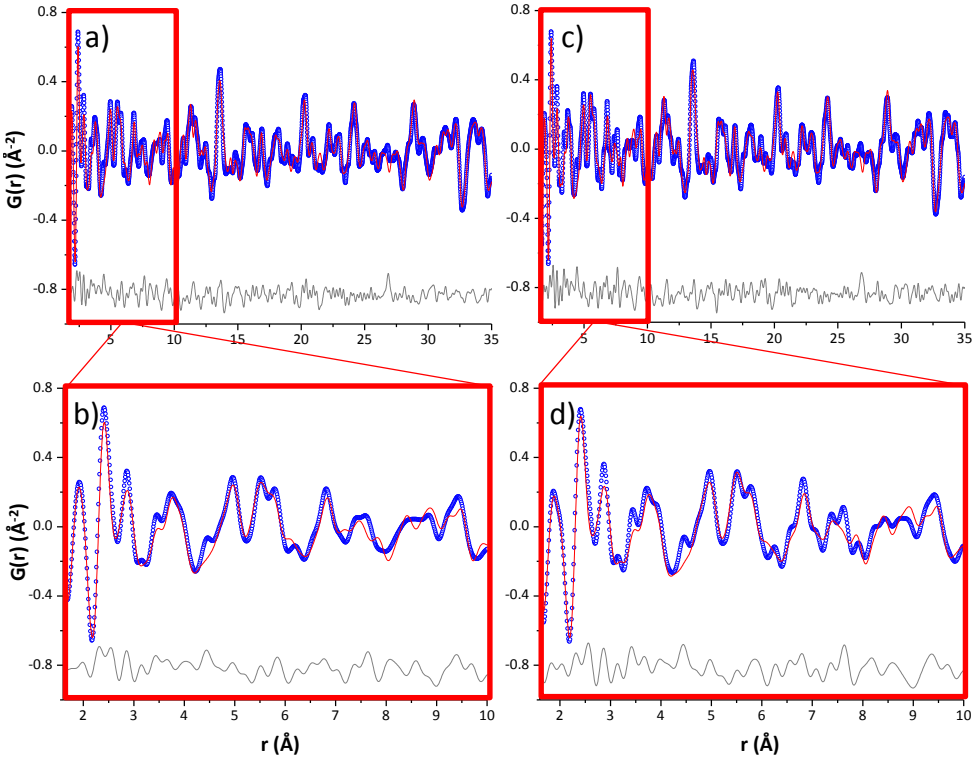

Figure 4.27. Experimental (blue circles) and fitted (red solid line) PDF patterns for the low r-range, 1.6 to 35 Å, for a) oSK-2016_gyp_1.20w/s_21d and b) oSK-2016_bas_1.20w/s_14d pastes hydrated at room temperature. Below: enlarged view of 1.6 to 10 Å (b and d). Difference curves are shown as grey lines. Adapted from article #1 in Annex I.

Table 4.12. Selected results for the synchrotron PDF analysis of the ye'elimite pastes in the 1.5-35 Å r-region. Adapted from article #1 in Annex I.

sample	R_w (%)	Ettringite (wt%)	$Al(OH)_3$ gel (wt%)	Spdiameter (Å)
oSK-2016_gyp_1.20w/s_21d	27.5	61.3	38.7	28
oSK-2016_bas_1.20w/s_14d	28.4	59.9	40.1	26

The Spdiameter parameter is related to the particle size of the aluminium hydroxide gel. Both gels obtained by mixing ye'elimite with different sulphate sources are very similar as well as the unit cell values. Consequently, neither the crystal hydrated phases nor the aluminium hydroxide gel obtained are influenced by the sulphate source.

4.2.3. Effect of the amount of anhydrite, particle size and w/s mass ratio on the hydration of $C_4A_3\bar{S}$-2017

This study was performed with a different sample of ye'elimite, oSK-2017, the one prepared in 2017. RQPA showed 0.4(1) wt% of tricalcium aluminate ($Ca_3Al_2O_6$) as impurity, see Figure 4.28a. The $D_{v,50}$ was 7.1 µm (see materials and methods section for more details). Figure 4.28b gives the PDF analysis of this anhydrous sample, fitted with the orthorhombic crystal structure of ye'elimite [152]. In addition, Figure 4.29 displays, the SXRPD pattern and the PDF patterns of five samples of oSK-2017 mixed with different percentages of anhydrite and different water to solid mass ratios at 35 days hydration time: oSK-2017_31anh_0.85w/s, oSK-2017_15.5anh_0.85w/s, oSK-2017_15.5anh_0.70w/s, oSK-2017_0.0anh_0.85w/s, oSK-2017_0.0anh_0.58w/s. Figure 4.29a displays the powder pattern for all samples in the 1.0 to 4.75° (2θ) range. It is worth noting that 4.75° for λ =0.18972 Å is equivalent to 39° for λ=1.546 Å (CuKα radiation). The data do not have high resolution, as the detector was placed quite close to the sample, but the relevant ettringite and AFm diffraction peaks are evident.

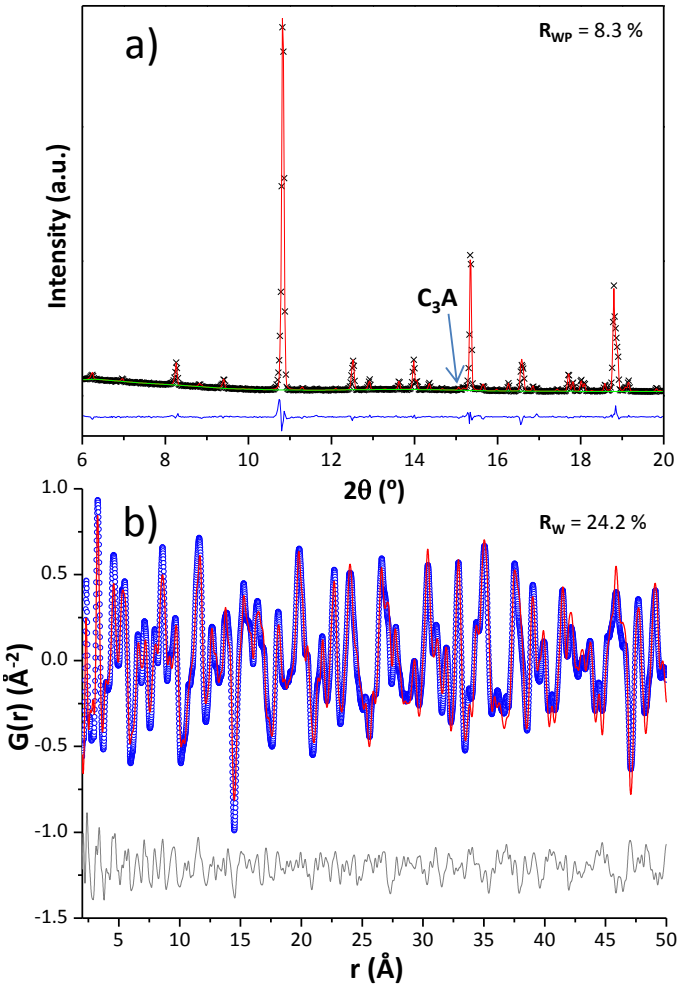

Figure 4.28. a) LXRPD Rietveld plot (MoKα_1 radiation, λ = 0.70932 Å) of oSK-2017 (fitted with ICSD # 237892). R_{WP} value is also included and the arrow points C_3A main diffraction peak. b) PDF refinement of oSK-2017 from 2 to 50 Å r-range. R_W is included. Taken from article #3 in Annex I. Reproduced with permission of ICE Publishing (Annex IV).

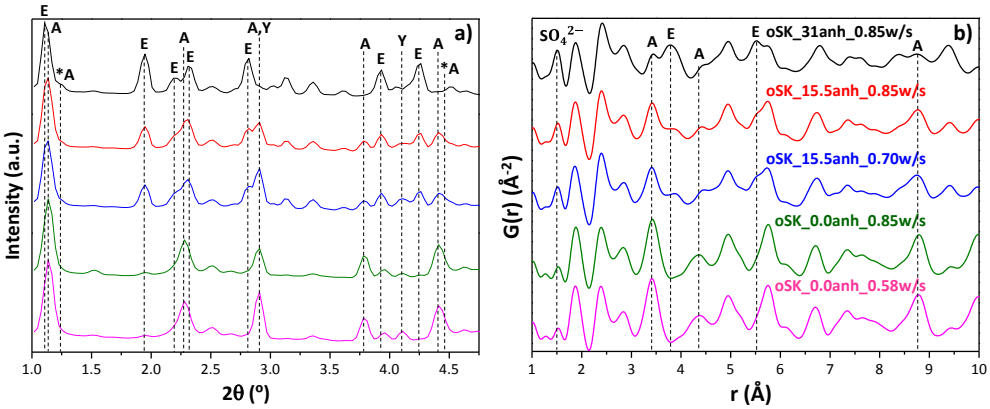

Figure 4.29. a) SXRPD patterns all pastes of orthorhombic ye'elimite-2017 mixed with different amounts of anhydrite and hydrated at different w/s ratios. The main peaks arising from the different phases are labelled, E=ettringite, A=AFm-c, *A=AFm-n, Y=ye'elimite. b) G(r) plots from 1 to 10 Å r-range for all pastes. Taken from article #3 in Annex I. Reproduced by permission of ICE Publishing (Annex IV).

The crystal structure of orthorhombic oSK-2017 was refined in the PDF data of the anhydrous ye'elimite over a large r-region, from 2 to 50 Å. The resulting refined parameters were used to fit its contribution in the hydrated pastes, i.e. the unreacted fraction. The unit cell values converged to a=12.962 Å, b=13.052 Å and c =9.140 Å and the final ADP values were 0.0543, 0.0119, 0.0053 and 0.0307 $Å^2$ for S, Ca, Al and O, respectively. The positional parameters were not optimised. Figure 4.29b displays the PDF patterns for the five samples of ye'elimite pastes in the low r-region from 1 to 10 Å interatomic distances.

All the PDF patterns for the hydrated samples were studied using the previously mentioned strategy, the multi-r range methodology. As mentioned before, the methodology consists on analysing a high interatomic distance region, where the contribution of the nanocrystalline phases is negligible, in order to establish only the crystalline phase contents, the unit cell parameters and ADP values for these phases. In this case, for samples containing aluminium hydroxide gel, the appropriate range to fit the contribution of the crystalline phases is above 30 Å, as mentioned above, the particle size of these aluminium hydroxide gels is close to 30 Å. Then, the analysis of the low interatomic r-range, here from 1.6 to 35 Å, was used to establish the nanocrystalline (and amorphous if applicable) phase contents, keeping fixed the refined parameters for the crystalline phases.

The pastes with anhydrite, oSK-2017_31anh_0.85w/s, oSK-2017_15.5anh_0.85w/s and oSK-2017_15.5anh_0.70w/s, contains ettringite and unreacted ye'elimite crystalline phases. The unit cell values for ettringite and the final ADP values, obtained in the r-range 30 to 50 Å are reported in Table 4.13.

Then, all parameters for the crystalline ettringite were kept fixed and the low r-region, 1.6 to 35 Å, was used to fit the nanocrystalline aluminium hydroxide gel contribution. After refining all the parameters, including atomic positional coordinates of aluminium hydroxide structure, the R_W obtained is shown in Table 4.14. The final fits are displayed in Figure 4.30. Table 4.14 shows the unit cell parameters and the final ADP values for nanocrystalline aluminium hydroxide (AH) gel. The phase contents and Spdiameter value for AH gel are given in Table 4.15.

Table 4.13. Refined unit cell and ADP values for ettringite and AFm-c in the high r-range (30-50 Å) of samples of oSK-2017. R_W is also included. Taken from article #3 in Annex I. Reproduced by permission of ICE Publishing (Annex IV).

Sample (30-50 Å r-range)	R_W (%)	Ettringite		AFm-c	
		Unit cell (Å)	ADP (Å^2)	Unit cell (Å)	ADP (Å^2)
oSK-2017_31anh_0.85w/s	25.2	a=11.209 c=21.427	Al=0.0068 Ca=0.0087 S=0.0079 O=0.0230	-	-
oSK-2017_15.5anh_0.85w/s	32.9	a=11.201 c=21.443	Al=0.0086 Ca=0.0076 S=0.0099 O=0.0240	-	-
oSK-2017_15.5anh_0.70w/s	31.6	a=11.202 c=21.435	Al=0.0086 Ca=0.0082 S=0.0120 O=0.0240	-	-
oSK-2017_0.0anh_0.85w/s	36.5	-	-	a=5.735 c=28.619	Al=0.0035 Ca=0.0129 S=0.0038 O=0.0268
oSK-2017_0.0anh_0.58w/s	36.5	-	-	a=5.733 c=28.573	Al=0.0039 Ca=0.0112 S=0.0043 O=0.0202

Table 4.14. Refined unit cell and ADP values for aluminium hydroxide gel and AFm-n in the low r-range (1.6-35 Å) of samples of oSK-2017 obtained by the PDF analysis. R_W is also included. Taken from article #3 in Annex I. Reproduced by permission of ICE Publishing (Annex IV).

Sample (1.6 – 35 Å r-range)	R_W (%)	AH gel		AFm-n	
		Unit cell (Å)	ADP (Å^2)	Unit cell (Å)	ADP (Å^2)
oSK-2017_31anh_0.85w/s	24.7	a=8.724 b=4.990 c=9.558 β=95.0°	Al=0.0063 O=0.0065	-	-
oSK-2017_15.5anh_0.85w/s	32.2	a=8.585 b=5.036 c=9.750 β=93.9°	Al=0.0054 O=0.0042	-	-
oSK-2017_15.5anh_0.70w/s	29.4	a=8.621 b=5.036 c=9.723 β=94.3°	Al=0.0072 O=0.0050	-	-
oSK-2017_0.0anh_0.85w/s*	36.1	-	-	a=5.731 c=26.982	Al=0.0037 Ca=0.0042 S=0.0112 O=0.0027
oSK-2017_0.0anh_0.58w/s*	35.2	-	-	a=5.729 c=26.778	Al=0.0051 Ca=0.0050 S=0.0074 O=0.0033

* The PDF r-range was 1.6 to 65 Å.

The fit of the 30 to 50 Å PDF r-range for the sample oSK-2017_15.5anh_0.85w/s was performed using ettringite, unreacted ye'elimite and crystalline AFm (AFm-c). For the two latter phases, only the scale factors were refined due to their low content. The unit cell parameters for ettringite and the ADP values are displayed in Table 4.13. Then, the low r-region, 1.6 to 35 Å, was analysed and the converged R_W is displayed in Table 4.14. The contributions from nanocrystalline AH gel and the scale factor of nanocrystalline AFm (AFm-n) were computed. The used structural description for AFm-n was that obtained from the PDF fit for the oSK-2017_0.0anh_0.85w/s paste, see below. The final fits in different r-regions are displayed in Figure 4.31. Moreover, Table 4.14 exhibits the unit cell values and the final ADP values obtained for AH gel. Table 4.15 shows the phase contents and Spdiameter value for AH gel.

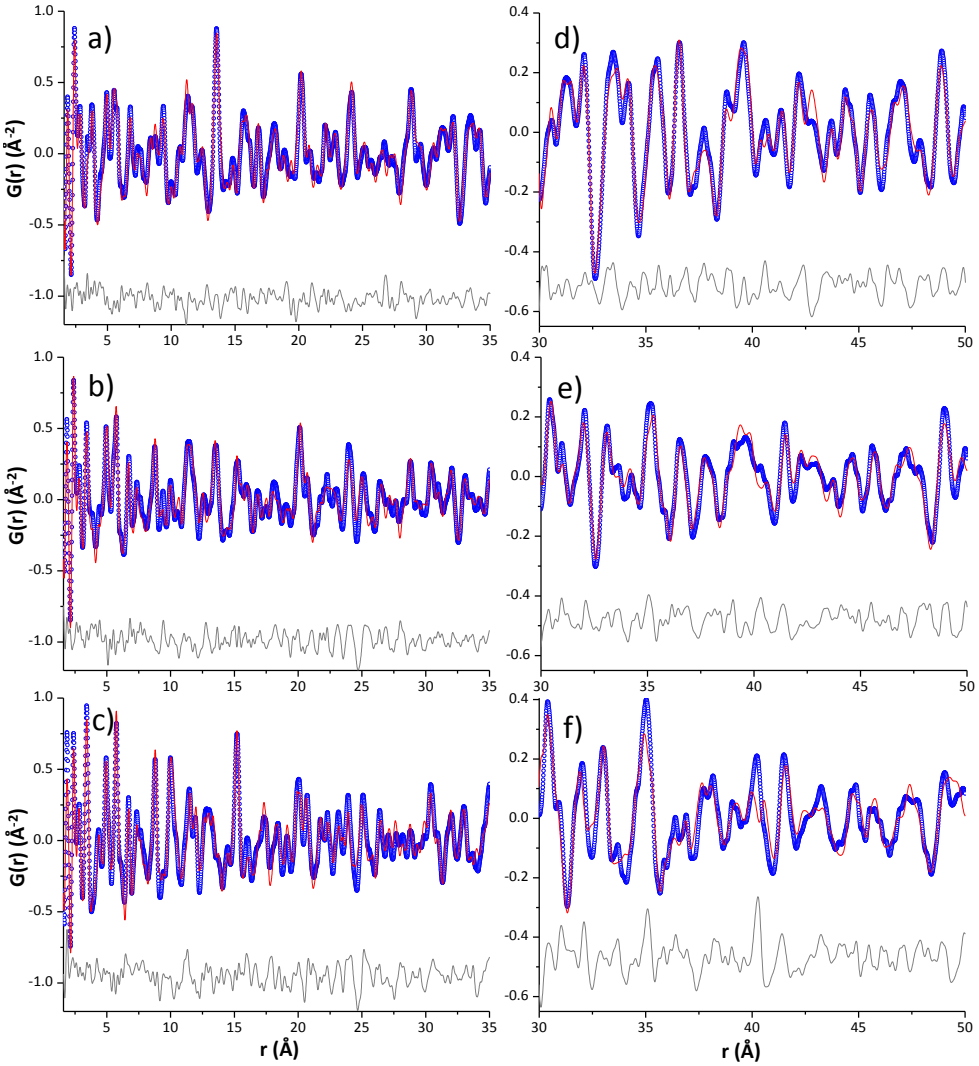

Figure 4.30. Experimental (blue circles) and fitted (red solid line) PDF patterns for a) and d) oSK-2017_31anh_0.85w/s; b) and e) oSK-2017_15.5anh_0.85w/s; and c) and f) oSK-2017_0.0anh_0.85w/s pastes hydrated at room temperature at low r-range: 1.6 to 35 Å a), b) and c); and high r-range: 30 to 50 Å d) e) and f). Difference curves are shown as grey lines. Adapted from article #3 in Annex I.

Table 4.15. Quantitative phase analysis results for the synchrotron PDF fits of the ye'elimite-2017 pastes. Spdiameter is also included for the nanocrystalline phases. Taken from article #3 in Annex I. Reproduced by permission of ICE Publishing (Annex IV).

Sample (low r-range)	R_w (%)	oSK (wt%)	AFt (wt%)	AFm-c (wt%)	AFm-n (wt%)	AH gel (wt%)	SpØ (Å)
oSK-2017_31anh_0.85w/s	24.7	5	62	-	-	33	35*
oSK-2017_15.5anh_0.85w/s	32.2	11	35	14	6	33	32*
oSK-2017_15.5anh_0.70w/s	29.4	15	35	10	7	34	29*
oSK-2017_0.0anh_0.85w/s	36.1	11	-	17	35	37	62#
oSK-2017_0.0anh_0.58w/s	35.2	17	-	15	32	36	64#

* Values related with the AH gel.
# Values related with the AFm-n.

PDF data of oSK-2017_15.5anh_0.70w/s were analysed as described just above for oSK-2017_15.5anh_0.85w/s. The unit cell parameters and ADP values for ettringite, the main phase, are also presented in Table 4.13. For this study, the unit cell parameters and ADPs for AH gel are included in Table 4.14. The quantitative phase analysis results and Spdiameter value for AH gel are also given in Table 4.15.

The particle size is related with Spdiameter parameter of the aluminium hydroxide gel. It can be found slightly differences in the Spdiameter values obtained by mixing ye'elimite with two different quantities of anhydrite and with two different water contents, oSK-2017_31.0anh_0.85w/s, oSK-2017_15.5anh_0.85w/s and oSK-2017_15.5anh_0.70w/s pastes, Table 4.15. On the one hand, aluminium hydroxide in the sample with higher amount of anhydrite and higher w/s, oSK-2017_31.0anh_0.85w/s, shows a slightly bigger crystal size than the other two pastes, maybe due to the quantity of sulphate source and the water content, while the unit cell parameters are very similar in the three pastes, see Tables 4.14 and 4.15. On the other hand, oSK_15.5anh_0.70w/s shows the lowest crystal size, Spdiameter, maybe due to the slightly lower anhydrite and water contents.

Consequently, the amount of anhydrite and w/s ratio in ye'elimite pastes seems to influence the particle size of aluminium hydroxide gel. The higher both parameters, the higher particle size.

The sample of ye'elimite without any sulphate source, oSK_0.0anh_0.85w/s, was analysed. PDF data shows that the main crystalline phase was AFm, named as AFm-c, which was computed for the high r-region, 30-50 Å. Moreover, the structure of ye'elimite was also introduced and its scale factor was refined. The final unit cell parameters for AFm-c are presented in Table

4.13. Subsequently, all parameters for the crystalline phases were kept fixed in the low r-region, 1.6-35 Å. This PDF region was fitted using the nanocrystalline gibbsite (aluminium hydroxide gel) obtained for the oSK_31anh_0.85w/s sample by refining only the scale factor. However, some misfits suggested the existence of another nanocrystalline phase. Consequently, a nanocrystalline AFm phase, named AFm-n, was also computed, where the relevant parameters were refined, i.e. scale factor, unit cell parameters, ADPs parameters and atomic positional coordinates excluding hydrogels (see Table 4.14). As the Spdiameter obtained for AFm in this region was larger than 35 Å, i.e. close to 60 Å, this r-region was expanded. A final refinement was performed in the r-region from 1.6 to 65 Å. Initially, the scale, unit cell and Spdiameter of nanocrystalline AFm were refined and also the scale factor of AH gel. Then, all the scale factors (including ye'elimite and AFm-c) were refined in the final fit. The unit cell parameters for AFm-n are given in Table 4.14. The quantitative phase analysis results and Spdiameter value for AFm-n are displayed in Table 4.15. The final fit is displayed in different r-regions, see Figure 4.31.

The influence of water content on the hydration of ye'elimite was studied by preparing oSK-2017_0.0anh_0.58w/s sample. This sample was analysed by PDF methodology with the same strategy as the previous sample with higher amount of water. The R_W, the unit cell parameters and ADPs for the main phase, AFm-c, obtained by fitting the 30 to 50 Å r-range are shown in Table 4.13. Then, the 1.6 to 65 Å r-region with the same components described above for oSK-2017_0.0anh_0.85w/s was fitted. The unit cell parameters and ADPs for AFm-n are given in Table 4.14. The phase contents and Spdiameter value for AFm-n are given in Table 4.15.

In the case of the pastes without sulphate source, oSK-2017_0.0anh_0.85w/s and oSK-2017_0.0anh_0.58w/s, the Spdiameter values are practically the same ~60 Å. Consequently, we can conclude that the water content does not have any effect on the crystal size of nanocrystalline AFm obtained in the hydration of ye'elimite, see Table 4.15. In addition, refined unit cell parameters and ADP values are also very similar, Table 4.14.

5. NEW ECO-CEMENTS – APPLIED SCIENCE

In this chapter, two new eco-cements, standard and doped ABY, have been synthesised in the laboratory and further characterised. The most important aim was to get eco-cements with comparable (or even higher) mechanical strengths than those developed by PC at any age, but emitting less carbon dioxide into the atmosphere in their production.

5.1. Optimisation of clinker synthesis

5.1.1. Goals

The main aim of this part was the clinkering, at relatively low temperature, of new eco-cements composed by alite, belite and ye'elimite as main phases, alite-belite-ye'elimite (ABY). The design of the raw mixture of this ABY clinker contains less amount of limestone which will contribute to a ~10% of reduction of CO_2 emissions due to decarbonation of the kilns, see Figure 1.3 in the Introduction section. Moreover, an extra reduction will be attained due to the lower clinkering temperature and the reduction of fuel and milling electricity, that makes the production of ABY clinkers to release ~17% less CO_2 than PC.

The research process was performed firstly by synthesising a standard ABY clinker (named as standard-ABY or ABY) with the maximum quantity of alite and ye'elimite using raw materials and some dopant agents. Secondly, another ABY clinker but with the activate forms of belite, α'_HC_2S, (named as doped-ABY or dABY) was prepared by adding different dopants, being borax the best one.

The clinkering and the corresponding scaling-up (to prepare 2 kg) have been gathered in three steps: firstly, synthesising 5 g of clinker and optimising the process (named as *sa*, from small amount); secondly, the raw material mixtures were reformulated to prepare a medium amount of 90 g (named as *ma*), and thirdly, 2 kg of both clinkers (named as *la* from large amount) were prepared. All of them, *sa*-, *ma*- and *la*- standard and doped ABY clinkers were characterised through LXRPD in combination with the Rietveld methodology, and FEG-SEM combined EDS. Finally, cements were prepared with the *la*-clinkers by adding anhydrite as sulphate source to control the hydration reactions.

5.1.2. Clinkering

First of all, to carry out the goal, small amounts of both clinkers (*sa*-ABY and sa-dABY), 5 g, were prepared. For that, the appropriated proportions of the raw materials (described in the Materials and Methods section) jointly with mineralisers, 1.0 wt% of ZnO and 1.0 wt% of CaF_2, as described in [70]. These percentages are referred to the total oxide compounds, including ZnO, present in the clinker. To get clinkers that present jointly alite and ye'elimite phases, the addition of CaF_2 to the raw materials was key. Thus, ZnO was also used to help in the formation of higher amounts of alite. The thermal treatment has been described in the Materials and Methods chapter. Table 5.1 gives the targeted composition of the desired standard ABY clinker, and also the mineralogical composition, determined by Rietveld method, of the as-prepared *sa*-ABY clinker. Further batches of 90 g (*ma*-ABY) and 2 kg (*la*-ABY) were prepared following the same clinkering procedure (same mixture of raw materials/mineralisers and clinkering cycle) but pellets of different size were used; viz. for the "small amount", *sa*-, 3 pellets of 3 g each were clinkered, for the "medium amount", *ma*-, 3 pellets of 35 g each were used, and for the "large amount", *la*-, 6 pellets of 35 g each were prepared. Figure 5.1 shows the Rietveld plot of the *la*-ABY clinker (after milling).

Table 5.1. Mineralogical composition of the lab-prepared standard-ABY clinkers obtained by RQPA. The targeted mineralogical composition is also included. Data taken from article #4 in Annex I. Copyright (2019) with permission from Elsevier (Annex IV).

Phases	*Targeted*	*sa*-ABY	*ma*-ABY	*la*-ABY
mC_3S	*45.0*	29.5(1)	37.5(2)	**41.5(2)**
βC_2S	*25.0*	44.3(2)	32.8(2)	**28.4(3)**
$oC_4A_3\bar{S}$	*20.0*	10.5(3)	10.0(3)	**9.3(3)**
$cC_4A_3\bar{S}$	-	7.3(3)	7.4(3)	**8.1(3)**
C_4AF	*5.0*	4.6(2)	4.1(1)	**3.8(1)**
C	*5.0*	-	0.5(1)	**0.4(1)**
C_3A	-	1.5(1)	0.4(1)	**0.3(1)**
$C_{12}A_7$	-	-	-	**0.6(1)**
CaF_2-$C_9S_3\bar{S}_3$	-	0.4(1)	4.2(2)	**4.3(2)**
CaO	-	-	1.2(1)	**1.9(1)**
MgO	-	-	1.0(1)	-
$C_2K\bar{S}_3$	-	1.8(1)	1.0(1)	**1.5(1)**

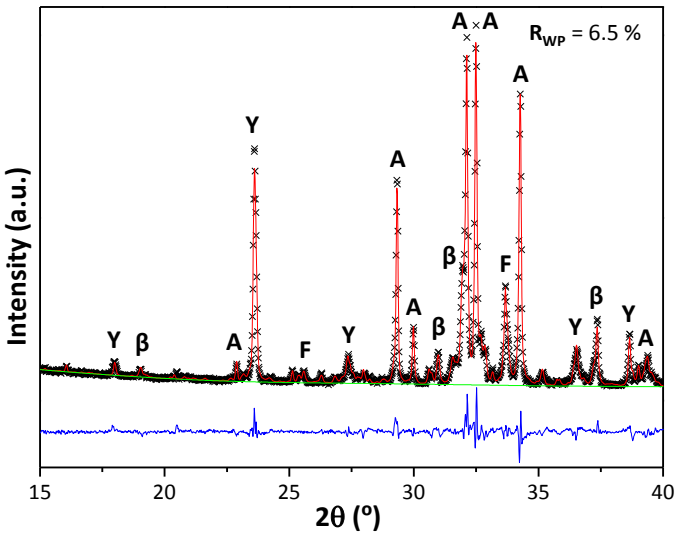

Figure 5.1. LXRPD Rietveld plot (CuKα_1 radiation, λ = 1.5406 Å) of *la*-ABY. R_{WP} value is also included and the main peaks are labelled as A=mC_3S, β= βC_2S, Y=$C_4A_3\overline{S}$, F=C_4AF. Taken from article #4 in Annex I. Copyright (2019) with permission from Elsevier (Annex IV).

Once the ABY clinker was prepared and characterised, the next step was to synthesise 5 grams of the doped ABY clinker, *sa*-dABY. Here, the main objective was to stabilise the α'_H polymorph of C_2S. To carry out this target, a deep study of the effect of different types and amounts of dopants (Na_2O, K_2O and B_2O_3) was performed. It has been previously described [40] that alkaline oxides stabilise alpha polymorphs (αC_2S and α'_HC_2S) in belite rich Portland clinkers. Nevertheless, the addition of 1.0 wt% of Na_2O (dABY_1N), added as Na_2CO_3, or 2.0 wt% of K_2O (dABY_2K), added as K_2CO_3, did not yield the stabilisation of any of the high temperature polymorphs of belite, see Table 5.2. These percentages are referred to the total oxide compounds, including Na_2O or K_2O, present in the clinker. Therefore, this strategy of activation was excluded.

Borax has been reported as an activator of belite sulphoaluminate clinkers [64, 118, 153, 154]. Therefore it was added, in different proportions, to the same mixture of raw materials used to prepare the *sa*-ABY clinker, until the highest quantity of mC_3S, α'_HC_2S and ye'elimite were obtained. According to previous studies [153, 154], the addition of 2.0 wt% of B_2O_3, added as borax, and referred to the total oxide compounds (including B_2O_3) present in the clinker, was high enough to stabilise all the dicalcium silicate as α'_HC_2S, in a clinker with more than 50 wt% of this phase. Therefore, the dABY clinker was prepared with 2.0 wt% of B_2O_3 and 0.9 wt% of Na_2O, added as borax, named hereafter as dABY_2B0.9N. The main problem was that the formation of mC_3S was hindered, as expected [155], see Table 5.2. Consequently, the amount of borax was reduced to half, 1.0 wt% of

B_2O_3 and ~0.5 wt% of Na_2O, obtaining the clinker dABY_1B0.5N, with a mixture of both belite polymorphs, α'_HC_2S and βC_2S, where the ratio β/α'_H was increased from 0.0 to 0.14, but mC_3S was still not present, Table 5.2.

Table 5.2. Mineralogical composition (in weight percentage), determined by Rietveld method, of *sa*-dABY clinkers doped with alkaline oxides and borax. Data taken from article #4 in Annex I. Copyright (2019) with permission from Elsevier (Annex IV).

Phases	*sa*-dABY_1N	*sa*-dABY_2K	*sa*-dABY_2B0.9N	*sa*-dABY_1B0.5N	*sa*-dABY_0.5B0.3N	*sa*-dABY_0.3B0.1N
mC_3S	31.6(2)	30.5(2)	-	-	**9.6(1)**	18.1(2)
βC_2S	44.9(2)	39.0(2)	-	9.0(3)	**49.4(2)**	52.1(2)
γC_2S	-	-	1.5(2)	0.5(1)	-	0.8(1)
α'_HC_2S	-	-	73.2(1)	64.7(1)	**15.1(3)**	3.9(4)
$oC_4A_3\bar{S}$	6.3(4)	5.2(3)	9.8(4)	6.4(4)	**7.4(2)**	8.8(3)
$cC_4A_3\bar{S}$	4.3(4)	5.4(3)	3.2(4)	3.0(4)	**6.0(3)**	7.4(3)
C_4AF	2.8(2)	3.7(1)	5.3(2)	3.8(1)	**4.5(2)**	4.0(1)
C_3A	1.5(1)	1.3(1)	2.2(1)	6.2(1)	**4.3(1)**	1.8(1)
$C_{12}A_7$	7.3(2)	7.6(1)	2.6(1)	3.1(1)	**0.5(1)**	-
CaF_2-$C_9S_3\bar{S}_3$	-	-	1.4(2)	1.9(1)	**1.2(2)**	1.2(2)
$C_2K\bar{S}_3$	1.3(1)	6.8(2)	1.0(1)	1.3(2)	**2.1(1)**	2.0(1)

Fluorite was used as mineraliser because it increases the primary crystallisation growth of C_3S [156]. Thus, the study of the addition of 1.5 and 2.0 wt% of CaF_2, referred to the total oxide compounds of the clinker, to the raw mixture with borax was performed to promote the formation of C_3S but maintaining the stabilising effect of boron on α'_H-polymorph of C_2S. Mineralogical compositions of these two resulting *sa*-clinkers prepared with fluorite (F), B_2O_3 (B) and Na_2O (N), named hereafter as dABY_1.5F_1B0.5N and dABY_2F_1B0.5N, are shown in Table 5.3. Nevertheless, this synthetic strategy was only partly successful as just 4.8 wt% of alite was formed in the clinker with the highest quantity of fluorite (2.0 wt%). Figure 5.2a gives the raw LXRPD patterns of these clinkers, where the main peaks are labelled, and Figure 5.2b shows the phase contents of alite, belite (β and α'_H) and ye'elimite in *sa*-dABY clinker batches when different amounts of CaF_2 were added. From the results, the strategy of increasing fluorite was discarded.

Table 5.3. Effect of calcium fluoride content (1.0, 1.5 and 2.0 wt%) on the phase assemblage of *sa*-dABY clinkers. Data taken from article #4 in Annex I. Copyright (2019) with permission from Elsevier (Annex IV).

Phases	*sa*-dABY_1F_1B0.5N	*sa*-dABY_1.5F_1B0.5N	*sa*-dABY_2F_1B0.5N
mC_3S	-	0.8(1)	4.8(2)
βC_2S	9.0(3)	12.2(3)	14.7(3)
γC_2S	0.5(1)	-	1.6(1)
$\alpha'_H C_2S$	64.7(1)	58.9(2)	50.1(2)
$oC_4A_3\bar{S}$	6.4(4)	4.6(3)	2.5(2)
$cC_4A_3\bar{S}$	3.0(4)	3.3(3)	2.0(2)
C_4AF	3.8(1)	4.5(2)	4.5(2)
C	6.2(1)	1.0(1)	1.5(1)
C_3A	3.1(1)	4.7(2)	2.1(2)
$C_{12}A_7$	1.9(1)	6.3(1)	10.9(1)
CaF_2-$C_9S_3\bar{S}_3$	1.3(2)	2.6(1)	4.1(1)
$C_2K\bar{S}_3$		1.0(1)	1.1(1)

Therefore, the amount of B_2O_3 was reduced to 0.5 and 0.3 wt%, maintaining 1.0 wt% of CaF_2, to assure the formation of alite [70]. The belite β/α'_H ratio increased as the percentage of boron oxide decreased, see Table 5.2. The addition of 0.3 wt% B_2O_3 was not desirable as the obtained β/α'_H ratio was ~13. Finally, the addition of 0.5 wt% of B_2O_3 allowed the preparation of a clinker containing the three main targeted phases, with 15 wt% of $\alpha'_H C_2S$, 10 wt% of mC_3S and 13 wt% of ye'elimite, see Table 5.2. The clinkers obtained with this methodology are belite rich ones as the C_2S contents are always higher than the alite quantities. However, the same nomenclature used for the standard clinkers, ABY, has been used for doped materials, i.e. dABY.

By increasing the B_2O_3 content (using borax), from 0.3 to 2.0 wt% (maintaining 1.0 wt% of CaF_2 in all samples), respect to the total oxide compounds including B_2O_3, the amounts of alite and βC_2S decrease, $\alpha'_H C_2S$ contents increases significantly and ye'elimite is kept almost constant, see Figure 5.3b.

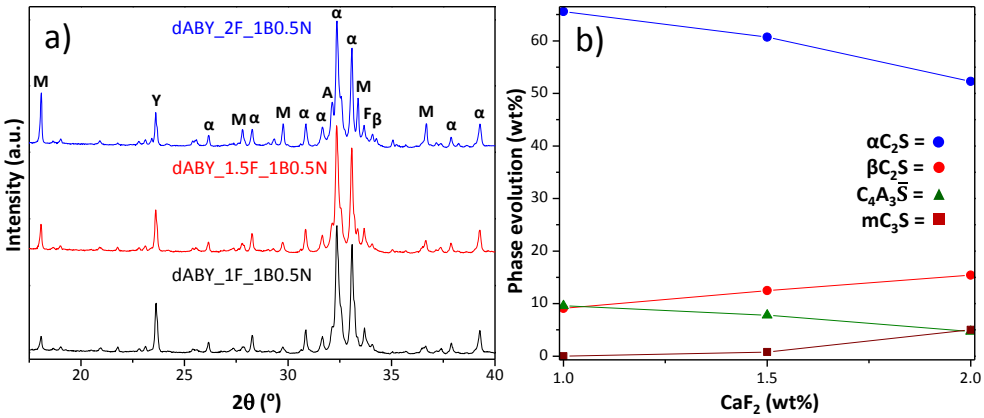

Figure 5.2. a) LXRPD of *sa*-dABY clinkers prepared with different amounts of CaF_2, with the main peaks labelled as: α= $\alpha'_H C_2S$, β= βC_2S, A=mC_3S, Y=$C_4A_3\bar{S}$, M=$C_{12}A_7$, F=C_4AF. b) Phase contents of the four main crystalline phases of the clinkers as a function of CaF_2 content. Adapted from article #4 in Annex I. Copyright (2019) with permission from Elsevier (Annex IV).

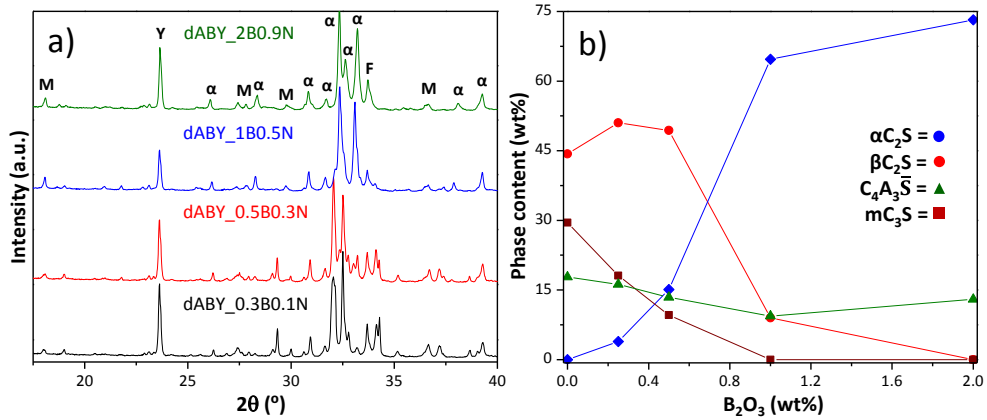

Figure 5.3. a) LXRPD of *sa*-dABY clinkers prepared with different amounts of borax with the main peaks labelled as: α= $\alpha'_H C_2S$, Y=$C_4A_3\bar{S}$, M=$C_{12}A_7$, F=C_4AF. b) Phase contents of the four main crystalline phases of the clinkers as a function of B_2O_3 content. Adapted from article #4 in Annex I. Copyright (2019) with permission from Elsevier (Annex IV).

From these studies, *sa*-dABY_0.5B0.3N was selected to prepare 90 g of this clinker (medium scale, *ma*-). The synthesis strategy was detailed in the Materials and Methods section but it is summed up here: 3 pellets of 35 g each, and the same clinkering cycle was followed (heated at 5 °C/min up to 900°C and holding for 30 min, increased up to 1300°C for 15 min at 5 °C/min and quenched). Table 5.4 gives the mineralogical composition obtained by this intermediate step for this composition, i.e. *ma*-dABY_0.5B0.3N. Unfortunately, the amount of $\alpha'_H C_2S$ was reduced by half when compared to the previous *sa*-clinker, likely due to the higher mass of material. Therefore, the amount of B_2O_3 was again optimised

under these experimental conditions. The increase of boron oxide from 0.5 wt% to 0.8 wt%, *ma*-dABY0.8B0.4N, produced a decrease of the belite β/α'_H ratio down to 0.8 and the amount of ye'elimite was also lower, see Table 5.4 and Figure 5.4.

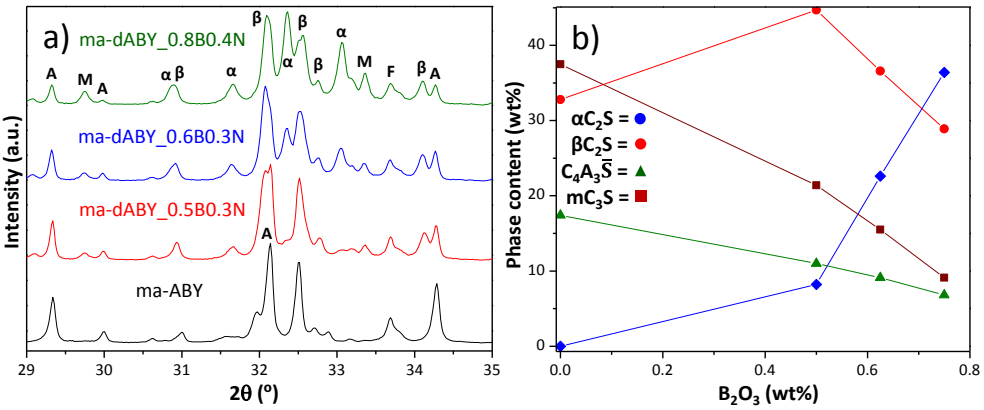

Figure 5.4. a) LXRPD of *ma*-dABY clinkers prepared with different amounts of boron, with the main peaks labelled as: $\alpha=\alpha'_HC_2S$, $\beta=\beta C_2S$, $A=mC_3S$, $Y=C_4A_3\bar{S}$, $M=C_{12}A_7$, $F=C_4AF$. b) Phase contents of the four main crystalline phases of the clinkers as a function of B_2O_3 content. Adapted from article #4 in Annex I. Copyright (2019) with permission from Elsevier (Annex IV).

Table 5.4. Mineralogical composition (in weight percentage) determined by RQPA of dABY clinkers doped with different amounts of borax. Taken from article #4 in Annex I. Copyright (2019) with permission from Elsevier (Annex IV).

Phases	*ma*-dABY 0.5B0.3N	*ma*-dABY 0.8B0.4N	*ma*-dABY 0.6B0.3N	*la*-dABY 0.6B0.3N
mC_3S	21.4(2)	9.1(2)	15.5(2)	**15.7(2)**
βC_2S	44.7(2)	28.9(3)	36.6(2)	**41.8(2)**
α'_HC_2S	8.2(3)	36.4(2)	22.6(3)	**18.0(3)**
$oC_4A_3\bar{S}$	6.0(2)	3.4(2)	5.9(5)	**2.9(2)**
$cC_4A_3\bar{S}$	5.0(2)	3.4(2)	3.2(5)	**4.8(2)**
C_4AF	3.8(1)	3.1(1)	3.3(1)	**3.2(1)**
C_3A	1.7(1)	3.4(2)	2.6(2)	**2.4(2)**
$C_{12}A_7$	5.5(1)	7.3(1)	4.7(1)	**6.6(1)**
CaO	-	-	1.0(1)	**1.0(1)**
CaF_2-$C_9S_3\bar{S}_3$	3.5(2)	4.2(2)	3.6(2)	**3.1(2)**
$C_2K\bar{S}_3$	1.2(1)	0.9(1)	0.8(1)	**0.6(1)**

Consequently, 0.6 wt% of B_2O_3 (and 0.3 wt% Na_2O) was selected for the production of 2 kg of clinker (large amount, or *la*-). The scaling-up procedure consisted on the preparation of batches of 6 pellets of 35 g each, and to repeat it for several times until all the raw mixture was used (3 kg). Table 5.4 also gives the final mineralogical composition of *la*-dABY (with 0.6 wt% of B_2O_3), *la*-

dABY0.6B0.3N. Figure 5.5 shows the Rietveld plot of this dABY clinker, where the main peaks are labelled, and the R_{WP} value of this sample is also shown.

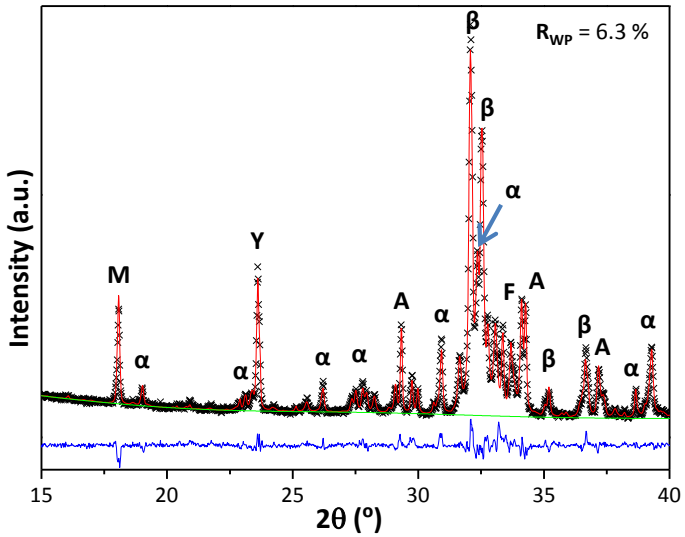

Figure 5.5. LXRPD Rietveld plot (CuKα_1 radiation, λ = 1.5406 Å) of *la*-dABY. R_{WP} value is also included and the main peaks are labelled as A=mC_3S, β=βC_2S, α=α'$_H C_2S$, Y=$C_4A_3\bar{S}$, F=C_4AF, M=$C_{12}A_7$. Taken from article #4 in Annex I. Copyright (2019) with permission from Elsevier (Annex IV).

Once 2 kg of both clinkers, *la*-ABY and *la*-dABY, were prepared, they were vibration-disc milled to obtain similar media particle sizes. Figure 5.6 shows the PSD after milling. From the PSD, it can be seen that *la*-ABY powder shows a trimodal behaviour (peaks are centred at ~0.7, ~9 and ~60 µm), and the *la*-dABY sample has a bimodal behaviour (peaks are centred at ~0.7 and ~10 µm). The values of $D_{v,10}$, $D_{v,50}$ and $D_{v,90}$ of both powders are also included as insets of Figures 5.6a and b. In addition, the surface area values obtained by BET and the corresponding Blaine values are also included in Figure 5.6. The $D_{v,50}$ value of *la*-dABY is higher than the corresponding for *la*-ABY; this is in agreement with its lower values of specific density (BET and Blaine). BET method gives more reliable results than Blaine method because it includes internal surfaces present in microcracks or in pores open only at one end [157]. The SEM micrographs of both clinker powders after milling are shown in Figures 5.6c and d, where the average particle size of the *la*-dABY clinker is bigger.

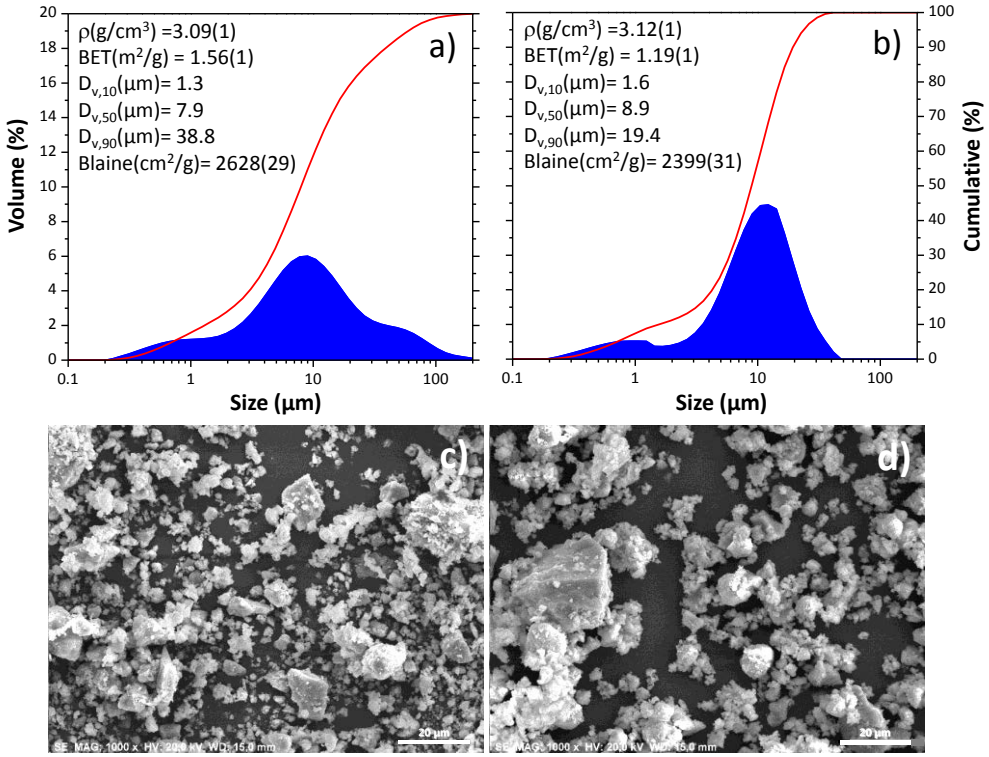

Figure 5.6. PSD plots of a) *la*-ABY and b) *la*-dABY clinkers after milling. Density (ρ), Blaine, BET area data and particle sizes are given as insets. SEM micrographs of c) la-ABY and d) *la*-dABY clinker powders after milling. Adapted from article #5 in Annex I. Copyright (2019) with permission from Elsevier (Annex IV).

5.1.3. Microstructural analysis of *la*-clinkers

On the one hand, non-polished pellets of *la*-clinkers were analysed by SEM. Figures 5.7a and d show the micrographs of the external surface and Figures 5.7b, c, e and f show the fracture for *la*-ABY (left) and *la*-dABY (right) clinkers. The particles have been identified according to their representative size and form as mC_3S, C_2S (α'_H and β polymorphs), ye'elimite and ferrite crystals. Two main conclusions can be drawn from this study:

i) *la*-ABY clinker is more porous than *la*-dABY, Figures 5.7a and d. This is mainly due to the addition of borax in the latter which decreased the liquid phase appearance temperature [155] and favoured the growth of the primary particle size.

ii) C_2S, which is present as rounded particles, is detected in both clinkers, with particle sizes lower than 5 µm in *la*-ABY and about 10 µm in *la*-

dABY, Figures 5.7b,c and e,f, respectively. Furthermore, alite was presented as irregular angular crystals of ~30 µm in both clinkers (Figures 5.7b, c and d). The elongated shape of alite observed in *la*-ABY was also detected in a previous work [70], and it was attributed to the presence of ZnO (Figures 5.7b and c). Nevertheless, the addition of B_2O_3 seems to have hampered the development of this elongated shaped mC_3S, favouring slightly larger angular particles.

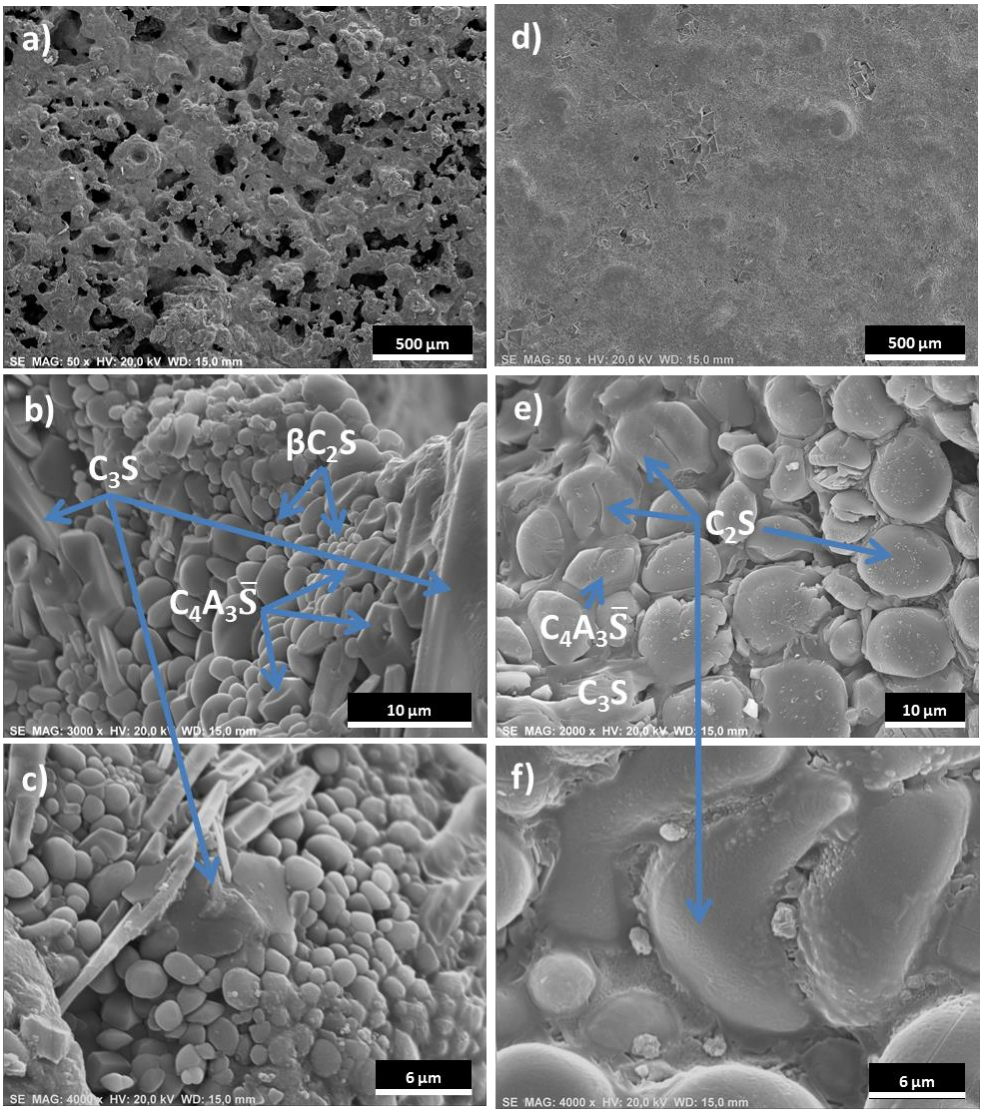

Figure 5.7. SEM micrographs of *la*-ABY (a, b, c) and *la*-dABY (d, e, f) at different magnifications, being a) and d) the external surface and b), c), e) and f) the fracture surface. The main crystalline phases are labelled in the images. Adapted from article #4 in Annex I. Copyright (2019) with permission from Elsevier (Annex IV).

On the other hand, polished *la*-ABY and *la*-dABY clinkers were analysed by EDS in the FEG-SEM microscope. The beam interaction volume is 1-2 μm^3, so the data have to be taken with caution. Figure 5.8 gives two triangle plots representing Al+Fe, Ca+Mg and Si+S atomic percentages for every measurement in each *la*-clinker. The theoretical values of these parameters for stoichiometric phases are also represented as solid red symbols (square for mC_3S, circle for C_2S, up-triangle for ye'elimite, rhombus for C_4AF, and down-triangle for fluor-ellestadite). The analysed points have naturally clustered surrounding the stoichiometric values, dashed red circles in Figure 5.8, indicating that these points should be assigned to that phase.

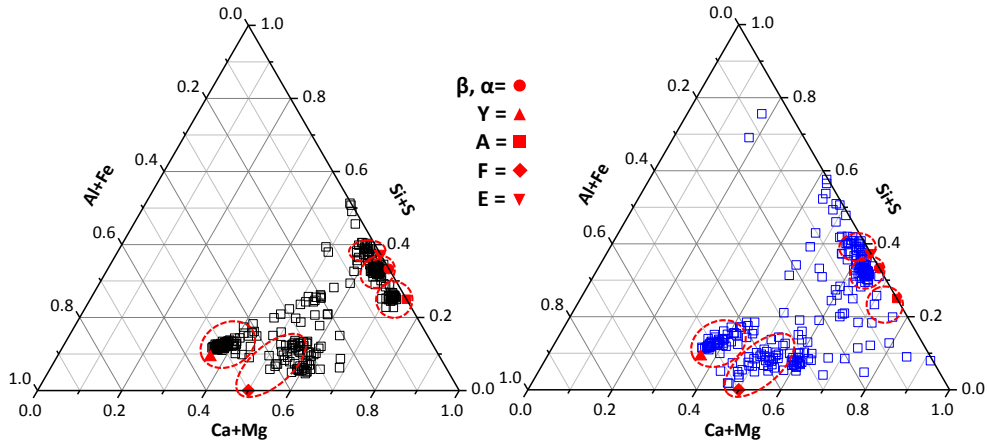

Figure 5.8. Triangle plots of EDS measurements of ABY (black empty symbols) and dABY (blue empty symbols) where Al+Fe, Si+S and Ca+Mg atomic percentages are represented. Red solid symbols stand for the theoretical values for stoichiometric phases. Red square: alite; red circle: belite; red triangle: ye'elimite; red rhombus: ferrite; down-triangle for fluor-ellestadite. Dashed circles: clusters of particles due to a given phase. Adapted from article #4 in Annex I. Copyright (2019) with permission from Elsevier (Annex IV).

Figure 5.9 shows two polished cross-section FEG-SEM micrographs with their respective elemental mapping, for *la*-ABY and *la*-dABY, which correlate the chemistry with the main crystalline phases, as an example. The shape and size of the particles match rather well with the phase assignation.

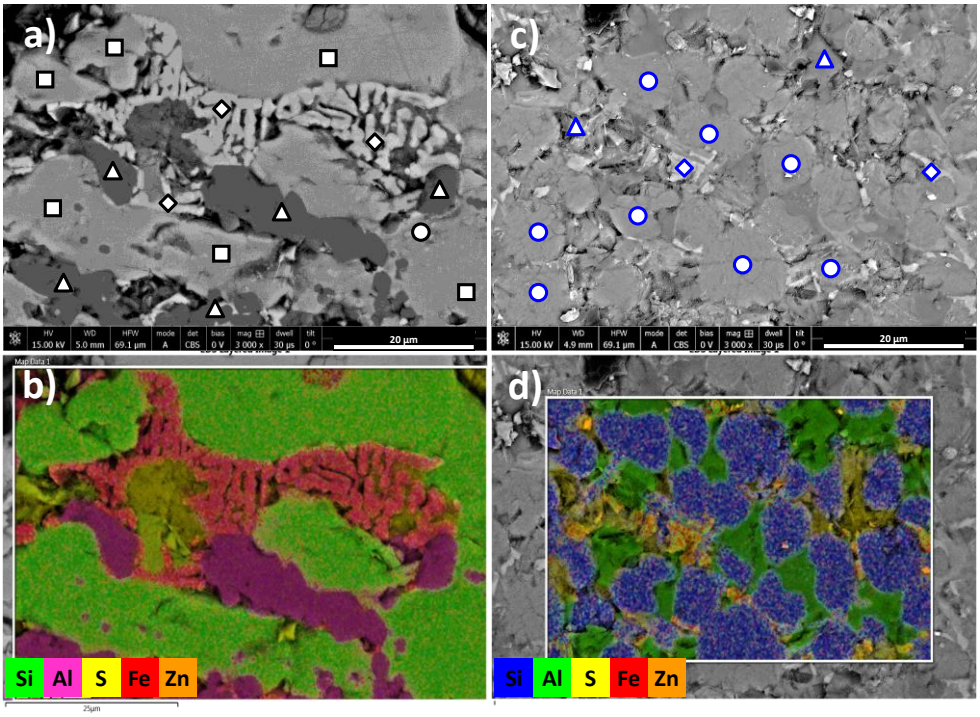

Figure 5.9. Polished cross-section FEG-SEM micrographs of a) *la*-ABY and c) *la*-dABY. Symbols represent the main crystalline phases: squares: alite; circle: belite; triangle: ye'elimite; rhombus: ferrite. b) and d) present the elemental mapping for each *la*-clinker. Adapted from article #4 in Annex I. Copyright (2019) with permission from Elsevier (Annex V).

A previous study [70] stated ZnO as a promoter of the alite formation. Figure 5.10a shows the zinc vs. fluorine atomic percentages and Figure 5.10b shows the iron vs. sulphur atomic percentages from EDS measurements for both *la*-clinkers. Here, the same symbol labelling, as in Figure 5.8, has been used. The stoichiometric values have also been included for the sake of comparison. It can be highlighted that fluor-ellestadite contains the highest amount of fluorine, as expected, and alite presents higher presence of fluorine and zinc than belite (α'_H and β polymorphs), as expected [70]. Moreover, both clinkers showed the same tendency. Furthermore, sulphur is mostly incorporated into fluor-ellestadite, ye'elimite (as expected) and, in lower percentages, in belite (both α'_H and β polymorphs) and ferrite [158].

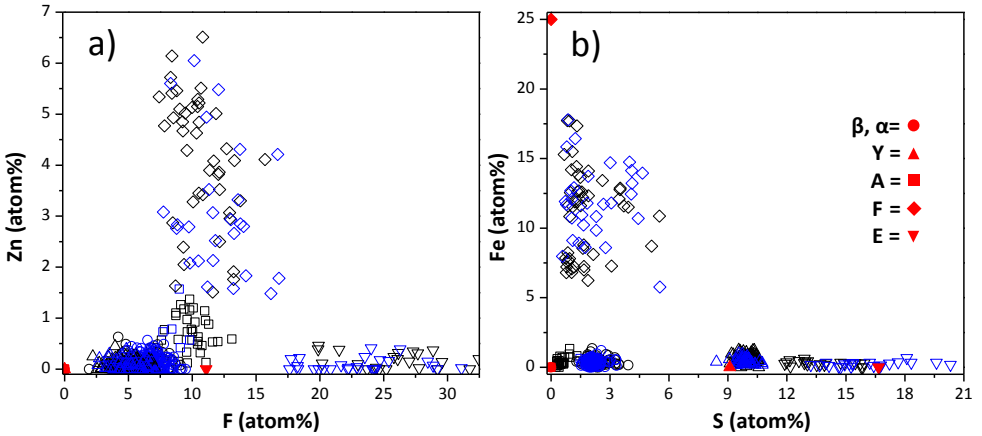

Figure 5.10. EDS measurements: a) Zn vs. F and b) Fe vs. S in atomic % of *la*-ABY (black symbols) and *la*-dABY (blue symbols). Symbols represent the main crystalline phases: squares: alite; circle: belite; triangle: ye'elimite; rhombus: ferrite. Taken from article #4 in Annex I. Copyright (2019) with permission from Elsevier (Annex IV).

From this EDS study, experimental formulations for alite and belite were determined. To do so both EDS analysis were used to calculate the chemical composition of alite. It was assumed that Mg^{2+} substitutes Ca and that Al^{3+} was placed in both the Ca and Si sites [159] giving $Ca_{2.64}Mg_{0.06}Al_{0.05}(Si_{0.95}Al_{0.05})O_{4.75}$ formula. To calculate the belite chemical composition in *la*-ABY and *la*-dABY, Al^{3+} and sulphur was assumed to substitute Si [160] giving $Ca_{1.79}(Si_{0.85}Al_{0.08}S_{0.07})O_{3.81}$ chemical formula. Unfortunately, in the EDS analysis of *la*-dABY it was not possible to distinguish between β and α'_H belites, consequently only one formula was obtained for the belite present in both clinkers.

5.1.4. Elemental and mineralogical composition of the final clinkers

A final characterisation of both *la*-clinkers is presented below. Firstly, RQPA including the ACn content was performed, see Table 5.5. Moreover, elemental analysis obtained from XRF and ICP, the latter to determine the quantity of sulphur and sodium was carried out, Table 5.6. A good exercise to characterise the clinkers is to correlate the elemental composition obtained directly by XRF and ICP with the derived elemental composition calculated from RQPA including the ACn content and with the elemental composition of the starting raw materials, also included in Table 5.6.

Table 5.5. Mineralogical composition (in weight percentage) determined by RQPA (using MoKα_1 radiation, λ = 0.7093 Å) of *la*-ABY and *la*-dABY clinkers, including the ACn. Data taken from article #4 in Annex I. Copyright (2019) with permission from Elsevier (Annex V).

Phases	*la*-ABY	*la*-dABY
mC_3S	32.6(3)	14.4(3)
βC_2S	30.4(4)	37.1(4)
$\alpha'_H C_2S$	-	18.5(5)
$oC_4A_3\bar{S}$	9.8(8)	2.8(7)
$cC_4A_3\bar{S}$	5.8(8)	4.7(7)
C_4AF	4.3(2)	3.9(2)
$C_{12}A_7$	1.2(1)	7.7(2)
CaF_2-$C_9S_3\bar{S}_3$	3.5(3)	4.2(4)
ACn	12.6(2)	6.6(2)

Firstly, by analysing Table 5.6, it can be deduced that part of the sulphur was lost during the clinkering of both materials. Therefore, as all the elemental composition was normalised to 100 wt%, the residual element contents seem to be partially overestimated when compared to the nominal composition.

Table 5.6 also includes the derived elemental composition calculated from RQPA, by using the chemical formulas for alite and belite obtained in the EDS study. Consequently, the elemental composition of the ACn can be estimated by comparing the differences between the elemental composition obtained from XRF & ICP and the derived elemental composition from RQPA, also included in Table 5.6. The negative value of the SiO_2 in ACn for *la*-dABY can be related with the semi-quantitative EDS analyses, which gave an approximate stoichiometry for mC_3S and βC_2S. In order to properly compare the chemical nature of both ACn contents for the *la*-clinkers, the data from this table have been renormalised to 100 wt% of oxides and not taking into account the negative values; the resulting values are presented in Table 5.7. It is important to highlight that these values indicate that the elemental composition of ACn is close to amorphous calcium aluminate in both clinkers. Nevertheless, *la*-dABY (amorphous phase) contains a slightly higher amount of minor elements different from Ca and Al, i.e. Zn or Mg. In addition, the amount of ACn content in both clinkers is also low and similar, considering that the quantification of amorphous contents below 10 wt% are subjected of high errors [161].

Table 5.6. Direct (from XRF and ICP) and derived (from LXRPD) elemental analyses, expressed as oxide weight percentages, of *la*-ABY and *la*-dABY clinkers. Taken from article #4 in Annex I. Copyright (2019) with permission from Elsevier (Annex IV).

	***la*-ABY**				***la*-dABY**			
	Nominal Elemental Composition	**XRF & ICP**	**Crystalline fraction from LXRPD#**	**Amorphous fraction from LXRPD***	**Nominal Elemental Composition**	**XRF & ICP**	**Crystalline fraction from LXRPD#**	**Amorphous fraction from LXRPD***
				wt%				
CaO	58.9	58.9	51.6	7.3	58.4	58.6	55.2	3.3
SiO_2	19.8	20.1	19.0	1.1	19.8	19.8	22.1	-2.3
Al_2O_3	10.7	12.3	10.9	1.4	12.2	12.2	9.9	2.3
SO_3	5.4	3.6	3.9	-0.3	5.3	3.4	3.2	0.2
Fe_2O_3	1.6	1.5	1.4	0.1	1.6	1.6	1.3	0.3
MgO	0.8	1.1	0.4	0.7	0.8	1.1	0.2	0.9
ZnO	1.0	1.0	-	1.0	1.0	1.0	-	1.0
K_2O	0.8	0.5	-	0.5	0.8	0.5	-	0.5
Na_2O	-	0.0	-	-	0.3	0.3	0.5	-0.2
CaF_2	1.0	1.0	0.3	0.7	1.0	1.0	0.3	0.7
B_2O_3	-	0.0	-	-	0.6	0.6	0.6	-
Total	100	100	87.4	12.6	100	100	93.4	6.6

* Elemental composition of ACn fraction = elemental composition from XRF&ICP – elemental composition of the crystalline fraction

Stoichiometric phases have been used for calculations, except: $Ca_{2.64}Mg_{0.06}Al_{0.05}(Si_{0.95}Al_{0.05})O_{4.75}$ for alite and $Ca_{1.79}(Si_{0.85}Al_{0.08}S_{0.07})O_{3.75}$ for βC_2S, both obtained from the EDS-FEG-SEM study, and $Ca_{1.85}Na_{0.15}(SiO_4)_{0.85}(BO_3)_{0.15}$ for $\alpha'_H C_2S$ from [162].

Table 5.7. Derived (from LXRPD) elemental analyses, expressed as oxide weight percentages of the amorphous fraction of *la*-ABY and *la*-dABY clinkers normalised to 100 wt%. Taken from article #4 in Annex I. Copyright (2019) with permission from Elsevier (Annex IV).

	***la*-ABY**	***la*-dABY**
	wt%	
CaO	57	36
SiO_2	9	-
Al_2O_3	11	25
SO_3	-	2
Fe_2O_3	1	3
MgO	5	10
ZnO	8	11
K_2O	4	5
Na_2O	-	-
CaF_2	5	8
B_2O_3	-	-
Total	100	100

Last but not least, a MAS-NMR solid state study was performed to check the differences between both *la*-clinkers, if any. ^{29}Si MAS NMR and ^{27}Al MAS NMR spectra were recorded and analysed, see Figure 5.11. The Q^0 signal of belite is

much broader in *la*-*d*ABY than in *la*-ABY, see blue deconvoluted curve in Figure 5.11. This indicates a higher degree of disorder in the former; that is related to the addition of boron [155] to the raw mixture, which will also affect the further hydration of belite forms. From Figures 5.11c and 5.11d, it can be seen how the signal of Al(IV) corresponding to ye'elimite is very similar in both clinkers. Thus, the most relevant difference between both figures is the higher content of $C_{12}A_7$ in *la*-dABY clinker, which is in agreement with the results obtained through RQPA, see Table 5.5.

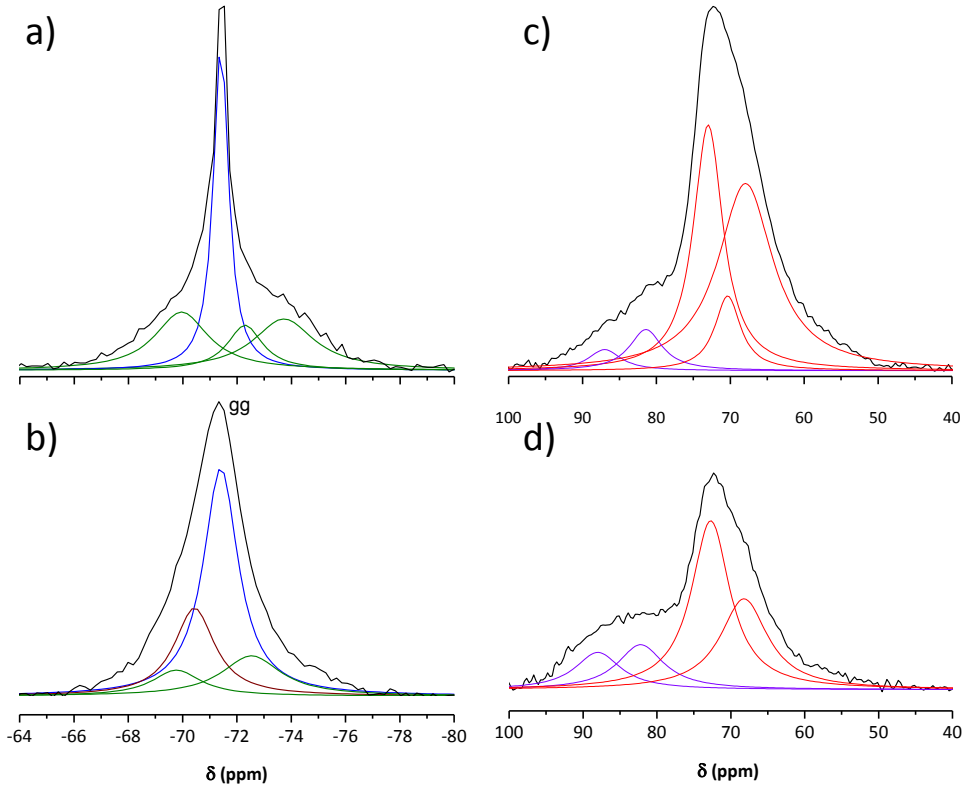

Figure 5.11. ^{29}Si MAS-NMR spectra for *l*a-ABY and *la*-dABY (a and b, respectively) and ^{27}Al MAS NMR spectra (c and d, respectively) with the deconvoluted signals included. Blue Q^0 for βC_2S, brown Q^0 for α'_HC_2S, green Q^0 for mC_3S in ^{29}Si MAS-NMR; red Al(IV) for ye'elimite and purple Al(IV) for $C_{12}A_7$.

5.2. Processing, Hydration & Mechanical properties

ABY and dABY cements were prepared by mixing *la*-ABY and *la*-dABY clinkers with 14 wt% of anhydrite, as detailed in the Materials and Methods

section. This percentage is referred to the cement weight. Table 5.8 gives the phase assemblage of both anhydrous cements, including the ACn.

Figure 5.12 gives the particle size distribution of the resulting cements. Density, BET and Blaine area data, and particle size values are also included as insets. A trimodal PSD was observed in both cements.

Table 5.8. Mineralogical composition (in weight percentage), determined by RQPA, of both cement powders, including ACn.

Phase Contents	ABY (wt%)	dABY (wt%)
mC_3S	25.9(3)	9.3(3)
βC_2S	22.8(4)	26.3(4)
α'_HC_2S	-	13.8(4)
$C_4A_3\bar{S}$*	12.2(6)	5.6(3)
C_4AF	3.4(2)	2.3(2)
$C\bar{S}$	13.5(5)	13.8(1)
$C_{12}A_7$	-	4.8(1)
CaO	0.5(1)	-
MgO	0.7(1)	-
CaF_2-$C_9S_3\bar{S}_3$	1.7(2)	1.9(2)
ACn	19(1)	22(1)

*Total ye'elimite, 5.6(6) wt% of orthorhombic and 6.6(6) wt% of cubic for ABY and 2.1(3) wt% of orthorhombic and 3.5(3) wt% of cubic for dABY.

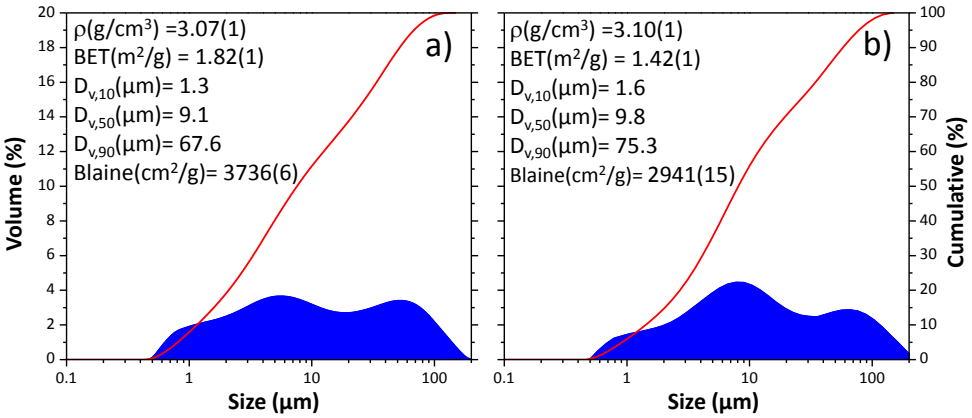

Figure 5.12. PSD plots of both cement powders after mixing with anhydrite a) ABY and b) dABY. Density (ρ), BET and Blaine area data and particle size values are given as insets.

5.2.1. Goals

This chapter studies the hydration of both (ABY and dABY) cements and mortars at 0.40 and 0.50 water-to-cement (w/c) mass ratios through the combination of different techniques. An *in-situ* study of the first hydration hours

was performed (using w/c mass ratio of 0.50). Moreover, these results were compared with the ones obtained by an *ex-situ* hydration study at larger hydration ages. The main aim of this part was to prove that the active form of belite ($\alpha'_H C_2S$) hydrates at a higher pace than the β-form, and consequently, it will develop higher mechanical properties. The challenge here is to unravel the hydration mechanism of these cements, the effect of w/c mass ratio and to check its impact on the corresponding mechanical properties. The behaviour of the cement pastes at very early-ages was investigated through rheology, calorimetry, SXRPD and LXRPD. RQPA was the main technique used to investigate the content of crystalline and ACn phases in pastes (in *in-situ* and *ex-situ* studies). Thermogravimetric analysis (DTA-TGA) was employed to confirm the mineralogy of the pastes and to determine the chemically bounded water.

A second objective of this work is the preparation of mortars with these ecocements that show comparable mechanical properties to those of PC. Because of that, the preparation of the fresh ABY and dABY pastes was optimised through rheological measurements (of the pastes) in terms of superplasticiser content and w/c ratio optimisation. The evolution of the phase assemblage during hydration was controlled through LXRPD, and the compressive strengths of the corresponding mortars were measured and discussed according to the processing parameters and phase assemblage. Finally, the processing parameters resulted to be the key to develop high mechanical strength values.

5.2.2. Hydration understanding of Alite-Belite-Ye'elimite cements

5.2.2.1. Early hydration age of fresh pastes: first 24 hours

A preliminary hydration study was performed with both cements to unravel their hydration kinetics and their behaviour.

Figure 5.13 shows the flow curves of both cement pastes prepared at w/c=0.50 (without SP), where both of them show a shear thinning behaviour. During the first minutes of hydration, the ABY paste shows higher viscosity and thixotropic cycle than the dABY one (as an example, viscosity values of 1.8 and 1.1 Pa·s at 100 s^{-1}, taken from the down-curves, and thixotropic cycles of 5201 and 2202 Pa/s, were measured for ABY and dABY, respectively). The higher viscosity of the ABY paste at this very early hydration time (without SP) may be due to the slightly higher Blaine and BET specific surface values, which are related with a

lower particle size of this cement and thus, more interactions between particles (Figure 5.12) compared to dABY. Furthermore, the slightly higher amount of total ye'elimite, see Table 5.8, is also affecting. These facts may be related with a quicker dissolution of certain phases, mainly ye'elimite and anhydrite, under the first 5 min of hydration.

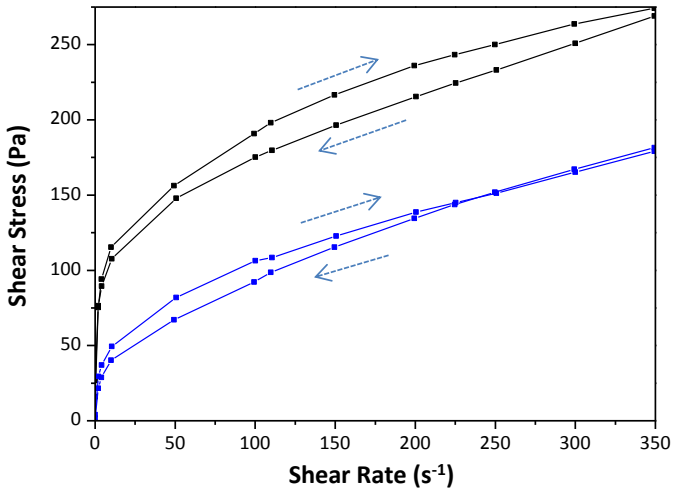

Figure 5.13. Flow curves for ABY (black) and dABY (blue) pastes at w/c mass ratio of 0.50. Taken from article #6 in Annex I.

Nevertheless, 10 minutes after hydration, the viscosity of the dABY paste suffers a harsh increase, which is much higher than that for the ABY paste, see Figure 5.14. This figure shows the evolution of viscosity with time, at the shear rate of 5 s^{-1}. This shear rate was selected because it is high enough to obtain trustable values, but low enough for not destroying/or minimum alteration of the paste structure. The quick increase in viscosity is in agreement with the higher cumulative heat released by dABY up to 3 hours of hydration, see also Figure 5.14. This behaviour can be explained through the higher dissolution/reactivity degree of some crystalline phases. Tables 5.9 and 5.10 show the phase assembly of both pastes (w/c=0.50) obtained from the *in-situ* SXRPD (up to 14 hours of hydration) and also at 1, 7, 28 and 90 days of hydration, obtained with *ex-situ* LXRPD, respectively. Figures 5.15 and 5.16 show some selected times of SXRPD and LXRPD patterns of ABY and dABY cement pastes, respectively. Analysing Tables 5.9 and 5.10, it is important to highlight that the presence of $C_{12}A_7$ in dABY cement is the responsible of the fast formation of ettringite and the higher increase of viscosity within the first 30 minutes of hydration [163], see Table 5.10 and Figure 5.14.

Figure 5.14 also presents the degree of reaction of mC_3S of both pastes (w/c=0.50) within the first 14 hours of hydration determined with the data given in Tables 5.9 and 5.10. As it is observed, the degree of hydration of alite in the

dABY cement paste, which contains less amount of total ye'elimite, is always higher than in ABY cement paste, see Table 5.9 and Figure 5.14. It has been previously reported [164] that the higher the amount of ye'elimite, the slower the reactivity of alite. Our results are in agreement with this statement.

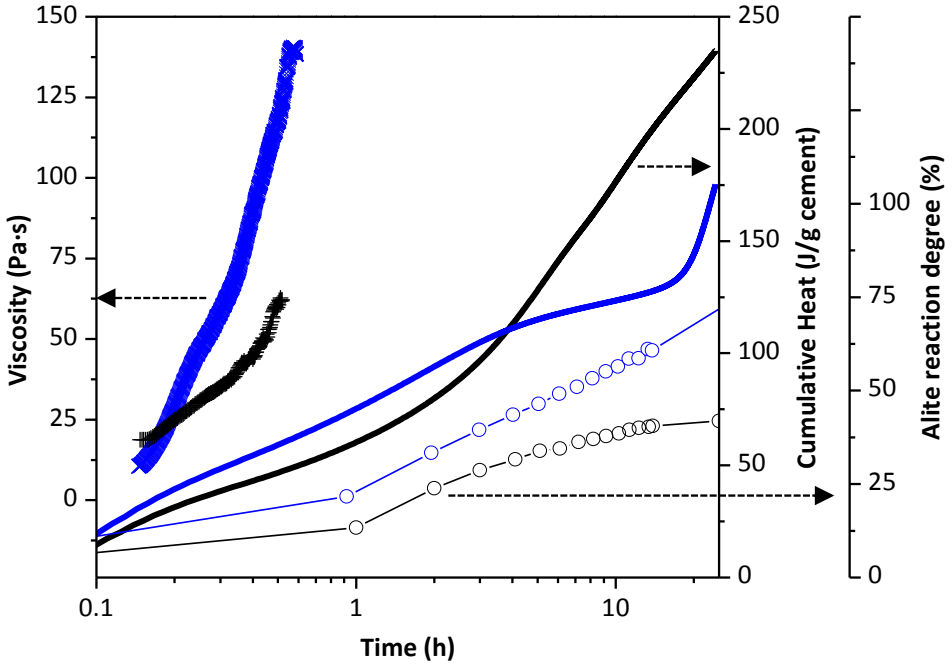

Figure 5.14. Viscosity as a function of time at the shear rate of 5 s^{-1} (left axis, crosses), cumulative heat (right axis, dashed lines) and alite degree of reaction (right axis, circles) of ABY (black data) and dABY (blue data) cement pastes hydrated at water to cement mass ratio of 0.50; these values were obtained from SXRPD data until 14 hours and LXRPD data for ~1 day. Taken from article #6 in Annex I.

Table 5.9. Normalised RQPA, including ACn and free water contents for ABY cement paste (w/c=0.50) during the first 14 hours of hydration obtained from SXRPD in-situ study and at 1, 7, 28 and 56 days (expressed in hours) from ex-situ LXRPD hydration study are also included.

	t(h)	$oC_4A_3\bar{S}$	$cC_4A_3\bar{S}$	$C\bar{S}$	mC_3S	βC_2S	C_4AF	CaF_2-$C_9S_3\bar{S}$	$C_{12}A_7$	AFt	AFm	CH	Katoite	ACn+ FW	FW
		wt%													
in-situ	**0**	5.4	4.2	7.4	18.7	17.1	2.9	1.0	0.2	-	-	-	-	9.8*	**33.3**
	1	4.3	2.7	1.8	16.2	16.3	2.2	1.2	-	27.8	-	-	-	27.6	-
	2	3.0	1.9	0.3	14.2	16.0	2.0	1.1	-	36.2	-	-	-	25.3	-
	3	2.5	1.4	-	13.3	15.8	1.9	1.0	-	37.6	-	-	-	26.4	-
	4	2.2	1.3	-	12.8	15.8	1.9	1.0	-	38.0	-	-	-	27.1	-
	5	2.0	1.2	-	12.4	15.8	1.9	1.0	-	38.5	-	-	-	27.2	-
	6	1.9	1.1	-	12.2	15.8	1.9	1.0	-	38.7	-	-	-	27.3	-
	7	1.7	1.1	-	11.9	15.8	1.9	1.0	-	38.7	-	-	-	27.9	-
	8	1.7	1.0	-	11.8	15.7	1.8	1.0	-	38.6	-	-	-	28.5	-
	9	1.6	0.9	-	11.6	15.7	1.8	1.0	-	38.7	-	-	-	28.7	-
	10	1.5	0.9	-	11.5	15.9	1.8	1.0	-	39.1	-	-	-	28.2	-
	11	1.4	0.9	-	11.3	15.8	1.8	1.0	-	39.0	-	-	-	28.8	-
	12	1.4	0.9	-	11.2	15.9	1.8	1.0	-	39.2	-	-	-	28.6	-
	13	1.2	0.8	-	11.2	15.7	1.7	1.0	-	38.9	-	-	-	29.5	-
	14	1.3	0.7	-	11.1	15.7	1.7	1.0	-	39.1	0.4	-	-	28.8	-
ex-situ	**#25**	0.7	-	-	10.1	16.2	2.0	1.7	-	26.1	3.8	-	-	39.5	-
	168	0.7	-	-	2.8	14.9	-	1.5	-	22.1	6.6	1.4	0.4	39.9*	**9.8**
	672	-	-	-	1.0	10.0	-	1.6	-	21.5	6.8	1.7	0.9	50.5*	**6.1**
	2160	-	-	-	1.2	7.1	-	2.1	-	24.2	8.4	2.3	1.3	49.1*	**4.3**

#Measured with CuKα$_1$ radiation. *ACn only.

Table 5.10. Normalised RQPA, including ACn and free water for dABY cement paste (w/c=0.50) during the first 14 hours of hydration obtained from SXRPD in-situ study and at 1, 7, 28 and 56 days (expressed in hours) from ex-situ LXRPD hydration study are also included.

	t(h)	$oC_4A_3\bar{S}$	$cC_4A_3\bar{S}$	$C\bar{S}$	mC_3S	βC_2S	α'_HC_2S	C_4AF	CaF_2-$C_9S_3\bar{S}_3$	$C_{12}A_7$	AFt	AFm	CH	Katoite	ACn + FW	FW
		wt%														
in-situ	**0**	2.5	2.1	7.4	8.6	19.6	6.4	1.7	1.0	4.3	-	-	-	-	13.1*	**33.3**
	1	2.6	1.8	1.5	6.7	20.1	7.8	1.6	1.1	2.0	27.7	-	-	-	27.1	-
	2	2.3	1.6	0.1	5.7	20.1	7.8	1.6	1.6	1.1	34.4	-	-	-	23.5	-
	3	2.1	1.6	-	5.2	19.2	7.8	1.6	1.0	0.7	35.4	-	-	-	25.3	-
	4	1.9	1.5	-	4.8	19.1	7.7	1.6	1.0	0.6	35.8	-	-	-	25.9	-
	5	1.8	1.4	-	4.6	19.3	7.7	1.6	1.0	0.6	36.0	1.1	-	-	25.0	-
	6	1.6	1.2	-	4.4	19.4	7.8	1.6	1.0	0.6	36.1	1.2	-	-	25.1	-
	7	1.4	1.1	-	4.2	19.4	7.7	1.6	0.9	0.6	36.3	1.4	-	-	25.3	-
	8	1.3	1.1	-	4.0	19.1	7.6	1.5	0.9	0.6	36.4	1.5	-	-	26.0	-
	9	1.2	1.0	-	3.8	18.9	7.6	1.5	0.9	0.6	36.5	1.5	-	-	26.4	-
	10	1.2	0.9	-	3.7	19.0	7.5	1.5	0.9	0.6	36.6	1.6	-	-	26.4	-
	11	1.2	0.8	-	3.6	18.8	7.5	1.5	0.9	0.6	36.6	1.6	-	-	27.1	-
	12	1.1	0.8	-	3.5	19.3	7.6	1.5	0.9	0.6	36.7	1.5	-	-	26.3	-
	13	1.0	0.7	-	3.3	18.7	7.4	1.5	0.9	0.6	36.7	1.6	-	-	27.4	-
	14	1.0	0.7	-	3.4	19.3	7.6	1.5	0.9	0.6	36.8	1.6	-	-	26.6	-
ex-situ	**#28**	0.6	-	-	2.5	19.2	6.6	1.2	1.3	-	21.9	4.7	-	-	42.0	-
	168	-	-	-	1.5	15.9	3.3	-	1.3	-	23.5	5.0	0.3	-	39.0*	**10.3**
	672	-	-	-	1.5	3.9	0.8	-	0.9	-	21.8	6.9	1.8	0.7	57.5*	**4.3**
	2160	-	-	-	1.7	2.9	0.9	-	0.6	-	25.0	6.3	1.9	1.3	56.5*	**3.0**

#Measured with CuKα_1 radiation. *ACn only.

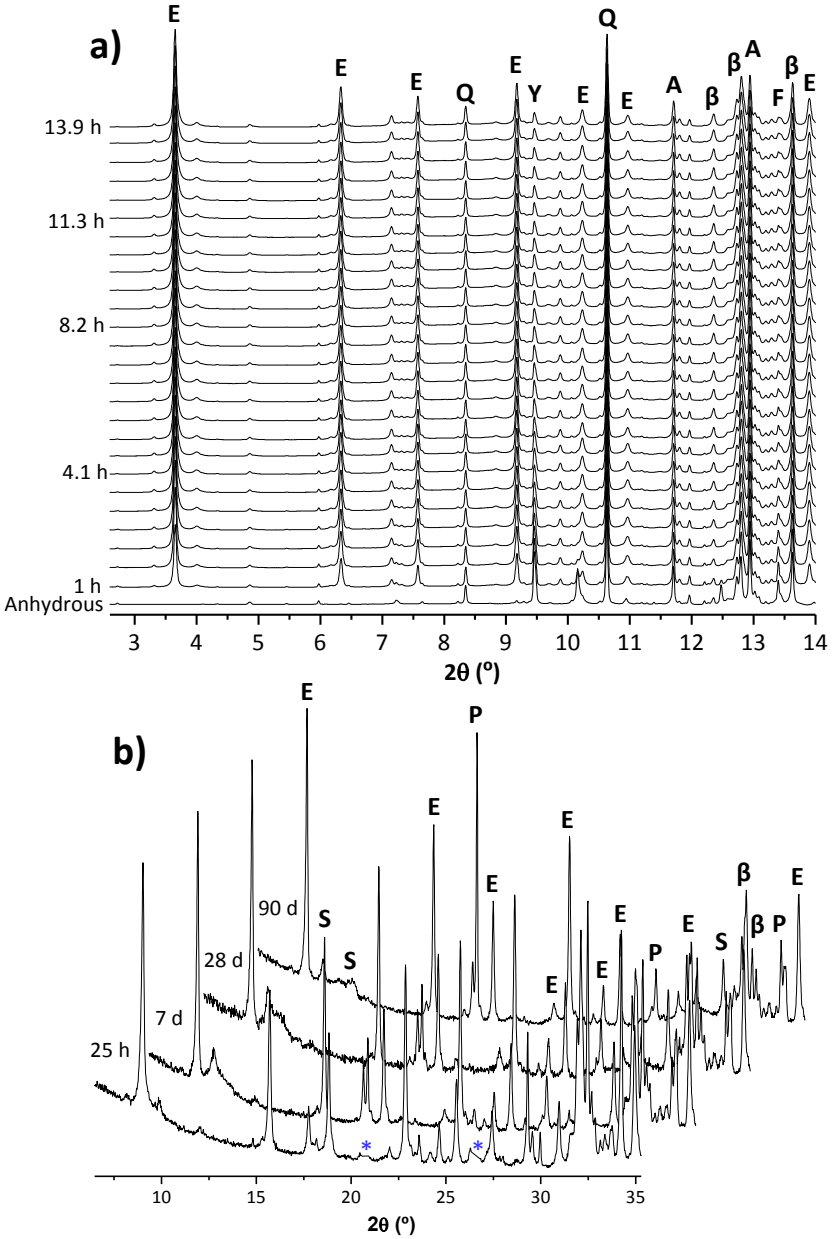

Figure 5.15. a) SXRPD raw patterns (λ=0.61391 Å) and b) LXRPD raw patterns (λ=1.5406 Å) of ABY_0.50w/c paste. The * symbol represent the two removed peaks from quartz added as internal standard in the 25 h sample. The main peaks are labelled as A=mC3S, β=βC2S, Y=C4A3$\overline{S}$, F=C4AF, E=ettringite, S=AFm. Modified figure from article #6 of Annex I.

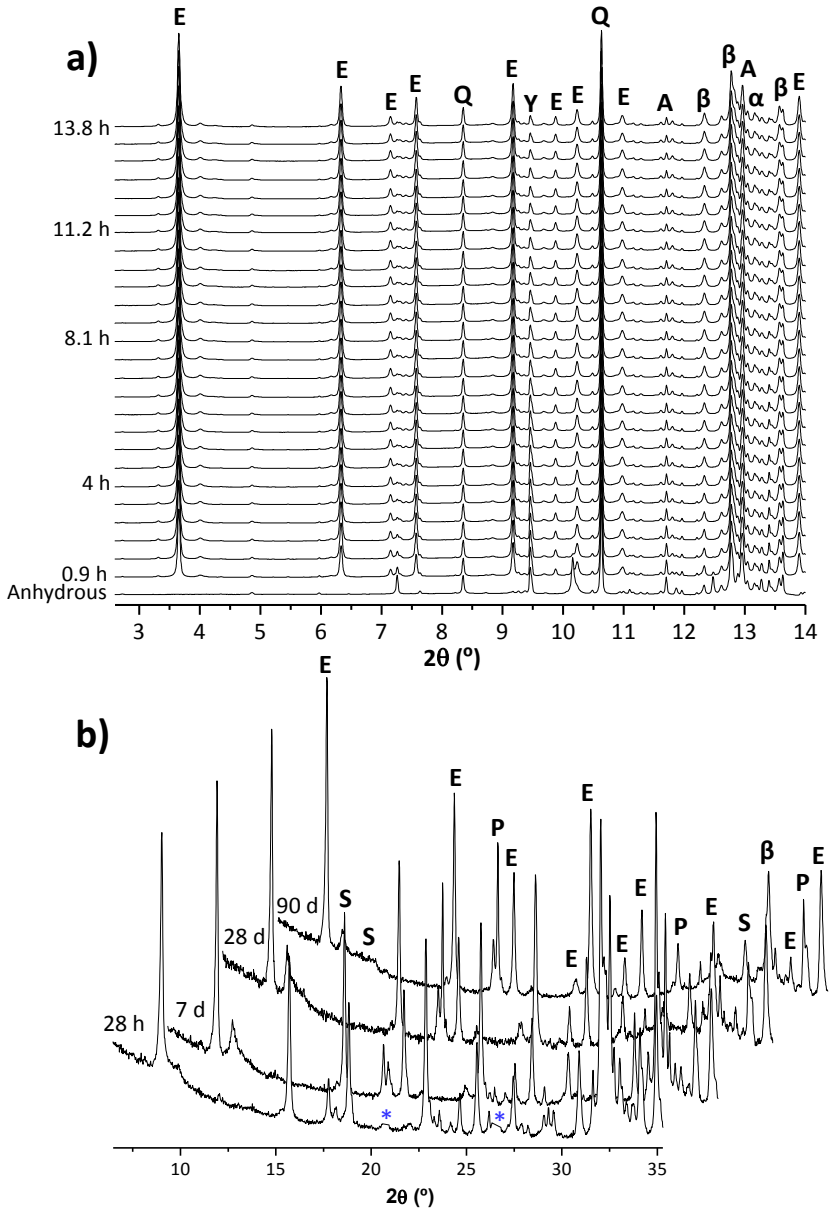

Figure 5.16. a) SXRPD raw patterns (λ=0.61391 Å) and b) LXRPD raw patterns (λ=1.5406 Å) of ABY_0.50w/c paste. The * symbol represent the two removed peaks from quartz added as internal standard in the 28 h sample. The main peaks are labelled as A=mC_3S, β=βC_2S, α=α'$_H$$C_2S$, Y=$C_4A_3\bar{S}$, F=$C_4AF$, E=ettringite, S=AFm. Modified figure from article #6 of Annex I.

5.2.2.2. The role of boron on the hydration process

Borax was added to the raw mixture to stabilise the α'$_H$ form of belite [63, 64]. However, it is important to highlight that the presence of boron on a cement

paste retards the hydration [165] and this causes that, in spite of a lower hydration degree of α'_H-form of C_2S, the mechanical properties are enhanced when compared to those without the addition of boron [64]. This effect has also been observed in the calorimetric measurements, Figure 5.17, where the calorimetric curves of both cements hydrated at w/c of 0.50 up to 7 days are presented. It is observed that dABY hydration is behind and after ~4 hours of hydration the heat released by dABY is lower than ABY. Furthermore, the acceleration period in dABY has been delayed ~15 hours.

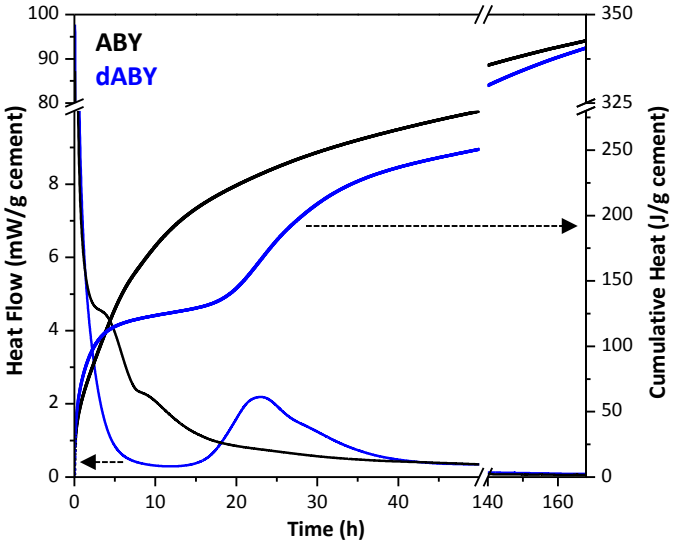

Figure 5.17. Calorimetric curves: heat flow (thin lines) and cumulative heat (thickness lines) of ABY and dABY pastes hydrated at w/c mass ratio 0.50 for 7 days. Modified from article #6 in Annex I.

5.2.2.3. Reactivity of aluminate and silicate phases in ABY and dABY cement pastes

Silicates (alite and belite forms) hydrate to yield calcium silicate hydrates, mainly C-S-H gel [166] or stratlingite [167]. The latter is usually formed in systems with both sources of aluminium and silicates as Belite-Ye'elimite-Ferrite cements [64]. Nevertheless, in ABY and dABY cements, stratlingite was not formed at any hydration time, as can be observed in Figure 5.18. This figure shows ^{27}Al MAS-NMR spectra for both anhydrous cements and the corresponding hydrated pastes at 28 and 90 days. Al(IV) of remaining ye'elimite is seen as a broad peak in the anhydrous spectra with its maximum at 70 ppm. The absence of signals at ~62 and 69 ppm in the 28 and 90 days spectra settles that stratlingite (Al(IV) signals

[168, 169]) was not formed under our experimental conditions, confirming XRD results, see Tables 5.9 and 5.10. The octahedrally coordinated Al present in ettringite, AFm and AH_3-gel is observed in the region from 0 to 20 ppm. Al(VI) of ettringite is observed by a peak centred at 13.4 ppm, which corresponds to non-resolved two distinct Al sites in ettringite [170]. Moreover, the Al(VI) in AFm and AH_3 appears as broader signals centred in the range from 9 to 11 ppm due to their poor crystallinity or less-ordered character. A clear difference is observed in the early hydration 27Al spectra for ABY and dABY. The resonance of Al(VI) corresponding to AH3 gel, close to 10 ppm, coming from the reaction of the aluminates (ye'elimite and mayenite) with anhydrite, is noticeable after 4 h for ABY, while it is not observed even at 24 h for dABY; see the right panel of Figure 5.18. In these experimental conditions, due to the role of boron, the precipitation of aluminum hydroxide gel has been delayed. Though, no significant differences are observed when comparing ABY and dABY pastes.

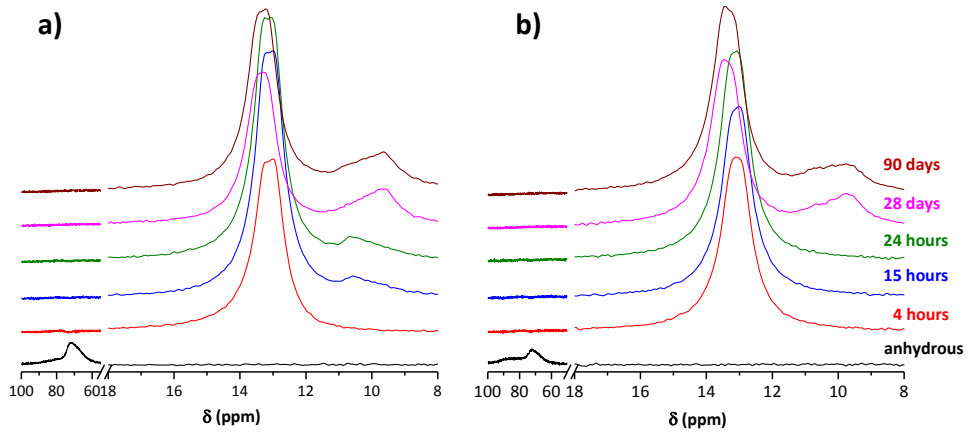

Figure 5.18. ^{27}Al MAS-NMR spectra for (a) ABY and (b) dABY, anhydrous (black line) and after 4, 15, 24 hours and 28 and 90 days of hydration. Taken from article #6 in Annex I.

ABY cement contains monoclinic M_3 C_3S and βC_2S, while dABY also contains $\alpha'_H C_2S$. The hydration of mC_3S gives C-S-H gel with a Ca to Si ratio of ~1.8, as discussed in the previous chapter (article #2 of Annex I). However, the C-S-H gel structure and stoichiometry formed from belite is still unclear. Table 5.11 presents the degree of hydration of silicate phases in both cements at longer hydration ages, calculated from data given in Tables 5.9 and 5.10. The results indicate that, at late ages, alite in ABY cement reacted at a higher pace than in dABY. Belite (all the polymorphs) are more reactive in the doped cement than in ABY (without boron). This is in disagreement with our previous results observed in BYF cements, in which βC_2S (in non-doped BYF) reaction was faster than that for the α'_H form (in boron-doped BYF [64]. In addition, as it was mentioned before, the hydration of

alite and the different polymorphs of belite have yielded the formation of C-S-H gel, meanwhile stratlingite was not formed.

Table 5.11. Degree of hydration of silicate phases in both cement 0.50 w/c pastes (without SP) at 28 and 90 days obtained from Rietveld quantitative phase analysis results given in Tables 5.9 and 5.10.

	ABY		dABY		
Time (days)	**mC_3S**	**βC_2S**	**mC_3S**	**βC_2S**	**$\alpha'_H C_2S$**
7	85	15	83	19	49
28	95	42	83	80	88
90	94	59	81	85	86

Figure 5.19 shows the raw ^{29}Si MAS-NMR spectra without any normalisation for both anhydrous cements and pastes hydrated at 28 and 90 days. Here, it can be highlighted the difference of intensities between the hydrated samples and the anhydrous ones. This is explained because the Si containing phases (alite and belite) are more crystalline than the C-S-H gel (much less intense and broader).

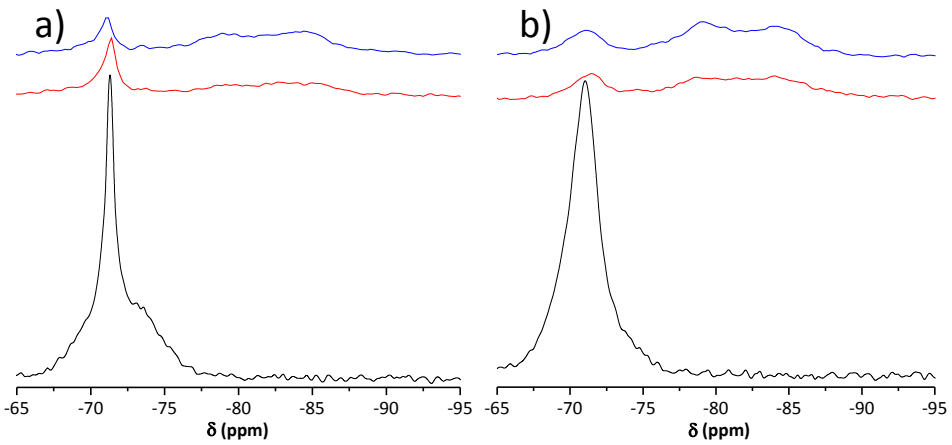

Figure 5.19. ^{29}Si MAS-NMR spectra for (a) ABY and (b) dABY, anhydrous (black line) and after 28 (red line) and 90 (blue line) days of hydration. Taken from article #6 in Annex I.

Figure 5.20 shows ^{29}Si MAS-NMR spectra of ABY and dABY pastes with the corresponding deconvolution. In this case, the spectra have been normalised with the objective of enhancement of the signals.

The first relevant result obtained from ^{29}Si MAS-NMR data is that the amount of silicon-bearing hydrated phases after 28 days is much lower in ABY than in dABY. From these data, the MCL [146] were calculated, being 6.1 and 6.0 for ABY and dABY pastes at 28 days, respectively. While, MCL of 5.0 and 3.9 were obtained for ABY and dABY at 90 days, respectively. These values are in agreement with previously published for similar systems [55, 171]. Furthermore, these MCL values and the slight decrease of them with hydration suggest that the

formed C-S-H gel is calcium rich and should contain a Ca/Si ratio over 1.5 [172]. The most important result obtained by ^{29}Si MAS-NMR is that dABY pastes have developed a higher amount of C-S-H gel due to the higher hydration degree of β and $\alpha'_H C_2S$, Table 5.11 and Figure 5.20. A quantitative study has also been performed by comparing the silicate rich phases obtained from XRD and Rietveld refinements and those ones obtained from ^{29}Si MAS-NMR data, Table 5.12. Table 5.12 contains the quantitative analysis of the silicon rich phases of the anhydrous materials obtained from XRD and ^{29}Si MAS-NMR. These values coincide pretty well certifying the reliability of this methodology.

The ACn value obtained from XRD and Rietveld refinement, jointly with the internal standard method, is the total amount of amorphous, disordered or nanocrystalline fraction of the pastes. Consequently, in order to estimate the amount of C-S-H gel, the stoichiometry $(CaO)_{1.8}SiO_2(H_2O)_4$ was assumed, as discussed in the previous chapter and in article #2 of Annex I, for the gel formed from the reaction of all silicates, i.e., alite, βC_2S and $\alpha'_H C_2S$. The derived values under this assumption are quite satisfactory when compared with those obtained from ^{29}Si MAS-NMR, in which no approximations are needed, as it takes the total area of the signals, Table 5.12.

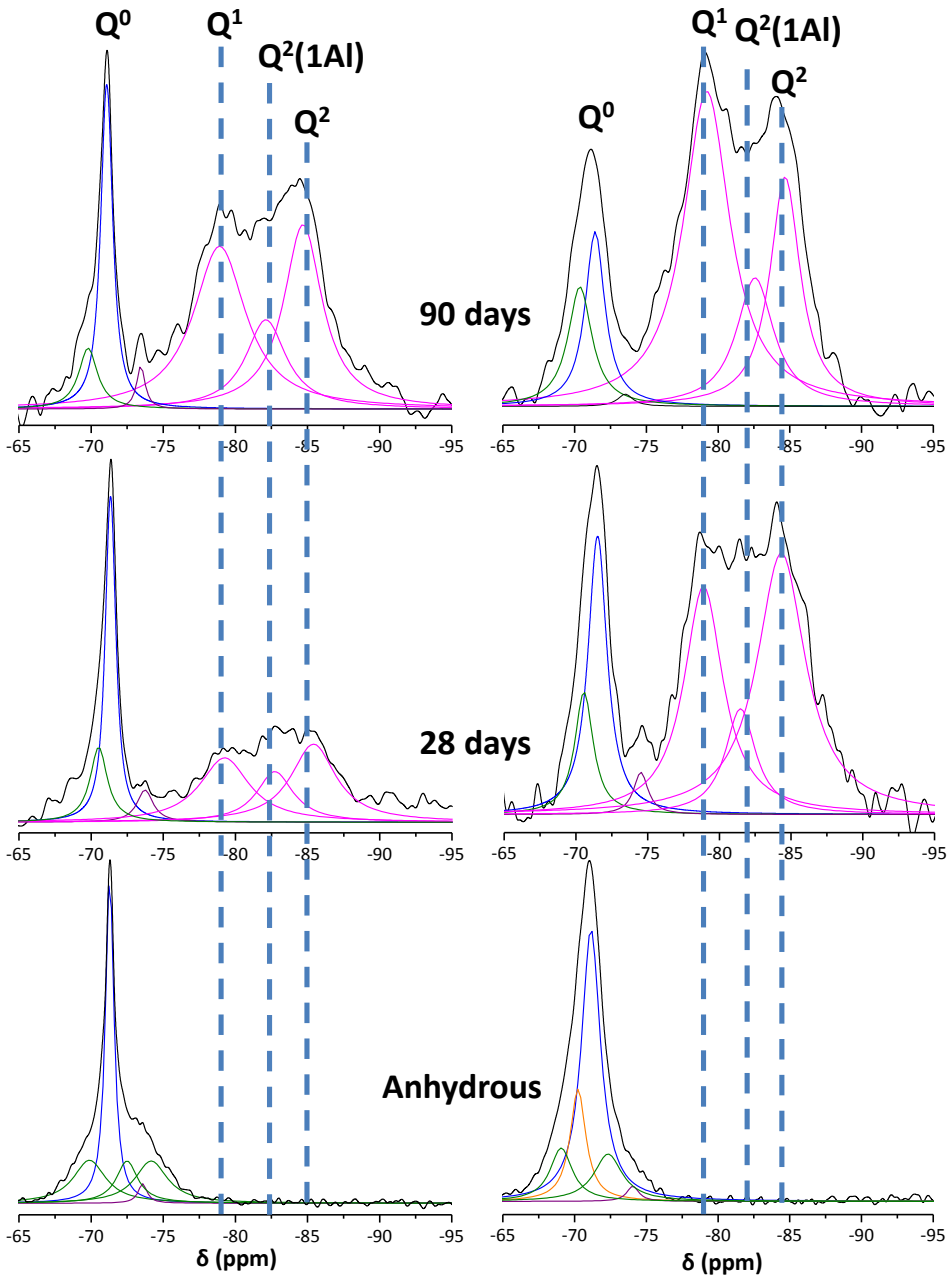

Figure 5.20. ^{29}Si MAS-NMR spectra of ABY (left) and dABY (right) with the deconvoluted signals included, bottom anhydrous, middle 28 days and top 90 days. Blue Q^0 for βC_2S, orange Q^0 for $\alpha'_H C_2S$, green Q^0 for mC_3S, pink Q^n for hydrated C-S-H gel. Taken from article #6 in Annex I.

Table 5.12. Quantitative phase analysis (wt%) of the silicon rich fraction of anhydrous ABY and dABY cements, and 0.50 w/c pastes at 28 and 90 days of hydration determined by XRD and ^{29}Si MAS-NMR. Taken from article #6 in Annex I.

days	sample	method	mC_3S	βC_2S	α'_HC_2S	CaF_2-$C_9S_3\bar{S}_3$	katoite	C-S-H gel
Anhydrous	ABY	XRD	51	46	-	3	-	-
		NMR	55	42	-	3	-	-
	dABY	XRD	24	55	18	3	-	-
		NMR	26	54	18	2	-	-
28	ABY	XRD	2	24	-	4	2	67*
		NMR	9	24	-	4	-	63
	dABY	XRD	3	9	2	2	2	82*
		NMR	7	15	-	2	-	76
90	ABY	XRD	3	16	-	5	3	73*
		NMR	5	15	-	2	-	80
	dABY	XRD	4	7	2	2	3	83*
		NMR	9	10	-	1	-	81

* $(CaO)_{1.8}SiO_2(H_2O)_4$ formula has been used to derive the amount of gel formed from the hydration of mC_3S, βC_2S and α'_HC_2S in each case.

5.2.2.4. Thermogravimetric evolution of hydrated ABY and dABY products with a w/c mass ratio of 0.50 at the studied ages

Figure 5.21 shows DTG-TGA plots for ABY and dABY pastes prepared with w/c=0.50 ratio (without SP) at 1, 7, 28 and 90 days. In all samples, three mass loss signals were observed. The first one, near to ~110°C, is due to the overlapped processes among the dehydration of C-S-H gel and the loss of 32 water molecules from ettringite [54, 117, 173]. The second group of signals was found between 150 and 180°C, and it is associated to the dehydration of AFm-type phases [174]. As can be seen in this figure, the AFm-type phases identified in these systems were monosulphate phase. The third signal located at ~270ºC was associated to the dehydroxylation of amorphous aluminium hydroxide, since it is a really broad signal, in concordance to the absence of crystalline gibbsite in LXRPD patterns. Finally, the weight loss due to the dehydration of crystalline portlandite has been detected between 400-450ºC. The total weight loss up to 600ºC is due to bounded water and it has been used to calculate the free water included in Tables 5.9 and 5.10 (*ex-situ* data) as detailed in the Materials and Methods chapter.

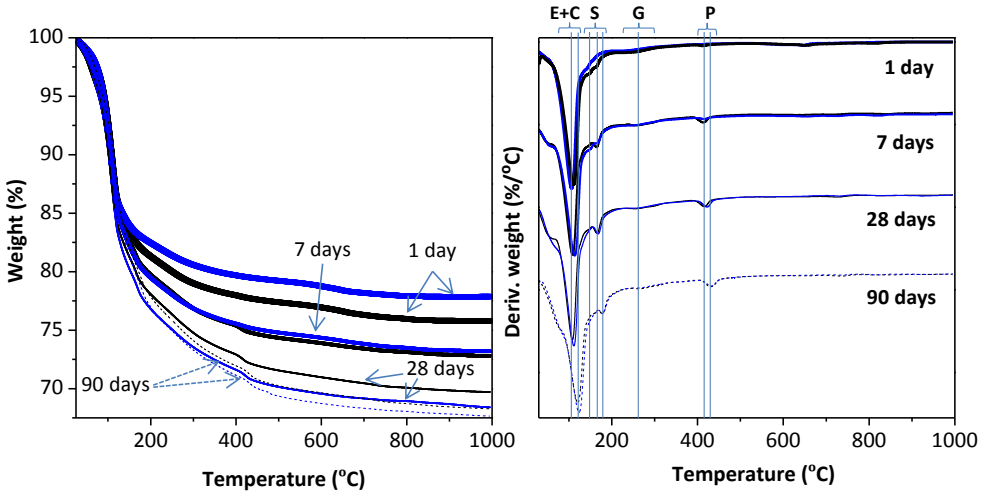

Figure 5.21. Thermogravimetric plots for ABY (black) and dABY (blue) cement (stopped hydration) pastes after 1, 7, 28 and 90 days of hydration at 0.50 w/c mass ratio (without SP). The signals have been labelled as due to the decomposition of E=ettringite, C=C-S-H gel, S=AFm, G=AH_3, P=CH.

Figure 5.21 shows that the weight losses of both pastes are in agreement with the degree of reaction of phases, and with the NMR results. In addition, this figure is also well related with the corresponding calorimetric curves (measured until 7 days), see Figure 5.17.

5.2.3. Processing optimisation and characterisation of ABY and dABY pastes and mortars

With the main aim of obtaining the highest mechanical strengths, the strategy of reducing w/c ratio was adopted. Consequently, both ABY and dABY cements and mortars prepared at w/c of 0.40 and 0.50 were studied through the combination of independent techniques.

Figure 5.22a shows the flow curves of ABY and dABY cement pastes prepared at 0.40 and 0.50 w/c (without superplasticiser, SP), where both pastes show a shear thinning behaviour. Figure 5.22b shows the evolution of the viscosity with time of the same pastes. As expected, the flow curves of pastes prepared at 0.40 w/c show higher shear stress and consequently higher viscosity values than 0.50 w/c pastes, Figure 5.22a, due to the lower water content. In addition, the viscosity (and shear stress) of the dABY paste at w/c 0.40 is higher than that for the ABY one during the whole studied time (Figure 5.22). This fact is related to the internal microstructure of the pastes, which is related to the

different composition of the cements, as discussed above, and a quicker dissolution of certain phases, mainly mayenite (and anhydrite). Moreover, the reduction of the water content caused a dramatic loss of workability, Figures 5.22 a and b. The time before mortars achieve the total loss of workability was just around 10-13 minutes. Thus, to overcome this drawback and assure the formation of homogeneous pastes and mortars at this low w/c mass ratio, it is crucial to add superplasticiser. Polycarboxylate based superplasticisers make possible the preparation of homogeneous and flawless pastes, with low viscosity, through electrosteric dispersion; in addition, it is known that it delays the beginning of the hydration. Thus, it would allow the preparation of homogeneous mortars with improved mechanical properties. Because of that, its addition was selected for further studies.

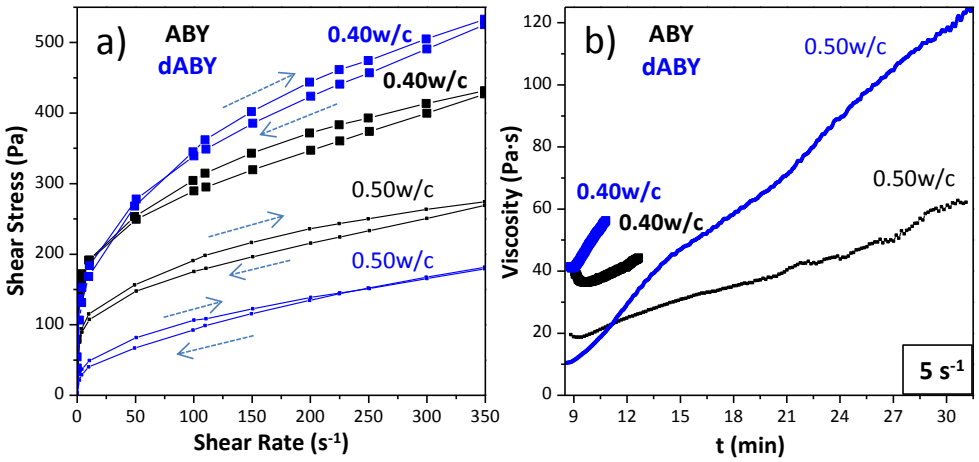

Figure 5.22. a) Flow curves and b) evolution of the viscosity with time (shear rate of 5 s^{-1}) for ABY (black) and dABY (blue) pastes at w/c mass ratios of 0.40 and 0.50 (without SP).

The amount of SP was optimised in both pastes prepared at w/c=0.40. Figures 5.23 show the flow curves of ABY and dABY pastes prepared with different SP contents (at w/c=0.40). The curves of pastes prepared at w/c=0.50 with selected amounts of SP (0.0, 0.4 and 1.0 wt%) are also shown for the sake of comparison. In general, the viscosity decreases with the SP content, down to a minimum, which is the saturation point, where all the particles are coated by the SP. In both cases, minimum viscosity values, and hence a good dispersion, was achieved when 0.4 wt% of SP was added. After that, the viscosity is kept constant or even slightly increases. However, it is worth to highlight that the dABY paste with 1.0 wt% SP (w/c=0.40), Figure 5.23b, shows the lowest viscosity values, within dABY family, at shear rates higher than 50 s^{-1}. This fact may be related with the retarder effect of the SP, which will be studied below.

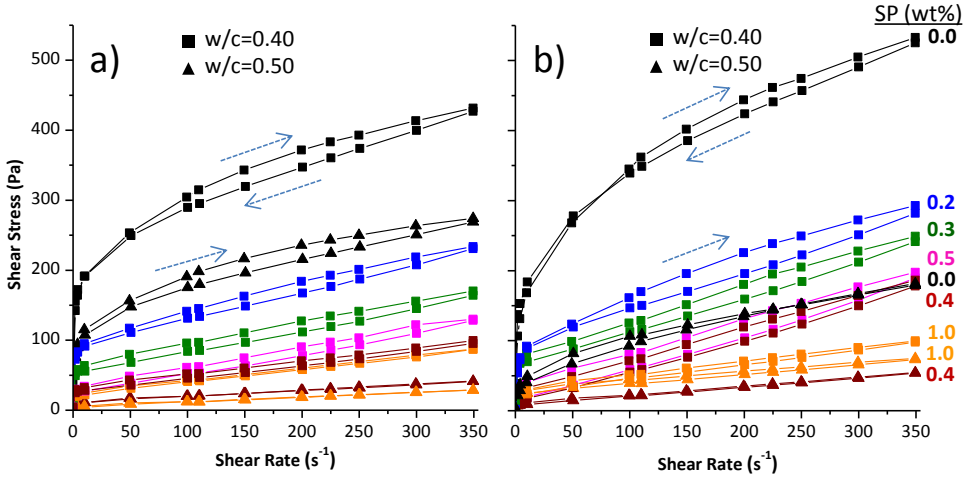

Figure 5.23. Flow curves; for ABY (a) and dABY (b) pastes, prepared at w/c=0.40 and different percentages of superplasticiser. Pastes prepared at w/c=0.50 with selected amounts of SP (0.0, 0.4 and 1.0 wt%) are also shown for the sake of comparison. The same colour code has been used in both figures. Taken from article #5 in Annex I. Copyright (2019) with permission from Elsevier (Annex IV).

In order to see this in a clearer way, Figure 5.24 shows the deflocculation curves of the pastes prepared at w/c=0.40 with different SP contents. Values were taken at the shear rates of 50, 100 and 200 s^{-1} (Figures 5.24 a, b and c, respectively) from the down-curves of the flow curves (viz. viscosity curves). It is clear that the viscosity values decrease by increasing the shear rate (shear thinning behaviour). ABY and dABY pastes show similar tendencies, where the viscosity values at 50 s^{-1} are very similar, although with some exceptions. At higher shear rates, the viscosity of dABY pastes is slightly higher than that for ABY pastes, as commented above.

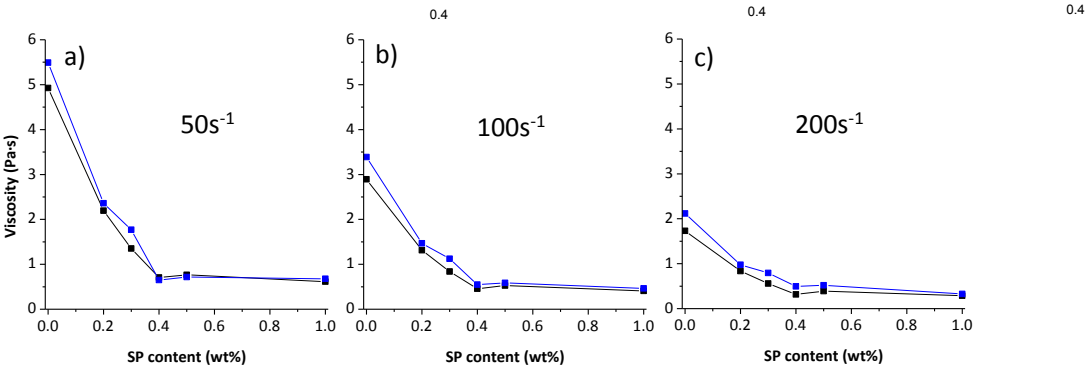

Figure 5.24. Deflocculation curves of ABY (black) and dABY (blue) pastes (w/c=0.40) at 50, 100 and 200 s^{-1} shear rates; values were taken from the down-curves. Adapted from article #5 in Annex I. Copyright (2019) with permission from Elsevier (Annex IV).

Table 5.13 depicts the plastic viscosity and apparent yield stress values, obtained from the Bingham fitting, and the thixotropic values of the ABY and dABY pastes prepared at 0.40 with different SP contents, and pastes at 0.50 prepared with the selected SP additions. In general, the yield stress is a consequence of the interparticle forces, so these links are often broken irreversibly by shear [175, 176]. Here, the apparent yield stress values, obtained by extrapolation using the Bingham model [177], are only shown for the sake of comparison. The thixotropic cycle is related with the effect of time and SP content. In general, the lowest values of thixotropy were obtained in pastes with 0.4 and 1.0 wt% SP. Due to this, and the low viscosity of those pastes (apparent viscosity, discussed in the previous figures, and plastic viscosity shown in Table 5.13), with 0.4 and 1.0 wt% of SP were selected for further studies. Plastic viscosity values, obtained from the down-curve using the Bingham model, show the same tendency than apparent viscosity values.

Table 5.13. Rheological properties of the fresh ABY and dABY pastes prepared at 0.40 and 0.50 w/c; and different SP contents. Taken from article #5 in Annex I. Copyright (2019) with permission from Elsevier (Annex IV).

Cement paste	w/c	SP (wt%)	Apparent Yield Stress (Pa)	$\eta_{plastic}$ (Pa·s)	Thixotropic cycle (Pa/s)
ABY	0.40	0.0	235.5	0.55	5333
		0.2	89.6	0.40	3863
		0.3	49.3	0.32	4248
		0.4	24.4	0.20	2025
		0.5	19.0	0.30	3410
		1.0	21.7	0.18	813
	0.50	0.0	139.2	0.37	5201
		0.4	11.4	0.08	243
		1.0	4.6	0.07	227
dABY	0.40	0.0	270.2	0.74	4874
		0.2	90.0	0.54	6716
		0.3	58.4	0.51	5431
		0.4	3.2	0.49	5802
		0.5	3.0	0.52	7736
		1.0	24.4	0.21	1834
	0.50	0.0	77.8	0.29	2202
		0.4	7.3	0.13	625
		1.0	24.2	0.14	1597

Figure 5.25 shows the evolution of the viscosity with time (at 5 s^{-1}) of ABY and dABY cement pastes prepared with the selected amounts of SP (0, 0.4 and 1.0 wt%) at w/c ratios of 0.40 and 0.50. As expected, the viscosity of all pastes

increases with time. ABY pastes with 0.50 w/c show lower viscosity values, at any time, than the corresponding pastes at 0.40 w/c for the same SP content. In all cases, the higher SP content, the later rise in viscosity, due to the retarder effect of the polycarboxylate [93], as mentioned before. For instance, the ABY paste at 0.50 w/c with 0.4 wt% SP shows lower initial viscosity than ABY paste at 0.40 w/c with 1.0 wt% SP (Figure 5.25a); however, after 14 min of hydration, the rise in viscosity of the former is much higher. In the case of dABY pastes, the viscosity of pastes with 1.0 wt% SP (w/c=0.40 or 0.50) also rises at a slower pace than those with 0.4 wt% SP, where the rise is even lower for the paste with w/c=0.50, as it happened for ABY pastes. The data of this figure is essential to assure not only a good initial dispersion but also to guarantee that the viscosity is not increasing dramatically during the mortar preparation. Consequently, the control of the viscosity of the pastes will allow the preparation of homogeneous mortars. This control of rheological behaviour is even more relevant for dABY pastes since their viscosity increase with time quicker than for ABY ones. All this will have effects on the homogeneity of the systems, and thus on the mechanical properties of the corresponding mortars.

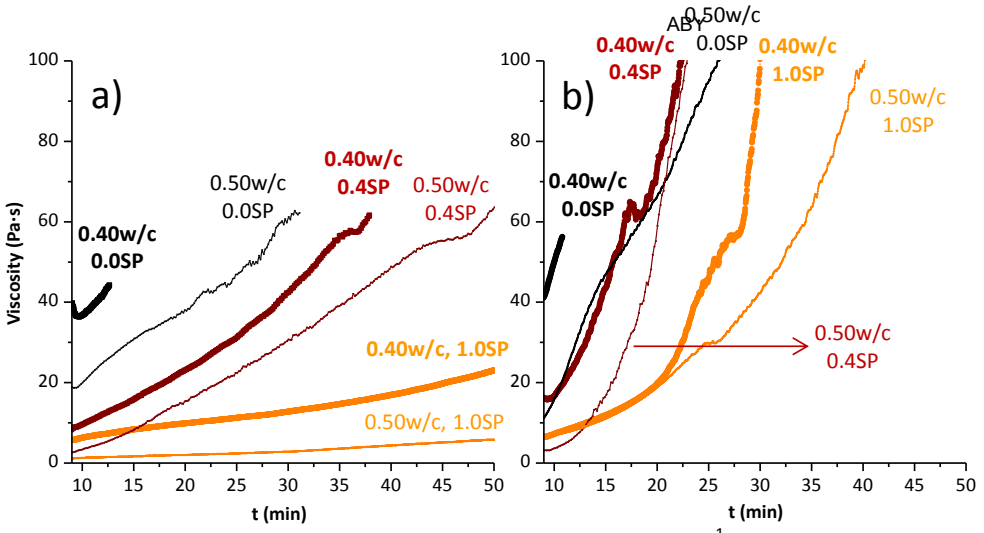

Figure 5.25. Evolution of the viscosity with time (shear rate, 5 s^{-1}) of a) ABY and b) dABY pastes, prepared with selected amounts of SP (0.0, 0.4 and 1.0 wt%) at w/c=0.40 (thick lines) and w/c=0.50 (thin lines). The percentage of SP is also marked in the figure. Adapted from article #5 in Annex I. Copyright (2019) with permission from Elsevier (Annex IV).

5.2.4. Compressive strength development of ABY and dABY mortars

Figure 5.26 shows the compressive strength development at 1, 7, 28, 56 and 180 hydration days of ABY and dABY mortars prepared at 0.40 w/c with 0.4 and 1.0 wt% of SP, and at 0.50 w/c with 0.4 wt% SP. The compressive strengths of PC prepared at 0.40 w/c with 0.2 wt% SP are also included for the sake of comparison. The high viscosity of mortars without SP did not allow the preparation of homogeneous mortars, so they were not measured. The low mechanical strengths developed by mortars prepared at 0.40 w/c with 0.4 wt% of SP can be justified due to the high viscosity of the fresh mortars. It was expected that those ABY mortars would have presented good mechanical strengths; however the initial viscosity of these mortars (and pastes) was high, and the rise in viscosity was also quick to prepare dense and homogeneous samples (see Figure 5.25, where the curves for the equivalent pastes measured at 5 s^{-1} are shown). Thus, heterogeneous mortars with cracks and entrapped porosity were obtained, see photograph "a" of Figure 5.26. However, ABY mortars prepared at 0.40 w/c with 1.0 wt% SP present the highest values of compressive strength at any hydration time within the ABY family. This is mainly due to the combination of the low initial viscosity of the mortar (and paste) and the retarder effect of the SP; the workability of the mortar was good enough to prepare homogeneous samples (see photograph "b" of the mortar, Figure 5.26), with the consequent increase in compressive strengths at any age. ABY mortars prepared with a higher water content, 0.50 w/c, showed lower mechanical strengths than the previous ones at any age, even when 0.4 wt% SP was added, due to the higher water content (Figure 5.25a).

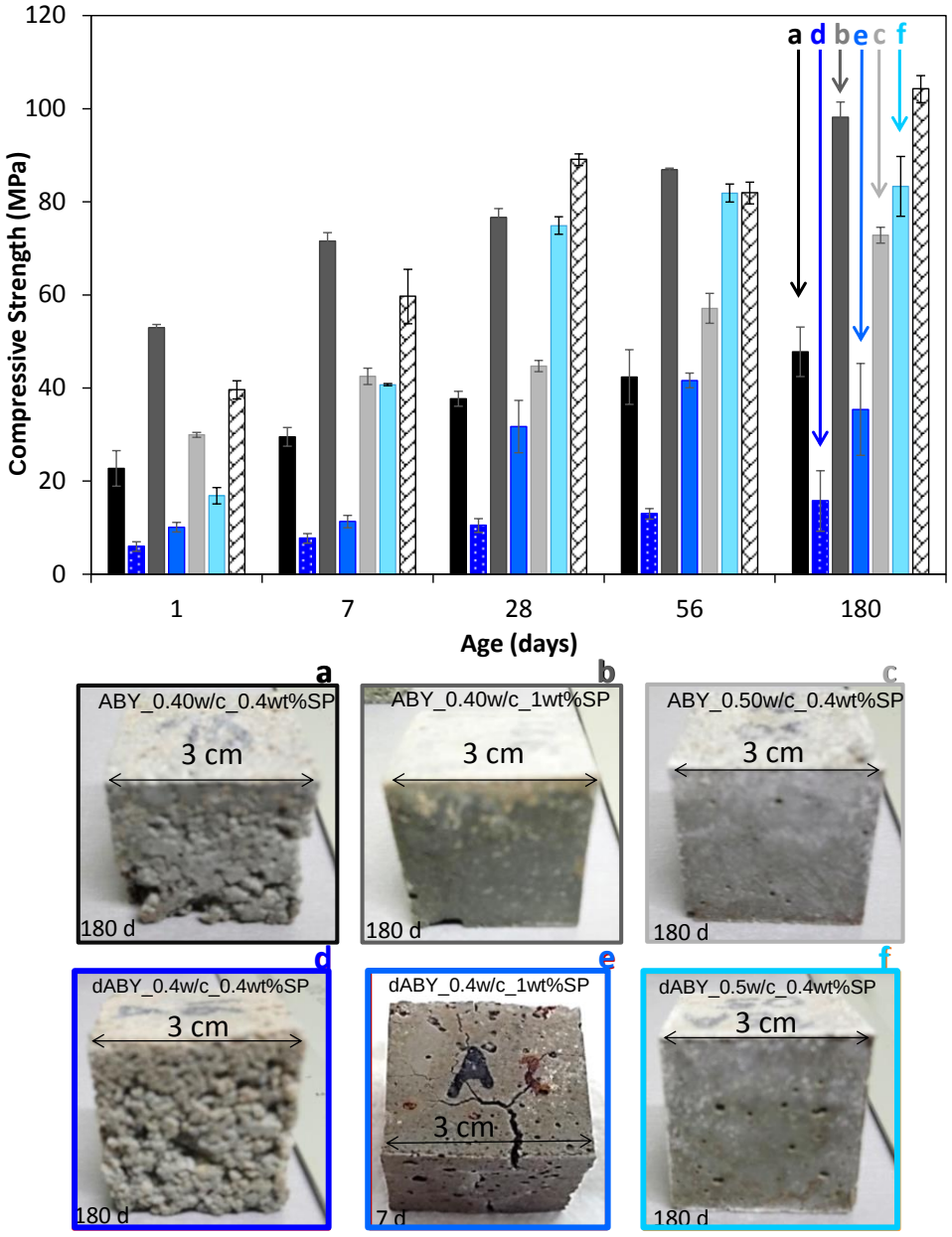

Figure 5.26. Compressive strength values of ABY and dABY mortars, prepared at 0.40 and 0.50 w/c, and 0.4 and 1.0 wt% SP. Insets show photographs of selected cubes (30x30x30 mm^3) mortars which are labelled as: a) ABY_0.40w/c_0.4wt%SP, b) ABY_0.40w/c_1wt%SP, c) ABY_0.50w/c_0.4%SP, d) dABY_0.40w/c_0.4wt%SP, e) dABY_0.40w/c_1wt%SP and f) dABY_0.50w/c_0.4wt%SP. Compressive strength values of PC with 0.2 wt% SP at 0.40 w/c, as striped bars, are included for the sake of comparison. Taken from article #5 in Annex I. Copyright (2019) with permission from Elsevier (Annex IV).

dABY mortars prepared at 0.50 w/c with 0.4 wt% SP show higher compressive strengths than the corresponding specimens prepared at 0.40 w/c

with 0.4 or 1.0 wt% SP, at any hydration time, despite the higher water content. Mortars prepared at 0.40 w/c with 0.4 wt% SP (photograph "d" of Figure 5.27) are porous and heterogeneous due to the high viscosity of the mortars during preparation, in agreement with Figure 5.25b where the initial viscosity of the corresponding paste is very high and it also increases quickly during the first hydration minutes. The viscosity of dABY mortars increases quicker than that of ABY within the first minutes of hydration, complicating the preparation of homogeneous mortars. Since dABY mortars prepared at 0.40 w/c with 1.0 wt% SP also show significant defects (photograph "e" of Figure 5.26), the measured compressive strength values are also low. Nevertheless, homogeneous dABY mortars were prepared when higher water content was added, 0.50 w/c, jointly with the optimised amount of SP (0.4 wt%), Figure 5.26. ABY and dABY mortars at 0.50 w/c with 1.0 wt% SP were not prepared to avoid excessive retardation.

In spite of having prepared homogeneous dABY mortars that show high mechanical strengths (dABY_0.50w/c_0.4wt%SP) through the control and optimisation of the different parameters (w/c and percentage of SP) and the evolution of the viscosity with time (Figure 5.25), the mechanical strengths of dABY mortars developed at ages below 28 days are lower than those for the optimised ABY mortars, Figure 5.26. However, from 7 to 28 days, the compressive strength of the optimised dABY mortars (0.50 w/c, 0.4 wt% SP) increases considerably (from 41±1 to 75±2 MPa). This is related with the higher degree of hydration of both belites in dABY, Table 5.14, thanks to the addition of boron. Moreover, optimised dABY mortars show quite high compressive strengths, mainly from 28 curing days (viz. 75±2, 82±2 and 83±6 MPa at 28, 56 and 180 hydration days). It is worth to highlight that the optimised ABY mortars (ABY_0.40w/c_1.0wt%SP) show compressive strength values higher to those obtained for PC (PC_0.40w/c_0.2wt%SP) at early ages (1 and 7 days) or equivalent to them at 56 or 180 days, Figure 5.26.

5.2.5. Correlation between mineralogical hydration assemblage and mechanical strengths

The ABY and dABY mortars that developed the highest mechanical strengths (0.40w/c with 1.0wt% SP and 0.50wc with 0.4wt% SP) were further studied with the goal of correlating the hydrated phase assemblage of the pastes with the mechanical strengths of the corresponding mortars. The phase assemblage of these four pastes (obtained through LXRPD in combination with

the external standard and TGA) are given in Tables VII and VIII from Annex III. They include the ACn and FW contents at 1, 7, 28 and 56 days. Figure 5.27 shows the evolution of the full phase assemblage of these pastes with time. Low disagreement factors in the Rietveld refinements were achieved for these four pastes. As representative examples, Figures 5.28a and b show the Rietveld plots of ABY and dABY cement pastes prepared at 0.50w/c with 0.4wt% SP, at 28 hydration days.

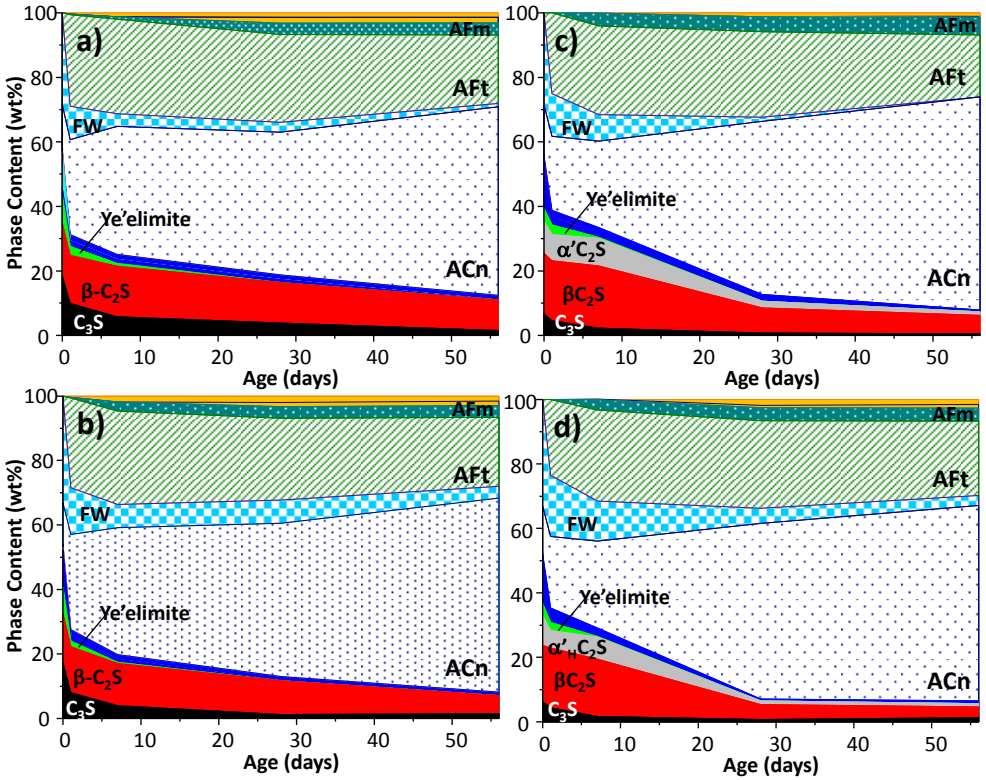

Figure 5.27. Evolution of phase assemblage extracted from RQPA and TGA of a) ABY_0.40w/c_1wt%SP, b) ABY_0.50w/c_0.4wt%SP, c) dABY_0.40w/c_1wt%SP and d) dABY_0.50w/c_0.4wt%SP pastes. Taken from article #5 in Annex I. Copyright (2019) with permission from Elsevier (Annex IV).

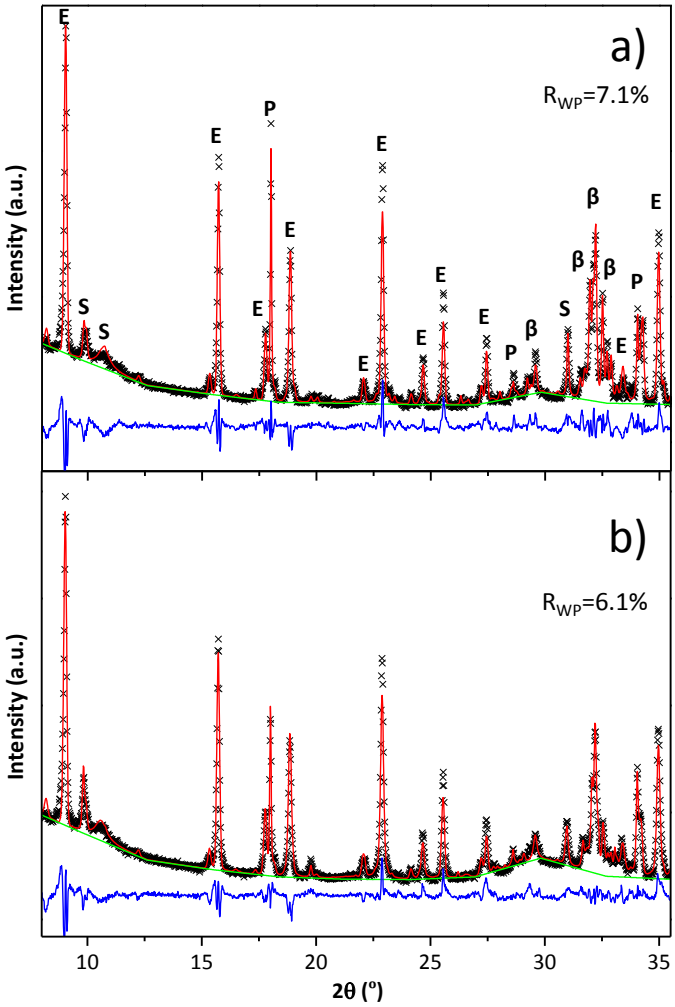

Figure 5.28. LXRPD Rietveld plots (CuKα_1 radiation, λ=1.54059 Å) for a) ABY and b) dABY pastes prepared at 0.50w/c with 0.4wt% SP at 28 days of hydration. The main peaks are labelled as β=βC_2S, E=ettringite, S=AFm and P=CH. R_{WP} values are included. Adapted from article #5 in Annex I. Copyright (2019) with permission from Elsevier (Annex IV).

The evolution of AFt, ACn and FW contents with time in these four selected pastes is presented in Figure 5.29. As a general comment, high contents of AFt, ACn, and low FW contents are indicative of the evolution of the hydration, and thus, related with high mechanical properties (in homogeneous specimens). However, at ages higher than 7 days, the AFt content of all pastes decreases due to its decomposition, probably due to the increase in pH and the silicate-rich environment [178].

It is important to highlight the increase of ACn content from 7 to 28 hydration days in dABY_0.50wc_0.4wt%SP which is coincident with the high increase in compressive strength. The latter is due to the high belite content of

dABY, jointly with the fact that all polymorphs of belite in dABY are more reactive. Table 5.14 gives the degree of reaction of the main phases present in the four selected pastes. Alite is very reactive in all the cements pastes, while β-belite is more reactive in the doped cement paste. However, in spite of these differences in the phase assemblage, they are not strong enough to support and justify the differences on mechanical strengths. Therefore, this confirms that the processing is the important issue to improve the mechanical strength of these materials.

Table 5.14. Degree of reaction (%) of the main phases (mC_3S, βC_2S and $\alpha'_H C_2S$) at the studied ages for the four selected samples (ABY and dABY with w/c of 0.40 and 0.50 and SP contents of 0.4 and 1.0 wt%). Adapted from article #5 in Annex I. Copyright (2019) with permission from Elsevier (Annex IV).

Cement paste	Sample	Phase	Degree of reaction			
			1d	7d	28d	56d
ABY	0.40w/c_1.0wt%SP	mC_3S	46	69	79	92
		βC_2S	8	4	22	41
	0.50w/c_0.4wt%SP	mC_3S	54	77	93	91
		βC_2S	6	14	31	63
dABY	0.40w/c_1.0wt%SP	mC_3S	32	67	89	92
		βC_2S	0	0	59	79
		$\alpha'_H C_2S$	18	13	79	89
	0.50w/c_0.4wt%SP	mC_3S	31	73	87	80
		βC_2S	0	0	73	81
		$\alpha'_H C_2S$	41	25	88	89

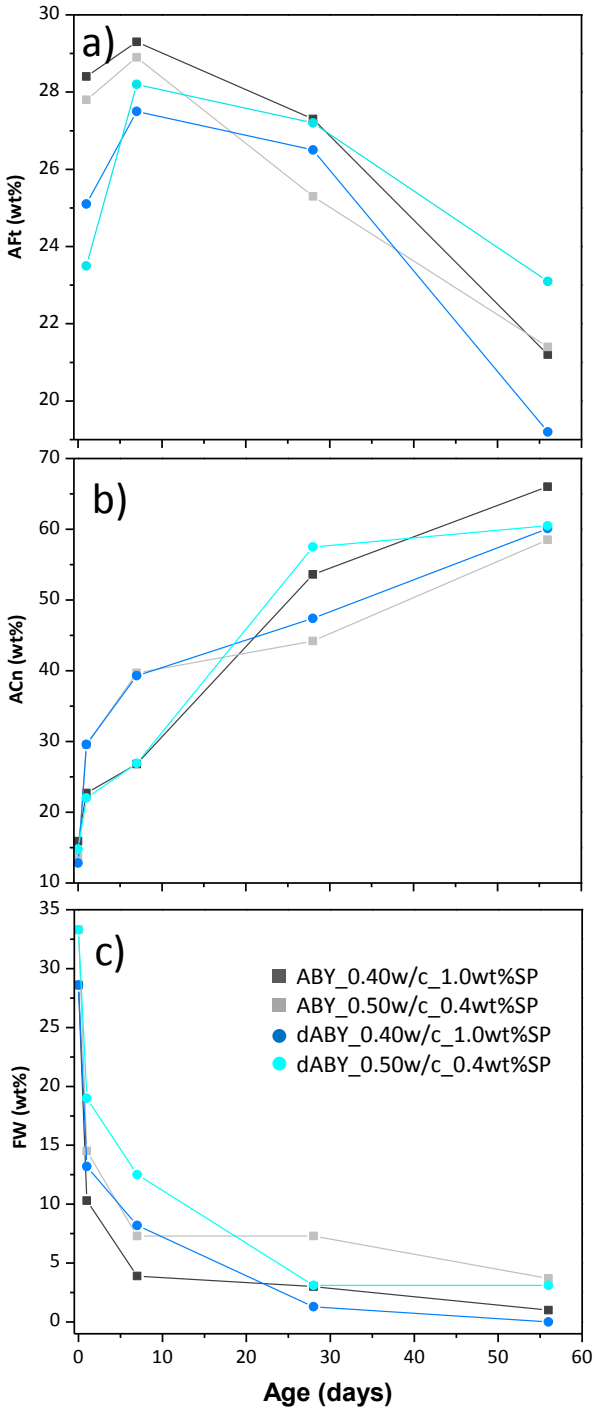

Figure 5.29. Evolution of a) AFt , b) ACn and c) FW with time at 1, 7, 28 and 56 days of hydration of the four selected pastes prepared at 0.40 w/c and 1.0wt% SP and at 0.50w/c with 0.4wt% SP. Taken from article #5 in Annex I. Copyright (2019) with permission from Elsevier (Annex IV).

Table 5.15 shows the cost to produce one tone of the optimised ABY and dABY mortars (ABY_0.40w/c_1.0SP and dABY_0.50w/c_0.4SP). The compressive strengths of those mortars measured at 28 days of hydration are also shown. The data for PC mortars are presented for the sake of comparison, which were prepared at 0.50 w/c (following the specifications of UNE-EN 196-1:2018) and at 0.40w/c with 0.2wt% of SP as it was previously optimised. Thus, the ratio of CO_2 emission per MPa of compressive strength has been calculated. It can be highlighted that PC_0.40w/c_0.2wt%SP, ABY_0.40w/c_1wt%SP and dABY_0.50w/c_0.4wt%SP show the lowest CO_2/MPa ratios. Thus, ABY and dABY materials can be great candidates to substitute PC. The cost of each raw material [179] and the used proportions to calculate the cost to produce one tone of mortar are included in Table 5.16.

Table 5.15. Costs and CO_2 emission per MPa of ABY and dABY mortars at 28 hydration days. PC samples data have been added for the sake of comparison.

	PC		**ABY**		**dABY**
	0.40w/c 0.2wt%SP	0.50w/c	0.40w/c 1wt%SP	0.50w/c, 0.4wt%SP	
Compressive Strength (MPa)	89.1	62.0	76.6	44.7	74.9
€/T mortar	28.1	26.0	50.1	42.6	49.1
CO_2	0.97	0.97	0.81	0.81	0.81
€/MPa	0.315	0.419	0.653	0.954	0.655
CO_2/MPa at 28d	0.011	0.016	0.011	0.018	0.011

Table 5.16. Costs and proportions of raw materials to produce the mortars of this study at 0.40 and 0.50 w/c. PC is also included for the sake of comparison.

Material	Unit Cost €/T	PC				ABY				dABY			
		0.40w/c 0.2wt%SP		0.50w/c		0.40w/c 1wt%SP		0.50w/c 0.4wt%SP		0.40w/c 1wt%SP		0.50w/c 0.4wt%SP	
		wt%	€	wt%	€	wt%	€	wt%	€	wt%	€	wt%	€
PC	84[#]	22.2	18.7	22.2	18.7	-	-	-	-	-	-	-	-
ABY/dABY	250-490[@]	-	-	-	-	22.7	56.7-111.1	22.2	55.5-108.8	22.7	56.7-111.1	22.2	**55.5-108.8**
sand	10.8[#]	66.7	7.2	66.7	7.2	68.0	7.4	66.6	7.2	68.0	7.4	66.6	**7.2**
water	0.9[#]	11.0	0.1	11.1	0.1	8.4	0.1	10.8	0.1	8.4	0.1	10.8	**0.1**
SP (25wt% active matter	1200*	0.2	2.2	-	-	0.9	10.9	0.4	4.3	0.9	10.9	0.4	**4.3**
Borax	1700*	-	-	-	-	-	-	-	-	0.4	6.6	0.4	**6.6**

***Cost from suppliers. [#]Taken from [179]. [@]These numbers have been calculated considering ABY material as a mixture of 60% of PC and 40% of CSA, marketed in Europe with a cost of 1100€/T or in China at 500 €/T (data from suppliers in Europe).**

6. CONCLUSIONS AND PERSPECTIVES

6.1. Conclusions

This PhD thesis can be gathered in two main parts correlated between them. The first of basic science, focused on the study and deep characterisation of model cements samples using the **PDF methodology** for a better understanding of the amorphous and nanocrystalline structure of these hydrated products. The second block, of applied science, is related with the synthesis, processing and characterisation of two **Alite-Belite-Ye'elimite** eco-cements (standard and doped), jointly with the understanding of their hydration mechanisms. Finally, mortars processing was optimised looking for the enhancement of mechanical strengths, highlighting the importance of controlling the homogeneity and workability.

All those studies have allowed fulfilling the main goal of understanding the hydration mechanism jointly with the achievement of mortars with competitive performances (mechanical strengths similar/better than PC), but reducing the CO_2 emissions up to 17% during their production (when compared to PC).

From the first part (basic science, PDF methodology) some conclusions can be highlighted:

1. A multi r-range PDF analysis approach has been established to characterise the different components (crystalline, nanocrystalline and amorphous) of hydrated samples. Specifically, for C-S-H gels coming from alite: (i) the 40–70 Å r-range allows determining the crystalline phase contents, also confirmed by Rietveld methodology; (ii) the 10–25 Å r-range allows the characterisation of the nanocrystalline atomic ordering in the calcium silicate hydrate constituent of the C-S-H gel; and (iii) the 2–10 Å r-range provides information about additional amorphous components, viz. a monolayer of portlandite.

2. Clinotobermorite (defective tobermorite) was confirmed to fit better the total scattering data of C-S-H gel produced by the hydration of alite than jennite or tobermorite-14. In addition, it has been also confirmed that different water to alite mass ratios, the polymorphism of alite or the temperature do not modify the nanocrystalline nature of the resulting C-S-H gels.

3. The *in-situ* hydration study with monoclinic C_3S confirmed the average stoichiometry of the gel formed in this hydration reaction to be $(CaO)_{1.8}SiO_2(H_2O)_{4.0}$. By multi-r PDF approach a model to describe the

heterogeneous nature of this gel with 1/9 moles of layers with formula $Ca_{11}Si_9O_{28}(OH)_2(H_2O)_{8.5}$, 0.58 moles of monolayers of $Ca(OH)_2$ and 2.36 moles of H_2O in the gel pores is proposed. This heterogeneous nanostructure justifies the observed mass densities and Ca/Si atomic ratios at the microscale.

4. By using synchrotron PDF data, it has also been demonstrated that the precipitated AH_3-gel in ye'elimite with calcium sulphate pastes has a nanocrystalline gibbsite nature. The spdiameter values for gibbsite, which measures the average particle sizes for the phases in the sulphoaluminate pastes, are close to 30 Å. The gibbsite peaks in the ye'elimite sulphate source paste are hardly visible and PDF analysis methodology gave a relatively good fit. Furthermore, the analysis of the thermogravimetric data for the ye'elimite pastes gave a large water content, close to $Al(OH)_3(H_2O)_{0.7}$. We justify these results as the very small particle sizes of the gel in the ye'elimite pastes, smaller than 30 Å, can retain the water in the inter-particle pores.

5. For the $C_4A_3\bar{S}$ pastes without sulphate source addition, ettringite was not found and two calcium aluminium monosulphate phases were required in order to properly fit the PDF data. One phase is the well-known crystalline AFm phase but the second phase is nanocrystalline, with particle size of ~60 Å, and a significantly smaller c-unit cell parameter value. This nanocrystalline AFm phase is also required for intermediate sulphate source dosage, 15.5 wt%, but its content is much smaller, ~6 wt% of the ye'elimite pastes. For a large sulphate source dosage, 31 wt%, ettringite is the main crystalline phase with the aluminium hydroxide having nano-gibbsite local structure. The particle size of nano-gibbsite was 30-40 Å when formed under the employed experimental conditions.

From the applied science part, about the synthesis, processing and hydration-understanding of two new alite-belite-ye'elimite eco-cements, important conclusions can be emphasized:

1. The methodology to prepare ~2 kg of standard ABY clinker (by combining natural raw materials) with coexistence of 41.5 wt% mC_3S, 28.4 wt% of βC_2S and 17.4 wt% $C_4A_3\bar{S}$, as main crystalline phases, was determined by adding 1.0 wt% of CaF_2 and 1.0 wt% of ZnO as mineralisers to the raw material. The optimised thermal treatment was: heating up to 900°C/30 min, and from there, to 1300°C for 15 min, and

finally quenching to RT in batches of 90 g of resulting clinker. Heating rate: 5ºC/min.

2. Additionally, another ABY clinker was synthesised by doping with 0.6 wt% B_2O_3 and 0.3 wt% Na_2O, added as borax. This doped ABY contains 15.7 wt% mC_3S, 41.8 wt% of βC_2S, 18.0 wt% of $\alpha'_H C_2S$ and 7.7 wt% $C_4A_3\bar{S}$, as main phases. The addition of other elements such as Na_2O or K_2O, or higher amounts of borax was ruled out as no stabilisation of high temperature belite polymorphs or coexistence of alite with ye'elimite were achieved.

3. An EDS study on ABY and dABY clinkers revealed that Zn and F are mainly incorporated into ferrite and alite, and sulphur is preferably incorporated into fluorellestadite, ye'elimite (as expected) and, in lower concentrations, in belite and ferrite. The elemental composition of the amorphous fraction is close to amorphous calcium aluminates in both clinkers.

4. The resulting cements (prepared by adding anhydrite) were hydrated (0.40 and 0.50 w/c) and some conclusions can be drawn:

   4.1. The higher quantity of $C_{12}A_7$ in dABY paste produces an increment in reactivity and consequently in viscosity and heat released up to 3 hours.

   4.2. mC_3S hydration behaviour is strongly affected by the amount of $C_4A_3\bar{S}$. Thus, the higher content of $C_4A_3\bar{S}$ in ABY paste is the responsible of the slower reactivity of mC_3S.

5. The study has also determined that borax addition plays two roles:

   5.1. Role of retarder: the acceleration period has been delayed up to ~15 hours in dABY.

   5.2. Role of activator: Dicalcium silicates in dABY are more reactive than in ABY, independently of the polymorphism type. The degree of hydration of βC_2S in ABY is 42% at 28 days of hydration while in dABY, it is 80 and 88% for βC_2S and $\alpha'_H C_2S$, respectively, at the same age. Consequently, the mechanical properties have been enhanced.

6. In both (ABY and dABY) systems, the hydration product of mC_3S and all polymorphs of C_2S is C-S-H gel, as no stratlingite was found at any hydration time (confirmed by XRD and ^{27}Al MAS-NMR). The nature of

this C-S-H gel seems to be similar in both systems, although higher amounts of this hydration product were found in dABY paste (due to its higher belite degree of reaction).

7. The optimisation of both cement pastes (in terms of percentage of superplasticiser and water content) through their rheological behaviour allowed the preparation of homogeneous ABY and dABY pastes and mortars. The control of the initial viscosity and its evolution with time during the first minutes of hydration is crucial to prepare homogeneous samples, with good performances. No relevant variances in the phase assemblage justify the differences in the mechanical strengths.

8. The processing results key to get good mechanical performances. The optimised ABY (0.40w/c_1.0wt%SP) and dABY (0.50w/c_0.4wt%SP) mortars showed compressive strengths close to PC, but saving up to ~17% CO_2. The optimised ABY mortar showed compressive strengths of 53.0, 71.6, 76.6, 86.9, 98.2 MPa and dABY 16.8, 40.7, 74.9, 81.9 and 83.3 MPa at 1, 7, 28, 56 and 180 days. The optimised dBAY mortar showed an important increase in compressive strength from 7 to 28 days due to the higher content and reaction of belite polymorphs forming C-S-H gel.

9. The objective of enhancing the performances of this type of material (ABY and dABY) by doping with boron has been achieved as the ratio CO_2/MPa has decreased from 0.018 to 0.011.

6.2. Perspectives

During this research work, some questions have been left open without an answer and some additional tasks will be needed to carry out in a near future:

1. The clinkering temperature of dABY could be reduced 50 or 100ºC (1200 or 1250ºC instead of 1300ºC) due to the boron fluxing effect, with the consequent save in energy consumption and emissions.

2. The heterogeneous description of C-S-H gel (nano, meso and micro-scale) will explain a striking feature of the hydration of blended cements with active pozzolanes, such as fly ash, where CH content is measured to decrease much less than predicted by thermodynamic modelling. Although portlandite is still present, the Ca/Si ratio in C-S-H gel is observed to decrease from close to 1.8 in plain pastes to close to 1.4 in

fly ash blends. This is now explained by the consumption of CH monolayer component (nano CH) of the C-S-H gel in the pozzolanic reaction. This needs further research that supports this hypothesis.

3. The full description of C-S-H gel from belite hydration.

4. The addition of fly ash, calcined clay or nano-SiO_2 to dABY cement to enhance mechanical properties. It needs to be clarify if the pozzolanic reaction takes place in these systems and if positive, the degree and the effect on hydration products, mechanical properties and durability.

5. The role of different sulphate sources (gypsum, bassanite and anhydrite) as setting time regulators.

7. REFERENCES

1. Garside M (2019) Major countries in worldwide cement production from 2014 to 2018 (in million metric tons). In: statista. https://www.statista.com/statistics/267364/world-cement-production-by-country/. Accessed 17 Jan 2020
2. Maddalena R, Roberts JJ, Hamilton A (2018) Can Portland cement be replaced by low-carbon alternative materials? A study on the thermal properties and carbon emissions of innovative cements. Journal of Cleaner Production 186:933–942. https://doi.org/10.1016/J.JCLEPRO.2018.02.138
3. Jennings HM (2000) A model for the microstructure of calcium silicate hydrate in cement paste. Cement and Concrete Research 30:101–116. https://doi.org/10.1016/S0008-8846(99)00209-4
4. Dharmawardhana CC, Misra A, Ching W-Y (2015) Quantum Mechanical Metric for Internal Cohesion in Cement Crystals. Scientific Reports 4:7332. https://doi.org/10.1038/srep07332
5. Mahlia TM. (2002) Emissions from electricity generation in Malaysia. Renewable Energy 27:293–300. https://doi.org/10.1016/S0960-1481(01)00177-X
6. Zhang XF, Zhang SY, Hu ZY, et al (2012) Identification of connection units with high GHG emissions for low-carbon product structure design. Journal of Cleaner Production 27:118–125. https://doi.org/10.1016/J.JCLEPRO.2012.01.011
7. Hewlett PC, Liska M (2017) Lea's Chemistry of Cement and Concrete, 5th ed. Elsevier
8. Jewell Sally, Kimball Suzette M. (2017) Mineral Commodity Summaries 2017. USGS science for a changing world, Virginia
9. Gartner E (2004) Industrially interesting approaches to "low-CO2" cements. Cement and Concrete Research 34:1489–1498. https://doi.org/10.1016/j.cemconres.2004.01.021
10. Armstrong T (2018) A review of global cement industry trends. In: International Cement Review. https://cmaindia.org/wp-content/themes/cmaindia/ppt/ppt3_icr.pdf. Accessed 17 Jan 2020
11. Miller SA, John VM, Pacca SA, Horvath A (2018) Carbon dioxide reduction potential in the global cement industry by 2050. Cement and Concrete Research 114:115–124. https://doi.org/10.1016/j.cemconres.2017.08.026
12. Habert G, Billard C, Rossi P, et al (2010) Cement production technology improvement compared to factor 4 objectives. Cement and Concrete Research 40:820–826. https://doi.org/10.1016/J.CEMCONRES.2009.09.031
13. Damtoft JS, Lukasik J, Herfort D, et al (2008) Sustainable development and climate change initiatives. Cement and Concrete Research 38:115–127. https://doi.org/10.1016/J.CEMCONRES.2007.09.008
14. Gartner E (2004) Industrially interesting approaches to "low-CO2" cements. Cement and Concrete Research 34:1489–1498. https://doi.org/10.1016/J.CEMCONRES.2004.01.021
15. Shi C, Qu B, Provis JL (2019) Recent progress in low-carbon binders. Cement and Concrete Research 122:227–250. https://doi.org/10.1016/J.CEMCONRES.2019.05.009
16. Schneider M (2019) The cement industry on the way to a low-carbon future. Cement and Concrete Research 124:105792. https://doi.org/10.1016/J.CEMCONRES.2019.105792
17. Olivier JGJ, Janssens-Maenhout G, Muntean M, Peters JAHW (2016) Trends in global CO2 emissions:2016 report. PBL Publishers, The Hague
18. UN Environment, Scrivener KL, John VM, Gartner E (2018) Eco-efficient cements: Potential, economically viable solutions for a low-CO2, cement-based materials

industry. Cement and Concrete Research 114:2–26. https://doi.org/10.1016/j.cemconres.2018.03.015
19. Chatziaras N, Psomopoulos CS, Themelis NJ (2014) Use of alternative fuels in cement industry. 12th International Conference on Protection and Restoration of the Environment 1:521–529. https://doi.org/ISBN 978-960-88490-6-8
20. Karstensen KH (2008) Formation, release and control of dioxins in cement kilns. Chemosphere 70:543–560
21. Gartner E, Hirao H (2015) A review of alternative approaches to the reduction of CO2 emissions associated with the manufacture of the binder in concrete. Cem Concr Res 78:126–142
22. Juenger MCG, Siddique R (2015) Recent advances in understanding the role of supplementary cementitious materials in concrete. Cement and Concrete Research 78:71–80. https://doi.org/10.1016/j.cemconres.2015.03.018
23. Scrivener K, Martirena F, Bishnoi S, Maity S (2018) Calcined clay limestone cements (LC3). Cement and Concrete Research 114:49–56. https://doi.org/10.1016/J.CEMCONRES.2017.08.017
24. Galvez-Martos J-L, Schoenberger H (2014) An analysis of the use of life cycle assessment for waste co-incineration in cement kilns. Resources, Conservation and Recycling 86:118–131. https://doi.org/10.1016/J.RESCONREC.2014.02.009
25. Juenger MCG, Snellings R, Bernal SA (2019) Supplementary cementitious materials: New sources, characterization, and performance insights. Cement and Concrete Research 122:257–273. https://doi.org/10.1016/J.CEMCONRES.2019.05.008
26. Schneider M (2015) Process technology for efficient and sustainable cement production. Cement and Concrete Research 78:14–23. https://doi.org/10.1016/J.CEMCONRES.2015.05.014
27. Hanein T, Galvez-Martos J-L, Bannerman MN (2018) Carbon footprint of calcium sulfoaluminate clinker production. Journal of Cleaner Production 172:2278–2287. https://doi.org/10.1016/j.jclepro.2017.11.183
28. Juenger MCG, Winnefeld F, Provis JL, Ideker JH (2011) Advances in alternative cementitious binders. Cement and Concrete Research 41:1232–1243. https://doi.org/10.1016/j.cemconres.2010.11.012
29. Aranda MAG, De la Torre AG (2013) Sulfoaluminate cement in Eco-efficient concrete; Pacheco-Torgal, F. Ed.; Jalali, S. Ed. Labrincha, J. Ed. Woodhead Publishing: Cambridge 488–522
30. Taylor HFW (1997) Cement chemistry, 2nd ed. Thomas Telford Pub
31. Odler I (2000) Special inorganic cements. E & FN Spon
32. Ectors D, Neubauer J, Goetz-Neunhoeffer F (2013) The hydration of synthetic brownmillerite in presence of low Ca-sulfate content and calcite monitored by quantitative in-situ-XRD and heat flow calorimetry. Cement and Concrete Research 54:61–68. https://doi.org/10.1016/J.CEMCONRES.2013.08.011
33. Aranda MAG (2020) Belite cements: status in 2020. Cement and Concrete Research submitted:
34. Popescu CD, Muntean M, Sharp JH (2003) Industrial trial production of low energy belite cement. Cement and Concrete Composites 25:689–693. https://doi.org/10.1016/S0958-9465(02)00097-5
35. Pimraksa K, Hanjitsuwan S, Chindaprasirt P (2009) Synthesis of belite cement from lignite fly ash. Ceramics International 35:2415–2425. https://doi.org/10.1016/j.ceramint.2009.02.006
36. Kacimi L, Simon-Masseron A, Salem S, et al (2009) Synthesis of belite cement clinker of high hydraulic reactivity. Cement and Concrete Research 39:559–565.

https://doi.org/10.1016/j.cemconres.2009.02.004
37. Chatterjee AK (1996) High belite cements - present status and future technological options: Part I. Cement and Concrete Research 26:1213–1225. https://doi.org/10.1016/0008-8846(96)00099-3
38. Van Vliet K, Pellenq R, Buehler MJ, et al (2012) Set in stone? A perspective on the concrete sustainability challenge. MRS Bulletin 37:395–402. https://doi.org/10.1557/mrs.2012.55
39. Morsli K, de la Torre Á G, Zahir M, Aranda MAG (2007) Mineralogical phase analysis of alkali and sulfate bearing belite rich laboratory clinkers. Cement and Concrete Research 37:639–646
40. Morsli K, De La Torre AG, Stöber S, et al (2007) Quantitative phase analysis of laboratory-active belite clinkers by synchrotron powder diffraction. Journal of the American Ceramic Society 90:3205–3212. https://doi.org/https://doi.org/10.1111/j.1551-2916.2007.01870.x
41. Chatterjee AK (2003) High-Belite Portland Cement – an Update on Development, Characterization and Applications. 11th International Congress on the Chemistry of Cement 31–40
42. Paul G, Boccaleri E, Buzzi L, et al (2015) Friedel's salt formation in sulfoaluminate cements: A combined XRD and 27Al MAS NMR study. Cement and Concrete Research 67:93–102. https://doi.org/10.1016/J.CEMCONRES.2014.08.004
43. European Technical Approval ETA 13/0418.
44. European Technical Approval ETA 13/0417.
45. Sahu S, Majling J (1993) Phase compatibility in the system CaO - SiO2 - Al2O3 - Fe2O3 - SO3 referred to sulphoaluminate belite cement clinker. Cement and Concrete Research 23:1331–1339
46. Imbabi MS, Carrigan C, McKenna S (2012) Trends and developments in green cement and concrete technology. International Journal of Sustainable Built Environment 1:194–216. https://doi.org/10.1016/J.IJSBE.2013.05.001
47. Winnefeld F, Lothenbach B (2010) Hydration of calcium sulfoaluminate cements — Experimental findings and thermodynamic modelling. Cement and Concrete Research 40:1239–1247
48. Glasser FP, Zhang L (2001) High-performance cement matrices based on calcium sulfoaluminate – belite compositions. Cement and Concrete Research 31:1881–1886
49. Péra J, Ambroise J (2004) New applications of calcium sulfoaluminate cement. Cement and Concrete Research 34:671–676. https://doi.org/10.1016/j.cemconres.2003.10.019
50. Ben Haha M, Winnefeld F, Pisch A (2019) Advances in understanding ye'elimite-rich cements. Cement and Concrete Research 123:105778. https://doi.org/10.1016/J.CEMCONRES.2019.105778
51. Allevi S, Marchi M, Scotti F, et al (2016) Hydration of calcium sulphoaluminate clinker with additions of different calcium sulphate sources. Materials and Structures 49:453–466. https://doi.org/10.1617/s11527-014-0510-5
52. Sharp JH, Lawrence CD, Yang R (1999) Calcium sulfoaluminate cements—low-energy cements, special cements or what? Advances in Cement Research 11:3–13. https://doi.org/10.1680/adcr.1999.11.1.3
53. García-Maté M, De La Torre AG, León-Reina L, et al (2013) Hydration studies of calcium sulfoaluminate cements blended with fly ash. Cement and Concrete Research 54:12–20. https://doi.org/10.1016/j.cemconres.2013.07.010
54. Trauchessec R, Mechling JM, Lecomte A, et al (2015) Hydration of ordinary Portland cement and calcium sulfoaluminate cement blends. Cement and Concrete

Composites 56:106–114. https://doi.org/10.1016/j.cemconcomp.2014.11.005
55. Le Saoût G, Lothenbach B, Hori A, et al (2013) Hydration of Portland cement with additions of calcium sulfoaluminates. Cement and Concrete Research 43:81–94. https://doi.org/10.1016/J.CEMCONRES.2012.10.011
56. Pelletier L, Winnefeld F, Lothenbach B (2010) The ternary system Portland cement–calcium sulphoaluminate clinker–anhydrite: Hydration mechanism and mortar properties. Cement and Concrete Composites 32:497–507. https://doi.org/10.1016/J.CEMCONCOMP.2010.03.010
57. Gartner E, Sui T (2017) Alternative cement clinkers. Cement and Concrete Research. https://doi.org/10.1016/j.cemconres.2017.02.002
58. Morsli K, De la Torre AG, Zahir M, Aranda MAG (2007) Mineralogical phase analysis of alkali and sulfate bearing belite rich laboratory clinkers. Cement and Concrete Research 37:639–646. https://doi.org/10.1016/j.cemconres.2007.01.012
59. Shi C, Jiménez AF (2011) New cements for the 21st century: The pursuit of an alternative to Portland cement. Cement and Concrete Research 41:750–763. https://doi.org/10.1016/J.CEMCONRES.2011.03.016
60. Li C, Wu M, Yao W (2019) Eco-efficient Cementitious System Consisting of Belite-Ye'elimite-Ferrite Cement, Limestone Filler, and Silica Fume. ACS Sustainable Chemistry & Engineering 7:7941–7950. https://doi.org/10.1021/acssuschemeng.9b00702
61. Bescher E, Kim J (2019) Belitic Calcium Sulfoaluminate Cement: History, Chemistry, Performance, and Use in the United States. In: Conference: 1st International Conference on Innovation in Low Carbon Cement and Concrete Technology. London, UK
62. Sorrentino F (2011) Chemistry and engineering of the production process: State of the art. Cement and Concrete Research 41:616–623. https://doi.org/10.1016/J.CEMCONRES.2011.03.013
63. Cuberos AJM, De la Torre AG, Alvarez-Pinazo G, et al (2010) Active iron-rich belite sulfoaluminate cements: clinkering and hydration. Environmental science technology 44:6855–6862
64. Álvarez-Pinazo G, Santacruz I, León-Reina L, et al (2013) Hydration reactions and mechanical strength developments of iron-rich sulfobelite eco-cements. Industrial and Engineering Chemistry Research 52:16606–16614. https://doi.org/10.1021/ie402484e
65. Martín-Sedeño MC, Cuberos AJM, De La Torre AG, et al (2010) Aluminum-rich belite sulfoaluminate cements: Clinkering and early age hydration. Cement and Concrete Research 40:359–369. https://doi.org/10.1016/j.cemconres.2009.11.003
66. Baxter DC, Faarinen M, Österlund H, et al (2011) Serum/plasma methylmercury determination by isotope dilution gas chromatography-inductively coupled plasma mass spectrometry. Analytica Chimica Acta 701:134–138. https://doi.org/10.1016/j.aca.2011.06.012
67. Ost BWA, Schiefelbein B, Summerfield JM (1975) Very high early strength cement
68. Álvarez-Pinazo G, Cuesta A, García-Maté M, et al (2014) In-situ early-age hydration study of sulfobelite cements by synchrotron powder diffraction. Cement and Concrete Research 56:12–19. https://doi.org/10.1016/j.cemconres.2013.10.009
69. De La Torre ÁG, Cuberos AJM, Álvarez-Pinazo G, et al (2011) In situ powder diffraction study of belite sulfoaluminate clinkering. Journal of Synchrotron Radiation 18:506–514. https://doi.org/10.1107/S0909049511005796
70. Pérez-Bravo R, Losilla ER, Álvarez-Pinazo G, et al (2014) Alite sulfoaluminate clinker: Rietveld mineralogical and SEM-EDX analysis. Advances in Cement Research 26:10–

20. https://doi.org/10.1680/adcr.12.00044
71. Londono-Zuluaga D, Tobón JI, Aranda MAGAG, et al (2017) Clinkering and hydration of belite-alite-ye'elimite cement. Cement and Concrete Composites 80:333–341
72. Chitvoranund N, Lothenbach B, Winnefeld F, Hargis CW (2016) Synthesis and hydration of alite-calcium sulfoaluminate cement. https://doi.org/10.1680/jadcr.16.00071
73. Ma S, Shen X, Gong X, Zhong B (2006) Influence of CuO on the formation and coexistence of 3CaO·SiO2 and 3CaO·3Al2O3·CaSO4 minerals. Cement and Concrete Research 36:1784–1787. https://doi.org/10.1016/J.CEMCONRES.2006.05.030
74. Liu X, Li Y (2005) Effect of MgO on the composition and properties of alite-sulphoaluminate cement. Cement and Concrete Research 35:1685–1687. https://doi.org/10.1016/j.cemconres.2004.08.008
75. Shoude W, Cheng C, Lingchao L, Xin C (2012) Effects of slag and limestone powder on the hydration and hardening process of alite-barium calcium sulphoaluminate cement. Construction and Building Materials 35:227–231. https://doi.org/10.1016/j.conbuildmat.2012.03.004
76. Londono-Zuluaga D, Tobón JI, Aranda MAG, et al (2018) Influence of fly ash blending on hydration and physical behavior of belite–alite–ye'elimite cements. Materials and Structures 51:128. https://doi.org/10.1617/s11527-018-1246-4
77. Meller N, Hall C, Jupe AC, et al (2004) The paste hydration of brownmillerite with and without gypsum: a time resolved synchrotron diffraction study at 30, 70, 100 and 150 °C. J Mater Chem 14:428–435. https://doi.org/10.1039/B313215C
78. Stöber S, Pöllmann H (2003) Investigations on the Hydration of Cac At 25 … 45 ° C By Isoperibolic Heat Flow Calorimetry and Xray Diffraction (Xrd). 11th International Congress on the Chemistry of Cement 719–726
79. Morin V, Walenta G, Gartner E, et al (2011) Hydration of a Belite-Calcium Sulfoaluminate-Ferrite cement : AetherTM. In: Palomo Á, Zaragoza A, López Agüí JC (eds) 13th International Congress on the Chemistry of Cements. Madrid, p 188
80. Dilnesa BZ, Lothenbach B, Renaudin G, et al (2014) Synthesis and characterization of hydrogarnet Ca3(AlxFe1 − x)2(SiO4)y(OH)4(3 − y). Cement and Concrete Research 59:96–111. https://doi.org/10.1016/J.CEMCONRES.2014.02.001
81. L'Hôpital E, Lothenbach B, Le Saout G, et al (2015) Incorporation of aluminium in calcium-silicate-hydrates. Cement and Concrete Research 75:91–103. https://doi.org/10.1016/J.CEMCONRES.2015.04.007
82. Dilnesa BZ, Wieland E, Lothenbach B, et al (2014) Fe-containing phases in hydrated cements. Cement and Concrete Research 58:45–55. https://doi.org/10.1016/j.cemconres.2013.12.012
83. Scrivener K, Snellings R, Lothenbach B (2016) A Practical Guide to Microstructural Analysis of Cementitious Materials. CRC Press, Boca Raton, FL
84. Palacios M, Houst YF, Bowen P, Puertas F (2009) Adsorption of superplasticizer admixtures on alkali-activated slag pastes. Cement and Concrete Research 39:670–677. https://doi.org/10.1016/J.CEMCONRES.2009.05.005
85. Papo A, Piani L (2004) Effect of various superplasticizers on the rheological properties of Portland cement pastes. Cement and Concrete Research 34:2097–2101. https://doi.org/10.1016/J.CEMCONRES.2004.03.017
86. Björnström J, Chandra S (2003) Effect of superplasticizers on the rheological properties of cements. Materials and Structures 36:685–692. https://doi.org/10.1007/BF02479503
87. Puertas F, Santos H, Palacios M, Martínez-Ramírez S (2005) Polycarboxylate superplasticiser admixtures: effect on hydration, microstructure and rheological

behaviour in cement pastes. Advances in Cement Research 17:77–89. https://doi.org/10.1680/adcr.2005.17.2.77
88. Gołaszewski J (2012) Influence of cement properties on new generation superplasticizers performance. Construction and Building Materials 35:586–596. https://doi.org/10.1016/J.CONBUILDMAT.2012.04.070
89. Ridi F, Dei L, Fratini E, et al (2003) Hydration Kinetics of Tri-calcium Silicate in the Presence of Superplasticizers. https://doi.org/10.1021/JP027346B
90. J. Rieger *,†, J. Thieme ‡ and, Schmidt‡ C (2000) Study of Precipitation Reactions by X-ray Microscopy: CaCO3 Precipitation and the Effect of Polycarboxylates. https://doi.org/10.1021/LA0004193
91. Chang W, Li H, Wei M, et al (2009) Effects of polycarboxylic acid based superplasticiser on properties of sulphoaluminate cement. Materials Research Innovations 13:7–10. https://doi.org/10.1179/143307509X402101
92. García-Maté M, Santacruz I, De La Torre ÁG, et al (2012) Rheological and hydration characterization of calcium sulfoaluminate cement pastes. Cement and Concrete Composites 34:684–691
93. García-Maté M, Londono-Zuluaga D, De la Torre AG, et al (2016) Tailored setting times with high compressive strengths in bassanite calcium sulfoaluminate eco-cements. Cement and Concrete Composites 72:39–47. https://doi.org/10.1016/j.cemconcomp.2016.05.021
94. Łaźniewska-Piekarczyk B (2014) The methodology for assessing the impact of new generation superplasticizers on air content in self-compacting concrete. Construction and Building Materials 53:488–502. https://doi.org/10.1016/j.conbuildmat.2013.11.092
95. De la Torre AG, Santacruz I, Cuesta A, et al (2017) Diffraction and crystallography applied to anhydrous cements. In: Pöllmann H (ed) Cementitious Materials. Composition, Properties, Application. De Gruyter Publising, Berlin, Germany, pp 3–29
96. Aranda MAG, Cuesta A, De la Torre AG, et al (2017) Diffraction and crystallography applied to hydrating cements. In: Pöllmann H (ed) Cementitious Materials. De Gruyter, Berlin, Boston, pp 31–60
97. Egami T, Billinge SJL (2012) Underneath the Bragg Peaks : Structural Analysis of Complex Materials., 2nd ed. Elsevier Science, Pergamon
98. Billinge SJL, Kanatzidis MG (2004) Beyond crystallography: the study of disorder, nanocrystallinity and crystallographically challenged materials with pair distribution functions. Chemical Communications 0:749–760. https://doi.org/10.1039/b309577k
99. Farrow CL, Billinge SJL (2009) Relationship between the atomic pair distribution function and small-angle scattering: Implications for modeling of nanoparticles. Acta Crystallographica Section A: Foundations of Crystallography 65:232–239. https://doi.org/10.1107/S0108767309009714
100. Billinge SJL, Kanatzidis MG (2004) Beyond crystallography: the study of disorder, nanocrystallinity and crystallographically challenged materials with pair distribution functions. Chemical Communications 749. https://doi.org/10.1039/b309577k
101. Billinge SJL, Thorpe MF (2002) Local Structure from Diffraction. 137–146. https://doi.org/10.1007/b119172
102. Toby BH, Egami T (1992) Accuracy of pair distribution function analysis applied to crystalline and non-crystalline materials. Acta Crystallographica Section A 48:336–346. https://doi.org/10.1107/S0108767391011327
103. Yavuz M (2016) Investigation of Local and Average Structure in Li-ion Battery Electrode Materials by X-ray Diffraction. Technische Universität Darmstadt
104. Peterson J, TenCate J, Proffen T, et al (2013) Quantifying amorphous and crystalline

phase content with the atomic pair distribution function. Journal of Applied Crystallography 46:332–336. https://doi.org/10.1107/S0021889812050595
105. Sławiński WA (2018) Calculation of pair distribution functions for multiphase systems. Journal of Applied Crystallography 51:919–923. https://doi.org/10.1107/S1600576718004089
106. Olds D, Saunders CN, Peters M, et al (2018) Precise implications for real-space pair distribution function modeling of effects intrinsic to modern time-of-flight neutron diffractometers. Acta Crystallographica Section A Foundations and Advances 74:293–307. https://doi.org/10.1107/S2053273318003224
107. Papatzani S, Paine K, Calabria-Holley J (2015) A comprehensive review of the models on the nanostructure of calcium silicate hydrates. Construction and Building Materials 74:219–234. https://doi.org/10.1016/j.conbuildmat.2014.10.029
108. Aranda MAG (2016) Recent studies of cements and concretes by synchrotron radiation crystallographic and cognate methods. Crystallography Reviews 22:150–196. https://doi.org/10.1080/0889311X.2015.1070260
109. Meral C, Benmore CJ, Monteiro PJM (2011) The study of disorder and nanocrystallinity in C–S–H, supplementary cementitious materials and geopolymers using pair distribution function analysis. Cement and Concrete Research 41:696–710. https://doi.org/10.1016/J.CEMCONRES.2011.03.027
110. Skinner LB, Chae SR, Benmore CJ, et al (2010) Nanostructure of Calcium Silicate Hydrates in Cements. Physical Review Letters 104:195502. https://doi.org/10.1103/PhysRevLett.104.195502
111. White CE (2016) Effects of temperature on the atomic structure of synthetic calcium–silicate–deuterate gels: A neutron pair distribution function investigation. Cement and Concrete Research 79:93–100. https://doi.org/10.1016/J.CEMCONRES.2015.09.001
112. White CE, Daemen LL, Hartl M, Page K (2015) Intrinsic differences in atomic ordering of calcium (alumino)silicate hydrates in conventional and alkali-activated cements. Cement and Concrete Research 67:66–73. https://doi.org/10.1016/j.cemconres.2014.08.006
113. Grangeon S, Fernandez-Martinez A, Baronnet A, et al (2017) Quantitative X-ray pair distribution function analysis of nanocrystalline calcium silicate hydrates: a contribution to the understanding of cement chemistry. Journal of Applied Crystallography 50:14–21. https://doi.org/10.1107/S1600576716017404
114. Billinge S (2008) Chapter 16. Local Structure from Total Scattering and Atomic Pair Distribution Function (PDF) Analysis. In: Powder Diffraction. Royal Society of Chemistry, Cambridge, pp 464–493
115. Proffen T, Kim H (2009) Advances in total scattering analysis. Journal of Materials Chemistry 19:5078. https://doi.org/10.1039/b821178g
116. Farrow CL, Juhas P, Liu JW, et al (2007) PDFfit2 and PDFgui: computer programs for studying nanostructure in crystals. Journal of Physics: Condensed Matter 19:335219. https://doi.org/10.1088/0953-8984/19/33/335219
117. Winnefeld F, Barlag S (2010) Calorimetric and thermogravimetric study on the influence of calcium sulfate on the hydration of ye'elimite. Journal of Thermal Analysis and Calorimetry 101:949–957. https://doi.org/10.1007/s10973-009-0582-6
118. Álvarez-Pinazo G, Cuesta A, García-Maté M, et al (2012) Rietveld quantitative phase analysis of Yeelimite-containing cements. Cement and Concrete Research 42:960–971. https://doi.org/10.1016/j.cemconres.2012.03.018
119. Barnett SJ, Macphee DE, Lachowski EE, Crammond NJ (2002) XRD, EDX and IR analysis of solid solutions between thaumasite and ettringite. Cement and Concrete

Research 32:719–730. https://doi.org/10.1016/S0008-8846(01)00750-5
120. Fauth F, Peral I, Popescu C, Knapp M (2013) The new Material Science Powder Diffraction beamline at ALBA Synchrotron. Powder Diffraction 28:S360–S370. https://doi.org/10.1017/S0885715613000900
121. Juhas P, Davis T, Farrow CL, Billinge SJL (2013) PDFgetX3: A rapid and highly automatable program for processing powder diffraction data into total scattering pair distribution functions. Journal of Applied Crystallography 46:560–566. https://doi.org/10.1107/S0021889813005190
122. Jeong IK, Proffen T, Mohiuddin-Jacobs F, Billinge S. JL (1999) Measuring Correlated Atomic Motion Using X-ray Diffraction. The Journal of Physical Chemistry C 103:921–924. https://doi.org/10.1021/JP9836978
123. Jeong IK, Heffner RH, Graf MJ, Billinge SJL (2003) Lattice dynamics and correlated atomic motion from the atomic pair distribution function. Physical Review B - Condensed Matter and Materials Physics 67:104301. https://doi.org/10.1103/PhysRevB.67.104301
124. Von Dreele RB, Larson AC (2004) General structure analysis system (GSAS). Los Alamos National Laboratory Report LAUR 748:86–748
125. Bragg WH, Bragg WL (1913) The Reflection of X-rays by Crystals References. Proc R Soc London Ser A 88:428–438. https://doi.org/10.1098/rspa.1913.0040
126. Thompson P, Cox DE, Hastings JB (1987) Rietveld Refinement of Debye-Scherrer Synchrotron X-ray Data from A1203. Journal of Applied Crystallography 20:79–83. https://doi.org/10.1107/S0021889887087090
127. Finger LW, Cox DE, Jephcoat AP (1994) Correction for powder diffraction peak asymmetry due to axial divergence. Journal of Applied Crystallography 27:892–900. https://doi.org/10.1107/S0021889894004218
128. Dollase WA (1986) Correction of intensities of preferred orientation in powder diffractometry: application of the march model. Journal of Applied Crystallography 19:267–272. https://doi.org/10.1107/S0021889886089458
129. De La Torre AG, Bruque S, Aranda MAG (2001) Rietveld quantitative amorphous content analysis. Journal of Applied Crystallography 34:196–202. https://doi.org/10.1107/S0021889801002485
130. Jansen D, Goetz-Neunhoeffer F, Stabler C, Neubauer J (2011) A remastered external standard method applied to the quantification of early OPC hydration. Cement and Concrete Research 41:602–608. https://doi.org/10.1016/j.cemconres.2011.03.004
131. O'Connor BH, Raven MD (1988) Application of the Rietveld Refinement Procedure in Assaying Powdered Mixtures. Powder Diffraction 3:2–6. https://doi.org/10.1017/S0885715600013026
132. Jansen D, Stabler C, Goetz-Neunhoeffer F, et al (2011) Does Ordinary Portland Cement contain amorphous phase? A quantitative study using an external standard method. Powder Diffraction 26:31–38. https://doi.org/10.1154/1.3549186
133. Winnefeld F, Lothenbach B (2010) Hydration of calcium sulfoaluminate cements — Experimental findings and thermodynamic modelling. Cement and Concrete Research 40:1239–1247. https://doi.org/10.1016/J.CEMCONRES.2009.08.014
134. Telesca A, Marroccoli M, Pace ML, et al (2014) A hydration study of various calcium sulfoaluminate cements. Cement and Concrete Composites 53:224–232. https://doi.org/10.1016/j.cemconcomp.2014.07.002
135. Song F, Yu Z, Yang F, et al (2015) Microstructure of amorphous aluminum hydroxide in belite-calcium sulfoaluminate cement. Cement and Concrete Research 71:1–6. https://doi.org/10.1016/j.cemconres.2015.01.013
136. Scrivener KL, Füllmann T, Gallucci E, et al (2004) Quantitative study of Portland

cement hydration by X-ray diffraction/Rietveld analysis and independent methods. Cement and Concrete Research 34:1541–1547. https://doi.org/10.1016/j.cemconres.2004.04.014

137. Puertas F, García-Díaz I, Palacios M, et al (2010) Clinkers and cements obtained from raw mix containing ceramic waste as a raw material. Characterization, hydration and leaching studies. Cement and Concrete Composites 32:175–186. https://doi.org/10.1016/j.cemconcomp.2009.11.011
138. Richardson IG (2014) Model structures for C-(A)-S-H(I). Acta Crystallographica Section B Structural Science, Crystal Engineering and Materials 70:903–923. https://doi.org/10.1107/S2052520614021982
139. Bonaccorsi E, Merlino S, Taylor HFW (2004) The crystal structure of jennite, Ca9Si6O18(OH)6·8H2O. Cement and Concrete Research 34:1481–1488. https://doi.org/10.1016/J.CEMCONRES.2003.12.033
140. Bonaccorsi E, Merlino S, Kampf AR (2005) The crystal structure of tobermorite 14 Å (plombierite), a C-S-H phase. Journal of the American Ceramic Society 88:505–512. https://doi.org/10.1111/j.1551-2916.2005.00116.x
141. Merlino S, Bonaccorsi E, Armbruster T (2001) The real structure of tobermorite 11Å: Normal and anomalous forms, OD character and polytypic modifications. European Journal of Mineralogy 13:577–590. https://doi.org/10.1127/0935-1221/2001/0013-0577
142. Merlino S, Bonaccorsi E, Armbruster T (1999) Tobermorites: Their real structure and order-disorder (OD) character. American Mineralogist 84:1613–1621
143. Hamid SA (1981) The crystal structure of the 11Å natural tobermorite Ca2.25[Si3O7.5(OH)1.5] · 1H2O. Zeitschrift für Kristallographie - Crystalline Materials 154:. https://doi.org/10.1524/zkri.1981.154.3-4.189
144. Merlino S, Bonaccorsi E, Armbruster T (2000) The real structures of clinotobermorite and tobermorite 9 Å: OD character, polytypes, and structural relationships. European Journal of Mineralogy 12:411–429. https://doi.org/10.1127/0935-1221/2000/0012-0411
145. Aranda MAG, De la Torre AG, Leon-Reina L (2012) Rietveld Quantitative Phase Analysis of OPC Clinkers, Cements and Hydration Products. Reviews in Mineralogy and Geochemistry 74:169–209. https://doi.org/10.2138/rmg.2012.74.5
146. Richardson I. (1999) The nature of C-S-H in hardened cements. Cement and Concrete Research 29:1131–1147. https://doi.org/10.1016/S0008-8846(99)00168-4
147. Sánchez-Herrero MJ, Fernández-Jiménez A, Palomo Á (2016) Alkaline Hydration Of C $_2$ S and C $_3$ S. Journal of the American Ceramic Society 99:604–611. https://doi.org/10.1111/jace.13985
148. Chen JJ, Sorelli L, Vandamme M, et al (2010) A Coupled Nanoindentation/SEM-EDS Study on Low Water/Cement Ratio Portland Cement Paste: Evidence for C-S-H/Ca(OH) $_2$ Nanocomposites. Journal of the American Ceramic Society 93:1484–1493. https://doi.org/10.1111/j.1551-2916.2009.03599.x
149. Gallucci E, Scrivener K, Groso A, et al (2007) 3D experimental investigation of the microstructure of cement pastes using synchrotron X-ray microtomography (μCT). Cement and Concrete Research 37:360–368. https://doi.org/10.1016/j.cemconres.2006.10.012
150. Cuesta A, Álvarez-Pinazo G, Sanfélix SG, et al (2014) Hydration mechanisms of two polymorphs of synthetic ye'elimite. Cement and Concrete Research 63:127–136. https://doi.org/10.1016/j.cemconres.2014.05.010
151. Cuesta A, De la Torre AG, Santacruz I, et al (2017) Chemistry and Mass Density of Aluminum Hydroxide Gel in Eco-Cements by Ptychographic X-ray Computed

Tomography. The Journal of Physical Chemistry C 121:3044–3054. https://doi.org/10.1021/acs.jpcc.6b10048
152. Cuesta A, De La Torre AG, Losilla ER, et al (2013) Structure, atomistic simulations, and phase transition of stoichiometric yeelimite. Chemistry of Materials 25:1680–1687. https://doi.org/10.1021/cm400129z
153. Gartner E, Li G (2006) High belite-containing sulfoaluminous clinker, method for the production and the use thereof for preparing hydraulic binders. French patent application 04-51586 (publication 2873366) WO2006/018569 A2
154. Walenta G, Comparet C, Morin V, Gartner E (2010) Hydraulic binder based on sulfoaluminate clinker and minerals additions. World Patent Application WO. 2010/070215 A1.
155. Koumpouri D, Angelopoulos GN (2016) Effect of boron waste and boric acid addition on the production of low energy belite cement. Cement and Concrete Composites 68:1–8. https://doi.org/10.1016/j.cemconcomp.2015.12.009
156. Blanco-Varela MT, Puertas F, Vázquez T, Palomo A (1996) Modelling of the burnability of white cement raw mixes made with CaF2 and CaSO4. Cement and Concrete Research 26:457–464. https://doi.org/10.1016/S0008-8846(96)85033-2
157. Alvarez-Pinazo G, Santacruz I, Aranda MAG, et al (2016) Hydration of belite – ye'elimite – ferrite cements with different calcium sulfate sources. Advances in Cement Research 28:529–543. https://doi.org/10.1680/jadcr.16.00030
158. Gies A, Knöfel D (1987) Influence of sulfur on the composition of belite-rich clinkers and the technological properties of the resulting cements. Cement and Concrete Research 17:317–328. https://doi.org/10.1016/0008-8846(87)90114-1
159. Porras-Vázquez JM, De la Torre AG, Losilla ER, Aranda MAG (2007) Oxide and proton conductivity in aluminum-doped tricalcium oxy-silicate. Solid State Ionics 178:. https://doi.org/10.1016/j.ssi.2007.05.004
160. Cuesta A, Aranda MAG, Sanz J, et al (2014) Mechanism of stabilization of dicalcium silicate solid solution with aluminium. Dalton Transactions 43:. https://doi.org/10.1039/c3dt52194j
161. Westphal T, Füllmann T, Pöllmann H (2009) Rietveld quantification of amorphous portions with an internal standard—Mathematical consequences of the experimental approach. Powder Diffraction 24:239–243. https://doi.org/10.1154/1.3187828
162. Cuesta A, Losilla ER, Aranda MAG, et al (2012) Reactive belite stabilization mechanisms by boron-bearing dopants. Cement and Concrete Research 42:598–606. https://doi.org/10.1016/j.cemconres.2012.01.006
163. Bullerjahn F, Zajac M, Ben Haha M, Scrivener KL (2019) Factors influencing the hydration kinetics of ye'elimite; effect of mayenite. Cement and Concrete Research 116:113–119. https://doi.org/10.1016/J.CEMCONRES.2018.10.026
164. Hanein T, Duvallet TY, Jewell RB, et al (2019) Alite calcium sulfoaluminate cement: chemistry and thermodynamics. Advances in Cement Research 31:94–105. https://doi.org/10.1680/jadcr.18.00118
165. Bullerjahn F, Schmitt D, Ben Haha M (2014) Effect of raw mix design and of clinkering process on the formation and mineralogical composition of (ternesite) belite calcium sulphoaluminate ferrite clinker. Cement and Concrete Research 59:87–95. https://doi.org/10.1016/j.cemconres.2014.02.004
166. Zhang X, Chang W, Zhang T, Ong CK (2004) Nanostructure of Calcium Silicate Hydrate Gels in Cement Paste. Journal of the American Ceramic Society 83:2600–2604. https://doi.org/10.1111/j.1151-2916.2000.tb01595.x
167. Kwan S, LaRosa J, Grutzeck MW (1995) 29Si and 27Al MASNMR Study of Stratlingite. Journal of the American Ceramic Society 78:1921–1926.

https://doi.org/10.1111/j.1151-2916.1995.tb08910.x
168. Rinaldi R, Sacerdoti M, Passaglia E (1990) Strätlingite: crystal structure, chemistry, and a reexamination of its polytpye vertumnite. European Journal of Mineralogy 2:841–850. https://doi.org/10.1127/ejm/2/6/0841
169. Santacruz I, De la Torre AG, Álvarez-Pinazo G, et al (2016) Structure of stratlingite and effect of hydration methodology on microstructure. Advances in Cement Research 28:13–22. https://doi.org/10.1680/adcr.14.00104
170. Skibsted J, Pedersen MT, Holzinger J (2017) Resolution of the Two Aluminum Sites in Ettringite by ^{27} Al MAS and MQMAS NMR at Very High Magnetic Field (22.3 T). The Journal of Physical Chemistry C 121:4011–4017. https://doi.org/10.1021/acs.jpcc.6b11875
171. Gastaldi D, Paul G, Marchese L, et al (2016) Hydration products in sulfoaluminate cements: Evaluation of amorphous phases by XRD/solid-state NMR. Cement and Concrete Research 90:162–173. https://doi.org/10.1016/j.cemconres.2016.05.014
172. Kunther W, Ferreiro S, Skibsted J (2017) Influence of the Ca/Si ratio on the compressive strength of cementitious calcium–silicate–hydrate binders. Journal of Materials Chemistry A 5:17401–17412. https://doi.org/10.1039/C7TA06104H
173. Tobón JI, Paya J, Borrachero M V., et al (2012) Determination of the optimum parameters in the high resolution thermogravimetric analysis (HRTG) for cementitious materials. Journal of Thermal Analysis and Calorimetry 107:233–239. https://doi.org/10.1007/s10973-010-0997-0
174. Matschei T, Lothenbach B, Glasser FP (2007) Thermodynamic properties of Portland cement hydrates in the system CaO-Al2O3-SiO2-CaSO4-CaCO3-H2O. Cement and Concrete Research 37:1379–1410. https://doi.org/10.1016/j.cemconres.2007.06.002
175. Lothenbach B, Winnefeld F, Figi R The influence of superplasticizers on the hydration of Portland cement
176. Banfill PFG THE RHEOLOGY OF FRESH CEMENT AND CONCRETE − A REVIEW
177. Alonso MM, Palacios M, Puertas F, et al (2007) Effect of polycarboxylate admixture structure on cement paste rheology. Materiales de Construcción 57:65–81
178. Sánchez-Herrero MJ, Fernández-Jiménez A, Palomo A (2013) C4A3Š hydration in different alkaline media. Cement and Concrete Research 46:41–49. https://doi.org/10.1016/J.CEMCONRES.2013.01.008
179. Dimitriou G, Savva P, Petrou MF (2018) Enhancing mechanical and durability properties of recycled aggregate concrete. Construction and Building Materials 158:228–235. https://doi.org/10.1016/j.conbuildmat.2017.09.137

8. ANNEXES

8.1. ANNEX I. ARTICLES THAT SUPPORT THIS THESIS

Article #1. Synchrotron Radiation Pair Distribution Function Analysis of Gels in Cements

crystals

MDPI

Article

Synchrotron Radiation Pair Distribution Function Analysis of Gels in Cements

Ana Cuesta [1], Jesus D. Zea-Garcia [2], Diana Londono-Zuluaga [2], Angeles G. De la Torre [2], Isabel Santacruz [2], Oriol Vallcorba [1] and Miguel A.G. Aranda [1,*]

[1] ALBA Synchrotron radiation facility, Carrer de la Llum 2-26, 08290 Cerdanyola del Vallès, Spain; acuesta@cells.es (A.C.); ovallcorba@cells.es (O.V.)
[2] Departamento de Química Inorgánica, Cristalografía y Mineralogía, Universidad de Málaga, 29071 Málaga, Spain; jdavidzea@uma.es (J.D.Z.-G.); dlondonoz@uma.es (D.L.-Z.); mgd@uma.es (A.G.D.l.T.); isantacruz@uma.es (I.S.)
* Correspondence: migarcia@cells.es; Tel.: +34-93-592-4305

Academic Editor: William Clegg
Received: 22 September 2017; Accepted: 17 October 2017; Published: 18 October 2017

Abstract: The analysis of atomic ordering in a nanocrystalline phase with small particle sizes, below ≈5 nm, is intrinsically complicated because of the lack of long-range order. Furthermore, the presence of additional crystalline phase(s) may exacerbate the problem, as is the case in cement pastes. Here, we use the synchrotron pair distribution function (PDF) chiefly to characterize the local atomic order of the nanocrystalline phases, gels, in cement pastes. We have used a multi r-range analysis approach, where the ~4–7 nm r-range allows determining the crystalline phase contents; the ~1–2.5 nm r-range is used to characterize the atomic ordering in the nanocrystalline component; and the ~0.2–1.0 nm r-range gives insights about additional amorphous components. Specifically, we have prepared four alite pastes with variable water contents, and the analyses showed that a defective tobermorite, $Ca_{11}Si_9O_{28}(OH)_2 8.5H_2O$, gave the best fit. Furthermore, the PDF analyses suggest that the calcium silicate hydrate gel is composed of this tobermorite and amorphous calcium hydroxide. Finally, this approach has been used to study alternative cements. The hydration of monocalcium aluminate and ye'elimite pastes yield aluminum hydroxide gels. PDF analyses show that these gels are constituted of nanocrystalline gibbsite, and the particle size can be as small as 2.5 nm.

Keywords: Portland cement; cementitious materials; C-S-H gel; amorphous phases; total scattering

1. Introduction

1.1. Cements

Portland cement (PC) is considered the most manufactured product in the world, as it is the main component of the construction industry [1]. PC is composed of the Portland clinker, the setting regulator (a calcium sulfate source), and in many cases additions and admixtures [2]. The four main phases of any Portland clinker are: ~65 wt% alite or Ca_3SiO_5; ~15 wt% belite, or Ca_2SiO_4; ~15 wt% ferrite, or $Ca_4Al_2Fe_2O_{10}$, and ~5 wt% tricalcium aluminate, or $Ca_3Al_2O_6$ [2].

The hydration of PC basically consists of two different types of reactions that interact with each other: the silicate hydration reactions, and the aluminate hydration reactions. The reaction kinetics of alite and tricalcium aluminate are quite fast; comparatively, the kinetics of belite and ferrite hydration reactions are much slower [2,3]. Hereafter, and for PC hydration, we restrict the introduction and discussion to the hydration of pure alite, although we are aware that this is a simplification.

Article #2. Multiscale understanding of tricalcium silicate hydration reactions

www.nature.com/scientificreports

OPEN

Multiscale understanding of tricalcium silicate hydration reactions

Received: 12 February 2018
Accepted: 14 May 2018
Published online: 04 June 2018

Ana Cuesta[1,2], Jesus D. Zea-Garcia[2], Diana Londono-Zuluaga[2], Angeles G. De la Torre[2], Isabel Santacruz[2], Oriol Vallcorba[1], Monica Dapiaggi[3], Susana G. Sanfélix[2,4] & Miguel A. G. Aranda[1]

Tricalcium silicate, the main constituent of Portland cement, hydrates to produce crystalline calcium hydroxide and calcium-silicate-hydrates (C-S-H) nanocrystalline gel. This hydration reaction is poorly understood at the nanoscale. The understanding of atomic arrangement in nanocrystalline phases is intrinsically complicated and this challenge is exacerbated by the presence of additional crystalline phase(s). Here, we use calorimetry and synchrotron X-ray powder diffraction to quantitatively follow tricalcium silicate hydration process: i) its dissolution, ii) portlandite crystallization and iii) C-S-H gel precipitation. Chiefly, synchrotron pair distribution function (PDF) allows to identify a defective clinotobermorite, $Ca_{11}Si_9O_{28}(OH)_2{\cdot}8.5H_2O$, as the nanocrystalline component of C-S-H. Furthermore, PDF analysis also indicates that C-S-H gel contains monolayer calcium hydroxide which is stretched as recently predicted by first principles calculations. These outcomes, plus additional laboratory characterization, yielded a multiscale picture for C-S-H nanocomposite gel which explains the observed densities and Ca/Si atomic ratios at the nano- and meso- scales.

Le Châtelier[1] already established that Portland cement hydration starts by the dissolution of calcium silicate species in water from the most soluble silicate phase. This process is followed by the precipitation of complex poorly-crystalline calcium-silicate-hydrates (generically named C-S-H gel) and the crystallization of $Ca(OH)_2$, portlandite, see overall reaction (1)[2]. C-S-H gel is the main hydrated component in Portland cement pastes, and it is the main responsible for the strength and durability of the resulting mortars and concretes. Alite, an impure form of tricalcium silicate Ca_3SiO_5, is the main phase present in Portland cements and it has a slightly variable composition due to element-substitutions[2]. The hydration of any alite shows, in addition to an initial fast (minor) dissolution, three main stages with time: i) induction (also known as dormant period), ii) acceleration; and iii) deceleration[3]. Similar kinetic profiles take place in various heterogeneous hydration processes, for instance mineral weathering[4] and glass alteration[5]. There are two main theories to explain this early-age hydration behaviour. The first is known as 'protective layer' and it consists in the precipitation of a C-S-H gel diffusion barrier on the surfaces of alite particles which density and adherence change with time. The second is known as 'geochemical model' and it is related to the alite dissolution mechanism evolving from etch pit formation to step retreat[6]. Despite one century of focused investigations, the underlying mechanism(s) for such time evolution is still strongly debated[7,8].

$$Ca_3SiO_5 + 5.2H_2O \rightarrow 1.2Ca(OH)_2 + (CaO)_{1.8}SiO_2(H_2O)_{4.0} \quad (1)$$

The hydration reactions of alite, (i) dissolution of crystalline alite, (ii) precipitation of C-S-H gel, and (iii) crystallization of portlandite, have been thoroughly studied by many techniques including laboratory X-ray powder diffraction[9–12], calorimetry[13–15], small-angle neutron scattering[16]; advanced electron microscopies[17,18], ^{29}Si magic-angle-spinning nuclear-magnetic-resonance[19,20], and theoretical simulations[21–23]. C-S-H gel has a nanocrystalline nature and so its understanding is very challenging[24] which includes the relationship with the solution

[1]ALBA Synchrotron, Carrer de la Llum 2-26. 08290 Cerdanyola del Vallès, Barcelona, Spain. [2]Departamento de Química Inorgánica, Cristalografía y Mineralogía. Universidad de Málaga, 29071, Málaga, Spain. [3]Department of Earth Sciences "Ardito Desio", University of Milan, Milano, Italy. [4]Faculty of Engineering, Østfold University College, N-1757, Halden, Norway. Correspondence and requests for materials should be addressed to M.A.G.A. (email: migarcia@cells.es)

Article #3. Synchrotron pair distribution function analyses of ye'elimite-based pastes

Cite this article
Cuesta A, Zea-Garcia JD, De la Torre AG, Santacruz I and Aranda MAG
Synchrotron pair distribution function analyses of ye'elimite-based pastes.
Advances in Cement Research,
https://doi.org/10.1680/jador.18.00097

Research Article
Paper 1800097
Received 08/06/2018; Revised 13/07/2018;
Accepted 13/07/2018

Keywords: diffraction (X-ray, neutron, electron)/nanostructure/sulfate-based cements

Advances in Cement Research

ice publishing

Synchrotron pair distribution function analyses of ye'elimite-based pastes

Ana Cuesta
Postdoctorate researcher, Department of Inorganic Chemistry, Crystallography and Mineralogy, University of Málaga, Málaga, Spain

Jesus D. Zea-Garcia
PhD student, Department of Inorganic Chemistry, Crystallography and Mineralogy, University of Málaga, Málaga, Spain

Angeles G. De la Torre
Associated Professor, Department of Inorganic Chemistry, Crystallography and Mineralogy, University of Málaga, Málaga, Spain

Isabel Santacruz
Associated Professor, Department of Inorganic Chemistry, Crystallography and Mineralogy, University of Málaga, Málaga, Spain

Miguel A. G. Aranda
Professor, ALBA Synchrotron, Barcelona, Spain (corresponding author: migarcia@cells.es) (Orcid:0000-0001-7708-3578)

The study of nanocrystalline phase atomic ordering is intrinsically complicated. The presence of additional crystalline phase(s) exacerbates this challenge. Here, a synchrotron pair distribution function (PDF) is used to characterise the local atomic order of the nanocrystalline phases in ye'elimite-containing pastes. A multi *r*-range analysis approach has been used, where the 3–5 nm *r*-range allows the crystalline phase contents to be determined and the 0·16–3·5 nm is used to characterise the atomic ordering in the nanocrystalline components. Quantitative phase contents have been also derived from these analyses. Specifically, five stoichiometric ye'elimite pastes with variable anhydrite and water contents have been prepared. For the pastes without anhydrite addition, ettringite was not present and two calcium aluminium monosulfate phases were required for good PDF fits. In addition to crystalline calcium aluminium monosulfate (AFm) ($c \approx 2{\cdot}86$ nm), a nanocrystalline AFm phase with a significantly smaller *c*-unit cell parameter value, $c \approx 2{\cdot}68$ nm, was required, having about a 6 nm particle size. For a paste obtained with 31 wt% of anhydrite addition, the main crystalline phase was ettringite with the aluminium hydroxide having a nano-gibbsite local structure with quite a small average particle size, ≈3·5 nm.

Introduction

Ye'elimite ($Ca_4Al_6O_{12}(SO_4)$), also known as Klein salt, is a key mineralogical phase in a number of alternative cements. The three main types of these cements are: (*a*) calcium sulfoaluminate (CSA), where the ye'elimite content is higher than 50 wt% (Aranda and De la Torre, 2013; Lothenbach and Winnefeld, 2017; Zhang *et al.*, 1999); (*b*) belite–ye'elimite–ferrite cements (BYF), where the contents are close to 60, 20, 20 wt%, respectively (Álvarez-Pinazo *et al.*, 2013; Chen *et al.*, 2012; Morin *et al.*, 2017); and (*c*) ternesite–ye'elimite–belite (TYB), where the contents are approximately 50, 25, 20 wt%, respectively (Bullerjahn *et al.*, 2014; Hanein *et al.*, 2017; Shen *et al.*, 2015). These three materials can be termed eco-cements because their manufacturing processes decrease the carbon dioxide (CO_2) footprint, when compared to that of Portland cement (type CEM-I), by approximately 40, 25 and 25% for CSA, BYF and TYB, respectively (Aranda and De la Torre, 2013; Bullerjahn *et al.*, 2014).

Ye'elimite hydrates very rapidly and most of the hydration heat is released during the first day. Its hydration reaction in the presence of a sulfate source has been reported (Hargis *et al.*, 2013; Winnefeld and Barlag, 2010) and it is shown in Equation 1, where the products are crystalline ettringite ($Ca_6Al_2(OH)_{12}(SO_4)_3{\cdot}26H_2O$, also known as AFt) and amorphous/nanocrystalline aluminium hydroxide (also known as aluminium hydroxide gel, A–H gel, nano-gibbsite or amorphous gibbsite). The full reaction of the reagents shown in Equation 1 should give a mixture of hydrates with 80·0 wt% of AFt and 20·0 wt% of nano-gibbsite. The volume percentage of the hydrates is much more complicated to determine as the density of nano-gibbsite regions is smaller than that of crystalline gibbsite owing to the poor packing with empty space as well as small gel pores which are likely to be filled with water. The density of A–H gel has been determined by synchrotron ptychographic X-ray computed tomography (Cuesta *et al.*, 2017a). Its density strongly depends upon the gel pore water content varying from 2·05 gcm^{-3} for an aluminium hydroxide without gel water at least up to 1·48 gcm^{-3} for an aluminium hydroxide ($Al(OH)_3$) with 2·3 moles of gel water per aluminium hydroxide.

$$1.\quad Ca_4Al_6O_{12}(SO_4) + 2CaSO_4 \cdot nH_2O + (38-2n)H_2O \rightarrow Ca_6Al_2(OH)_{12}(SO_4)_3{\cdot}26H_2O + 4Al(OH)_3{-}gel$$

The hydration reaction of ye'elimite in the absence of additional sulfate sources has also been reported and it is displayed in Equation 2, where the products are crystalline calcium aluminium monosulfate ($Ca_4Al_2(OH)_{12}(SO_4){\cdot}6H_2O$, also known as AFm) and A–H gel. However, the reactivity of ye'elimite under these conditions is still not fully understood. Some researchers have published that only reaction (2) takes place (Winnefeld and Barlag, 2010), whereas others have reported that mixtures of AFm and AFt phases are formed

Article #4. Alite-belite-ye'elimite cements: Effect of dopants on the clinker phase composition and properties

Cement and Concrete Research 115 (2019) 192–202

Contents lists available at ScienceDirect

Cement and Concrete Research

journal homepage: www.elsevier.com/locate/cemconres

Alite-belite-ye'elimite cements: Effect of dopants on the clinker phase composition and properties

Jesus D. Zea-Garcia[a], Isabel Santacruz[a], Miguel A.G. Aranda[a,b], Angeles G. De la Torre[a,*]

[a] Departamento de Química Inorgánica, Cristalografía y Mineralogía, Universidad de Málaga, Málaga 29071, Spain
[b] ALBA Synchroton, Carrer de la Lum, 2-26, Cerdanyola 08290, Barcelona, Spain

ARTICLE INFO

Keywords:
Clinkering
Ca_3SiO_5
$3CaO{\cdot}3Al_2O_3{\cdot}CaSO_4$
C_2S polymorphism
Boron
Fluor
Zinc
Alkaline oxides
X-ray diffraction & Rietveld method
EDS

ABSTRACT

Clinkers with alite-belite-ye'elimite (ABY) are considered as eco-friendly cements. Clinkering (2 Kg) of two types of ABY clinkers was optimized: standard-ABY, with CaF_2 and ZnO as dopants (32.6 wt% alite, 30.4 wt% β-C_2S and 15.6 wt% ye'elimite) and αABY, with CaF_2, ZnO, B_2O_3, Na_2O (14.4 wt% alite, 37.1 wt% β-C_2S, 18.5 wt% α'_H-C_2S and 7.5 wt% ye'elimite). Zn and F were mainly incorporated in alite and ferrite as dopants determined by EDS semi-quantitative analysis. The effect of dopants on the hydration of the cement mortars has been tested. Thus, standard-ABY develops 29.9 MPa compressive strengths at 1 day while αABY does 16.8 MPa, mainly due to the higher amount of alite of the former. The presence of α'_H-C_2S in αABY increases mechanical strengths at 28 days of hydration from 44.7 MPa of standard-ABY to 74.9 MPa.

1. Introduction

Portland Cement (PC) is the most used binder all over the world. However, during the manufacturing of one ton of PC, ~0.97 tons of CO_2 are released to the atmosphere, mainly due to the limestone calcination to achieve the desired composition [1]. As an example, during the formation of alite, C_3S, which is the main component of PC (> 65 wt%), 0.58 tons of CO_2 (per ton of alite) are released. Thus, the cement industry is responsible of ~6% of the anthropogenic CO_2 emissions [2]. An eco-friendly approach may consist on the design and fabrication of alternative cements, called eco-cements, which are composed by less calcite demanding phases, such as ye'elimite ($C_4A_3\bar{S}$) [2,3]. There are different ye'elimite-rich cements [4] such as Calcium SulphoAluminate (CSA) cements, which present > 50 wt% of ye'elimite, and consequently release up to 37% less CO_2 than PC. However, they are expensive due to the need of high purity bauxite. In recent studies, dicalcium silicate-rich CSA cements, sometimes referred as Belite-Ye'elimite-Ferrite (BYF) cements, have been thought as the potential substitute of PC at large scales [5,6]. These BYF cements generally contain belite, C_2S (> 50 wt%), as their main phase and ye'elimite (~30 wt%) as secondary phase. Some BYF cements (with the following composition: 33 wt% of β-C_2S and 19 wt% of orthorhombic-ye'elimite) develop low mechanical strengths [6] at intermediate ages, which is a technological disadvantage that has to be defeated.

The activation of BYF clinkers by stabilizing α'_H-polymorph of C_2S or getting modified β-C_2S, a distorted form due to the inclusion of foreign elements in the structure [7], may be the key to reach the objective of substituting PC [5,6,8,9]. In addition, cements with coexistence of alite, belite and ye'elimite (ABY) have also been examined to improve the final performances of BYF meanwhile CO_2 emissions are lower than PC [10–13]. Nevertheless, there are some problems concerning the clinkering of ABY binders since the optimum temperatures for the synthesis of alite and ye'elimite are quite different. Alite formation is promoted by the appearance of melting phases, such as iron, silicates, and alkali sulfates [14], and requires at least 1350 °C, while ye'elimite starts its decomposition at 1300–1350 °C [15]. This can be addressed by using small amounts of fluorite (CaF_2) [16,17] in the raw mixture, which will act as flux and mineralizer, permitting the coexistence of both phases at temperatures ranging between 1250 and 1300 °C [14,15]. Moreover, the influence of zinc oxide on clinkering is described in the literature for PC and ABY [17–21]. The addition of ZnO promotes the formation of higher amounts of alite, which contains this element in its structure; in addition, it also stimulates physical changes in alite crystals: big and hexagonal alite crystals are transformed into smaller and elongated particles [21]. The addition of other mineralizers, such as MnO_2 [22] or P_2O_5 [23] on the phase composition during clinkering is also described in the literature.

In this work, the addition of different mineralizers and activators

* Corresponding author.
E-mail address: mgd@uma.es (A.G. De la Torre).

https://doi.org/10.1016/j.cemconres.2018.10.019
Received 26 July 2018; Received in revised form 16 October 2018; Accepted 19 October 2018

Article #5. Processing and characterisation of standard and doped alite-belite-ye'elimite ecocement pastes and mortars

Cement and Concrete Research 127 (2020) 105911

Contents lists available at ScienceDirect

Cement and Concrete Research

journal homepage: www.elsevier.com/locate/cemconres

Processing and characterisation of standard and doped alite-belite-ye'elimite ecocement pastes and mortars

Jesus D. Zea-Garcia[a], Angeles G. De la Torre[a], Miguel A.G. Aranda[a,b], Isabel Santacruz[a,*]

[a] Departamento de Química Inorgánica, Cristalografía y Mineralogía, Universidad de Málaga, Málaga 29071, Spain
[b] ALBA Synchroton, Carrer de la Lum, 2-26, Cerdanyola 08290, Barcelona, Spain

ARTICLE INFO

Keywords:
Alite-belite-ye'elimite ecocements
Processing
Rheology
X-ray diffraction
Compressive strength

ABSTRACT

Here, we report the processing optimisation of two laboratory-prepared alite-belite-ye'elimite ecocements (standard and doped) that release to the atmosphere ~13% less CO_2 than Portland Cement during fabrication. The processing was optimised through rheological measurements, where homogeneous pastes and mortars were finally prepared through the study and optimisation of both the superplasticiser content and the water-to-cement ratio. Both parameters were correlated with the phase assembly of selected pastes and compressive strength of the corresponding mortars. After optimisation, mortars with high compressive strengths (~72 and ~77 MPa for the standard mortar, and ~41 and ~75 MPa for the doped one, at 7 and 28 days, respectively) were prepared. Furthermore, the important increase in compressive strength from 7 to 28 days of the optimised mortar prepared from the doped ecocement is due to its composition (the higher content of belite jointly with the reaction of its active polymorph (α'_H-belite)).

1. Introduction

During the fabrication of Portland Cement (PC), large amounts of CO_2 are released to the atmosphere (~0.98 tons of CO_2 per ton of PC) [1], which makes the cement industry responsible of ~6% of the anthropogenic CO_2 emissions [2]. These emissions are mainly due to the decarbonation of calcite to achieve the desired composition after clinkering. PC is mainly composed of ~65 wt% of alite (Ca_3SiO_5 or $3CaO{\cdot}SiO_2$) and ~15 wt% of belite (Ca_2SiO_4 or $2CaO{\cdot}SiO_2$), which are high calcite-demanding phases, mainly alite. There is a phase named ye'elimite ($Ca_4Al_6SO_{16}$ or $4CaO{\cdot}3Al_2O_3{\cdot}SO_3$) that is not present in PC, which contributes with 0.22 tons of CO_2 per ton of phase produced while alite contributes with 0.58 tons/ton of phase (~38% less emissions). Thus, ye'elimite rich-cements may be a good alternative to PC, if they can achieve similar performance, achieving savings around 25–30% of CO_2 emissions depending on the composition [3]. Alite-Belite-Ye'elimite (ABY) cement, where alite has been partially substituted by ye'elimite, may be a good alternative [4–8]. These cements can be considered as ecocements due to the lower amount of CO_2 that it is released during fabrication, where the reduction achieved depends on the composition. It is known that belite can present polymorphism, where the polymorph found in PC is β-belite; however, α-forms of belite or modified β-belite promote higher mechanical strengths than the beta form at early ages [9]. This fact is interesting in order to achieve high mechanical properties.

To achieve good performance, it is essential to optimise the processing of cement pastes/mortars to improve their workability and obtain homogeneous and dense materials. This is reached through the preparation of well dispersed cement pastes [10,11]. In addition, low water contents, within certain limits, are usually related with improved mechanical properties [12,13]. The use of superplasticisers is a common practice in the building industry since it helps the dispersion of the cement particles, reduces viscosity and allows the preparation of lower water-to-cement (w/c) ratios. The superplasticiser is adsorbed onto the surface of cement particles causing the repulsion of the particles through electrostatic, steric or electrosteric repulsions [14–18]. The repulsion will depend [9] on the superplasticiser (type and amount), the composition of the cement powder, particle size distribution and hence specific surface area, and so on. Specific additives (retarders and/or specific superplasticisers, such as polycarboxylate-based superplasticisers) can slow down the reactions which may be beneficial to improve the workability in particular systems [12,19]. The addition of the right amount of chemical admixture is key to improve the dispersion, reduce the viscosity and control the setting time, to finally improve the homogeneity and performance of the corresponding cements and mortars. Because of that, in this work, the superplasticiser content and the water-to-cement ratio have been optimised.

Furthermore, the hydration reactions need to be fully understood

* Corresponding author.
E-mail address: isantacruz@uma.es (I. Santacruz).

https://doi.org/10.1016/j.cemconres.2019.105911
Received 27 May 2019; Received in revised form 23 September 2019; Accepted 29 September 2019

Article #6. Hydration Activation of Alite-Belite-Ye'elimite Cements by Doping with Boron

ACS Sustainable Chemistry & Engineering

pubs.acs.org/journal/ascecg

Research Article

Hydration Activation of Alite-Belite-Ye'elimite Cements by Doping with Boron

Jesus D. Zea-Garcia, Susana G. Sanfelix, Oriol Vallcorba, Miguel A. G. Aranda, Isabel Santacruz, and Angeles G. De la Torre*

Cite This: ACS Sustainable Chem. Eng. 2020, 8, 3583−3590

Read Online

ACCESS | Metrics & More | Article Recommendations | Supporting Information

ABSTRACT: The hydration behavior of two alite-belite-ye'elimite (ABY) cements has been studied. The production of these materials releases into atmosphere ~17% less CO_2 compared to Portland cement. The ABY cement contains alite, β-C_2S, and ye'elimite as main phases, while dABY (activated by adding borax) contains not only these three phases but also α'_H-C_2S. The role of boron in these systems is 2-fold: (i) acting as a retarder at early hydration ages since the precipitation of AH_3 gel has been delayed from over 4 h in ABY to over 24 h in dABY; and (ii) as an activator at late hydration ages by stabilizing highly reactive β- and α'_H-belites. The degree of hydration of β-C_2S in ABY is 42% at 28 days, while that of β-C_2S and α'_H-C_2S in dABY at the same age is 80 and 88%, respectively. Moreover, the main hydration products in both systems are ettringite and C−S−H gel. The local structure of these hydrated products has been studied by ^{27}Al and ^{29}Si magic angle spinning nuclear magnetic resonance (MAS−NMR) and found to be similar in both cements. However, the amount of C−S−H gel is 63% of all silicon-bearing phases in ABY after 28 days while it is 76% (determined by ^{29}Si MAS−NMR) in dABY, which justifies the higher mechanical strengths of dABY mortars.

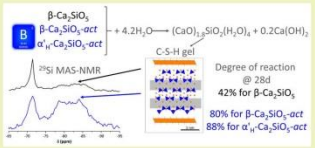

KEYWORDS: *ecocements, calcium sulfoaluminate, boron effect, retardant, synchrotron radiation, X-ray diffraction, solid-state MAS−NMR, calorimetric study, C−S−H gel, compressive strength*

INTRODUCTION

The challenge of reducing greenhouse emissions is one of the most important issues that scientists are facing. Portland cement (PC) production releases up to ~0.98 tons of CO_2 per ton of cement type-I manufactured, taking into account the limestone calcination (0.54 tons), the burning of the fossil fuels (0.34 tons), and electricity for grinding (0.09 tons). Thus, the cement industry is responsible for ~7% of the total CO_2 emissions due to human activities.[1−3] There are several approaches to reduce these emissions,[4] such as lowering the amount of clinker in the final cement by blending with supplementary cementitious materials (SCMs)[5] or modifying the raw materials and, consequently, the chemical composition of the final product.[2] The main component of PC is Ca_3SiO_5 (alite or C_3S), which is a high calcium demanding phase. Calcite is the main calcium source in cement production, and CO_2 comes from the decarbonation of calcite in the kilns. Hereafter, the cement nomenclature will be adopted: C═CaO, S═SiO_2, A═Al_2O_3, F═Fe_2O_3, $\bar{S}$═SO_3, and H═H_2O. Alite hydration products are mainly responsible for the high mechanical strengths developed by PC at early ages. Calcium sulfoaluminate ($C_4A_3\bar{S}$ or ye'elimite) containing cements are included in the second approach, as this phase is a less calcite demanding phase.[4,6] In recent years, an economical and environmental alternative known as belite-ye'elimite-ferrite (BYF) cements have been proposed.[7−10] These BYF cements usually contain belite, C_2S (>50 wt %), and ye'elimite (~30 wt %) as their main phases. A reduction of 0.15 tons of CO_2 due to decarbonation of raw materials in the kiln is achieved in the production of BYF cements. Additionally, the lower clinkering temperature and the more friable material obtained cause a reduction of 0.06 extra tons of carbon dioxide due to the burning of the fuel and the consumption of electricity during milling. The development of these materials is still under research[11,12] due to the three main issues; (i) the early hydration of the ye'elimite phase with anhydrite or gypsum and the rheological behavior should be controlled to obtain the desired mechanical performances,[13] (ii) the durability performances are still unknown and likely related to those of calcium sulfoaluminate cements,[14] and (iii) the development of mechanical strengths with a strength gain vs time similar to that of PC by activation/enhancing the reactivity of the main phase, i.e., belite.[10,15,16] There have been several approaches to achieve this latter goal, stabilizing α-polymorphs of C_2S by the

Received: October 7, 2019
Revised: February 6, 2020
Published: February 11, 2020

https://dx.doi.org/10.1021/acssuschemeng.9b05975
ACS Sustainable Chem. Eng. 2020, 8, 3583−3590

8.2. ANNEX II. OTHER PUBLICATIONS

Article I.

Zea-Garcia JD, De la Torre AG, Aranda MAG, Cuesta A. (2019) Comparative Study of Experimental Configurations in Synchrotron Pair Distribution Function. *Materials* 12, 1347. DOI: 10.3390/ma12081347

Article II.

Fraga E, **Zea-Garcia JD**, Yánez-Casal A, De la Torre AG, Cuesta A, Valcárcel-Fernández R, Farré-París F, Malfois M, Aranda MAG. (2019) High-pressure and temperature spinning capillary cell for in situ synchrotron X-ray powder diffraction. *Journal of Synchrotron Radiation* 26, 1238-1244. DOI: 10.1107/S1600577519005150

Article III.

Fraga E, Cuesta A, **Zea-Garcia JD**, De la Torre AG, Yánez-Casal A, Aranda MAG. (2019) Rietveld Quantitative Phase Analysis of Oil Well Cement: In situ Hydration Study at 150 Bars and 150ºC. *Materials* 12, 1897. DOI: 10.3390/ma12121897

Article IV.

Sanfelix SG, **Zea-García JD**, Romero-Espinosa A, Londoño D, Santacruz I, De la Torre AG, Kjøniksen A. (2020) Hydration development and thermal performance of calcium sulphoaluminate cements containing microencapsulated change materials. *Cement and Concrete Research* 132, 106039. DOI: 10.1016/j.cemconres.2020.106039.

8.3. ANNEX III. OTHER TABLES

Table I. Full phase assemblage of mC_3S_21µm_0.45w/s paste at all the studied ages. The *in-situ* was recorded up to 52 hours. The *ex-situ* study starts at 7 days.

Hydration age (hours)	mC_3S_21µm_0.45w/s			
	mC_3S	CH	ACn	= (FW+C-S-H)
5.00	66.8	-	33.2	(30.1+3.1)
7.00	65.9	0.1	34.0	(29.7+4.3)
9.00	65.9	0.1	34.0	(29.7+4.3)
12.00	63.6	0.4	36.0	(28.8+7.2)
14.00	63.3	0.7	36.0	(28.7+7.3)
18.50	60.0	2.7	37.3	(27.3+10.0)
25.00	55.6	3.5	41.0	(25.5+15.5)
28.00	52.4	5.5	42.1	(24.2+17.9)
30.00	50.4	6.5	43.2	(23.4+19.8)
36.00	44.1	6.8	49.1	(20.8+28.3)
39.00	42.1	7.1	50.8	(20.0+30.8)
44.50	41.8	7.8	50.4	(19.9+30.5)
48.00	40.2	9.4	50.4	(19.2+31.2)
52.00	37.7	9.9	52.4	(18.2+34.2)
168 (7 days)	22.9	14.8	62.3	(12.1+50.2)
336 (14 days)	20.8	14.9	64.4	(11.2+53.2)
672 (28 days)	21.1	15.2	63.7	(11.4+52.3)
2400 (100 days)	21.5	15.7	62.7	(11.5+51.2)

Table II. Full phase assemblage of mC_3S_21µm_0.45w/s paste at all the studied ages and the phase assemblages were renormalized by removing the FW content. The *in-situ* was recorded until 52 hours. The *ex-situ* study starts at 7 days.

Hydration age (hours)	mC_3S_21µm_0.45w/s		
	mC_3S	CH	C-S-H
5.00	95.5	-	4.5
7.00	93.8	0.2	6.0
9.00	*93.8*	0.2	6.0
12.00	89.2	0.6	10.2
14.00	88.7	1.0	10.3
18.50	82.6	3.7	13.8
25.00	74.6	4.7	20.7
28.00	69.1	7.3	23.6
30.00	65.7	8.4	25.9
36.00	55.7	8.6	35.7
39.00	52.6	8.9	38.5
44.50	52.2	9.8	38.1
48.00	49.8	11.6	38.6
52.00	46.1	12.1	41.8
168 (7 days)	26.0	16.9	57.1
336 (14 days)	23.4	16.7	59.9
672 (28 days)	23.8	17.2	59.0
2400 (100 days)	24.3	17.8	57.9

Table III. Full phase assemblage of mC_3S_21µm_0.80w/s paste at all the studied ages. The *in-situ* was recorded until 52 hours. The *ex-situ* study starts at 7 days.

Hydration age (hours)	mC_3S_21µm_0.80w/s			
	mC_3S	CH	ACn	= (FW+C-S-H)
5.00	52.6	-	47.4	(43.2+4.2)
5.50	52.6	-	47.4	(43.2+4.2)
6.00	52.6	-	47.4	(43.2+4.2)
6.50	52.6	-	47.4	(43.2+4.2)
7.00	52.6	-	47.4	(43.2+4.2)
7.50	52.5	0.1	47.4	(43.1+4.3)
8.00	52.5	0.1	47.4	(43.1+4.3)
8.75	52.5	0.2	47.4	(43.1+4.3)
9.25	51.9	0.2	47.9	(42.9+5.0)
9.75	51.9	0.2	47.9	(42.9+5.0)
10.25	51.8	0.3	47.9	(42.8+5.1)
10.75	51.2	0.3	48.5	(42.6+5.9)
11.25	51.1	0.5	48.4	(42.6+5.9)
11.75	50.9	0.6	48.4	(42.5+5.9)
12.25	50.2	0.8	49.0	(42.2+6.8)
13.00	49.9	1.1	49.0	(42.1+6.9)
13.50	49.6	1.4	49.0	(42.0+7.0)
14.00	47.8	1.7	50.5	(41.2+9.3)
14.50	47.8	1.7	50.5	(41.2+9.3)
15.00	47.3	2.2	50.5	(41.0+9.5)
15.50	46.8	2.2	51.0	(40.8+10.2)
17.50	45.2	3.3	51.5	(40.1+11.4)
22.00	43.6	3.5	52.9	(39.5+13.4)
24.00	42.6	4.5	52.9	(39.1+13.8)
27.50	39.8	5.1	55.1	(37.9+17.2)
36.00	35.8	5.6	58.6	(36.3+22.3)
39.00	34.4	5.6	60.0	(35.7+24.3)
42.00	32.4	7.5	60.0	(34.9+25.1)
44.00	32.2	7.8	60.0	(34.8+25.2)
48.00	31.1	7.4	61.5	(34.3+27.2)
52.00	30.0	9.3	60.7	(33.9+26.8)
168 (7 days)	19.2	12.7	68.1	(29.5+38.6)
336 (14 days)	16.3	16.3	67.3	(28.3+39.0)
672 (28 days)	11.8	19.0	69.2	(26.4+ 42.8)
2400 (100 days)	8.8	17.0	74.2	(25.2+49.0)

Table IV. Full phase assemblage of mC_3S_21µm_0.80w/s paste at all the studied ages and the phase assemblages were renormalized by removing the FW content. The *in-situ* was recorded until 52 hours. The *ex-situ* study starts at 7 days.

Hydration age (hours)	mC_3S_21µm_0.80w/s		
	mC_3S	CH	C-S-H
5.00	92.7	-	7.3
5.50	92.7	-	7.3
6.00	*92.7*	-	7.3
6.50	92.7	-	7.3
7.00	92.7	-	7.3
7.50	92.4	0.2	7.4
8.00	92.4	0.2	7.4
8.75	92.2	0.3	7.5
9.25	90.9	0.3	8.8
9.75	90.9	0.3	8.8
10.25	90.6	0.5	8.9
10.75	90.5	0.6	8.9
11.25	88.9	0.8	10.3
11.75	88.5	1.1	10.4
12.25	86.9	1.4	11.7
13.00	86.2	1.9	11.9
13.50	85.5	2.4	12.1
14.00	81.3	2.8	15.8
14.50	81.2	2.9	15.9
15.00	80.1	3.8	16.2
15.50	79.0	3.8	17.3
17.50	75.6	5.5	19.0
22.00	72.0	5.8	22.2
24.00	69.9	7.4	22.7
27.50	64.1	8.2	27.6
36.00	56.2	8.8	35.0
39.00	53.5	8.7	37.8
42.00	49.8	11.6	38.6
44.00	49.4	11.9	38.6
48.00	47.3	11.3	41.4
52.00	45.3	14.1	40.5
168 (7 days)	27.3	18.0	54.7
336 (14 days)	22.8	22.8	54.5
672 (28 days)	16.0	25.9	58.1
2400 (100 days)	11.8	22.7	65.5

Table V. Full phase assemblage of mC_3S_7µm_0.80w/s paste at the all studied ages. The *in-situ* was recorded until 52 hours. The *ex-situ* study starts at 7 days.

Hydration age (hours)	mC_3S_7µm_0.80w/s			
	mC_3S	CH	ACn	= (FW+C-S-H)
2.00	51.4	0.2	48.4	(42.7+5.7)
4.00	51.2	0.9	47.9	(42.6+5.3)
5.75	50.3	1.3	48.4	(42.2+6.2)
6.25	50.1	1.4	48.4	(42.2+6.2)
6.75	49.4	1.7	48.9	(41.9+7.0)
7.25	49.2	1.9	48.9	(41.8+7.1)
7.75	48.9	2.2	48.9	(41.6+7.3)
8.25	48.1	2.4	49.5	(41.3+8.2)
8.75	47.3	2.8	50.0	(41.0+9.0)
9.25	46.5	3.1	50.5	(40.7+9.8)
10.00	45.6	3.4	51.0	(40.3+10.7)
10.50	45.2	3.9	51.0	(40.1+10.9)
11.00	44.3	4.3	51.4	(39.8+11.6)
11.50	43.0	4.6	52.4	(39.2+13.2)
12.00	42.1	5.0	52.9	(38.9+14.0)
12.50	41.7	5.5	52.8	(38.7+14.1)
13.00	40.8	5.9	53.3	(38.3+15.0)
13.50	39.7	6.2	54.2	(37.9+16.3)
14.00	38.9	6.5	54.6	(37.6+17.0)
14.50	38.1	6.9	55.0	(37.2+17.8)
15.00	37.4	7.2	55.4	(36.9+18.5)
15.50	36.7	7.5	55.8	(36.7+19.1)
18.00	32.7	8.8	58.5	(35.0+23.5)
20.00	32.0	9.5	58.5	(34.7+23.8)
24.00	30.1	10.0	59.9	(34.0+25.9)
28.00	28.3	11.2	60.6	(33.2+27.4)
35.00	25.5	10.8	63.7	(32.1+31.6)
38.50	23.8	11.4	64.8	(31.4+33.4)
42.50	22.4	13.7	64.0	(30.8+33.2)
48.00	21.8	14.0	64.2	(30.5+33.7)
52.00	20.5	14.2	65.3	(30.0+35.3)
168 (7 days)	12.9	17.3	69.7	(26.9+42.8)
336 (14 days)	9.7	17.9	72.3	(25.6+46.7)
672 (28 days)	7.2	17.8	75.0	(24.6+50.4)
2400 (100 days)	6.8	19.1	74.1	(24.4+49.7)

Table VI. Full phase assemblage of mC_3S_7µm_0.80w/s paste at all the studied ages and the phase assemblages were renormalized by removing the FW content. The *in-situ* was recorded until 52 hours. The *ex-situ* study starts at 7 days.

Hydration age (hours)	mC_3S_7µm_0.80w/s		
	mC_3S	CH	C-S-H
2.00	89.6	0.4	10.0
4.00	89.3	1.5	9.2
5.75	87.1	2.2	10.7
6.25	86.7	2.5	10.8
6.75	85.0	2.9	12.2
7.25	84.4	3.3	12.3
7.75	83.7	3.7	12.5
8.25	82.0	4.2	13.9
8.75	80.1	4.7	15.2
9.25	78.3	5.2	16.5
10.00	76.4	5.7	17.8
10.50	75.4	6.5	18.1
11.00	73.5	7.1	19.4
11.50	70.7	7.6	21.6
12.00	69.8	8.3	21.9
12.50	67.9	9.0	23.1
13.00	66.2	9.5	24.2
13.50	63.9	9.9	26.2
14.00	62.3	10.4	27.3
14.50	60.7	11.0	28.3
15.00	59.3	11.4	29.3
15.50	57.9	11.8	30.3
18.00	50.2	13.6	36.2
20.00	49.1	14.5	36.4
24.00	45.6	15.1	39.3
28.00	42.3	16.7	41.0
35.00	37.5	15.9	46.5
38.50	34.7	16.6	48.7
42.50	32.3	19.8	47.9
48.00	31.4	20.1	48.5
52.00	29.3	20.3	50.5
168 (7 days)	17.7	23.7	58.6
336 (14 days)	13.1	24.1	62.8
672 (28 days)	9.5	23.6	66.9
2400 (100 days)	9.0	25.3	65.8

Table VII. RQPA of both optimised ABY and dABY *ex-situ* pastes (0.40w/c and 1.0wt% SP) as a function of time. Taken from article #5 in Annex I. Copyright (2019) with permission from Elsevier (Annex IV).

	ABY					dABY				
t (days) / wt%	0	1	7	28	56	0	1	7	28	56
$C_4A_3\bar{S}$	8.7	2.8	0.9	-	-	4.0	3.0	0.3	-	-
$C\bar{S}$	9.7	-	-	-	-	9.8	-	-	-	-
mC_3S	18.5	9.9	5.8	3.8	1.5	6.6	4.5	2.2	0.7	0.5
βC_2S	16.2	14.9	15.6	12.6	9.5	18.8	18.6	19.3	7.8	5.7
α'_HC_2S	-	-	-	-	-	9.9	8.1	8.6	2.1	1.1
C_4AF	2.4	1.7	1.2	0.9	-	1.7	1.6	1.1	0.6	-
$CaF_2C_9S_3\bar{S}_3$	1.2	1.9	1.6	1.5	1.4	1.3	1.8	1.9	1.5	0.6
$C_{12}A_7$	-	-	-	-	-	3.4	1.2	-	-	-
AFt	**-**	**28.4**	**29.3**	**27.3**	**21.2**	**-**	**25.1**	**27.5**	**26.5**	**23.1**
AFm	-	0.2	0.8	3.5	3.8	-	-	4.0	4.7	4.0
CH	-	0.4	1.2	1.5	1.5	-	-	0.2	1.2	1.6
Katoite	-	-	-	1.8	1.7	-	-	-	-	1.1
ACn	**13.7**	**29.5**	**39.7**	**44.2**	**58.5**	**15.9**	**22.9**	**26.8**	**53.6**	**60.6**
FW	**28.6**	**10.3**	**3.9**	**3.0**	**1.0**	**28.6**	**13.2**	**8.2**	**1.3**	**3.1**

Table VIII. RQPA of both optimised ABY and dABY *ex-situ* pastes (0.50w/c and 0.4wt% SP) as a function of time. Taken from article #5 in annex I. Copyright (2019) with permission from Elsevier (Annex IV).

	ABY					dABY				
t (days) / wt%	0	1	7	28	56	0	1	7	28	56
$C_4A_3\bar{S}$	8.2	1.7	0.4	-	-	3.8	2.6	0.2	-	-
$C\bar{S}$	9.0	-	-	-	-	9.2	-	-	-	-
mC_3S	17.	8.0	4.0	1.2	1.5	6.2	4.3	1.7	0.7	1.3
βC_2S	15.2	14.3	13.0	10.5	5.6	17.5	18.6	17.7	4.7	3.3
α'_HC_2S	-	-	-	-	-	9.2	5.4	6.9	1.1	1.0
C_4AF	2.3	1.7	0.9	-	-	1.6	1.6	0.9	-	-
$CaF_2C_9S_3\bar{S}_3$	1.2	1.8	1.5	1.3	1.1	1.3	1.6	1.7	0.6	0.9
$C_{12}A_7$	-	-	-	-	-	3.2	1.2	-	-	-
AFt	**-**	**27.8**	**28.9**	**25.3**	**21.4**	**-**	**23.5**	**28.2**	**27.2**	**23.1**
AFm	-	0.17	2.9	3.6	3.7	-	-	3.2	4.0	4.0
CH	-	0.41	1.9	2.0	1.5	-	-	0.2	1.9	1.6
Katoite	-	-	-	1.3	1.4	-	-	-	0.8	1.1
ACn	**12.8**	**29.6**	**39.3**	**47.5**	**60.1**	**14.8**	**22.2**	**26.9**	**54.4**	**60.6**
FW	**33.3**	**14.5**	**7.3**	**7.3**	**3.7**	**33.3**	**19.0**	**12.5**	**4.7**	**3.1**

8.4. ANNEX IV. COPYRIGHT AGREEMENTS

Article #1. Synchrotron Radiation Pair Distribution Function Analysis of Gels in Cements

Cuesta A, Zea-Garcia JD, Londono-Zuluaga D, De la Torre AG, Santacruz I, Vallcorba O, Aranda MAG. (2017) Synchrotron Radiation Pair Distribution Function Analysis of Gels in Cements. *Crystals* 7(10), 317. DOI: 10.3390/cryst7100317

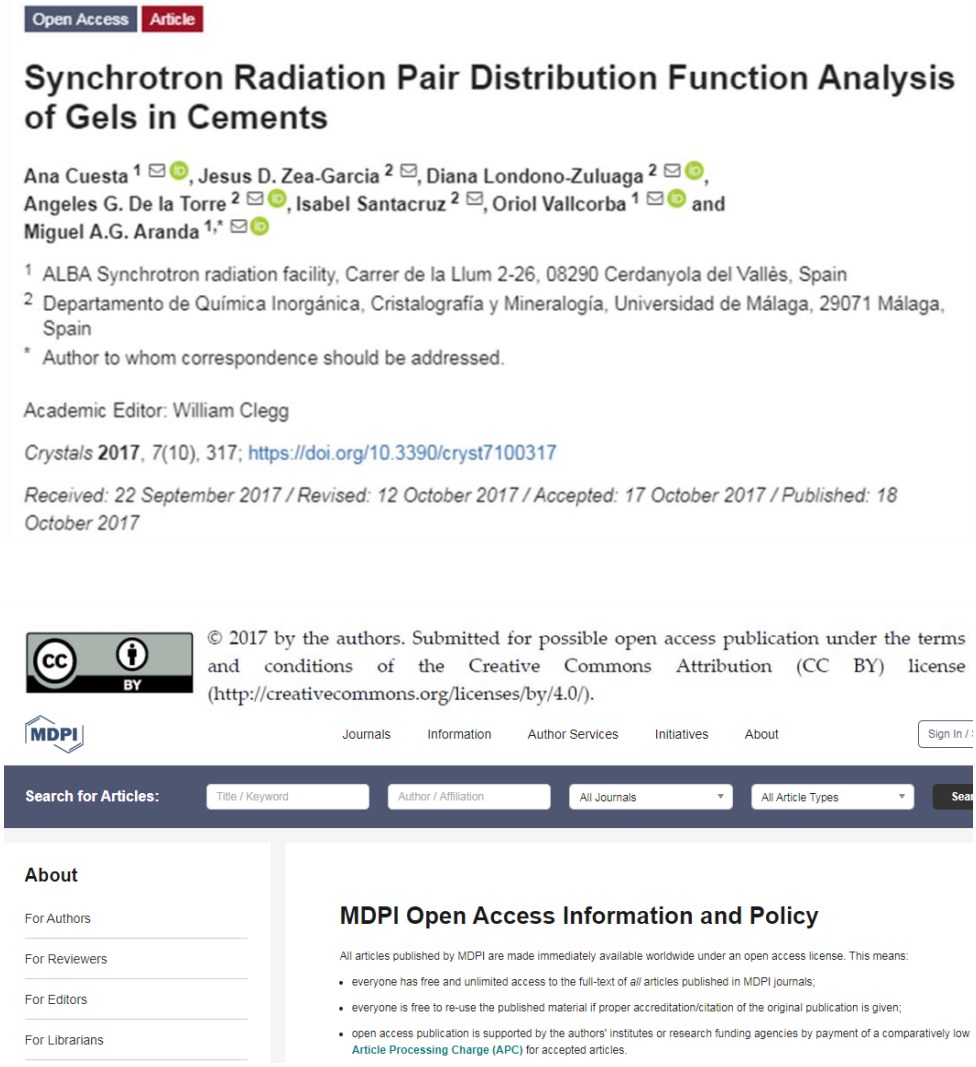

Open Access Article

Synchrotron Radiation Pair Distribution Function Analysis of Gels in Cements

Ana Cuesta [1], Jesus D. Zea-Garcia [2], Diana Londono-Zuluaga [2], Angeles G. De la Torre [2], Isabel Santacruz [2], Oriol Vallcorba [1] and Miguel A.G. Aranda [1,*]

[1] ALBA Synchrotron radiation facility, Carrer de la Llum 2-26, 08290 Cerdanyola del Vallès, Spain
[2] Departamento de Química Inorgánica, Cristalografía y Mineralogía, Universidad de Málaga, 29071 Málaga, Spain
* Author to whom correspondence should be addressed.

Academic Editor: William Clegg

Crystals **2017**, 7(10), 317; https://doi.org/10.3390/cryst7100317

Received: 22 September 2017 / Revised: 12 October 2017 / Accepted: 17 October 2017 / Published: 18 October 2017

MDPI Journals Information Author Services Initiatives About Sign In /

Search for Articles: Title / Keyword Author / Affiliation All Journals All Article Types

About

For Authors

For Reviewers

For Editors

For Librarians

MDPI Open Access Information and Policy

All articles published by MDPI are made immediately available worldwide under an open access license. This means:

- everyone has free and unlimited access to the full-text of *all* articles published in MDPI journals;
- everyone is free to re-use the published material if proper accreditation/citation of the original publication is given;
- open access publication is supported by the authors' institutes or research funding agencies by payment of a comparatively low Article Processing Charge (APC) for accepted articles.

Article #2. Multiscale understanding of tricalcium silicate hydration reactions

Cuesta A, Zea-Garcia JD, Londono-Zuluaga D, De la Torre AG, Santacruz I, Vallcorba O, Dapiaggi M, Sanfélix SG, Aranda MAG. (2018) Multiscale understanding of tricalcium silicate hydration reactions. *Scientific Reports* 8:8544. DOI: 10.1038/s41598-018-26943-y

www.nature.com/scientificreports

OPEN

Multiscale understanding of tricalcium silicate hydration reactions

Received: 12 February 2018
Accepted: 14 May 2018
Published online: 04 June 2018

Ana Cuesta[1,2], Jesus D. Zea-Garcia[2], Diana Londono-Zuluaga[2], Angeles G. De la Torre[2], Isabel Santacruz[2], Oriol Vallcorba[1], Monica Dapiaggi[3], Susana G. Sanfélix[2,4] & Miguel A. G. Aranda[1]

www.nature.com/scientificreports/

Article #3. Synchrotron pair distribution function analyses of ye'elimite-based pastes

Cuesta A, Zea-Garcia JD, De la Torre AG, Santacruz I, Aranda MAG. (2019) Synchrotron pair distribution function analyses of ye'elimite-based pastes. *Advance in Cement Research* 31(3), 138-146. DOI: 10.1680/jadcr.18.00097

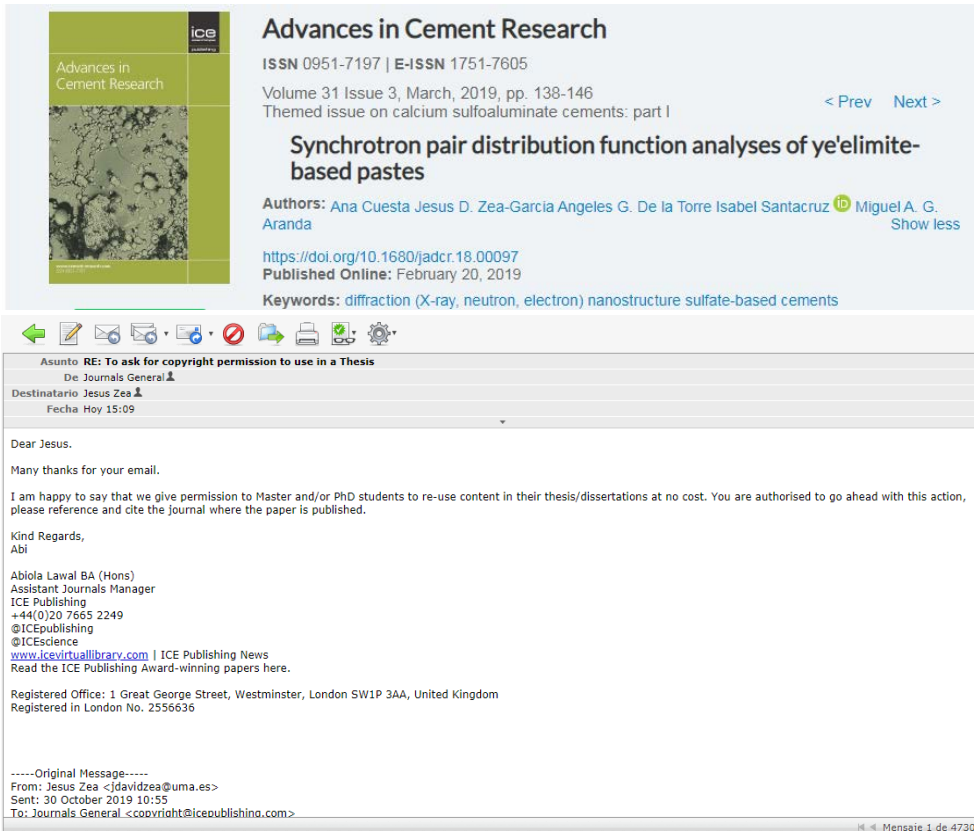

Advances in Cement Research

ISSN 0951-7197 | E-ISSN 1751-7605

Volume 31 Issue 3, March, 2019, pp. 138-146
Themed issue on calcium sulfoaluminate cements: part I

< Prev Next >

Synchrotron pair distribution function analyses of ye'elimite-based pastes

Authors: Ana Cuesta Jesus D. Zea-Garcia Angeles G. De la Torre Isabel Santacruz Miguel A. G. Aranda Show less

https://doi.org/10.1680/jadcr.18.00097
Published Online: February 20, 2019

Keywords: diffraction (X-ray, neutron, electron) nanostructure sulfate-based cements

Asunto RE: To ask for copyright permission to use in a Thesis
De Journals General
Destinatario Jesus Zea
Fecha Hoy 15:09

Dear Jesus.

Many thanks for your email.

I am happy to say that we give permission to Master and/or PhD students to re-use content in their thesis/dissertations at no cost. You are authorised to go ahead with this action, please reference and cite the journal where the paper is published.

Kind Regards,
Abi

Abiola Lawal BA (Hons)
Assistant Journals Manager
ICE Publishing
+44(0)20 7665 2249
@ICEpublishing
@ICEscience
www.icevirtuallibrary.com | ICE Publishing News
Read the ICE Publishing Award-winning papers here.

Registered Office: 1 Great George Street, Westminster, London SW1P 3AA, United Kingdom
Registered in London No. 2556636

-----Original Message-----
From: Jesus Zea <jdavidzea@uma.es>
Sent: 30 October 2019 10:55
To: Journals General <copyright@icepublishing.com>

Mensaje 1 de 4730

Acknowledgement***: Reproduced by permission of ICE Publishing.***

Article #4. Alite-belite-ye'elimite cements: Effect of dopants on the clinker phase composition and properties

Zea-Garcia JD, Santacruz I, Aranda MAG, De la Torre AG. (2019) Alite-belite-ye'elimite cements: Effect of dopants on the clinker phase composition and properties. *Cement and Concrete Research* 115, 192-202. DOI: 10.1016/j.cemconres.2018.10.019

Copyright Clearance Center RightsLink®

Home | Account Info | Help

Title: Alite-belite-ye'elimite cements: Effect of dopants on the clinker phase composition and properties

Author: Jesus D. Zea-Garcia,Isabel Santacruz,Miguel A.G. Aranda,Angeles G. De la Torre

Publication: Cement and Concrete Research

Publisher: Elsevier

Date: January 2019

Logged in as:
Jesús David Zea García
LOGOUT

Please note that, as the author of this Elsevier article, you retain the right to include it in a thesis or dissertation, provided it is not published commercially. Permission is not required, but please ensure that you reference the journal as the original source. For more information on this and on your other retained rights, please visit: https://www.elsevier.com/about/our-business/policies/copyright#Author-rights

BACK | CLOSE WINDOW

Article #5. Processing and characterization of standard and doped alite-belite-ye'elimite ecocement pastes and mortars

Zea-Garcia JD, De la Torre AG, Aranda MAG, Santacruz I. (2019) Processing and characterization of standard and doped alite-belite-ye'elimite ecocement pastes and mortars. *Cement and Concrete Research* 127, 105911. DOI: 10.1016/j.cemconres.2019.105911

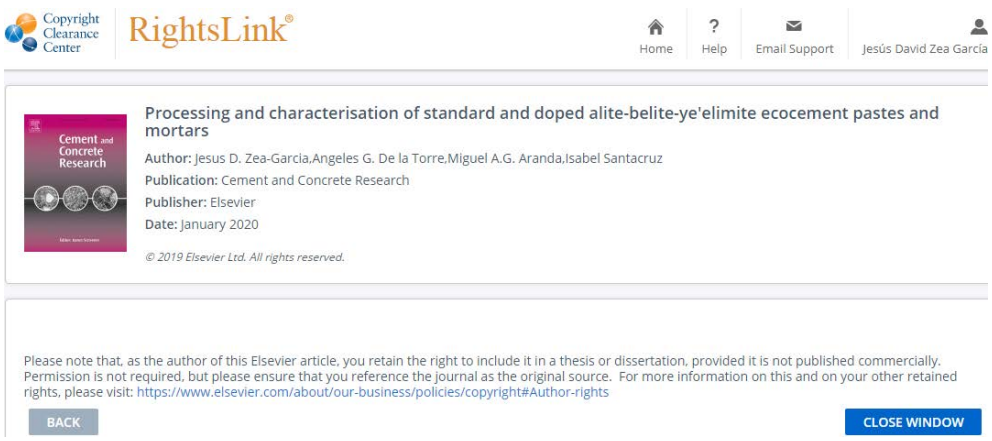

Article #6. Hydration Activation of Alite-Belite-Ye'elimite Cements by Doping with Boron

Zea-Garcia JD, Sanfelix SG, Vallcorba O, Aranda MAG, Santacruz I, De la Torre AG. (2020) Hydration Activation of Alite-Belite-Ye'elimite Cements by Doping with Boron. *ACS Sustainable Chemistry & Engineering* 8, 3583−3590. DOI: 10.1021/acssuschemeng.9b05975

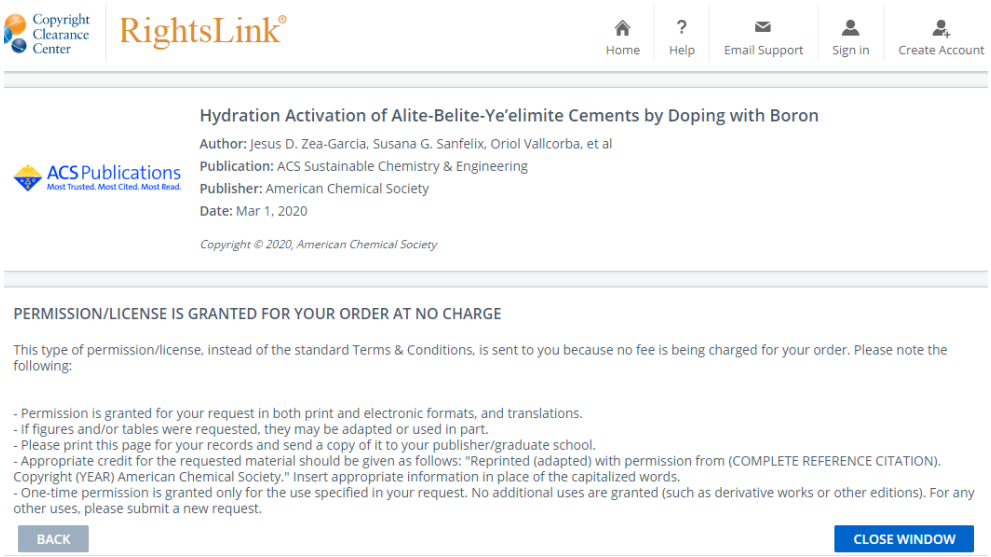

Copyright Clearance Center RightsLink®

Home | Help | Email Support | Sign in | Create Account

Hydration Activation of Alite-Belite-Ye'elimite Cements by Doping with Boron

Author: Jesus D. Zea-Garcia, Susana G. Sanfelix, Oriol Vallcorba, et al

Publication: ACS Sustainable Chemistry & Engineering

Publisher: American Chemical Society

Date: Mar 1, 2020

Copyright © 2020, American Chemical Society

ACS Publications
Most Trusted. Most Cited. Most Read.

PERMISSION/LICENSE IS GRANTED FOR YOUR ORDER AT NO CHARGE

This type of permission/license, instead of the standard Terms & Conditions, is sent to you because no fee is being charged for your order. Please note the following:

- Permission is granted for your request in both print and electronic formats, and translations.
- If figures and/or tables were requested, they may be adapted or used in part.
- Please print this page for your records and send a copy of it to your publisher/graduate school.
- Appropriate credit for the requested material should be given as follows: "Reprinted (adapted) with permission from (COMPLETE REFERENCE CITATION). Copyright (YEAR) American Chemical Society." Insert appropriate information in place of the capitalized words.
- One-time permission is granted only for the use specified in your request. No additional uses are granted (such as derivative works or other editions). For any other uses, please submit a new request.

BACK | CLOSE WINDOW

Figure 1.1. The worldwide cement production, by major producing countries, from 2014 to 2018. Modified from [6].

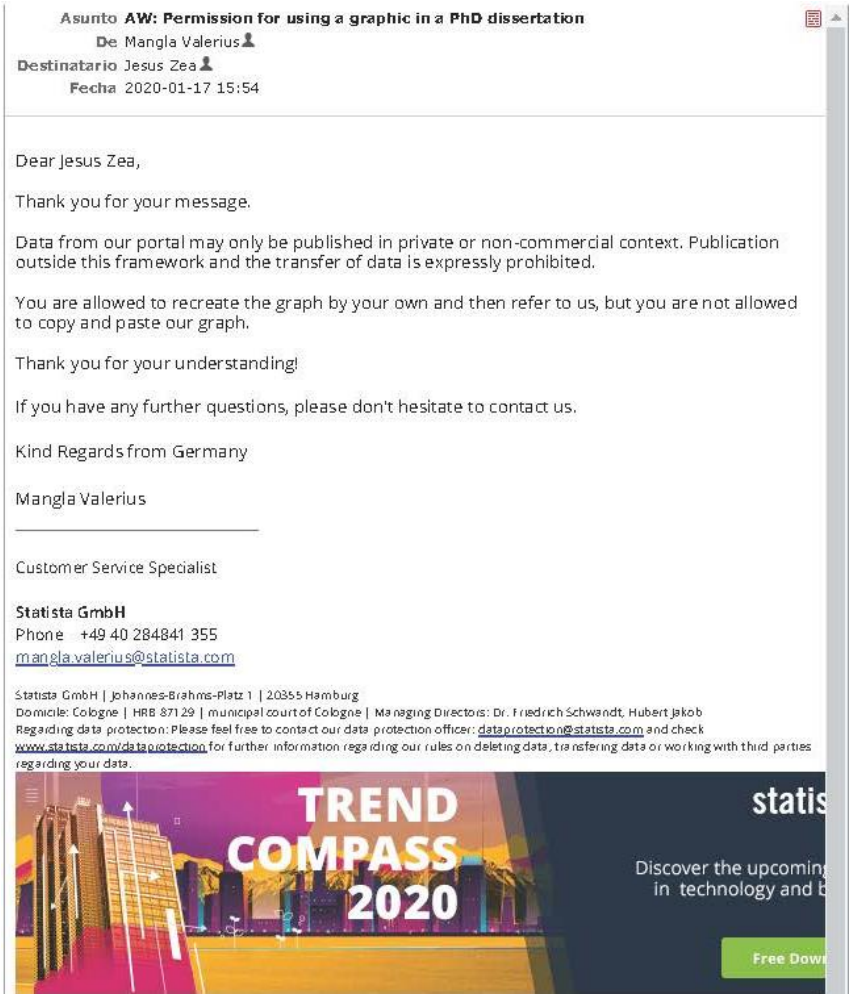

Asunto AW: Permission for using a graphic in a PhD dissertation
De Mangla Valerius
Destinatario Jesus Zea
Fecha 2020-01-17 15:54

Dear Jesus Zea,

Thank you for your message.

Data from our portal may only be published in private or non-commercial context. Publication outside this framework and the transfer of data is expressly prohibited.

You are allowed to recreate the graph by your own and then refer to us, but you are not allowed to copy and paste our graph.

Thank you for your understanding!

If you have any further questions, please don't hesitate to contact us.

Kind Regards from Germany

Mangla Valerius

Customer Service Specialist

Statista GmbH
Phone +49 40 284841 355
mangla.valerius@statista.com

Statista GmbH | Johannes-Brahms-Platz 1 | 20355 Hamburg
Domicile: Cologne | HRB 87129 | municipal court of Cologne | Managing Directors: Dr. Friedrich Schwandt, Hubert Jakob
Regarding data protection: Please feel free to contact our data protection officer: dataprotection@statista.com and check www.statista.com/dataprotection for further information regarding our rules on deleting data, transfering data or working with third parties regarding your data.